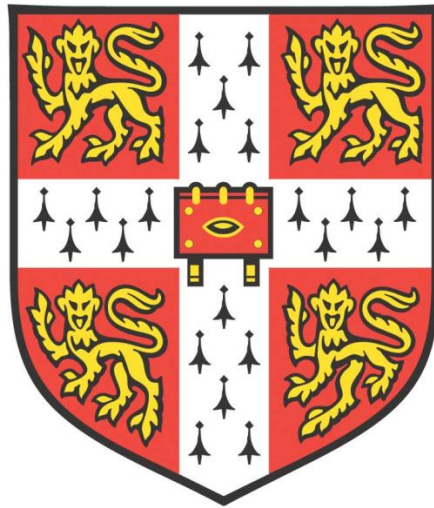


*VALIDATION OF PHOTOACOUSTIC IMAGING  
BIOMARKERS IN CANCER BIOLOGY*



**Lina Hacker**

Corpus Christi College

Supervisor: Prof. Sarah E. Bohndiek

Department of Physics and Cancer Research UK Cambridge Institute

University of Cambridge

This dissertation is submitted for the degree of

Doctor of Philosophy

April 2022



*To my family.*



## DECLARATION

This thesis is the result of my own work and includes nothing which is the outcome of work done in collaboration except as declared in the preface and specified in the text. It is not substantially the same as any work that has already been submitted before for any degree or other qualification except as declared in the preface and specified in the text. It does not exceed the prescribed word limit for the Clinical Medicine and Clinical Veterinary Medicine Degree Committee of 60,000 words.

Signed: [Signature redacted]

---

Date: 15.04.2022

Lina Hacker, BSc, MEng

Cambridge



# SUMMARY

## VALIDATION OF PHOTOACOUSTIC IMAGING BIOMARKERS IN CANCER BIOLOGY

Lina Hacker

Perfusion-limited hypoxia, referring to spatial and temporal fluctuations in oxygen levels, has emerged as a key driver of malignant disease progression in cancer, promoting higher metastatic potential, increased therapy resistance and poorer patient outcome<sup>1,2</sup>. However, the origin and impact of these hypoxic fluctuations on tumour progression have not yet been fully understood. Harnessing the photoacoustic effect, photoacoustic imaging (PAI) holds significant potential to elucidate these dynamics, but to fulfil this potential, a need for a thorough technical and biological validation arises. This thesis presents technical validation of PAI systems, which builds confidence in the subsequent biological validation performed using relevant biomarkers in the studies of perfusion-limited hypoxia.

First, the current state-of-the-art phantom materials in biophotonics are surveyed and general design considerations for preparation of tissue-mimicking phantoms are discussed to guide the development of a stable phantom material in PAI. Acoustic and optical material characterisation systems are then established and validated to enable thorough characterisation of phantom materials. Building up on this groundwork, a phantom material is developed for use in PAI, which exhibits stable acoustic, optical and mechanical properties with tuneable tissue-mimicking characteristics. Using custom phantom setups, a thorough technical characterisation study of a commercial mesoscopic PAI system is then conducted, outlining strengths and limitations of the system in characterising vessel-related biomarkers in tissues. Following these technical validation studies, the thesis embarks on applying photoacoustic mesoscopy and macroscopy in studies of perfusion-limited hypoxia in two distinct murine xenograft models, and validating this work using histopathological and transcriptomic analyses. These studies indicate that tumour vasculature undergoes rapid fluctuations in perfusion that are impacted by the underlying maturity of the vascular network, leading to variations in tumour oxygenation.

Building up on an extensive validation framework, this thesis highlights the promise of PAI to advance our understanding on perfusion- and oxygenation dynamics in tumour tissues, thereby assisting the development of targeted treatment regimes in future.



## ACKNOWLEDGEMENTS

This thesis owes a lot to a lot of people.

First and foremost, I wish to express my deepest gratitude to Prof. Sarah Bohndiek for offering me this extraordinary opportunity to conduct a PhD in her research group. Thank you, Sarah, for listening whenever it is needed, for magically transforming my (often incoherent) scribbles into something readable, for guiding me whenever I lose sight of the next steps, and for creating such a wonderful working environment in which encouragement, friendliness and camaraderie keep pace with scientific brilliance. I am most grateful for your tremendous support and patience, for your constant availability and understanding, and for being such an inspiring researcher, advisor, and mentor.

I also wish to express my deepest gratitude for the support, advice, and technical expertise of my second supervisor from the National Physical Laboratory, Dr. Srinath Rajagopal, whose insightful suggestions always helped to push the work forward. My thanks also extend to my Thesis Committee members, and to all the brilliant collaborators I was honoured to work with during my PhD, particularly Dr. James Joseph, Dr. Heidrun Wabnitz, Dr. Aoife Ivory and Dr. Bajram Zeqiri. Their support has proved to be invaluable for the work conducted in this thesis. In addition, I wish to acknowledge the generous funding support from the National Physical Laboratory.

Furthermore, I would like to highlight the exceptional research support of the core facilities at the CRUK Cambridge Institute, particularly the biorepository, genomics, and histopathology unit. Their unwavering patience and assistance were indispensable to the work conducted here.

Jo, Isa, and James – thank you for guiding me when I first arrived, and for patiently answering all my questions as a naïve novice. Paul, Calum, Graham, Michaela, Janek, Katie-Lou, Marlous — thank you all for being amazing co-workers, brilliant minds, and good friends. I will miss our interesting discussions, both scientific and beyond. Tom, Marilena, Adrian, Thierry, Ellie, Emma — I am so fortunate to have you in my life, helping me to look forward to arriving at the Department every day. Thank you for the coffee and lunch breaks, nights out in College bars, and fun Friday evenings, and for all the laughter and warm words. I am whole-heartedly grateful for your friendship and encouragement, which proved fundamental to the accomplishment of this thesis

I also wish to express my deepest gratitude to Dale for being an exceptional friend and supporter, for always bringing a smile to my face, and for giving me a second home in London on the occasions when Cambridge became a bit too small — and thanks to his brother Aaron for being such a kind and patient person, enduring our science talks (and senseless chatter).

I am also most grateful for all my friends at Corpus Christi College who accompanied me on this journey. In particular, I wish to thank Lotta who was always able to bring a light into grey lockdown weekends with her kind-hearted, compassionate nature. Immense thanks also go to Céline and Lorenzo

— the best housemates I could have asked for. I will miss our weekend dinners and brunches, the bike rides home on a long Saturday night out, the celebrations of each other's accomplishments. I am also indebted to my old friends in Münster, and Bonn, particularly Sophie R., Lena, Sophie C., and Nina, for always making it feel like no time has passed whenever we see each other.

Finally, I wish to thank my family, my parents, my sister Hannah, and my brother Stefan, for their love and trust over the years, for teaching me how to not give up and stay optimistic, and for always believing in me. Their love and advice always stay with me, shaping me into who I am today.

My four years in Cambridge have truly been one of the most exciting, challenging, and inspiring times of my life — years for which I will be forever grateful and whose precious memories I will treasure.



# CONTENTS

<b>1 INTRODUCTION .....</b>	<b>1</b>
1.1 HYPOXIA IN ONCOLOGY.....	1
1.1.1 <i>Structural abnormalities of the tumour vasculature</i> .....	1
1.1.2 <i>The role of hypoxia in treatment response</i> .....	3
1.2 DIFFUSION- VERSUS PERFUSION-LIMITED HYPOXIA.....	3
1.2.1 <i>Diffusion-limited hypoxia</i> .....	4
1.2.2 <i>Perfusion-limited hypoxia</i> .....	4
1.2.3 <i>Differences in biological effects between diffusion- and perfusion-limited hypoxia</i> ....	5
1.2.4 <i>Methods to detect perfusion-limited hypoxia</i> .....	7
1.3 CONCEPT OF PAI .....	9
1.3.1 <i>Potential of PAI to evaluate perfusion-limited hypoxia at different scales</i> .....	11
1.3.2 <i>Challenges in measuring perfusion-limited hypoxia with PAI</i> .....	12
1.4 THESIS OBJECTIVES AND OUTLOOK .....	14
<b>2 PHANTOM MATERIALS IN BIOPHOTONICS .....</b>	<b>15</b>
2.1 INTRODUCTION .....	16
2.1.1 <i>General phantom design considerations</i> .....	16
2.1.2 <i>Physical properties of soft tissues</i> .....	17
<i>The role of phantoms in the translational research pipeline</i> .....	18
2.1.3 <i>Phantom design properties</i> .....	19
2.2 MATERIALS AND METHODS FOR PREPARATION OF BIOPHOTONIC PHANTOMS .....	21
2.2.1 <i>Tuning of optical and acoustic properties</i> .....	23
2.2.2 <i>Aqueous suspensions</i> .....	28
2.2.3 <i>Hydrogels</i> .....	28
2.2.4 <i>Non-water-based materials</i> .....	29
2.3 CONCLUSION: PHANTOM MATERIALS AND STANDARDISATION EFFORTS FOR PHOTOACOUSTIC IMAGING.....	32
<b>3 VALIDATION OF MATERIAL CHARACTERISATION METHODS.....</b>	<b>35</b>
3.1 VALIDATION OF THE DOUBLE-INTEGRATING SPHERE OPTICAL CHARACTERISATION SYSTEM	36
3.1.1 <i>Introduction</i> .....	36
3.1.2 <i>Methods</i> .....	37
3.1.3 <i>Results</i> .....	42
3.1.4 <i>Discussion</i> .....	48
3.2 CREATION AND VALIDATION OF SMALL-SCALE ACOUSTIC SYSTEM.....	51
3.2.1 <i>Introduction</i> .....	51
3.2.2 <i>Methods</i> .....	51

3.2.3 Results.....	55
3.2.4 Discussion.....	57
3.3 CONCLUSION.....	59
<b>4 DEVELOPMENT OF A COPOLYMER-IN-OIL TISSUE MIMICKING PHANTOM MATERIAL .....</b>	<b>61</b>
4.1 INTRODUCTION .....	62
4.2 METHODS.....	63
4.2.1 Phantom fabrication.....	63
4.2.2 Acoustic characterisation.....	65
4.2.3 Optical characterisation.....	67
4.2.4 Stability studies.....	67
4.2.5 Photoacoustic imaging.....	68
4.2.6 Image and Statistical analysis.....	69
4.3 RESULTS.....	71
4.3.1 Systematic optimisation of copolymer-in-oil materials results in high speed of sound.....	71
4.3.2 Negligible optical absorption and scattering of the copolymer-in-oil material facilitates tuning of optical properties through additives.....	73
4.3.3 The copolymer-in-oil material demonstrates good photo and thermomechanical stability.....	74
4.3.4 Defined acoustic and optical properties in the material are repeatable and temporally stable.....	76
4.3.5 Phantom design and field testing .....	77
4.4 DISCUSSION .....	79
4.5 CONCLUSION.....	81
<b>5 EVALUATION OF PRECISION AND ACCURACY IN PHOTOACOUSTIC MESOSCOPY</b>	<b>83</b>
5.1 INTRODUCTION .....	84
5.2 METHODS.....	86
5.2.1 Phantom preparation.....	86
5.2.2 Animal handling.....	88
5.2.3 Image acquisition.....	88
5.2.4 Image and statistical analysis .....	89
5.3 RESULTS.....	91
5.3.1 Overview of the dominant artefact types in photoacoustic mesoscopy.....	91
5.3.2 Geometric sensitivity of photoacoustic mesoscopy.....	92
5.3.3 Photoacoustic mesoscopy shows high precision for repeated measurement.....	94
5.3.4 Photoacoustic mesoscopy shows high precision during in vivo application.....	95

5.4 DISCUSSION .....	98
<b>6 APPLICATION OF PHOTOACOUSTIC MESOSCOPY AND MACROSCOPY TO STUDIES ON PERFUSION-LIMITED HYPOXIA .....</b>	<b>101</b>
6.1 INTRODUCTION .....	102
6.2 METHODS.....	103
6.2.1 <i>Cell lines</i> .....	103
6.2.2 <i>Mouse models</i> .....	103
6.2.3 <i>Tomographic photoacoustic imaging</i> .....	104
6.2.4 <i>Mesoscopic photoacoustic imaging</i> .....	107
6.2.5 <i>Tissue processing for histopathology and image analysis</i> .....	107
6.2.6 <i>RNA analysis</i> .....	108
6.2.7 <i>Photoacoustic data analysis</i> .....	109
6.2.8 <i>Statistical analysis</i> .....	111
6.3 RESULTS.....	112
6.3.1 <i>MDA-MB-231 shows more aggressive tumour growth than MCF7</i> .....	112
6.3.2 <i>Photoacoustic tomography reveals differences in oxygen availability and distribution     between both models</i> .....	112
6.3.3 <i>MDA-MB-231 tumours show higher variability in oxygenation than MCF7 tumours</i> .....	113
6.3.4 <i>OE- and DCE-OT underline differences in vascular functionality and perfusion</i> ..	115
6.3.5 <i>Photoacoustic mesoscopy reveals morphological changes along tumour growth</i> ..	116
6.3.6 <i>Photoacoustic mesoscopy reveals differences in perfusion</i> .....	118
6.3.7 <i>Immunohistochemistry analysis supports the finding of a less mature, more hypoxic vascular     phenotype in MDA-MB-231</i> .....	120
6.3.8 <i>Gene expression supports a more hypoxic, angiogenic phenotype of MDA-MB-231</i> .....	123
6.3.9 <i>Histopathological and photoacoustic biomarkers correlate with underlying genetic     phenotype</i> .....	127
6.4 DISCUSSION .....	128
<b>7 CONCLUSION AND OUTLOOK .....</b>	<b>133</b>
<b>8 REFERENCES .....</b>	<b>137</b>

# LIST OF TABLES

TABLE 1.1: TYPES OF VESSEL FORMATION IN TUMOUR TISSUE <sup>16</sup> .....	2
TABLE 1.2: OVERVIEW OF DIRECT METHODS USED FOR MEASURING PERFUSION-LIMITED HYPOXIA. .....	8
TABLE 1.3: COMPARISON OF PRECLINICAL IMAGING MODALITIES.....	11
TABLE 2.1: DEFINITION OF RELEVANT OPTICAL AND ACOUSTIC MEASUREMENT PARAMETERS IN BIOPHOTONIC IMAGING.....	18
TABLE 2.2: RELEVANT OPTICAL AND ACOUSTIC PARAMETERS OF DIFFERENT MATERIALS WITHOUT THE USE OF ADDITIVES.....	22
TABLE 2.3: COMMON ADDITIVES FOR TUNING INTRINSIC PROPERTIES IN WATER-BASED PHANTOM MATERIALS PROPOSED FOR BIOPHOTONIC IMAGING.....	25
TABLE 2.4: ADDITIVES FOR TUNING RELEVANT ACOUSTIC AND OPTICAL PROPERTIES IN NON-WATER- BASED PHANTOM MATERIALS PROPOSED FOR BIOPHOTONIC IMAGING.....	26
TABLE 2.5: COMPARISON OF RELEVANT PROPERTIES OF MATERIALS USED FOR BIOPHOTONIC PHANTOMS.....	27
TABLE 3.1: COMPOSITION OF AGAR PHANTOM SAMPLES.....	40
TABLE 3.2: CONCENTRATIONS OF SCATTERER AND ABSORBER IN COPOLYMER-IN-OIL PHANTOM SAMPLES.....	40
TABLE 3.3: REPEATABILITY OF REFERENCE MEASUREMENTS.....	42
TABLE 3.4: REPEATABILITY OF SAMPLE MEASUREMENTS FOR OPTICAL ABSORPTION ( $\mu_a$ ) AND REDUCED SCATTERING COEFFICIENTS ( $\mu_s'$ ). .....	43
TABLE 3.5: OVERVIEW OF PERCENTAGE DIFFERENCE BETWEEN DOUBLE-INTEGRATING SPHERE AND TIME-DOMAIN OPTICAL CHARACTERISATION METHODS.....	47
TABLE 3.6: POLYNOMIAL COEFFICIENTS $A_i$ FOR FORMULA DESCRIBING THE TEMPERATURE DEPENDENCE OF SPEED OF SOUND IN WATER <sup>421</sup> .....	55
TABLE 4.1: OVERVIEW OF ACOUSTIC AND OPTICAL PROPERTIES FOUND IN SOFT TISSUES.....	63
TABLE 4.2: SUMMARY OF THE PHANTOM COMPOSITIONS FOR THE ACOUSTIC ANALYSIS.....	65
TABLE 4.3: SUMMARY OF THE PHANTOM COMPOSITIONS FOR THE OPTICAL ANALYSIS. ....	65
TABLE 5.1: COEFFICIENTS OF VARIATION (COV) FOR TEMPORAL STABILITY OF THE PHOTOACOUSTIC MESOSCOPY SYSTEM.....	94

TABLE 6.1: OVERVIEW OF SAMPLE DISTRIBUTIONS. ....	106
TABLE 6.2: OVERVIEW OF HISTOLOGICAL AND IHC MARKERS USED.....	108
TABLE 6.3: CORRELATION BETWEEN PERFUSION-LIMITED HYPOXIA PAI BIOMARKERS AND IHC MARKERS.....	123
TABLE 6.4: CORRELATION BETWEEN PERFUSION-LIMITED HYPOXIA PAI BIOMARKERS AND GSVA SCORES. ....	127

# LIST OF FIGURES

FIGURE 1.1: DIFFERENCES BETWEEN DIFFUSION-LIMITED (CHRONIC) AND PERFUSION-LIMITED (CYCLING) HYPOXIA.....	3
FIGURE 1.2: PHOTOACOUSTIC SIGNAL GENERATION.....	10
FIGURE 1.3: ABSORPTION SPECTRA OF THE MAIN ENDOGENOUS CHROMOPHORE.....	10
FIGURE 2.1: TASKS OF PHANTOMS ALONG THE TRANSLATIONAL PIPELINE.....	19
FIGURE 2.2 : BASE REQUIREMENTS FOR A PAI PHANTOM.....	20
FIGURE 3.1: SETUP OF THE DOUBLE-INTEGRATING SPHERE SYSTEM FOR DETERMINATION OF ABSORPTION AND SCATTERING COEFFICIENT.....	38
FIGURE 3.2: DIS REFERENCE SPECTRA.....	43
FIGURE 3.3: REPEATABILITY OF SAMPLE MEASUREMENT OF THE DIS SYSTEM.....	44
FIGURE 3.4: IMPACT OF VARIATION OF IAD INPUT VARIABLES ON RESULTING OPTICAL ABSORPTION AND REDUCED SCATTERING COEFFICIENT.....	45
FIGURE 3.5: COMPARISON OF EXPERIMENTAL $\mu_s'$ VALUES WITH SIMULATED ONES USING MIE THEORY.....	46
FIGURE 3.6: COMPARISON OF THE DIS TECHNIQUE WITH TIME-DOMAIN OPTICAL CHARACTERISATION METHOD.....	47
FIGURE 3.7: SETUP OF THE ACOUSTIC CHARACTERISATION SYSTEM.....	53
FIGURE 3.8: RAW ACOUSTIC PULSES.....	54
FIGURE 3.9: PERFORMANCE OF THE ACOUSTIC CHARACTERISATION SYSTEM IN MEASURING LIQUID AND SOLID SAMPLES.....	55
FIGURE 3.10: IMPACT OF VARIATION IN SAMPLE THICKNESS AND TEMPERATURE ON ACOUSTIC PROPERTIES.....	57
FIGURE 4.1: COMPARISON OF SPEED OF SOUND AND ACOUSTIC ATTENUATION COEFFICIENT OF SAMPLES COMPOSED OF DIFFERENT POLYMER TYPES.....	72
FIGURE 4.2: INDEPENDENT TUNING OF THE REDUCED SCATTERING AND OPTICAL ABSORPTION COEFFICIENTS BY VARIATION OF TITANIUM DIOXIDE AND NIGROSIN CONCENTRATIONS.....	74
FIGURE 4.3: PHOTO AND THERMOMECHANICAL STABILITY OF THE PHANTOM MATERIAL.....	75
FIGURE 4.4: STABILITY OF ACOUSTIC AND OPTICAL PROPERTIES OVER TIME.....	77

FIGURE 4.5: COPOLYMER-IN OIL MATERIAL ALLOWS THE CREATION OF VERSATILE PHANTOM DESIGNS FOR DIFFERENT SYSTEM CONFIGURATIONS.....	78
FIGURE 5.1: PHANTOM DESIGN FOR THE TECHNICAL VALIDATION STUDIES. ....	87
FIGURE 5.2: OVERVIEW OF THE PHOTOACOUSTIC MESOSCOPY SYSTEM. ....	89
FIGURE 5.3: OVERVIEW OF ARTEFACTS ARISING IN PHOTOACOUSTIC MESOSCOPY. ....	92
FIGURE 5.4: GEOMETRIC SENSITIVITY OF THE PHOTOACOUSTIC MESOSCOPY SYSTEM. ....	93
FIGURE 5.5: TEMPORAL STABILITY OF THE PHOTOACOUSTIC MESOSCOPY SYSTEM. ....	95
FIGURE 5.6: OVERVIEW OF BIOLOGICAL AND TECHNICAL VARIATION FACTORS IN PHOTOACOUSTIC IMAGING (MSU=MULTISPECTRAL UNMIXING).....	96
FIGURE 5.7: TRANSDUCER COMPRESSION IMPACTS VESSEL VISUALISATION. ....	96
FIGURE 5.8: IMPACT OF TIME, POSITIONING, TISSUE AND OPERATOR-DEPENDENT VARIATION SOURCES ON THE SIGNAL STABILITY OF THE MESOSCOPIC SYSTEM <i>IN VIVO</i> . ....	97
FIGURE 6.1: SCHEMATIC OVERVIEW ON THE EXPERIMENTAL SCHEDULE.....	104
FIGURE 6.2: SYSTEM CONFIGURATIONS OF THE TOMOGRAPHIC AND MESOSCOPIC PAI SYSTEM.	105
FIGURE 6.3: 3D-COREGISTRATION OF MESOSCOPIC PAI TIME SERIES DATA. ....	111
FIGURE 6.4: GROWTH CURVES OF MDA-MB-231 (N=12, BLACK) AND MCF7 (N=14, PINK) TUMOURS. ....	112
FIGURE 6.5: PHOTOACOUSTIC TOMOGRAPHY REVEALS POORER OXYGENATION AND GREATER HETEROGENEITY IN OXYGENATION IN MDA-MB-231 TUMOURS COMPARED TO MCF7.	113
FIGURE 6.6: OXYGEN VARIABILITY ANALYSIS OF THE $SO_2^{MSOT}$ CURVES IN MDA-MB-231 AND MCF7 TUMOUR-BEARING MICE. ....	114
FIGURE 6.7: PHOTOACOUSTIC TOMOGRAPHY REVEALS SPATIAL DISTRIBUTION OF OXYGEN AND PERFUSION DYNAMICS. ....	115
FIGURE 6.8: PHOTOACOUSTIC MESOSCOPY REVEALS DEVELOPMENT OF DISTINCT VASCULAR PHENOTYPES OVER TIME.....	117
FIGURE 6.9: VASCULAR MORPHOLOGY METRICS OF MCF7 AND MDA-MB-231 TUMOURS INVESTIGATED LONGITUDINALLY DURING TUMOUR GROWTH.....	118
FIGURE 6.10: VARIATION OF VASCULAR MORPHOLOGY METRICS IN MDA-MB-231 AND MCF7 TUMOURS.....	119
FIGURE 6.11: MDA-MB-231 AND MCF7 DISPLAY VARIATION IN PERFUSION OVER TIME.....	119

FIGURE 6.12: MDA-MB-231 ARE CHARACTERISED BY HIGHER HYPOXIA AND NECROSIS AT THE FINAL TIME POINT. ....	121
FIGURE 6.13: MDA-MB-231 SHOW HIGHER VESSEL DENSITY WITH LOWER MATURITY AT THE FINAL TIME POINT. ....	122
FIGURE 6.14: NON-CYCLING FRACTIONS QUALITATIVELY APPEAR TO MAP TO NECROTIC REGIONS. ....	123
FIGURE 6.15: MDA-MB-231 AND MCF7 DISPLAY SIGNIFICANT DIFFERENCES IN HYPOXIA AND ANGIOGENESIS-RELATED GENE EXPRESSION. ....	124
FIGURE 6.16: HEATMAP DISPLAYING RELATIVE EXPRESSION OF 196 GENES IN A HYPOXIA GENE SIGNATURE IN MCF7 AND MDA-MB-231 TUMOURS.....	125
FIGURE 6.17: HEATMAP DISPLAYING RELATIVE EXPRESSION OF 33 GENES IN AN ANGIOGENESIS GENE SIGNATURE IN MCF7 AND MDA-MB-231 TUMOURS.....	126

## LIST OF ABBREVIATIONS AND ACRONYMS

---

<b>Acronym</b>	<b>Definition</b>
<b>3D</b>	Three-dimensional
<b>ACR</b>	American College of Radiology
<b>Al<sub>2</sub>O<sub>3</sub></b>	Aluminium oxide
<b>ASMA</b>	Alpha smooth muscle actin
<b>CAD</b>	Computer aided design
<b>CAS</b>	Chemical abstract service numbers
<b>CAIX</b>	Carbonic anhydrase IX
<b>COV</b>	Coefficient of variation
<b>CRUK</b>	Cancer Research UK Cambridge Institute
<b>CT</b>	Computed tomography
<b>DIS</b>	Double-integrating sphere system
<b>DMSO</b>	Dimethyl sulfoxide
<b>FWHM</b>	Full width at half maximum
<b>HbO<sub>2</sub></b>	Oxyhaemoglobin
<b>H&amp;E</b>	Haematoxylin and eosin
<b>HIF</b>	Hypoxia-inducible factor
<b>GSEA</b>	Gene set enrichment analysis
<b>GSVA</b>	Gene set variation analysis
<b>IAD</b>	Inverse adding-doubling
<b>ICG</b>	Indocyanine green
<b>IHC</b>	Immunohistochemistry
<b>IPASC</b>	International Photoacoustic Standardisation Consortium
<b>LDPE</b>	Low-density polyethylene
<b>MIP</b>	Maximum intensity projection
<b>MRI</b>	Magnetic resonance imaging

<b>MSOT</b>	Multispectral optoacoustic tomography
<b>MW</b>	Molecular weight
<b>NIR</b>	Near infrared
<b>NPL</b>	National Physical Laboratory
<b>PAI</b>	Photoacoustic imaging
<b>PET</b>	Positron-emission-tomography
<b>pO<sub>2</sub></b>	Partial pressure of oxygen
<b>PMMA</b>	Polymethylmethacrylate
<b>PTB</b>	Physikalisch-Technische Bundesanstalt
<b>PVA</b>	Polyvinyl alcohol
<b>PVCP</b>	Polyvinyl chloride plastisol
<b>RHb</b>	Deoxyhaemoglobin
<b>ROS</b>	Reactive oxygen species
<b>RSOM</b>	Raster-scanning optoacoustic mesoscopy
<b>RTV</b>	Room-temperature vulcanizing
<b>SBS</b>	Poly(styrene-butadiene-styrene)
<b>SD</b>	Standard deviation
<b>SEBS</b>	Polystyrene-block-poly(ethylene-ran-butylene)-block-polystyrene
<b>SEM</b>	Standard error of the mean
<b>SI</b>	International system of units
<b>sO<sub>2</sub></b>	Oxygen saturation
<b>SPECT</b>	Single-photon emission computed tomography
<b>STA</b>	Structural and topological data analysis
<b>THb</b>	Total haemoglobin
<b>TiO<sub>2</sub></b>	Titanium dioxide
<b>UK</b>	United Kingdom
<b>ZiO</b>	Zinc oxide

---

# LIST OF PUBLICATIONS

## *First author:*

**L. Hacker**, T. Else, T. Lefebvre, P. Sweeney, E. Brown, S. E. Bohndiek, “Optoacoustic imaging reveals differences in perfusion-limited hypoxia in murine breast cancer models”, *in preparation*.

**L. Hacker**, E. Brown, T. Lefebvre, P. Sweeney, S. E. Bohndiek, “Performance evaluation of mesoscopic photoacoustic imaging”, *in submission*.

**L. Hacker**, H. Wabnitz, A. Pifferi, B. W. Pogue, T. J. Pfefer and S. E. Bohndiek, “Criteria for the design of tissue-mimicking phantoms for the standardization of biophotonic instrumentation”, *Nature Biomedical Engineering*, May 2022, doi: 10.1038/s41551-022-00890-6.

J. Gröhl\* and **L. Hacker\***, B. T. Cox, K. K. Dreher, S. Morscher, A. Rakotondrainibe, F. Varray, L. Yip, W. C. Vogt, S. E. Bohndiek, and Members of the International Photoacoustic Standardisation Consortium (IPASC) “The IPASC data format: A consensus data format for photoacoustic imaging”, *Photoacoustics*, March 2022, doi: 10.1016/j.pacs.2022.100339.

**L. Hacker**, J. Joseph, A. M. Ivory, M. O. Saed, B. Zeqiri, S. Rajagopal, S. E. Bohndiek, “Polymer-in-oil tissue-mimicking material with tuneable optical and acoustic characteristics for technical validation of optoacoustic imaging systems”, *IEEE Transactions in Medical Imaging*, Nov. 2021, doi: 10.1109/tmi.2021.3090857.

**L. Hacker**, J. Brunner, E. S. Smith, I. Quirós-Gonzalez, S. E. Bohndiek, "Photoacoustics resolves species-specific differences in hemoglobin concentration and oxygenation," *Journal of Biomedical Optics*, September 2020, doi: 10.1117/1.JBO.25.9.095002.

## *Co-author:*

M. Taylor-Williams, S. Mead, T. W. Sawyer, **L. Hacker**, C. Williams, M. Berks, A. Murray, S. E. Bohndiek, “Multispectral imaging of nailfold capillaries using LED illumination”, *Journal of Biomedical Optics*, November 2022, *accepted for publication*.

E. L. Brown\*, P. W. Sweeney\*, T. Lefebvre\*, B. Stolz, J. Gröhl, **L. Hacker**, Z. Huang, D. Couturier, H. A. Harrington, H. Byrne, S. E. Bohndiek “Quantifying vascular networks in photoacoustic mesoscopy”, *Photoacoustics*, April 2022, doi: 10.1016/j.pacs.2022.100357.

I. Quiros-Gonzalez , M. R. Tomaszewski , M. Golinska , E. Brown , L. Bollepalli , **L. Hacker** , D. Couturier , R. M. Sainz, S. E. Bohndiek "Photoacoustic tomography detects response and resistance to Bevacizumab in breast cancer mouse models.", *Cancer Research*, April 2022, doi: 10.1158/0008-5472.CAN-21-0626.

T. L. Lefebvre, E. Brown, **L. Hacker**, T. Else, M. Oraiopoulou, M. Tomaszewski, S. E. Bohndiek, “The potential of photoacoustic imaging in radiation oncology “, *Frontiers in Oncology*, March 2022, doi: 10.3389/fonc.2022.803777.

J. Gröhl, T. Kirchner, T. J. Adler, **L. Hacker**, N. Holzwarth, A. Hernández-Aguilera, M. A. Herrera, E. Santos, S. E. Bohndiek, L. Maier-Hein, “Learned spectral decoloring enables photoacoustic oximetry”, *Scientific Reports*, March 2021, doi: 10.1038/s41598-021-83405-8.

S. E. Bohndiek; B. Cox; J. Joseph; J. Gröhl; **L. Hacker**; S. Morscher; W. C. Vogt, “IPASC: a Community-Driven Consensus-Based Initiative Towards Standardisation in Photoacoustic Imaging”, *Proc IEEE IUS*, Nov. 2020, doi: 10.1109/IUS46767.2020.9251362.

I. Quiros-Gonzalez, M.R. Tomaszewski, S.J.Aitken, L. Ansel-Bollepalli, L.A. McDuffus, M. Gill, **L. Hacker**, J. Brunker, S.E. Bohndiek. “Optoacoustics delineates murine breast cancer models displaying angiogenesis and vascular mimicry”, *British Journal of Cancer*, April 2018; doi: 10.1038/s41416-018-0033-x.

A. Cait, M. R. Hughes, F. Antignano, J. Cait, P. A. Dimitriu, K. R. Maas, L. A. Reynolds, **L. Hacker**, J. Mohr, B. B. Finlay, C. Zaph, K. M. McNagny, W. W. Mohn “Microbiome-driven allergic lung inflammation is ameliorated by short-chain fatty acids”, *Nature Mucosal Immunology*, July 2017, doi:10.1038/mi.2017.7.

\*these authors contributed equally.



# 1 INTRODUCTION

## 1.1 Hypoxia in Oncology

In common with healthy tissues, tumours are in constant need of oxygen and nutrient supplies together with a means to remove metabolic waste. As a tumour outgrows its local blood supply, an imbalance between oxygen supply and demand arises, leaving tissues unable to support aerobic metabolic functions. This emerging physiological condition of low oxygen (below 1.3 % oxygen/10 mmHg<sup>2</sup>) is referred to as hypoxia<sup>3</sup>. Tumour hypoxia is linked with disease progression and therapy resistance, leading to a poor prognosis<sup>4</sup> and has therefore been at the centre of many research studies in the last decades<sup>1,5-8</sup>. Understanding causes, consequences and spatial-temporal dynamics of hypoxia within the tumour microenvironment is essential for the delivery of personalised cancer treatment and improvement of patient outcomes<sup>9</sup>.

### 1.1.1 Structural abnormalities of the tumour vasculature

When a tumour grows, its existing vasculature eventually ceases to provide the tumour cells with sufficient nutrients and oxygen<sup>10</sup>. A state of hypoxia arises, caused by increasing diffusion distances ( $>70 \mu\text{m}^4$ ) for oxygen to pass from blood vessels to the surrounding tumour cells, termed *chronic* or *diffusion-limited* (Section 1.2.1). This initial state of hypoxia drives the activation of hypoxia inducible factors (HIFs) that lead to the transcription of a wide range of downstream genes, in particular affecting angiogenesis, energy metabolism, and erythropoiesis<sup>1,11</sup>. Angiogenesis-related signalling pathways result in the activation of pro-angiogenic factors, such as the vascular endothelial growth factor (VEGF). When pro-angiogenic signalling is dominant, initiation of blood vessel formation is induced, a process that in tumours has been termed the “angiogenic switch”<sup>12</sup>. The angiogenic switch sparks rapid formation of new blood vessels<sup>13,14</sup> resulting in a chaotic and heterogeneous vascular network characterised by many immature vessels with irregular branching and varying diameter. In addition to

angiogenesis, a range of other vessel formation mechanisms exist that can contribute towards the torturous network growth (Table 1.1) in tumour tissue<sup>15</sup>.

The chaotic vascular morphology causes inefficient blood flow along with deficient vessel stability and function<sup>3,13,16</sup>. Poor pericyte coverage and unevenly distributed basement membranes of the tumour vessels can lead to increased vessel fragility and risk of haemorrhage<sup>17,18</sup>. Variation in red blood cell flux can be aggravated by arterio-venous shunting and collapsing vessels, further hindering the transport of oxygen and nutrients. Such irregular tumour perfusion – which often depends on only a few feeding vessels – results in conditions where some tumour areas are exposed repeatedly to periods of hypoxia, followed by reoxygenation<sup>1</sup>. This perfusion-dependent variation in oxygenation is therefore referred to as *perfusion-limited*, or *cycling hypoxia* (Section 1.2.2). Perfusion-limited hypoxia can aggravate effects related to metastatic potential<sup>19–21</sup>, tumour inflammation<sup>22</sup>, and therapy resistance<sup>23–28</sup>.

Enhanced vessel permeability caused by disrupted endothelial junctions and fragile vessel structures can also lead to increased interstitial fluid pressure<sup>29</sup>. Interstitial fluid pressure is further reinforced in tumours by a dense network of collagen fibres, populated with high numbers of fibroblasts and macrophages<sup>30</sup>, and a lack of a functional lymphatic vessel network to efficiently remove interstitial fluid and soluble proteins<sup>13,30</sup>. Poor perfusion combined with interstitial hypertension are important causes for aggravated drug delivery and reduced therapy efficacy in tumours<sup>31</sup>.

Apart from affecting angiogenesis, HIF expression can also deregulate energy metabolism, causing a shift from conventional oxidative phosphorylation towards anaerobic glycolysis for cellular energy production, and thereby enabling cell survival under hypoxic periods<sup>32</sup>. Due to poor perfusion, products of glycolysis, such as lactic acid, can accumulate in the tumour microenvironment giving rise to acidosis<sup>33</sup>, thereby further enhancing tumour cell invasion and metastatic potential<sup>34,35</sup>.

The extent of all these structural and functional abnormalities vary greatly with tumour type, anatomical location, and tumour sub-area<sup>15</sup>, turning tumour masses into multivariate complex problems that require targeted treatment strategies.

**Table 1.1: Types of vessel formation in tumour tissue<sup>15</sup>.**

<b>Process</b>	<b>Definition</b>
sprouting angiogenesis	formation of new capillaries can bud from parental vessels
intussusceptive angiogenesis	formation of new vasculature where a pre-existing vessel splits in two
vasculogenesis	recruitment of circulating endothelial progenitor cells
vascular mimicry	matrix-embedded fluid-conducting meshwork formed by tumour cells
cancer stem cell differentiation	neo-vascularization by trans-differentiation of cancer stem cells to endothelial cells

### 1.1.2 The role of hypoxia in treatment response

Hypoxia has considerable implications for cancer therapy, acting as one of the main causes for impaired efficacy of radiation therapy<sup>36-39</sup>, chemotherapy, and immuno- and photodynamic therapy<sup>40</sup>. Resistance to radiotherapy is mediated as the lack of oxygen impedes the formation of free radicals, thereby decreasing DNA damage and therapy efficacy<sup>9</sup>. Chemotherapy is compromised since hypoxia initiates apoptosis-resistance pathways, for example via the increased expression of drug efflux transporters<sup>41</sup>. Drug delivery and efficacy is also hampered by the increased diffusion distance<sup>42,43</sup>, and decreased proliferation rate<sup>42,43</sup>, as hypoxic cells often divide at slower rates<sup>44</sup>. Furthermore, the activity of many chemotherapeutic drugs is altered at low oxygen concentrations protecting hypoxic tumour populations<sup>2,40,44</sup>. Hypoxia has been shown to impede the immune responses to tumours via multiple mechanisms<sup>45</sup>, and to promote metastatic disease and tumour proliferation<sup>4,46-48</sup>. The latter is thought to be caused by alterations in gene expression and/or clonal selection of cells that can better survive under hypoxic conditions<sup>4,40</sup>, enhancing a malignant phenotype and driving tumour aggressiveness and proliferation<sup>4,40</sup>.

## 1.2 Diffusion- versus perfusion-limited hypoxia

Tumour hypoxia is often classified into chronic (also known as long-term or diffusion-limited hypoxia) and perfusion-limited (also known as cycling, acute, transient, intermittent, or fluctuating hypoxia) hypoxia (Figure 1). In the recent years, it has become increasingly apparent that this distinction is an oversimplification<sup>9,49</sup>, and does not sufficiently capture the complex dynamics of the tumour microenvironment with its continuously changing gradients of pH, oxygen and nutrients. For simplification, this thesis will use these terms to distinguish the two main facets of hypoxia, but the complex and heterogenous nature of tumour hypoxia should be kept in mind.

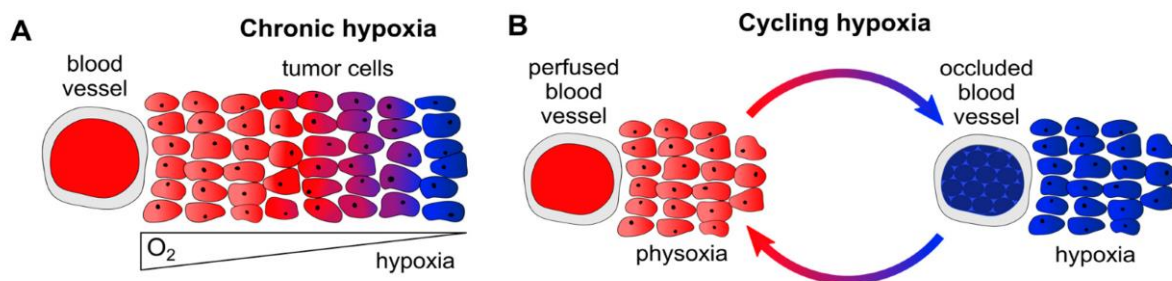


**Figure 1.1: Differences between diffusion-limited (chronic) and perfusion-limited (cycling) hypoxia.** (A) Diffusion-limited chronic hypoxia due to high interstitial spacing between tumour blood vessels and tumour cells. (B) Perfusion-limited cycling hypoxia due to variations in perfusion caused by the chaotic, dysfunctional tumour vasculature. Red: oxygenated tumour cells, Blue: hypoxic tumour cells. Reproduced from <sup>50</sup>.

### 1.2.1 Diffusion-limited hypoxia

Chronic hypoxia is characterised by a constant low partial pressure of oxygen ( $pO_2$ ) resulting from an insufficient oxygen supply by the dysfunctional tumour vasculature<sup>6,51,52</sup>. Three main factors contribute to the occurrence of chronic hypoxia. These include (1) the disorganised geometry of tumour vascular networks<sup>53</sup>, which can lead to higher intervascular spacing and increased oxygen diffusion distance<sup>54</sup>, (2) a lack of arteriolar supply<sup>51,55</sup> as arterioles typically do not enter the tumour parenchyma; and (3) stiffening and shrinkage of hypoxic red blood cells compared to normally oxygenated red blood cells, causing increased blood viscosity and inadequate blood flow<sup>51,53</sup>. It has also been argued that tumour cells have a higher oxygen consumption rate than normal cells, but studies have shown that measurements of oxygen consumption rates of tumours were found to be in the midrange between normal tissues with high and low metabolic rates<sup>56,57</sup> suggesting that oxygen consumption is likely to be site and subtype specific.

### 1.2.2 Perfusion-limited hypoxia

In contrast to chronic hypoxia, perfusion-limited hypoxia refers to spatio-temporal cycles of low oxygen distribution with subsequent reoxygenation caused by varying red blood cell flux<sup>1,7</sup>. These oxygen fluctuations appear (at least) at two time-scales: Short-term (minutes to an hour) or long-term (hours to days). While short-term fluctuations are thought to be caused by variations in red cell flux or haemoglobin oxygen saturation ( $sO_2$ ), long-term fluctuations have been attributed to vascular remodelling<sup>2,5,58,59</sup>. Vascular stasis has also been suggested as a reason for short-term cycling hypoxia, but studies using window chambers have shown that it only accounts for around 4% of the events<sup>60</sup>. Regions of cycling hypoxia appear to be heterogeneously distributed across the tumour, with patterns that appear to be tumour type-dependent<sup>61,62</sup>. Studies have shown that the fraction of acutely hypoxic cells seems to be significantly higher than the fraction of chronically hypoxic cells<sup>63-66</sup>.

Historically, the phenomenon of varying hypoxia levels has been first observed by Yamaura et al<sup>67</sup> who identified radio-resistant regions in tumour peripheries that were also characterized by unstable blood flow and episodes of transient vascular stasis. He suggested that these areas might be experiencing transient hypoxia caused by variations in perfusion, thereby leading to temporary radioresistance. In parallel, Brown et al<sup>68</sup> made similar observations, proposing that transient levels of hypoxia can occur in tumours which significantly affect radiosensitivity. In his experiment, he eliminated hypoxic tumour cells by using a hypoxic cytotoxin, but could still observe a radioresistant cell fraction 24 hours later suggesting that an aerobic cell fraction turned hypoxic during this period. These two early experiments already highlighted the different time scales in which perfusion-limited hypoxia can occur, with periods of a few minutes (Yamaura) to variations ranging from hours to days (Brown). Later on, Chaplin and Durand<sup>25</sup> confirmed the connection between intermittent hypoxia and transient changes in tumour perfusion. They injected the fluorescent molecule Hoechst 33342 – a double strand DNA dye which

stains cells adjacent to blood vessels – either throughout the time of irradiation or 20 minutes before the start of irradiation. For the first protocol, brightly stained cells were much more radiosensitive (more oxyc) than cells dimly stained, whereas for the second protocol, radiosensitivity did not differ between brightly and dimly stained cells, reflecting changes in perfusion and oxygenation between dye injection and irradiation. In the following years, these observations could be confirmed with the help of a ‘double labelling’ fluorescence technique revealing the presence of transient perfusion in murine tumours<sup>69,70</sup>, and later on transient hypoxia<sup>58,71</sup>. Since then, the phenomenon of perfusion-limited hypoxia has been studied and verified by many<sup>1,7</sup>, employing various imaging and validation techniques, and uncovering it as a key driver of tumour malignancy.

### 1.2.3 Differences in biological effects between diffusion- and perfusion-limited hypoxia

In many ways, perfusion-limited hypoxia appears to be associated with a more aggressive tumour phenotype than diffusion-limited hypoxia<sup>1,7</sup>. Importantly, tumour cells exposed to perfusion-limited hypoxia are characterised by increased tumour inflammation<sup>22</sup>, metastatic potential<sup>19-21</sup> and higher resistance to radiotherapy<sup>23-27</sup> and chemotherapy<sup>28</sup>.

**Increased oxidative stress markers.** In contrast to chronic hypoxia, intermittent hypoxia has been shown to lead to higher expression of oxidative stress markers<sup>72,73</sup>, and production of reactive oxygen species (ROS)<sup>23,74</sup>. ROS can perturb normal cell function and play important roles in cellular signalling pathways critical to proliferation, host cell defence, autophagy, and stem cell differentiation<sup>75-78</sup>. Higher expression of ROS during perfusion-limited hypoxia results in an increased accumulation of DNA damage during the reoxygenation periods<sup>73,79-81</sup>. Additionally, ROS signalling causes increased transcription of HIF-1<sup>2,23</sup>, nuclear factor (erythroid-derived 2)-like 2 (Nrf2)<sup>82</sup> and nuclear factor kappa B (NF-κB)<sup>22</sup>, which play key pro-survival roles in the response to oxidative stress<sup>75,83,84</sup>. Following the activation of these transcription factors, perfusion-limited hypoxia affects cell behaviour through profound changes in gene expression.

**Altered cell metabolism.** Not much is yet known about the impact of perfusion-limited hypoxia on cell metabolism<sup>7</sup>. However, it has been suggested that a switch to the glycolytic pathway is an adaptation to perfusion-limited hypoxia, facilitating cell survival during the hypoxic episodes<sup>32</sup>. Increased HIF levels lead to enhanced transcription of downstream targets such as glucose transporter 1 (GLUT1) and Pyruvate Dehydrogenase Kinase 1 (PDK1), which can increase glycolysis and downregulate oxidative phosphorylation, respectively<sup>7</sup>. These metabolic changes are thought to allow cells the generation of sufficient energy in low oxygen environments, contributing to the enhanced treatment resistance found in tumour cells exposed to intermittent hypoxic episodes in contrast to constant hypoxia exposure<sup>85,86</sup>.

**Increased genomic instability.** While chronic hypoxia prevents DNA replication following reoxygenation, cells exposed to hypoxic cycles are able to restart DNA replication during reoxygenation

periods despite the occurrence of reoxygenation-induced DNA damage<sup>87</sup>. Moreover, exposure to cycling hypoxia can alter tumour cell cycle checkpoint control and the sensing and repair of DNA damage<sup>43,88</sup>. Pre-clinical studies have shown that chronic hypoxia suppresses the homologous recombination DNA repair pathway, whilst acute hypoxia stimulates DNA damage-associated checkpoint cell cycle arrest and non-homologous end joining<sup>89</sup>. These factors promote genomic instability, providing an overall selective advantage for malignant growth<sup>43</sup>, and can lead to radio-resistance, decreased delivery of cytotoxins, and increased metastatic potential<sup>49</sup>.

**Angiogenesis.** Perfusion-limited hypoxia also appears to impact vessel formation differently than chronic hypoxia. In *in vitro* studies, exposure to intermittent hypoxic cycles increased endothelial cell migration and tube-like structure formation<sup>24,90</sup>. It was also shown that perfusion-limited hypoxia enhances vessel density by increasing the number of smaller vessels and decreasing interstitial distances, but paradoxically delayed blood supply<sup>91</sup>. Transient oxygenation appears to favour angiogenesis that exacerbates the dysfunctional tumour vasculature, thereby aggravating the varying oxygenation cycles<sup>1</sup>.

**Stemness.** Intermittent hypoxia has been shown to enlarge the stem/progenitor subpopulation of cells in the tumour microenvironment compared to chronic hypoxia<sup>92</sup>, and increase the invasive activity of these cells mediated via HIF-1<sup>93</sup>. This is supported by the observation that HIF downstream targets can impact the epithelial-mesenchymal transition process, and thereby increase tumour cell invasiveness<sup>94</sup>.

**Increased metastasis and tumour inflammation.** In addition to an increase in cell migration, cycling hypoxia has been demonstrated to increase tumour metastasis to a greater extent than chronic hypoxia<sup>19-21</sup>. Exposure of endothelial cells to cycling hypoxia was also shown to promote tumour inflammation more strongly than chronic hypoxia<sup>22</sup>, apparently by modulating the behaviour of endothelial cells toward a pro-inflammatory state and by increasing leukocyte infiltration<sup>1</sup>.

**Higher treatment resistance.** Finally, it has been demonstrated that perfusion-limited hypoxia leads to increased resistance to both radiotherapy<sup>23-27</sup> and chemotherapy<sup>28</sup>. It has been suggested that fluctuating tumour perfusion may provide a protective effect in tumour cells during therapy, enabling proliferation once adequate blood flow and nutrient supply is restored<sup>36</sup>. *In vitro* studies have shown that – possibly mediated via HIF1 – perfusion-limited hypoxia promotes endothelial cell survival and angiogenesis after irradiation<sup>24</sup>. *In vivo* it has been found that preconditioning of cycling hypoxia in tumour-bearing mice enhanced tumour regrowth and reduced apoptosis after radiotherapy compared to chronic hypoxic conditions<sup>24</sup>.

### 1.2.4 Methods to detect perfusion-limited hypoxia

As spatio-temporal dynamics in oxygenation have severe implications for tumour development and treatment resistance, characterising and understanding the causes and consequences of these fluctuations is of utmost importance. For detection and investigation of perfusion-limited hypoxia, both *ex vivo* and *in vivo* methods of detection have been employed<sup>95</sup> (Table 2). The types of measurements vary greatly, from absolute measurements of pO<sub>2</sub> or oxygen concentration to indirect measurements of a related parameter, such as haemoglobin sO<sub>2</sub>.

*In vivo* methods for assessment of oxygenation dynamics measure changes in oxygenation in living subjects in real-time and encompass both invasive and non-invasive techniques. Invasive probes, such as needle pO<sub>2</sub> probes<sup>96–98</sup>, enable direct measurement of tissue pO<sub>2</sub>, but measurements disrupt the tissue and are only point-based, lacking spatial information. Non-invasive techniques involve various imaging methods, for example, magnetic resonance imaging (MRI)<sup>49,99–101</sup>, positron emission tomography (PET)<sup>102,103</sup>, optical imaging or electron paramagnetic resonance imaging<sup>52,104</sup> (Table 1.2). Importantly, only some of these techniques measure tissue oxygenation (e.g., PET, electron paramagnetic resonance imaging (EPRI)), whilst others assess oxygenation in blood vessels (e.g., BOLD-MRI, optical imaging techniques, photoacoustic imaging). EPRI and PET based techniques enable direct tissue oxygenation measurements and have shown promising potential in preclinical models<sup>52,104–107</sup>, but rely on injected probes, thereby only providing an assessment of the oxygenation state limited to a particular time frame. MRI-based techniques are widely available and have been shown to correlate with tissue oxygenation and histological markers of hypoxia<sup>108,109</sup>, but are — similar to EPRI and PET- based techniques — associated with high cost. Optical spectroscopy techniques can be deployed for *in vivo* microscopy, enabling micron resolution visualisation of capillary networks in window chamber preclinical models<sup>110–112</sup>, but are ultimately limited by their penetration depth and narrow field of view.

*Ex vivo* methods measure differences in perfusion and hypoxia by injecting relevant markers at different time points and analysing tumour tissue, for example, by fluorescence-activated cell sorting (FACS)<sup>58</sup>, fluorescent microscopy<sup>69</sup> or immunohistochemistry (IHC) techniques<sup>25,59</sup>. IHC markers to assess hypoxia include endogenous proteins, such as HIF-1 $\alpha$  (the  $\alpha$  subunit of the transcription factor HIF-1) and HIF-1 downstream target genes, e.g., VEGF-A or carbonic anhydrase IX (CAIX), or exogenous markers such as pimonidazole, which binds to thiol-containing molecules (e.g., glutathione) in hypoxic cells. While *ex vivo* methods are helpful for validation of *in vivo* observations, *in vivo* methods inform more clearly on amplitude, frequencies and (3D) spatial location of the hypoxia fluctuations.

An ideal imaging technique for investigating perfusion-limited hypoxia would offer: (1) a robust delineation of relevant oxygenation and perfusion parameters; (2) a high spatial resolution; (3) a high temporal resolution and temporal stability; (4) non-invasiveness; (5); safety; (6) independence of external contrast agents; (7) capabilities to co-register with other imaging/histopathological techniques for validation purposes; and (8) scalability for clinical applications. At present, the available modalities

are not able to meet all these criteria. One imaging modality that has the potential to fulfil these outlined aspects in future, and has shown some promise in investigating perfusion-limited hypoxia in animal models<sup>113</sup>, is photoacoustic (also referred to as optoacoustic) imaging (PAI).

**Table 1.2: Overview of direct methods used for measuring perfusion-limited hypoxia.**

PET=positron emission tomography; SPECT=single-photon emission computed tomography; BOLD-MRI=blood oxygen level dependent MRI, OE-MRI=oxygen-enhanced MRI; EPRI=electron paramagnetic resonance imaging; <sup>18</sup>F-FMISO= <sup>18</sup>F-fluoromisonidazole; PAI=photoacoustic imaging. Adapted from <sup>7</sup>.

Measurement Techniques	Frequency of detection	Invasiveness	Spatial Resolution	Contrast agent	Direct pO <sub>2</sub> Measurement	Ref.
<b>Polographic O<sub>2</sub> microelectrodes</b>	<<1 s	Yes	20–30 μm	No	Yes	96
<b>Oxylite optical probe</b>	<<1 s	Yes	250 μm	No	Yes	96–98
<b>Phosphorescence lifetime imaging</b>	2-2.5 min		<mm-cm	Pd-porphyrin dendrimer, IV	Yes	114
<b>Optical Spectroscopy</b>	30 s	Yes	mm-cm	No	No	110–112
<b>PET/SPECT</b>	>24 h	No	Several mm	E.g., PET: <sup>18</sup> F-FMISO	No	103,106,107
<b>MRI: BOLD, OE</b>	1-4 min	No	Sub mm-mm	No	No	49,99–101,109,115–117
<b>MRI: F-19 MRI</b>	1.5 min	No	2 mm	Hexafluorobenzene	Yes	118
<b>EPRI</b>	10-60 s	No (probe implantation)	mm-cm	Implantable O <sub>2</sub> sensitive spin probe with resonator	Yes	105
	2-3 min	Yes	1.6–1.8 mm	O <sub>2</sub> sensitive spin probe, IV	Yes	52,104
<b>PAI</b>	1s	No	100 μm	No	No	113

### 1.3 Concept of PAI

PAI is based on the photoacoustic effect, which refers to the generation of ultrasound waves from the absorption of electromagnetic energy<sup>119</sup> (Figure 1.2): short laser pulses in the nanosecond range illuminate a sample; part of the electromagnetic energy is absorbed by the imaged object and converted into heat; the rise in temperature leads to an increase in pressure; and the pressure rise generates broadband ultrasound waves that propagate through the tissue and are detected by ultrasound transducers. The amplitude of the recorded pressure wave provides information about the local absorption of optical energy within the object. The time interval between the illumination pulse and arrival of the ultrasound wave at the detector can be used to calculate the distance between the detector and the absorbers. For illumination in tissues, light in the near-infrared (650-1350 nm) window is often chosen to optimise penetration depth<sup>120</sup>.

By utilising pulses at multiple wavelengths, spectroscopic photoacoustic systems are able distinguish between endogenous chromophores or exogenous contrast agents, such as nanoparticles or organic dyes<sup>121,122</sup>. The primary endogenous absorbers in tissue are oxy- and deoxy-haemoglobin (HbO<sub>2</sub> and RHb), lipids, melanin, collagen, and water (Figure 1.3). The optical absorption coefficients vary with wavelength, and thus the relative concentration of each chromophore can be extracted through spectroscopic inversion. Functional parameters such as sO<sub>2</sub> can be calculated from the absorption difference between HbO<sub>2</sub> and RHb ( $sO_2 = HbO_2 / (HbO_2 + RHb)$ )<sup>123,124</sup>. Using only endogenous contrast, PAI therefore has the potential to non-invasively visualise simultaneously various important tissue parameters within a single imaging session.

PAI is a safe, low-cost, and non-invasive imaging modality that overcomes many of the aforementioned limitations of other imaging modalities (Table 1.3), albeit at the sacrifice of imaging penetration depth. Current state-of-the-art technology can achieve two-dimensional (2D) imaging in almost real-time, and three-dimensional (3D) images in time scales of seconds to minutes<sup>121,125</sup>. Importantly, the modality is also able to image across scales, from whole tumour volumes (macroscopic, cm depth) over to vascular networks (mesoscopic, mm depth) down to individual cells (microscopic,  $\mu\text{m}$  depth)<sup>125</sup>. Due to its ability to provide 3D multi-parametric information with high temporal resolution, PAI has found a wide range of applications in both pre-clinical and clinical environments<sup>126</sup>.

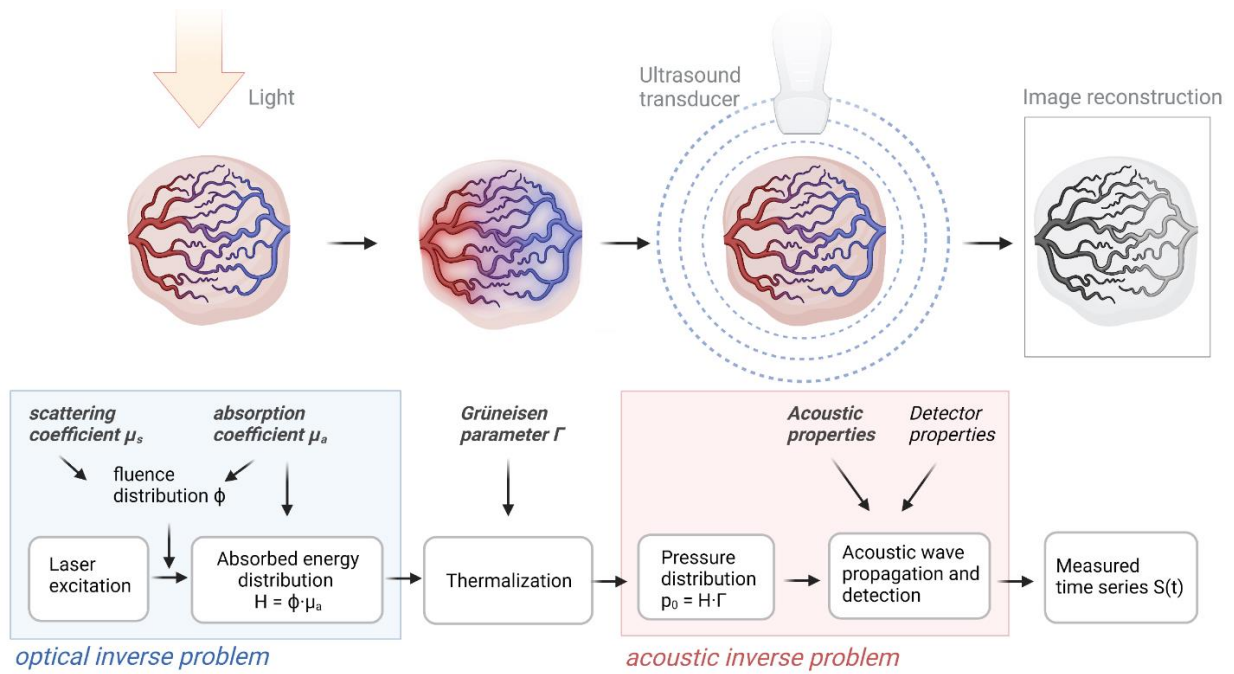


**Figure 1.2: Photoacoustic signal generation.**

A pulsed light source illuminates the object to be imaged (e.g., tumour tissue). As the light propagates through the tissue, it is scattered and absorbed by spatially varying endogenous or exogenous chromophores. The absorption and scattering coefficients,  $\mu_a$  and  $\mu_s$ , determine the fluence distribution  $\Phi$  and consequently, the absorbed energy distribution  $H$ . The absorbed energy generates a pressure distribution  $p_0$ . The combined photoacoustic efficiency of conversion from heat into pressure is represented by the Grüneisen parameter  $\Gamma$ . Due to the elastic nature of the tissue the generated pressure propagates as an acoustic wave through the tissue and is detected by ultrasound sensors. This process is affected by the acoustic properties of the tissue and the sensor response. Finally, image reconstruction is performed to visualize the recorded data. Created with BioRender.

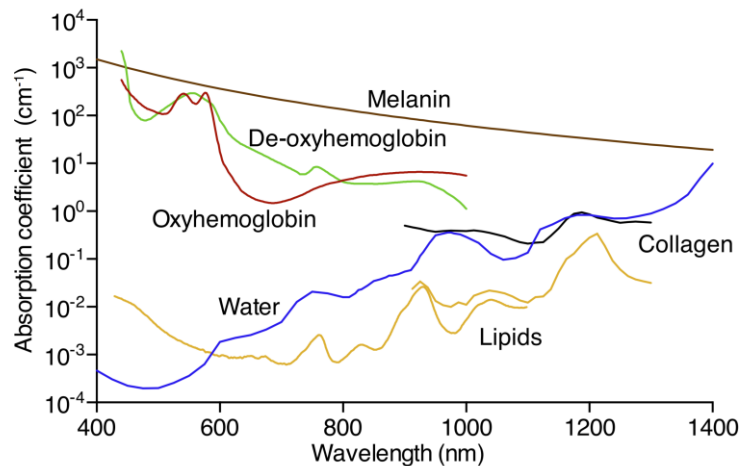


**Figure 1.3: Absorption spectra of the main endogenous chromophore.**

Absorption spectra are displayed for melanin (brown); oxy- (red) - and deoxy-haemoglobin (green; both  $150 \text{ gL}^{-1}$ ); water (blue; 80% by volume in tissue); lipids (yellow; 20% by volume in tissue); and collagen (black) in the wavelength range of 400 nm to 1400 nm. Data from <http://omlc.org.edu/spectra/> and <sup>127</sup>.

**Table 1.3: Comparison of preclinical imaging modalities.**

(CT=Computed tomography, MRI=Magnetic resonance imaging, PET=Positron-emission tomography, SPECT=Single-photon emission computed tomography, Rf=Reference).

Imaging method	Anatomical contrast	Molecular/functional contrast	Sensitivity	Temporal resolution	Spatial resolution	Penetration depth	Costs	Safety	Rf
X-ray CT	medium	poor	$\mu\text{mol}$ ( $10^{-6}$ )	mins	10–500 $\mu\text{m}$ scalable	Whole body	medium	medium	122, 128
MRI	good	good	$\mu\text{mol}$ ( $10^{-6}$ )– $\text{nmol}$ ( $10^{-9}$ )	Mins-hrs	10–500 $\mu\text{m}$ scalable	Whole body	high	good	122, 128
PET/SPECT	poor	good	$\text{fmol}$ ( $10^{-15}$ )	Min-hrs	1–2mm	Whole body	high	medium	122, 128
Ultrasound	good	medium (micro-bubbles)	$\text{nmol}$ ( $10^{-8}$ )	Sec-mins	50–500 $\mu\text{m}$ scalable	2-6 cm	low	good	122
Optical imaging	good	good	$\text{pmol}$ ( $10^{-12}$ )	Sec-mins	>0.3 $\mu\text{m}$	Superficial <1 mm	medium	good	122, 128
PAI	good	good	$\text{pmol}$ ( $10^{-12}$ )	Sec-mins	5–500 $\mu\text{m}$ scalable	up to 5 cm	low	good	122

### 1.3.1 Potential of PAI to evaluate perfusion-limited hypoxia at different scales

PAI affords a scalable spatiotemporal resolution, which could be applied to analyse perfusion-limited hypoxia in tumour tissue non-invasively. PAI has already been widely exploited for cancer imaging as it enables the visualisation of two key characteristics of solid tumours<sup>129</sup>: (1) Hypoxia, assessed in PAI via the readout of blood oxygen saturation ( $s\text{O}_2=\text{HbO}_2/\text{THb}$ ) and (2) Angiogenesis, assessed in PAI via the total blood volume content in tissue ( $\text{THb}=\text{RHb}+\text{HbO}_2$ )<sup>123,124,130–133</sup>. PAI has been used to monitor vascular development during tumour growth<sup>132–134</sup>, quantify microvasculature in 3D with high resolution<sup>135–137</sup>; detect response to antiangiogenic therapies<sup>138,139</sup>, and predict radiotherapy response<sup>140</sup>. While promising, these studies only inform on static, average perfusion parameters, lacking quantitative insight into the spatial and temporal heterogeneity of oxygenation state and vascular function. In early stages, PAI has been applied to look at temporal dynamics of tumour oxygenation<sup>113,141</sup>, but these studies do not provide a thorough biological validation, spatial analysis of the fluctuations, or detailed assessment of the underlying molecular and anatomical features.

### 1.3.2 Challenges in measuring perfusion-limited hypoxia with PAI

Despite the promise of PAI to resolve temporal oxygenation dynamics in tumour tissue, the development of the technology is still relatively immature. Substantial limitations remain that need to be carefully understood and where possible, compensated. Robust and stable signals are required to resolve relevant capillary sizes and quantify sO<sub>2</sub> and THb over time. Limited-view and motion-related artefacts can impact image quality and need to be well understood to extract meaningful data. In an *in vivo* setting, additional variation factors can impact the imaging data, such as temperature, breathing, or anaesthesia, and hence require careful delineation. Furthermore, optical attenuation and wavelength-dependent spectral colouring can alter the acquired signal and subsequently affect the spectral unmixing of HbO<sub>2</sub> and RHb. Correcting for spectral distortions would allow absolute quantification of optically absorbing molecules, but remains a significant challenge *in vivo* and hence is an active research area in the field<sup>142,143</sup>. To exploit PAI for assessing spatio-temporal characteristics of tumour oxygenation with high accuracy and precision, a thorough performance evaluation of the device to be applied, including technical and biological validation, is required.

Technical validation is defined as the process of establishing the accuracy, repeatability, reproducibility and lack of bias of a biomarker measurement<sup>144</sup>. Technical validation is necessary to establish the temporal precision of PAI, to provide confidence that any measured fluctuations in oxygenation or vascular structures are indeed caused by biological sources rather than imaging artefacts or system errors. Additionally, the impact of different target positions on signal intensity and resolution needs to be evaluated and standard operating procedures of image acquisition and analysis need to be established. Early studies of accuracy and precision have already been made for PAI tomographic systems<sup>141,145</sup> but none have been reported for mesoscopy or microscopy systems, which are important for studying dynamic fluctuations in vascular perfusion in solid tumours in relation to perfusion-limited hypoxia.

Many technical validation studies rely on stable test objects, also termed “phantoms”. PAI phantoms are particularly challenging to create, due to the need to account for both optical illumination and acoustic signal propagation. An ideal PAI phantom should be: (1) tissue-mimicking with tuneable acoustic and optical properties; (2) mechanically robust; (3) stable over time; (4) simple and highly reproducible to manufacture; (5) flexible in geometry and architecture; (6) non-toxic; (7) made with ingredients widely available from scientific suppliers; and finally, (8) low cost. Many phantom materials have been tested for PAI, including hydrogels<sup>146,147</sup>, PVA<sup>148,149</sup>, silicone<sup>150,151</sup>, PVC<sup>152–158</sup> and copolymer-in-oil materials<sup>159–161</sup>. Inclusions have been made by embedding fluid-filled channels<sup>156,162</sup> or solid absorbers such as wires or filaments<sup>163</sup>, or by creating simple<sup>138,158,164</sup> or more complex vessel-mimicking<sup>157,165</sup> inserts. Despite these early efforts, PAI lacks a widely accepted standardised phantom that meets all of the outlined requirements. Development of such test object that can be applied in a multi-centre setting is vital for routine quality assurance and control from the perspective of clinical

translation, and of particular importance for PAI studies of the subtle dynamics of perfusion-limited hypoxia<sup>166</sup>.

Besides technical validation, biological validation of biomarkers is required to associate imaging signals with the underlying physiology, pathology or anatomy<sup>144</sup>. Previous work has already gone some way towards biological validation of haemoglobin and sO<sub>2</sub> biomarkers. For signal validation, (blood flow) phantoms, pO<sub>2</sub> probes<sup>162,167</sup>, haematology analysers<sup>168</sup> and co-registration with IHC methods<sup>169</sup> such as pimonidazole staining<sup>134,170</sup>, or other haemoglobin-sensitive imaging techniques such as BOLD-MRI<sup>139,140,171</sup>, high-resolution- and DCE-ultrasound<sup>172-174</sup> or laser-speckle imaging<sup>175</sup> have been used. Validating techniques that measure temporal oxygenation dynamics *in vivo* is particularly challenging, as validation should ideally be performed in parallel to the measuring technique to capture the dynamic nature of the fluctuations. A thorough analysis of the underlying molecular phenotype by histopathological and genotypic techniques can help to overcome this challenge, and enable the first steps towards validation of the imaging data.

## 1.4 Thesis objectives and outlook

This thesis will address the challenge of developing and validating PAI biomarkers that can shed light on perfusion-limited hypoxia in cancer. A thorough technical as well as biological validation will be performed, summarised as followed:

1. Aim 1: Technical validation of PAI:
  - a. Evaluation of phantom materials and standardisation efforts in biophotonics to guide standardised phantom development in PAI;
  - b. Establishing stable and precise means for robust phantom characterisation;
  - c. Development of generalizable test phantoms for assessing photoacoustic precision and accuracy;
  - d. Application of phantoms for technical characterisation of a PAI mesoscopy system.
2. Aim 2: Biological validation of PAI:
  - a. Application of PAI at mesoscopic and macroscopic scale for characterising perfusion-limited hypoxia in two murine breast cancer models;
  - b. Validation of PAI biomarkers using RNA sequencing and IHC techniques.

To address these tasks, Chapter 2 of this thesis will give a general overview on phantom materials and standardisation approaches in optical imaging, guiding the phantom development in the subsequent chapters. Chapter 3 will focus on establishing and validating material characterisation systems that are required for precise description of photoacoustic phantom properties. Chapter 4 will describe the development of a tissue-mimicking copolymer-in-oil material with tuneable optical and acoustic properties that is suitable for widespread use in PAI. Chapter 5 will concentrate on the application of phantoms to characterise a PAI mesoscopy system. Chapter 6 will focus on applying mesoscopic and macroscopic PAI to assess hypoxia dynamics in two murine breast cancer models, and on validating PAI biomarkers using RNA sequencing and IHC techniques. Finally, Chapter 7 will conclude with a general summary and a discussion of future directions of this work.

# 2 PHANTOM MATERIALS IN BIOPHOTONICS

*This chapter uses material from Hacker et al (2022) “Criteria for the design of tissue-mimicking phantoms for the standardization of biophotonic instrumentation”, Nature Biomedical Engineering. (see publications list). The manuscript was researched and prepared by myself, with revisions and discussions made together with all co-authors.*

## 2.1 Introduction

Test objects to calibrate imaging systems have an important subset known as tissue-mimicking phantoms. In biophotonics, they are used for performance evaluation of a given technology by mimicking light-tissue interactions of human tissue, as well as other crucial elements of the process<sup>176,177</sup>. The diverse landscape of biophotonic applications means that it is likely impossible to have an all-encompassing phantom that fulfils the needs of every optical sub-speciality. In particular, in the context of this thesis, phantoms for PAI are challenging to define, requiring both biologically relevant optical and acoustic properties, as well as architectural flexibility to satisfy the needs of the diverse landscape of instrument geometries. As such, a wide range of phantom materials have been proposed<sup>178,179</sup>, but there has been no consensus on a widely applicable material type nor fabrication method to produce such phantoms. Nevertheless, finding consensus on broadly applicable materials would be beneficial to enable comparison of devices between vendors and institutions; advance hybrid modalities; allow complementary use of different modalities within one clinical session; and further the development of internationally-recognised standards<sup>180,181</sup>.

In this chapter, the current state-of-the-art in phantom materials in biophotonics is surveyed to guide phantom development for PAI, and address Aim 1a of this thesis. First, phantom design considerations are outlined, underlining important base requirements for an ideal PAI phantom. Second, biophotonic phantom materials and their methods of preparation are discussed, emphasizing individual strengths and weaknesses in the context of standardisation efforts. The chapter concludes by highlighting promising material types for phantom applications in PAI, and summarizing current standardisation efforts in this field.

### 2.1.1 General phantom design considerations

Phantoms can be broadly divided into physical phantoms and numerical (computational) phantoms<sup>182</sup>. Numerical phantoms cover *in silico* frameworks, which will not be reviewed here; physical phantoms are material objects that can be artificially composed or tissue derived. Artificially composed phantoms can be homogeneously, heterogeneously, or anthropomorphically designed. Tissue-derived phantoms can include both *ex vivo* and bioengineered tissues.

### 2.1.2 Physical properties of soft tissues

Understanding the physical properties of soft tissues is a fundamental requirement for development, application, and evaluation of PAI phantoms. Average values for the optical<sup>183,184</sup>, acoustic<sup>185,186</sup> and thermoelastic<sup>187</sup> properties of soft tissues are summarised in (Table 2.1). To understand light propagation in turbid media, knowledge of the probability of a scattering or absorption event per unit path length is essential. These parameters are captured by the linear scattering coefficient  $\mu_s(\lambda)$  and the linear absorption coefficient  $\mu_a(\lambda)$ ; the refractive index  $n$  is also relevant for light reflection and refraction at interfaces. For certain microscopic or mesoscopic applications, or interactions near a light source, knowledge of the anisotropy factor  $g$  of the phantom medium is important as well. After several scattering events, light transport is diffuse, and scattering can be assumed to be isotropic. In these regimes, the reduced scattering coefficient  $\mu_s'(\lambda)$  (defined by  $\mu_s'(\lambda)=(1-g)\mu_s(\lambda)$ ) is sufficient to describe the apparent scattering coefficient under the assumption that the source-to-measurement distance is much larger than  $1/\mu_s(\lambda)$ .

Both scattering and absorption effects are wavelength-dependent and determined by the constituents of the medium. In the visible wavelength range in soft tissues, RHb and HbO<sub>2</sub> as well as melanin are the main endogenous chromophores. Moving towards near infrared (NIR) wavelengths (800–2500 nm), water, lipids, and proteins (mostly collagen) become increasingly absorbent as well. In order to measure optical properties, a wide range of methods can be employed such as spectrophotometers, double-integrating sphere (DIS) systems, spatial frequency domain imaging and multi-distance frequency domain photon migration techniques as well as time-domain photon migration techniques<sup>188–190</sup>. Yet, the accurate assessment of optical properties of a turbid medium is highly challenging due to the strong absorption-to-scattering coupling for light attenuation and different limitations of the analysis models. Multi-laboratory studies of a liquid phantom showed an agreement within 2% of the estimate for both  $\mu_a$  and  $\mu_s'$ <sup>191</sup>, but discrepancies for solid phantoms are commonly found to up to  $\pm 15\%$ <sup>192</sup>.

PAI phantoms also need to mimic acoustic properties, meaning it is important to assess how fast an acoustic wave can propagate within a medium and how strongly the medium attenuates the wave. This is captured by the material-specific speed of sound  $c$  and acoustic attenuation coefficient  $\alpha$ , respectively. The extent of backscattering of an acoustic wave is determined by the backscattering coefficient  $\mu_{bs}$ , which is difficult to determine and therefore rarely reported<sup>193</sup>. A well-characterised broadband frequency description of these parameters is essential.

**Table 2.1: Definition of relevant optical and acoustic measurement parameters in biophotonic imaging.**

Notes: \*These are just representative values. For more accurate numbers please refer to the literature. Speed of sound can vary with temperature.

	Parameter	Symbol	Unit	Definition	Average value in soft tissue*	Ref
Optical	Optical absorption coefficient	$\mu_a$	$\text{cm}^{-1}$	Probability of photon absorption per unit length travelled by the photon	0.1-0.5	183,194
	Refractive index	$n$	none	Ratio of the velocity of light in a vacuum to the velocity of light in a medium	1.33-1.51	183,194
	Anisotropy factor	$g$	none	Represents the effects of directionally dependent scattering	0.7-0.9	183,194
	Reduced scattering coefficient	$\mu_s'$	$\text{cm}^{-1}$	Probability of photon scattering per unit length travelled by the photon	10-20	183,194
Acoustic	Acoustic attenuation coefficient	$\alpha$	$\text{dB}\cdot\text{cm}^{-1}\cdot\text{MHz}^{-1}$	Extent of reduction of an acoustic wave when propagating within a medium	0.1-1.6	186,193
	Speed of sound	$c$	$\text{m}\cdot\text{s}^{-1}$	Velocity of acoustic wave propagation within a medium	1450-1730	186,193
	Backscattering coefficient	$\mu_{bs}$	$\text{m}^{-1}\text{sr}^{-1}$	Differential scattering cross section per unit volume at a scattering angle of $180^\circ$	$3.5 \times 10^{-4}$ - $9 \times 10^{-4}$	193,195
Thermoelastic	Grüneisen Parameter	$\Gamma$	none	Measure of thermoelastic efficiency	0.25-0.9	196

## The role of phantoms in the translational research pipeline

Phantoms play a fundamental role in standardisation and clinical translation of new devices<sup>176</sup>. In the context of this thesis, standardisation refers to the process of establishing documentary consensus on a specific technical modality/task outlining precise guidelines, specifications and relevant definitions<sup>197</sup>. While different definitions of the translational pipeline exist<sup>198</sup>, most approaches agree that translational research includes those efforts that transform scientific discoveries into novel tools that are actively applied in clinical practice. Along this (not always strictly linear) path, phantoms fulfil a range of tasks that can be roughly divided into instrument-specific tasks (e.g., device development, validation, and surveillance) and application-specific tasks (e.g., testing or validation of an anticipated physical measurement; replacement of *in vivo* models) (Figure 2.1).

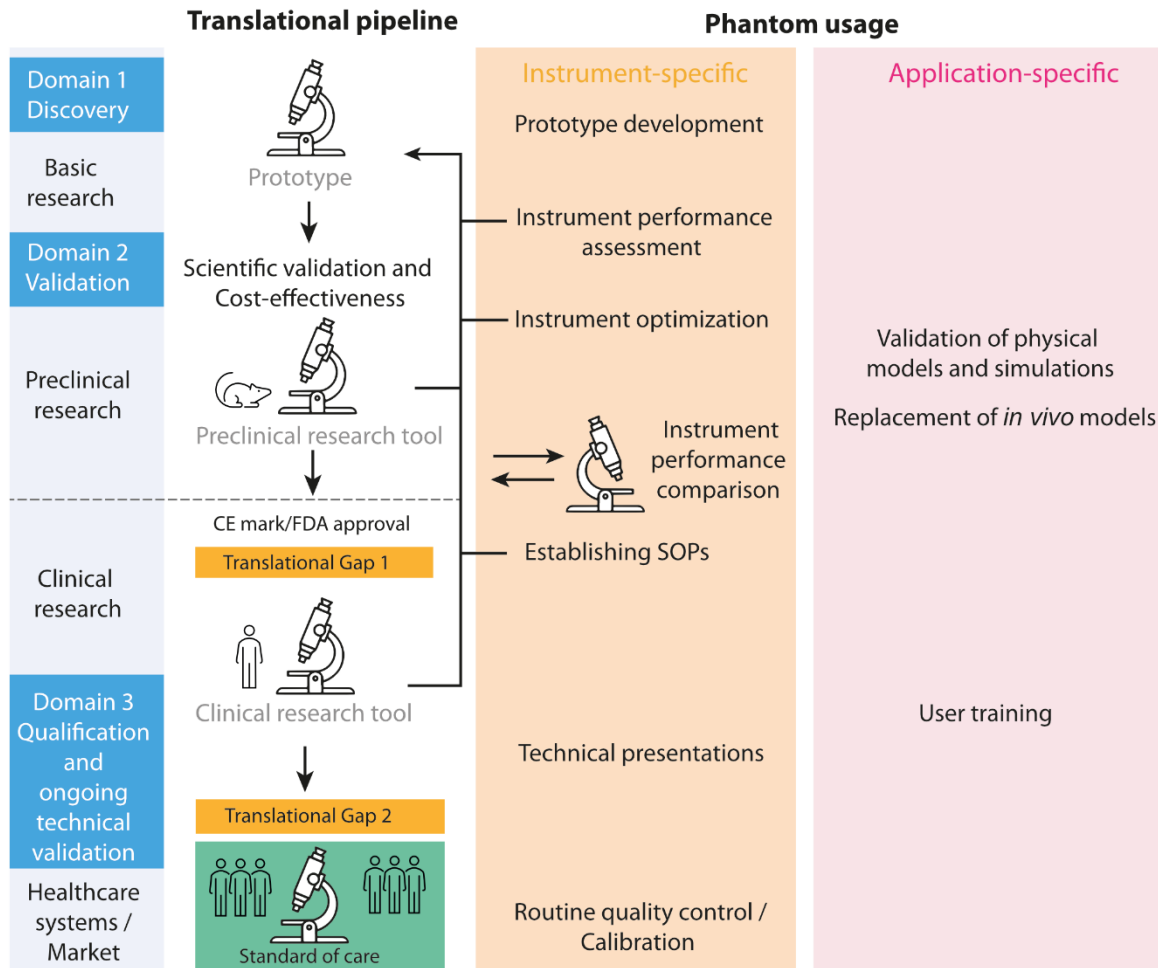


**Figure 2.1: Tasks of phantoms along the translational pipeline.**

Instrument- and application-specific tasks of phantoms are presented along the translational pipeline for optical imaging devices. Translational gap 1 refers to the step of transferring a research tool from a preclinical into a clinical research environment. Translational gap 2 refers to the step of integrating a tool from clinical research into clinical standard-of-care and routine patient-use. (pipeline designed after<sup>144,199</sup>; SOPs=Standard operating procedures).

### 2.1.3 Phantom design properties

An ideal PAI phantom material, which intends to cover all outlined tasks and builds confidence in the reproducibility of PAI systems, should possess eight important properties (Figure 2.2). Usually, however, phantoms are targeted to specific applications, such as the assessment of precision or accuracy.

Precision phantoms are focused on instrument-specific tasks, for example, evaluating repeatability (same subject, same scanner, same operator, short interval) and reproducibility (comparable subjects, different scanner make/model, centres). These can add value in multi-centre clinical trials by providing a common calibration of all instruments across sites<sup>200,201</sup>. For this purpose, temporal and mechanical stability as well as reproducible fabrication are key requirements.

For accuracy phantoms, tissue-mimicking properties are of utmost importance, as they aim to faithfully recapitulate the expected signal, which can be either static (replicating a tissue type) or dynamic (replicating a physiological process). Accuracy phantoms are adapted to tissue type, pathology, and species (e.g., with differing skin pigmentation, model organism) of interest, and can be complex, representing, for example, different layers present in tissue as well as the different chromophores and fluorophores that contribute to the overall optical behaviour of the tissue or pathology. They are most often used for clinical training and testing purposes, or to validate physical models or simulations. In contrast, precision phantoms are employed to evaluate basic device performance metrics, such as signal stability, signal-to-noise, contrast, or resolution, and therefore, only require simpler geometries<sup>202</sup>. Devices that generate quantitative outputs (e.g., blood oxygenation) may require approaches for determining additional metrics such as precision, bias, linearity, and sensitivity.

The distinction between these two phantom types is necessary as the final application of the phantom dictates its design and composition.

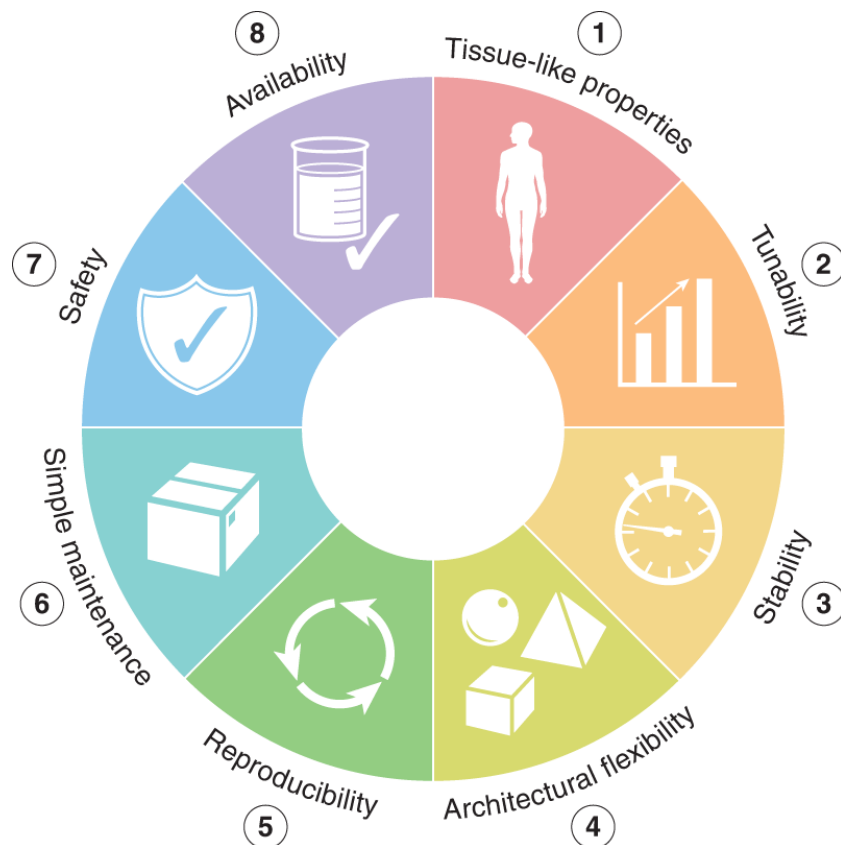


**Figure 2.2 : Base requirements for a PAI phantom.**

An ideal PAI phantom material should possess the eight following characteristics: (1) Ability to provide biologically-relevant properties (including optical, acoustic, mechanical and thermoelastic properties); (2) Tunability of properties to mimic different tissue types; (3) Stability of all intrinsic properties over time and under different environmental conditions (including temporal, mechanical and photo-stability); (4) Architectural flexibility and ability to include absorbers/molecules of interest; (5) Simple and reproducible preparation; (6) Low maintenance (ease of storage and transport); (7) Safe to prepare and handle; (8) Readily available, low-cost ingredients, and non-specialist fabrication equipment.

## 2.2 Materials and methods for preparation of biophotonic phantoms

Materials for optical phantoms that could be adopted for use in PAI can be broadly divided into water-based and non-water-based materials (Table 2.2), with respective additives used to tune optical and acoustic properties (Table 2.3 and Table 2.4). The key features that are typically considered when comparing different materials are their tissue-mimicking capabilities and the ease of handling and fabrication (summarised in Table 2.5), which together with the intended phantom type, determine the overall design and suitability for use in a given application.

**Table 2.2: Relevant optical and acoustic parameters of different materials without the use of additives.**

Optical properties refer to a wavelength range of 600 – 900 nm.

Material	Optical				Acoustic		
	Intrinsic $\mu_a$ (cm <sup>-1</sup> )	Intrinsic $\mu_s'$ (cm <sup>-1</sup> )	Refr. index	Ref.	c (m·s <sup>-1</sup> )	(dB·cm <sup>-1</sup> ) at frequency (MHz)	Ref.
General soft tissue	0.1-0.5	10-20	1.33-1.51	183	1450–1730	0.1–1.6 dB·cm <sup>-1</sup> ·MHz <sup>-1</sup>	186,193
Aqueous suspension	negligible*	negligible	1.34	203	1480-1574	0.0022 at 1 MHz	186
Agar/Gelatin	negligible	negligible	1.35	204	1490-1650	0.1–1.5 dB·cm <sup>-1</sup> ·MHz <sup>-1</sup>	205–212
Polyacrylamide (10%-20%)	negligible	negligible	1.35	213	1540-1590	0.08-0.14 at 1 MHz 0.7 at 5 MHz	207,214
PVA	Dependent on preparation*	Dependent on preparation**	1.35	215,216	1510-1570	0.075–0.56 dB·cm <sup>-1</sup> ·MHz <sup>-1</sup>	149,207, 217,218
Co-polymer in oil	negligible (dependent on polymer)	negligible (dependent on polymer)	1.47	219	1420-1510	0.4-7 at 3.5 MHz	160,168, 220,221
PVCP (including 0 - 90% softener)	negligible	negligible	1.52	156	1350-1580	0.6-0.9 at 1 MHz 1-30 at 4 MHz 6.45-8.24 at 5 MHz	153,156, 158,222 –225
Silicone	negligible	negligible	1.4	226	970-1200	1.8 at 3 MHz 14.0 at 5 MHz 14.7 at 7 MHz	207,227 –229
Polyurethane	negligible	negligible	1.5	230	1400-1470	0.5–0.7 dB·cm <sup>-1</sup> ·MHz <sup>-1</sup>	229
Polyester, Epoxy resin	negligible	negligible	1.54	231–233	1844-3118	7–17 at 0.5 MHz	234

\*Absorption spectra of water can be obtained from Hale and Querry et al.<sup>235</sup>

\*\*Dependent on the number, length and rate of freeze and thaw cycles, by the grade of the PVA (molecular weight, degree of saponification) and its concentration in the aqueous solution, by the presence of additives and by the type of solvent<sup>218,236–240</sup>.

### 2.2.1 Tuning of optical and acoustic properties

The molecular composition of a material type determines its intrinsic properties and the types of additives that can be used to tune such properties. Nevertheless, similar classes of additives have been used in water (Table 2.3) and non-water based (Table 2.4) materials to tune optical and acoustic properties<sup>178</sup>.

Additives that adjust optical scattering can be broadly classed into (i) lipids, (ii) white metal oxide suspensions, (iii) polymer microspheres and, more rarely, (iv) gold nanoparticles. Lipid-based emulsions such as milk or intralipid are popular in water-based phantoms due to their simple application and biological similarity to fat-based structures found in tissue, allowing incorporation of aqueous absorbers or fluorophores. Here, Intralipid<sup>241,242</sup> (or similar compounds<sup>243</sup> such as Nutrilipid, Lyposyn, Vasolipid, Lipofundin etc), a suspension of soybean oil, egg phospholipids, and glycerol in water, is most commonly employed due to its high stability, low absorption coefficient, regulatory controlled low batch-to-batch variability<sup>243,244</sup> and extensive validation in the literature<sup>191,241–246</sup>. Microspheres are a favourable option for precision phantoms due to their well-controlled size, refractive index and predictable scattering properties in Mie theory<sup>247</sup>, but they are typically high cost, limiting their use to small volumes. Metal oxide powders are cost-effective and widely available due to their industrial production for all white pigmented materials such as paint, and commonly used in non-water-based phantoms. However, thorough mixing and/or sonication needs to be employed to create homogeneous, repeatable materials without sedimentation or clustering. Titanium dioxide (TiO<sub>2</sub>) has been a preferred choice due to its negligible NIR absorption and high refractive index<sup>231</sup>, but metal oxides with different particle sizes<sup>248</sup> and refractive indices (e.g., aluminium oxide [Al<sub>2</sub>O<sub>3</sub>]<sup>249</sup> or zinc oxide [ZnO]<sup>250,251</sup>) have also been used. Gold nanoparticles<sup>252</sup> have also been employed as a scattering agent<sup>253</sup>, but they are relatively high in cost and exhibit optical absorption.

To adjust optical absorption, either natural tissue chromophores (e.g., haemoglobin or melanin) or synthetic absorbers (e.g., pigment-based inks, molecular dyes, etc.) can be used<sup>178</sup>. The biological chromophores are able to provide absorption spectra similar to soft tissue, but are often unstable and restricted to use in aqueous environments<sup>178</sup>. Synthetic absorbers can exhibit both flat (e.g., India ink<sup>254,255</sup>) or peaked (e.g., Naphthol Green<sup>256</sup>, Trypan Blue<sup>257</sup>) absorption spectra, but with higher stability. Care must be taken when employing molecular dyes in water-based phantoms, as diffusion and degradation processes can occur<sup>254</sup>. Also, subtle fluorescence emission can produce strong artefacts in turbid materials due to long photon pathlengths increasing fluorescence contamination. In contrast to molecular dyes, pigment-based inks consist of larger particles and cannot diffuse through a gel or polymer-matrix, but their optical absorption is often accompanied by additional scattering<sup>255</sup>. India ink, a suspension of insoluble carbon particles in aqueous medium, is one of the most popular options as the ink is chemically and spectroscopically stable, non-toxic, non-fluorescent and offers a flat absorption spectrum with little variation over the visible and NIR region<sup>254,255</sup>. In general, absorbers

need to be chosen carefully with regard to the base material as solubility may be limited and hardening of the base material can impact the absorption properties<sup>258</sup>.

The acoustic properties of a material are closely connected to its mechanical composition and are, therefore, more difficult to tune with external agents. In water-based materials the speed of sound can be increased by the addition of alcohol-based substances (e.g., n-propanol<sup>206,209</sup>, glycerol<sup>259</sup> etc), or decreased by the addition of oils<sup>260</sup>. Popular additives for tuning the acoustic attenuation include graphite<sup>206,209</sup> or Al<sub>2</sub>O<sub>3</sub> powder<sup>249,259</sup>, whilst for backscattering silica spheres or glass beads<sup>208,209,224,261</sup> are often used. These additives may also affect optical properties, further challenging the preparation of multimodal phantoms.

**Table 2.3: Common additives for tuning intrinsic properties in water-based phantom materials proposed for biophotonic imaging.**

Function	Additive	
Optical adjustment	Scattering $\mu_s'(\lambda)$	Lipids (oil/fat <sup>245,262-264</sup> , milk <sup>265</sup> , intralipid <sup>241-244,246</sup> and similar <sup>266</sup> ) Microspheres <sup>267,268</sup> Metal oxide suspensions (e.g., Al <sub>2</sub> O <sub>3</sub> (1-10 $\mu\text{m}$ ) <sup>249</sup> , TiO <sub>2</sub> (< 1 $\mu\text{m}$ ))
	Absorption $\mu_a(\lambda)$	Whole blood/erythrocytes/haemoglobin <sup>264,267,269-273</sup> Melanin <sup>274</sup> Pigment-based inks (e.g., India ink) <sup>255,275-277</sup> Molecular dyes <sup>278-281</sup>
	Fluorescence $\mu_{af}(\lambda)$ , $I_e(\lambda)$ , $\Phi_{OY}$ , $\tau$	Biological Fluorophores (e.g., NADH, FAD, Collagen, Porphyrins) <sup>282</sup> Quantum Dots <sup>283</sup> Biomedical contrast agents (e.g., ICG, 800CW, Fluorescein) <sup>284,285</sup> Laser dyes (e.g., IR125) <sup>247</sup>
Acoustic adjustment	Speed of sound $c(f)$	n-propanol <sup>206,209</sup> Ethanol <sup>266</sup> Glycerol <sup>259</sup> Oil <sup>260</sup> Formaldehyde <sup>287</sup>
	Acoustic attenuation $\alpha(f)$	Graphite powder <sup>206,209</sup> Evaporated milk <sup>208</sup> Al <sub>2</sub> O <sub>3</sub> <sup>249,259</sup>
	Acoustic backscattering $\mu_{bs}(f)$	Glass beads <sup>208,209,224,261</sup> Silicon carbide <sup>259</sup>
Miscellaneous	Stability	Benzalkonium chloride <sup>259,288</sup> Thimerosal <sup>208</sup> Formaldehyde <sup>289</sup> EDTA Penicilin <sup>290</sup> ,
	Deoxygenation	Yeast <sup>272,273,291</sup> , sodium azide, sodium dithionite <sup>162,292,293</sup> , glucose & glucose oxidase catalase, nitrogen gas
	Oxygenation	Oxygen gas, hydrogen peroxide <sup>162</sup>
	Thermal damage	Albumen <sup>256,294</sup> Bovine Serum Albumin (BSA) <sup>295-298</sup>
	Melting temperature	Formaldehyde <sup>289</sup>

**Table 2.4: Additives for tuning relevant acoustic and optical properties in non-water-based phantom materials proposed for biophotonic imaging.**

	Resin-based materials	Silicone	Polyvinyl chloride plastisol (PVCP)	Co-polymer in oil
	TiO <sub>2</sub> <sup>202,230</sup> Al <sub>2</sub> O <sub>3</sub> <sup>299</sup> Glass or silica spheres <sup>233</sup> Polystyrene microspheres <sup>231,232,300</sup>	TiO <sub>2</sub> <sup>252,301-308</sup> , Al <sub>2</sub> O <sub>3</sub> <sup>226,277,309,310</sup> , Ba <sub>2</sub> SO <sub>4</sub> <sup>311</sup> , polystyrene <sup>310</sup> silica <sup>252,312</sup>	TiO <sub>2</sub> <sup>153,154,222,313</sup> ZiO <sup>250,251</sup>	TiO <sub>2</sub> <sup>164</sup>
Optical adjustment	India Ink <sup>300,314</sup> Dyes (e.g., 900NP) <sup>230,233,258,300,315-317</sup> Carbon powder <sup>318,319</sup>	India ink <sup>307</sup> Carbon black <sup>277</sup> Alcohol soluble Nigrosin <sup>301</sup> Freeze dried bovine zinc phthalocyanine <sup>302</sup> Yellow food dyes <sup>302</sup> Infra-red dyes <sup>302</sup>	Black plastic colorant, Pigments <sup>153,156,222</sup> Black ink <sup>155</sup> Trypan blue <sup>155</sup> Melanin powder <sup>155</sup>	Oil-based dyes <sup>164</sup>
	Quantum Dots <sup>202,317,320,321</sup> Biomedical contrast agents (e.g., ICG, 800CW, Fluorescein) <sup>284</sup> Laser dyes (IR125) <sup>285</sup>	Biomedical contrast agents (e.g., ICG, Cy5, Fluorescein) <sup>322,323</sup>	-	Quantum dots <sup>324</sup>
		Silicone oil, Vaseline Glycerin <sup>325</sup>	Hardener/softener <sup>156</sup> Type of plasticizer <sup>156</sup>	Variation of polymer concentration (eg. SEBS, LDPE) glycerol <sup>161,220,221</sup>
Acoustic adjustment		-	Glass microspheres <sup>156</sup> , Type of plasticizer <sup>156</sup> , Graphite powder <sup>325-327</sup>	Variation of polymer concentration (e.g., SEBS, LDPE) glycerol <sup>161,220,221</sup>
		-	Glass beads <sup>157,328</sup>	Glass spheres <sup>165,220</sup> , Silica/graphite powder spheres <sup>221</sup> , glycerol <sup>161</sup>

**Table 2.5: Comparison of relevant properties of materials used for biophotonic phantoms.**

(TMM=Tissue-mimicking). Legend: green (++)=excellent performance; light green (+)=above-average performance; light red (-)=below-average performance; red (--)=poor performance in respective category.

Material	TMM Properties			Handling			Fabrication			Biocompatibility	References
	Optical	Acoustic	Tunability	Temporal Stability	Mechanical Stability	Storage/Transport	Architectural Flexibility	Complexity	Safety		
Aqueous suspension	++	-	+	--	--	--	-	++	++	Yes	255,329,330
Agar/Gelatin	++	++	++	-	-	-	++	++	++	Yes	204,206,208,209,224,289,331,332
Polyacrylamide	++	++	++	-	+	-	++	+	-	Yes	333
PVA	++	++	++	+	+	-	++	-	++	Yes	148,334-338
Co-polymer in oil	++	+	+	++	++	++	++	+	++	No	161,220,221,339
PVCP	++	+	+	++	++	++	+	+	+	No	138,156,158
Silicone	++	-	+	++	++	++	++	+	++	No	290,309,310
Polyurethane	++	+	+	++	++	++	++	+	+	No	202,230,258
Polyester, Epoxy resin	++	--	+	++	++	++	+	+	++	No	231,232,314,315
<i>Ex vivo</i> tissues	++	++	--	-	++	-	--	++	++	Yes	178

### 2.2.2 Aqueous suspensions

Aqueous suspension phantoms are one of the most popular phantom types in optical imaging due to their availability, cost-effectiveness, easy preparation, and excellent reproducibility<sup>191,245,278,279,255,262–268</sup>. Water has negligible scattering and absorption properties in the visible wavelength range<sup>235</sup>, but a lower speed of sound ( $1480 \text{ m}\cdot\text{s}^{-1}$ ) and acoustic attenuation coefficient ( $0.002 \text{ dB}\cdot\text{cm}^{-1}\cdot\text{MHz}^{-2}$ ) relative to most soft tissues<sup>185,186</sup>. The speed of sound can be increased by the addition of ethanol (e.g., 7.4% by mass for  $1540 \text{ m}\cdot\text{s}^{-1}$ )<sup>286</sup>. For tuning optical scattering properties, fat emulsions<sup>241,242,266,243–246,262–265</sup> or microspheres<sup>267,268</sup> are preferred, while optical absorption can be tuned by adding whole blood or extracted erythrocytes<sup>264,267,273</sup>, inks<sup>255,275,276</sup>, molecular dyes<sup>278,279</sup>. Blood-based phantoms<sup>267,269–273</sup> can also mimic changes in  $\text{sO}_2$ , by addition of oxygenating (e.g., oxygen) or deoxygenating compounds (e.g., yeast<sup>269,272,273</sup>). Due to their excellent reproducibility<sup>243,244,254</sup>, aqueous phantoms with ink have been considered in several multi-laboratory studies<sup>191,340</sup>.

Despite their advantages, liquid phantoms have a limited shelf life of only a few hours to days, with storage below  $4^\circ\text{C}$  and careful maintenance<sup>341</sup>. Moreover, mismatches of the refractive index and acoustic impedance of the container walls or embedded inclusions can cause optical and acoustic channelling artefacts, especially at the surfaces<sup>342–344</sup>. Water and water-based materials are also known to have a strong dependence on temperature, with the speed of sound in water varying up to  $50 \text{ m}\cdot\text{s}^{-1}$  in the temperature range of  $20\text{--}40^\circ\text{C}$ <sup>193</sup>.

### 2.2.3 Hydrogels

Hydrogels refer to water-swollen, cross-linked polymer networks and can be formulated from natural or synthetic sources. The popularity of hydrogels for phantom fabrication stems from their well-characterised performance, ease of fabrication and flexible architecture. They are largely optically transparent and their optical and acoustic properties can be easily tuned (Table 2.3). ‘Intelligent’ hydrogels can also be sensitive to external stimuli, such as  $\text{pH}$ <sup>345</sup>, temperature or light<sup>346</sup>.

In the field of biophotonic phantoms, four main types of hydrogels have been used: (i) agarose<sup>204,249,256,261,289,332,341,347,348</sup>; (ii) gelatin<sup>205,224,257,260,289,349,350</sup>; (iii) polyacrylamide<sup>213,351</sup>; and (iv) poly(vinyl alcohol) (PVA)<sup>148,149,240,277,336</sup>. Agarose is a hydrophilic colloid that is derived from seaweed and red algae, whereas gelatin is a homogeneous colloid gel produced by physical, thermal, or chemical degradation of collagen extracted from animal tissues. Agarose and gelatin hydrogels are prepared by mixing with water, heating to crosslink, then cooling. Agarose gels exhibit a higher melting temperature ( $40^\circ\text{C}$  vs  $90^\circ\text{C}$ ) and higher stiffness, but lower toughness compared to gelatin<sup>224</sup>. Despite their widespread use in research settings, agar and gelatin gels suffer from short-term stability<sup>204,255</sup>, being highly susceptible to dehydration, bacterial ingrowth, thermal and mechanical damage, limiting reuse<sup>147,352</sup>. Extending longevity is possible by careful storage<sup>208</sup> and addition of chemicals such as

formaldehyde<sup>289</sup> or benzalkonium chloride<sup>259,288</sup>, though this increases fabrication complexity. Moreover, well defined inserts within hydrogels are usually short-lived due to diffusion of absorbers<sup>158</sup>. Targets can be encapsulated, but this creates refractive index mismatches and acoustic boundaries.

While agarose and gelatin are formed by physical crosslinking, polyacrylamide gels are formed by chemical reaction of acrylamide monomer and *N,N'*-methylene-bis-acrylamide and subsequent polymerization using a reaction initiator–activator pair. Polyacrylamide gels have higher melting temperature and optical transparency than gelatin or agarose<sup>333</sup>. However, their preparation process is more complex and requires a higher level of precautionary measures as polyacrylamide may contain residual amounts of the known neurotoxin acrylamide monomer<sup>207</sup>. Moreover, polyacrylamide gels are more likely to suffer from cluster formation resulting in structural inhomogeneities and have a more limited shelf life, ranging from a few hours upon air exposure to a few weeks in airtight containers<sup>333</sup>. A special, proprietary type of polyacrylamide called *Zerdine*<sup>TM</sup> forms the base material of a commercially available standard ultrasound phantom accredited by the American College of Radiology (ACR)<sup>353</sup>.

PVA is a water soluble, biodegradable synthetic polymer derived from the hydrolysis of poly(vinyl acetate). The material is widely available, cost-effective, non-toxic and exhibits greater longevity and structural rigidity than agar-, gelatin- or polyacrylamide-based hydrogels<sup>149,336</sup>. While crosslinking can also occur chemically or by radiation, the base material is usually formed by physical crosslinking with alternate freezing (-20°C) and thawing (+20°C) cycles as it yields gels with higher mechanical strength and without toxic residues<sup>354</sup>. The optical<sup>149</sup>, acoustic<sup>218,240</sup>, mechanical<sup>238</sup>, and electrical properties<sup>355</sup> can be tuned by changing: the number, length and rate of freeze and thaw cycles; the grade and concentration of the PVA; as well as additives and solvents<sup>218,236–238,240,356</sup>. By keeping the number of freeze-thaw cycles low and choosing a water/dimethyl sulfoxide (DMSO) mixture as a solvent, high optical transparency<sup>337</sup> and speed of sound<sup>149</sup> can be achieved. PVA phantoms can be stable for a 6-month period<sup>357</sup>, if stored hydrated in sealed containers, yet the preparation process is time-consuming and tedious. Slight variations in fabrication can lead to inhomogeneities<sup>148</sup>, compromising reproducibility. Moreover, as variation of preparation parameters affect acoustic, optical, and mechanical parameters simultaneously, independent tunability is limited.

#### 2.2.4 Non-water-based materials

Given the long-term stability and tunability concerns associated with aqueous suspensions and some hydrogels, the biophotonic community has also sought to adopt non-water-based materials for phantom preparation. These materials are of particular value for the PAI community, as water-based coupling media are often used for photoacoustic image acquisition which could interact with a water-based phantom medium. The most common examples are: (i) resins; (ii) room-temperature-vulcanizing (RTV) silicone; (iii) polyvinyl chloride plastisol (PVCP); and (iv) copolymer-in-oil materials.

First introduced by Firbank, Delpy<sup>358,359</sup> and Vernon<sup>230</sup> in the optical field, polyester<sup>231–233,299,315,360</sup>, epoxy resin<sup>231,299,300,316,318,361</sup> and polyurethane<sup>202,230,258,317,362</sup> are transparent, solid materials that are formed by combining a resin with a hardener and are stable over years<sup>258</sup>. To create a homogenous, air-bubble-free base, the components are thoroughly mixed by mechanical stirring and/or sonication, then degassed and cured. Optical scattering is introduced by metal oxide powders<sup>299</sup> or microspheres<sup>231–233,300,359</sup> and absorption by pigment<sup>314</sup>- or dye-based inks<sup>230,233,258,315–317</sup> or (carbon) powders<sup>318,319</sup>.

Polyester and epoxy-based materials are characterised by high speed of sound ( $>2000 \text{ m}\cdot\text{s}^{-1}$ )<sup>234</sup>, and have therefore been only considered as acoustic phantoms for hard tissues such as cortical or trabecular bone<sup>234,363–365</sup>. In contrast, polyurethane phantoms have a more tissue-like speed of sound ( $1400\text{—}1470 \text{ m}\cdot\text{s}^{-1}$ )<sup>229,366</sup>. They also exhibit better compatibility with NIR dyes<sup>258</sup>, less photobleaching and shorter hardening time<sup>230</sup> and have therefore been a popular choice in fluorescence imaging<sup>202,285,317,320,362</sup>. While final cured polyurethane is chemically inert, some of its unreacted ingredients such as isocyanates are toxic<sup>367</sup>.

RTV silicone<sup>252,309,310,368,369</sup> exhibits similar properties to resin-based materials, but allows greater versatility in phantom design. It is composed of liquid polyorganosiloxanes that crosslink upon addition of a catalyst and is widely available in different hardness shores. Silicone has shown high popularity in optical imaging applications due to its high stability (over 10 years depending on the formulation)<sup>370</sup> and tunability of optical properties. However, it is characterised by high acoustic attenuation and low speed of sound ( $<1000 \text{ m}\cdot\text{s}^{-1}$ )<sup>207,229</sup> with little tunability, so has limited potential for use in multimodal or hybrid applications.

More recently, a suspension of a poly(vinyl chloride) (PVC) resin in a liquid plasticizer known as PVCP has been demonstrated for biophotonic phantoms. It is usually purchased as a two-part suspension of PVC resin and plasticizer forming a plastisol at room temperature<sup>371</sup>. While several preparation methods for PVCP phantoms have been proposed<sup>153,156,158,222,325</sup>, the common procedure<sup>223</sup> involves sonication of additives with the plastisol mixture, degassing then gradual heating and subsequent cooling. The availability of various PVC-based formulations and additives gives scope for tuning the properties of the resulting material<sup>372</sup>. PVCP is generally optically transparent after preparation, so optical properties are adjusted by the addition of pigment-based absorbers<sup>154</sup> or black plastic colorant<sup>153,156,157,222</sup>, and scatterers such as  $\text{TiO}_2$ <sup>153–155,222</sup> or  $\text{ZiO}$ <sup>250,251</sup>. The typical speed of sound is relatively low ( $1400 \text{ m}\cdot\text{s}^{-1}$ )<sup>325</sup> but can be tuned by the addition of softener or hardener or by the type of plasticizer<sup>156</sup>. Solid PVCP inclusions within PVCP base material have been shown to be stable up to six months<sup>153</sup>. Unfortunately, PVCP suffers a major drawback, which is the lack of a supply chain with standard scientific suppliers<sup>154</sup>. Moreover, some plasticizers are based on phthalates, which can act as reproductive and developmental toxicants<sup>373</sup>, subject to regulatory oversight in some regions.

Copolymer-in-oil materials are a relatively new class of phantom material based on thermoplastic styrenic elastomers, such as polystyrene-block-poly(ethylene-ran-butylene)-block-polystyrene (SEBS). Thermoplastic elastomers are composed of a rigid phase made of styrene structures and a rubber phase made of elastomeric structures and are easily processable as a melt at elevated temperatures<sup>374</sup>. Oil-based materials can be purchased off the shelf in the form of ‘gel wax’<sup>164,165,375</sup> or can be manufactured from a choice of polymers and oil, where SEBS and mineral oil have proven popular<sup>161,220,221</sup>. The fabrication procedure typically requires sonication of additives with the plasticizer, mixing with the polymer and heating to the respective melting temperature, before degassing and curing. Oil-based materials are non-toxic, cost-effective, readily available, mechanically robust, have excellent temporal stability and short curing times<sup>221,376</sup>. Depending on their formulation, copolymer-in-oil materials can be optically transparent<sup>164,377</sup> with scattering and absorbing properties tuneable by additives such as oil-based dyes<sup>164</sup> and metal oxide powders<sup>164,375</sup>. The mechanical and acoustic properties are similar to breast fat<sup>220</sup> and can be modified by variation of polymer concentration<sup>220,221</sup>, polymer<sup>220</sup> or plasticizer<sup>221</sup> type. The speed of sound also approaches soft tissue at  $1500 \text{ m}\cdot\text{s}^{-1}$ <sup>160</sup>. Fortunately, they are also cost-effective, non-water absorbing, non-toxic and biologically inert<sup>221,339</sup>, although recipes based on commercial polymer or gel wax<sup>164,339</sup> result in high batch-to-batch variation, impairing the reproducibility of the phantom fabrication. Moreover, copolymer-in-oil materials can be highly thermosensitive and the reported tunability of the acoustic properties is currently limited to  $1480 \text{ m}\cdot\text{s}^{-1}$ <sup>220</sup> for the speed of sound, which is lower than the ultrasound soft tissue standard of  $1540 \text{ m}\cdot\text{s}^{-1}$ <sup>378</sup>.

## 2.3 Conclusion: Phantom materials and standardisation efforts for photoacoustic imaging

A wide range of material have been proposed for biophotonic phantoms, some of which show high potential for application in PAI. Materials that have been specifically proposed for PAI phantoms include hydrogels<sup>146,147</sup>; polyvinyl alcohol (PVA)<sup>148,149,274,379</sup>; polyvinyl chloride plastisol (PVCP)<sup>153,155–158,167,222</sup>; silicone<sup>150,151</sup>; and resin-based materials<sup>231,315</sup>. Standards for phantom material properties and fabrication have not yet been established for PAI. In 2018, the International Photoacoustic Standardisation Consortium (IPASC)<sup>166</sup> was founded, aiming to reach consensus on standardised PAI performance test methods, test objects and data management<sup>166</sup>. To reach this goal, IPASC combines stakeholders from academia, industry, and government. Establishing standards for PAI phantom properties, fabrication, characterisation and application – similar to standards existing in ultrasound<sup>211,380</sup> – would be advantageous for PAI from a translational perspective.

For PAI precision phantoms, where solid, temporally stable non-water-based materials are required, copolymer-in-oil materials appear to be a promising option due to their biologically relevant optical, acoustic, and mechanical properties, easy handling, and non-toxic ingredients. Additionally, they are cost-effective, non-water absorbing, and biologically inert<sup>221,339</sup>. These characteristics in combination with their potential 3D-printability<sup>219</sup> suggest that copolymer-in-oil materials may have the potential to become more widespread in biophotonic applications, particularly for those with a multi-modal aspect. Despite the high promise copolymer-in-oil materials hold, certain drawbacks remain (as outlined in Section 2.2.4) that would need to be overcome, such as the limited tunability of their acoustic properties and relatively low fabrication reproducibility.

For biological accuracy phantoms in PAI, hydrogels can also be considered due to their excellent biologically relevant properties and biocompatibility, despite their more complex handling requirements, allowing incorporation of tissue-derived components such as blood, fat, or other endogenous molecules. Recent progress in the development of tough hydrogels<sup>381</sup> may provide strategies for creating water-based phantoms with higher temporal and mechanical stability. Tissue-engineered phantoms could also become a promising option as the technology advances, affording increased reproducibility and reduced costs. While the field is still in its infancy, new technologies such as 3D-bioprinting offer tremendous potential to create phantoms of enhanced biological realism with higher accuracy and precision. The importance of mimicking different target tissues as closely as possible becomes apparent in recent studies such as from Sjoding et al<sup>382</sup> highlighting the impact of different skin pigmentation on the accuracy of pulse oximeter readings.

The material review performed in this chapter provides the necessary background for considering the development of test objects and methods for PAI towards Aim 1 of this thesis. Copolymer-in-oil materials feature high long-term stability which are necessary to assess temporal stability of PAI

systems for longitudinal studies of perfusion-limited hypoxia during tumour development. Owing to their flexibility, hydrogel materials will be considered for use in accuracy studies of a mesoscopic PAI system to be used for detailed visualisation of the tumour vasculature. Importantly in both cases, characterisation systems that enable accurate phantom material validation must be established to enable objective evaluation of performance. Development of the required optical and acoustic characterisation systems are introduced in Chapter 3.



# 3 VALIDATION OF MATERIAL CHARACTERISATION METHODS

*I would like to thank Dr. Heidrun Wabnitz for performing the time-domain optical measurements, Jason Hardy for manufacturing the components of the acoustic characterisation system, Dr. James Joseph and Dr. Srinath Rajagopal for their advice on acoustic system design, and Dr. Srinath Rajagopal for the code contribution for acoustic data post-processing.*

To establish a reliable phantom platform for technical validation of PAI measurements, accurate characterisation of material properties is fundamental. Here, this task is addressed using two methodologies: First, the performance of a custom-built double-integrating sphere (DIS) system for optical characterisation was established using Mie theory simulations and comparison to time-domain optical measurements performed at a national metrology institute. Second, a through-transmission setup for acoustic characterisation was constructed and validated using reference measurements in water. These validation efforts lay the foundation for the subsequent precision phantom development work in Chapter 4.

## 3.1 Validation of the double-integrating sphere optical characterisation system

### 3.1.1 Introduction

Accurate characterisation of optical properties in material samples has long been a significant challenge. In 2005, a study comparing the performance of eight different photon migration instruments for optical characterization revealed inter-system variation up to 32% for the absorption coefficient ( $\mu_a$ ) and 41% for the reduced scattering coefficient ( $\mu_s'$ ) for a given phantom<sup>192</sup>, emphasizing the need for thorough assessment of accuracy and precision of optical characterisation instruments.

A large variety of optical characterisation methods exist, including time-resolved experimental techniques, integrating-sphere base systems, spatial-domain measurement techniques, frequency domain photon migration (FDPM) methods or fibre-based multi-distance reflectance measurements<sup>188</sup>. One of the most widely used methods — and often regarded as the “gold standard” — is the DIS technique, which is based on transmitted and reflected light collection in two integrating spheres<sup>188,383</sup>. DIS systems have distinct advantages compared to other optical characterisation techniques, including: ease of construction, ability to characterise a broad range of optical properties, a fast inversion procedure, and ability to measure solid as well as liquid samples (in a cuvette)<sup>188</sup>.

A DIS system measures the total reflectance and transmittance of a sample. Based on these two measurements, the reduced scattering coefficient ( $\mu_s'$ ) and optical absorption coefficient ( $\mu_a$ ) are calculated, typically using an inverse adding doubling (IAD) routine<sup>384–386</sup>. Using a range of input parameters, the IAD algorithm estimates the optical properties and calculates the total reflectance and transmittance of a sample via an approximation of the radiative transport equation. The algorithm is iteratively repeated until a match between the calculated and experimentally observed data is determined.

Here, validation was performed of a custom-built DIS system available in Prof Bohndiek’s laboratory at the University of Cambridge. In the present work, the measurement repeatability of reference and sample measurements was first assessed. Secondly, the impact of measurement variables, such as sample thickness, anisotropy factor and refractive index on the IAD output parameters was estimated. Lastly, validation of the DIS measurements of reduced scattering coefficient was performed by comparison to theory as well as time-domain optical measurements.

## 3.1.2 Methods

### 3.1.2.1 System setup and optical measurements

The in-house DIS system was constructed according to the method of Pickering et al<sup>383</sup>. It is composed of two integrating spheres (50 mm internal diameter, Avantes, Netherlands), each connected to a spectrometer (Avantes Starline Avaspec-2048, Netherlands) via an optical fibre (Figure 3.1A, B). The reflectance sphere is connected to a light source (Avantes Avalight-HAL-s-mini, serial number: LS-1505017, Netherlands) via a third optical fibre. The total reflectance and transmittance are determined by six measurements:

- a) Sample in Place: Reflectance  $R_s$  and transmittance  $T_s$  values are measured while the sample is placed between the two integrating spheres (Figure 3.1C).
- b) Incident Beam: Transmittance value  $T_1$  is recorded while reflectance and transmittance spheres are aligned with light source turned on (Figure 3.1D).
- c) Reference in Place: Reflectance value  $R_1$  is measured while a reference standard (99%, white, 1.25" diameter, Labsphere, USRS-99-010, AS-01158-060) is held in front of reflectance sphere (Figure 3.1E).
- d) Blocked beam: Transmittance value  $T_0$  is measured while reflectance and transmittance spheres are aligned, and light source is turned off (Figure 3.1F).
- e) Open Port: Reflectance value  $R_0$  is measured with transmittance sphere removed and light source turned on (Figure 3.1G).

The normalized reflectance  $M_R$  and transmittance  $M_T$  values are then calculated using the following formulae<sup>383</sup>:

$$M_R = r_{std} \cdot \frac{R_s - R_0}{R_1 - R_0} \quad \mathbf{1}$$

$$M_T = \frac{T_s - T_0}{T_1 - T_0} \quad \mathbf{2}$$

where  $r_{std}$  depicts the intensity reflected from the 99% reflectance standard. The measured values are used by the IAD algorithm developed by Dr. Scott Prahl (Source code: <http://omlc.org/software/iad/>) to estimate the optical properties of the material. As compression of the sample can impact the measurements<sup>387</sup>, the reflectance sphere was placed on a motorized stage (Thorlabs MTS50) to accurately control the distance between the spheres. The stage was set to zero at the position where the integrating spheres were perfectly aligned and the set distance was then adjusted according to the measured sample thickness. Measurements were performed in the wavelength range of 450 nm to 900 nm.

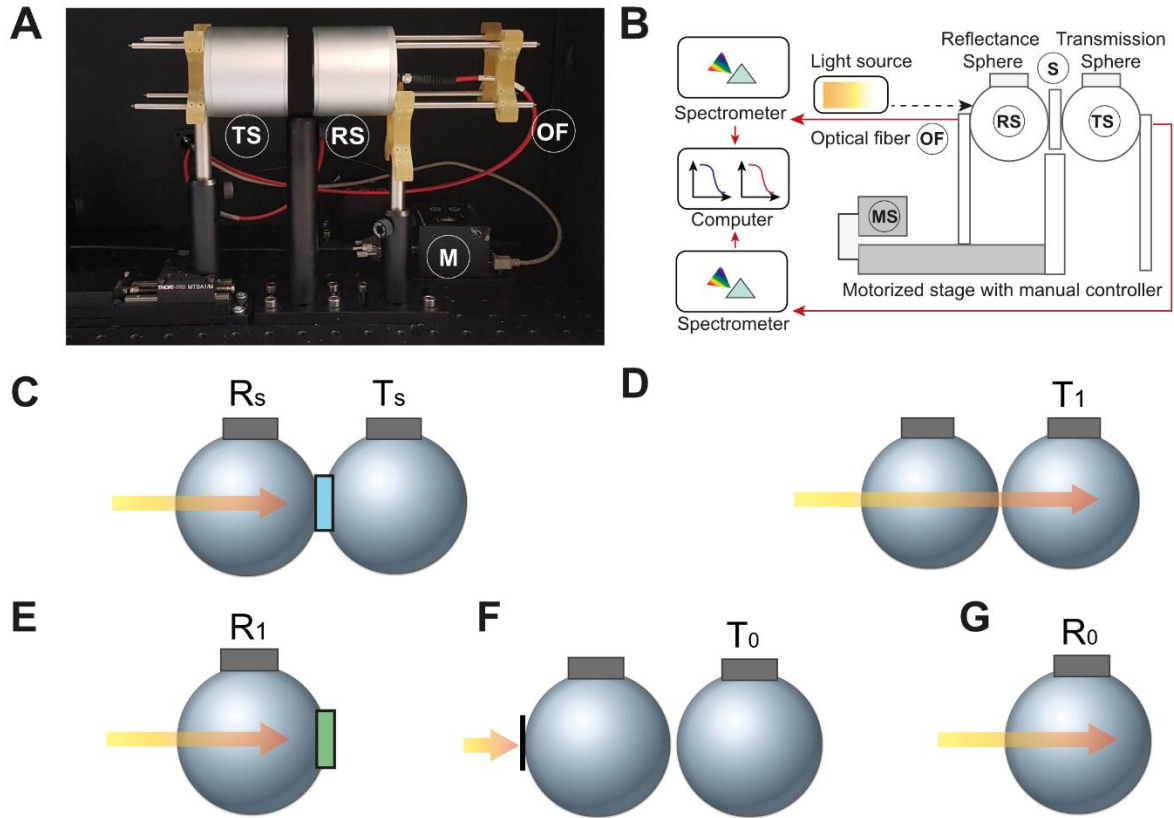


**Figure 3.1: Setup of the double-integrating sphere system for determination of absorption and scattering coefficient.**

A photograph (A) and schematic (B) of the DIS system for the evaluation of the optical absorption coefficient and reduced scattering coefficient are shown. Individual system components are denoted by the following annotations: S (Sample), RS (Reflectance Sphere), TS (Transmission Sphere), OF (Optical Fibre) and MS (Motorized Stage) in the photo and schematic. Schematics of the sphere and sample arrangement for the required six reference measurements: sample in place (C), incident beam (D), reference in place (E), blocked beam (F) and open port (G).

### 3.1.2.2 Time-domain measurements

Time-domain measurements were performed at Physikalisch-Technische Bundesanstalt (PTB) in Berlin, Germany, by means of recording and analysing time-of-flight distributions (DTOFs) of photons with picosecond time resolution. Picosecond light pulses were provided by a supercontinuum laser (SuperK Fianium FIU-15 PP, NKT Photonics, Germany) at a repetition rate of 39 MHz. A variable bandpass filter (VARIA, NKT Photonics, Germany) was used to select the desired wavelength (532 nm, 586 nm, 620 nm, 660 nm, 700 nm, 770 nm, 800 nm, 808 nm) with a bandwidth of 10 nm. The light was guided to the source position and collected from the detector position on the phantom by multimode graded-index fibres. The DTOFs were recorded by means of an ultrafast hybrid photomultiplier HPM-100-07C (Becker&Hickl GmbH, Germany) and a time-correlated single photon counting (TCSPC) module (SPC-150, Becker&Hickl GmbH, Germany). The time resolution (half width of the instrument response function, IRF) of the instrument was 59 ps at 532 nm and 33 ps at 800 nm. More details on the instrumentation are provided in previous work<sup>388</sup>. The measurements on the phantoms were

performed in reflection geometry, with a source-detector separation of 1 cm. DTOFs were recorded with 1 s collection time and 20 repetitions, with a photon count rate of  $\sim 5 \times 10^5 \text{ s}^{-1}$ .

The optical properties were retrieved by fitting the measured DTOFs with a Monte-Carlo (MC) model. MC databases (specific for each phantom's thickness) were created for multiple values of the scattering coefficient while the absorption coefficient was included following the "white Monte Carlo" approach. The GPU-based simulations of light propagation in a homogeneous turbid slab were implemented on the basis of previously established pipelines<sup>389,390</sup> with time-resolved recording. The fit parameters were  $\mu_s'$ ,  $\mu_a$  and the DTOF's time origin. The refractive index of the phantoms was assumed to be 1.43. More details of the methods applied and the results obtained in these measurements are presented in<sup>391</sup>.

### 3.1.2.3 Phantom preparation

#### *Agar phantoms*

For validation of the  $\mu_s'$  values provided by the DIS system, agar (1.5% agarose, Sigma Aldrich 9012-36-6) phantoms with microspheres (Polysciences, Inc., Warrington, PA) as scattering agents were prepared following the protocol by Joseph et al<sup>145</sup>. As the IAD algorithm (if no constraints are set) does not converge in purely scattering, non-absorbing media<sup>387</sup>, Nigrosin (Sigma Aldrich, 211680-100G; 0.62 v/v% of a 0.5 g/l stock solution in deionised water) was added to all samples to achieve a mean absorption of  $0.05 \text{ mm}^{-1}$ . Nigrosin is a widely available, polyaniline-based black dye that is often used in biophotonic phantom studies due to its broad, featureless absorption in the visible and near-infrared spectrum<sup>392</sup>.

Mie scattering refers primarily to the elastic scattering of light from atomic and molecular particles whose diameter is equal to or slightly larger than the wavelength of the incident light<sup>183</sup>. It is regarded as the dominant type of light scattering in soft tissues<sup>393</sup>. As data were analysed in the wavelength range of 450 to 900 nm, carboxylate microspheres with diameters of 0.5, 0.75 or 2  $\mu\text{m}$  were chosen for the experiments (Table 3.1). For the phantoms, volume fractions generating reduced scattering coefficients similar to those found in soft tissue<sup>183</sup> were chosen (Table 3.1). To calculate the required amount of microspheres from the volume fractions  $f_v$ , the volume  $V_m$  of one microsphere was calculated:  $V_m = (4/3) \pi (d/2)^3$  where  $d$  is the diameter of one microsphere. The amount of the microsphere solution  $V_s$  for a total phantom volume  $V_t$  was then derived via  $V_s = (f_v \cdot V_t) / (c_m \cdot V_m)$ , where  $c_m$  is the microsphere concentration of the solution provided by the manufacturer (Table 3.1). To provide a homogenous distribution of the scattering agents, the solution was thoroughly vortexed and then pipetted into the sample moulds. The sample moulds were composed of two microscopy glass slides (Polysciences, 22245-1) placed around 3D-printed PETG (Polyethylene Terephthalate Glycol, RS components 202-0385) spacers of 1 mm and 2 mm thickness, respectively. All samples had a length of 60 mm and a width of 20 mm. After 30 minutes of curing time, samples were measured using the DIS system. Sample thickness was confirmed by vernier calliper measurements before DIS data acquisition.

### Copolymer-in-oil phantoms

For additional validation, the DIS system was compared with an independent measurement system, a time-domain optical setup. Copolymer-in-oil phantoms were prepared using the recipe that will be outlined in Chapter 4. In total, five phantom materials were prepared with varying optical properties (Table 3.2). The base material was always composed of 30% high molecular weight SEBS (Sigma Aldrich 200557-250G), 8% low-density Polyethylene (LDPE, Alfa Aesar 43949.30), and 5% of the stabilizer butylated hydroxytoluene (HT, Sigma Aldrich W218405-1KG-K) with all components mixed in mineral oil (Sigma Aldrich-330779-1L).  $\text{TiO}_2$  (Sigma Aldrich 232033-100g) was added as a scatterer and Nigrosin (Sigma Aldrich 211680-100G) as optical absorber in the concentrations outlined in Table 3.2. A working stock solution of Nigrosin in mineral oil (2.5 mg/mL) was prepared to enable a more accurate adjustment of the optical absorption. From each material preparation, two phantoms were fabricated; one for the DIS system (rectangular geometry: width=60 mm, length=20 mm, thickness=3 mm) and one for the time-domain system (circular geometry: diameter=90 mm, thickness=20 mm).

**Table 3.1: Composition of agar phantom samples.**

$d_m$ = diameter of one microsphere,  $V_m$ =volume of one microsphere,  $c_m$ =microsphere concentration as stated by the manufacturer,  $f_v$ =volume fraction.

Phantom purpose	$d_m$ ( $\mu\text{m}$ )	$V_m$ ( $\mu\text{m}^3$ )	$C_m$ (beads/mL)	$f_v$
Sample variability	2	4.189	$5.68 \cdot 10^9$	0.06
Sample thickness	0.5	0.065	$3.64 \cdot 10^{11}$	0.002
IAD input variables	0.75	0.221	$1.08 \cdot 10^{11}$	0.001
Mie simulations	0.75	0.221	$1.08 \cdot 10^{11}$	0.002
	0.75	0.221	$1.08 \cdot 10^{11}$	0.003
	0.75	0.221	$1.08 \cdot 10^{11}$	0.004
	0.75	0.221	$1.08 \cdot 10^{11}$	0.005

**Table 3.2: Concentrations of scatterer and absorber in copolymer-in-oil phantom samples.**

Phantom number	$\text{TiO}_2$ (w/v %)	Nigrosin stock solution (v/v %)
1	0.07	0.018
2	0.07	0.036
3	0.07	0.009
4	0.17	0.009
5	0.27	0.009

#### 3.1.2.4 Data analysis and Mie scattering simulations

All data were analysed in MATLAB (version 2016b, Mathworks, USA). The coefficient of variation (COV) was calculated as the standard deviation (SD) divided by the mean. Mie theory provides a simple first approximation to model scattering in soft tissues following a few assumptions, which have been

summarized by Jacques et al<sup>393</sup>. For this work, the experimental  $\mu_s'$  values were compared with Mie scattering amplitudes simulated using MATLAB code written by Christian Mätzler (Source code: <https://omlc.org/software/mie/>)<sup>394</sup>. Reference values stated in the literature were used as input parameters for the refractive indices  $n$ , specifically  $n=1.34$ <sup>395</sup> for the medium and  $n=1.6$ <sup>396</sup> for the scattering particle in the agar phantoms. The anisotropy factor was simulated over all relevant wavelengths (450-900 nm) using the same source code, and the mean of the anisotropy factor was taken as input for the IAD algorithm. For both the time-domain and DIS measurements of the copolymer-in-oil material, the scattering anisotropy factor  $g$  was taken to be  $g=0.7$  and the refractive index  $n=1.43$  based on previous reports<sup>375</sup> of a similar material (gel wax). For the Bland Altman analysis, the percentage difference [(DIS method – validation method)/average %] was plotted as a function of the average of the two methods<sup>397</sup>.

### 3.1.3 Results

#### 3.1.3.1 Assessment of instrument precision

First, the measurement repeatability of the DIS system was tested. For the reference measurements (see definitions in Section 3.1.2.1), the system showed good precision across all wavelengths with a mean COV of 0.1% and 2.0% respectively for the *incident beam* (Figure 3.2A) and *blocked beam* (Figure 3.2B, COV of fitted lines) reflectance spectra, and 0.1% and 1.2% for the *reference in place* (Figure 3.2C) and *open port* (Figure 3.2D) transmission spectra (Table 3.3, n=3). For the sample measurements, low COVs were found for both  $\mu_a$  and  $\mu_s'$  values of phantom samples measured at the same spot without replacement ( $COV_{\mu_a}=0.7\%$ ,  $COV_{\mu_s'}=0.5\%$ ). The COV values increased slightly when measured with phantom replacement between the measurement runs, at the same spot ( $COV_{\mu_a}=0.9\%$  and  $COV_{\mu_s'}=1.5\%$ ) and at different spots across the phantom surface ( $COV_{\mu_a}=2.2\%$  and  $COV_{\mu_s'}=1.9\%$ ) (Table 3.4, n=3).

The impact of the sample thickness on measurement repeatability was also assessed (Figure 3.3A,B; Table 12). No significant differences between the intra-sample COVs of 1 mm and 2 mm phantoms could be found for  $\mu_a$  ( $COV_{1mm}=0.9 \pm 0.8\%$  vs  $COV_{2mm}=1.2 \pm 0.4\%$ ,  $p=0.58$ , Figure 3.3A) or  $\mu_s'$  ( $COV_{1mm}=3.4 \pm 0.8\%$  vs  $COV_{2mm}=3.2 \pm 0.8\%$ ,  $p=0.77$ ; Figure 3.3B; all measurements at different spots with displacement). When comparing the inter-sample COVs for  $\mu_a$  and  $\mu_s'$  between three independently fabricated phantoms, the COV values of 2 mm thickness were found to be considerably lower than those for samples with 1 mm thickness (1 mm:  $COV_{\mu_a}=13.9\%$ ,  $COV_{\mu_s'}=6.1\%$ ; 2 mm:  $COV_{\mu_a}=6.8\%$ ,  $COV_{\mu_s'}=4.5\%$ ), suggesting that inhomogeneities in sample composition and thickness may have a more pronounced effect on the results in samples of smaller thickness. The actual  $\mu_a$  and  $\mu_s'$  values for each wavelength were found to be comparable between 1 and 2 mm samples (Figure 3.3A,B).

**Table 3.3: Repeatability of reference measurements**

COV=Coefficient of variation.

Reference measurement		COV (%)	Sample size (n)
Reference Transmission	Incident beam	0.1	3
	Blocked beam	2.0	3
Reference Reflection	Reference in place	0.1	3
	Open port	1.2	3

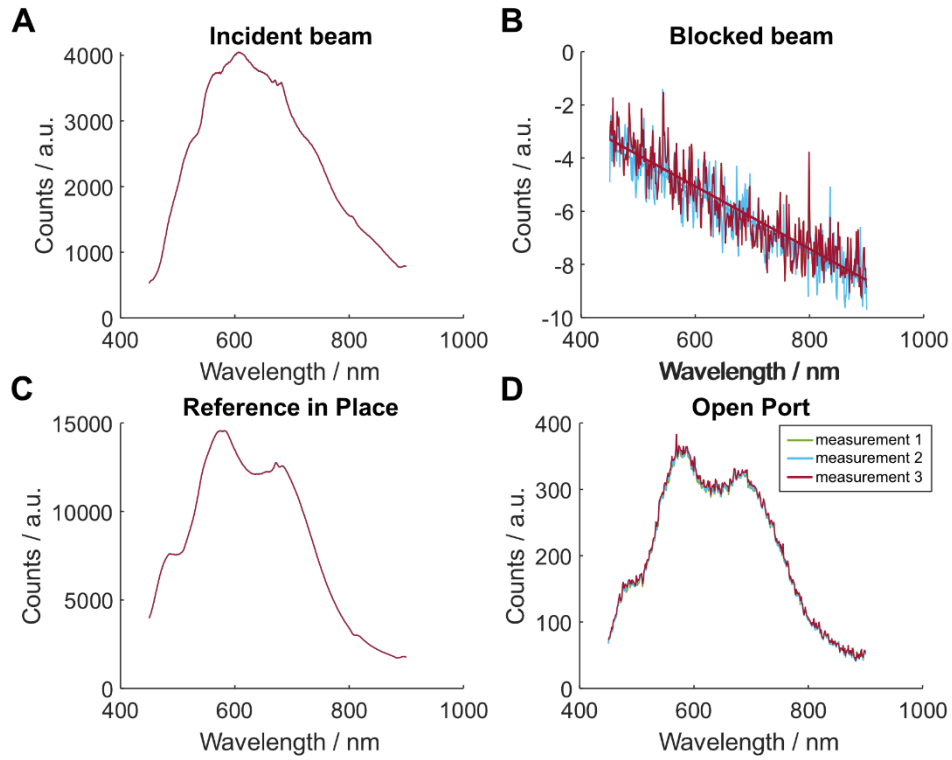


**Figure 3.2: DIS reference spectra.**

Graphs to show the replicate ( $n=3$ ) transmission reference measurements [incident beam (A), blocked beam (B, with fitted lines)], and reflectance reference measurements [reference in place (C), open port (D)].

**Table 3.4: Repeatability of sample measurements for optical absorption ( $\mu_a$ ) and reduced scattering coefficients ( $\mu_s'$ ).**

COV=Coefficient of variation.

Sample information		COV $_{\mu_a}$ [%]	COV $_{\mu_s'}$ [%]	Sample size n
Intra-sample variability	same spot without replacement (2 mm)	0.7	0.5	3
	same spot with replacement (2 mm)	0.9	1.5	3
	different spot with replacement (2 mm)	2.1	1.9	3
Inter-sample variability	1 mm	13.9	6.1	3
	2 mm	6.8	4.5	3

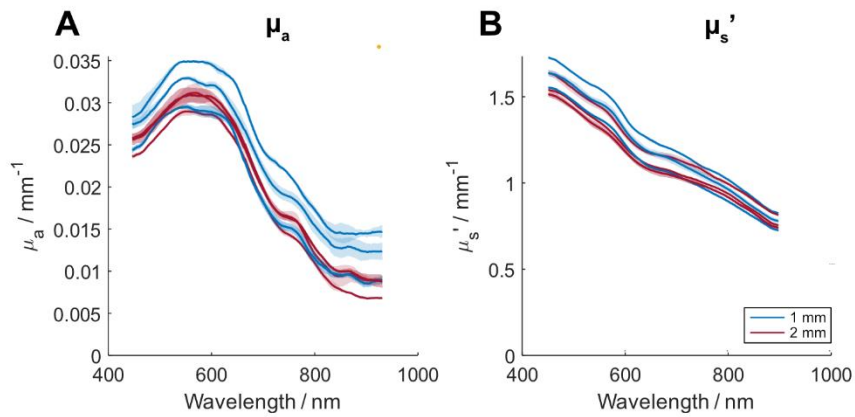


**Figure 3.3: Repeatability of sample measurement of the DIS system.**

Optical absorption (A) and reduced scattering coefficient (B) of  $n=3$  different samples of 1 mm (blue) and 2 mm (red) thickness. Data displayed as mean  $\pm$  SD (shaded regions).

### 3.1.3.2 Impact of IAD input variables on measured properties

For the IAD analysis, three sample-related input variables need to be known to estimate the optical properties of a material: the anisotropy factor, refractive index and sample thickness<sup>387</sup>. It is important to evaluate the impact that errors or inaccuracies in these values have on the output of the IAD analysis, as averages across all wavelengths or literature values are often used due to a lack of widely available characterisation systems. To investigate these effects, a representative sample measurement was processed using anisotropy factors, refractive indices and sample thicknesses in an expected error range, and the percentage change of the resulting  $\mu_a$  and  $\mu_s'$  values was assessed. A change of up to  $\pm 0.1$  (10%) for the anisotropy factor led to a mean change of  $\pm (2.4 \pm 0.9\%)$  for  $\mu_a$  (Figure 3.4A), and  $\pm (1.2 \pm 0.7\%)$  for  $\mu_s'$  across all wavelengths (Figure 3.4B). For the refractive index, a smaller error range of  $\pm 1.5\%$  was chosen as the refractive index can be usually measured/estimated very accurately (up to several decimal points)<sup>398</sup>. A change of  $\pm 0.02$  (1.5%) for the refractive index led to a change of  $\pm (6.9 \pm 0.5\%)$  for  $\mu_a$  (Figure 3.4C), and  $\pm (2.1 \pm 0.8\%)$  for  $\mu_s'$  (Figure 3.4D) across all wavelengths. For the  $\mu_s'$  values, a linear increase of the absolute change could be observed with increasing wavelengths (0.6% at 450 nm to 3.2% at 900 nm). Finally, a change of  $\pm 0.2$  mm (10%) of the sample thickness led to a change of  $\pm (16.8 \pm 3.6)\%$  for  $\mu_a$  (Figure 3.4E) and  $\pm (9.5 \pm 3.2)\%$  for  $\mu_s'$  (Figure 3.4F) across all wavelengths. The results suggest that variations in the anisotropy factor and refractive index only minimally affect the  $\mu_s'$  and  $\mu_a$  values, whilst variations in sample thickness are a major source of inaccuracy on the IAD output and hence must be carefully controlled.

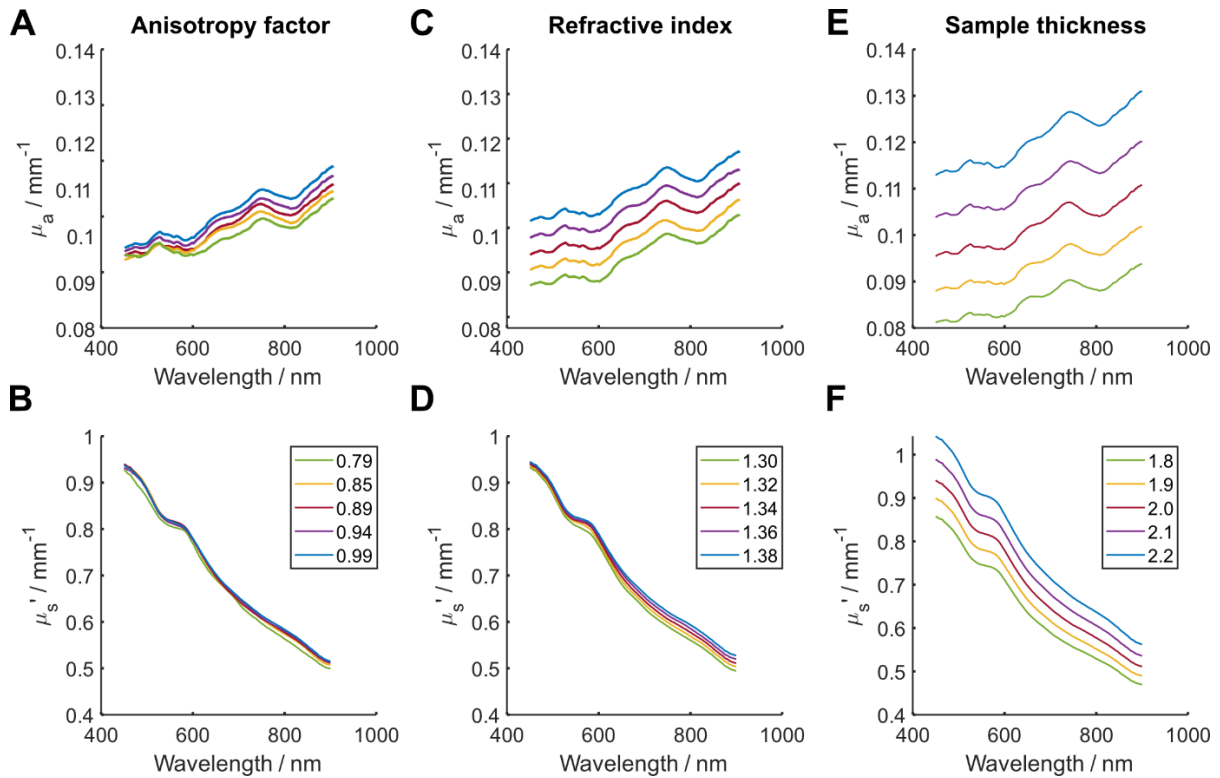


**Figure 3.4: Impact of variation of IAD input variables on resulting optical absorption and reduced scattering coefficient.**

The impact of variation of anisotropy factor (A,B), refractive index (C,D), and sample thickness (E,F, units in mm) on the optical absorption coefficient (A,C,E) and reduced scattering coefficient (B,D,F) output of the IAD is shown. Measurements are based on a total reflectance and transmission measurement of an agar sample containing a volume fraction of 0.001 0.75  $\mu\text{m}$  carboxylate microspheres (Anisotropy factor: 0.89, refractive index: 1.34, sample thickness: 2 mm, red line).

### 3.1.3.3 Assessment of instrument accuracy

#### *Comparison of DIS reduced scattering values with simulated values using Mie theory*

$\mu_s'$  values measured with the DIS system can be directly compared against Mie theory calculations. Thus, a comparison between  $\mu_s'$  values of agar microsphere phantoms measured by DIS and simulated  $\mu_s'$  values using Mie theory<sup>394</sup> was performed. The DIS system was found to overestimate the  $\mu_s'$  values in the microsphere phantom samples compared to the theoretical predictions (Figure 3.5A–C, Bias: +15.86%). Whilst experimental and theoretical values were found to agree reasonably well at higher wavelengths, a larger disagreement was observed at lower wavelengths for all scattering concentrations (Figure 3.5A,B)<sup>183</sup>. The shape of the curves was found to be similar with a descending slope and a small peak at 580 nm (Figure 3.5A). The percentage difference appeared relatively constant across different scattering concentrations (Figure 3.5C).

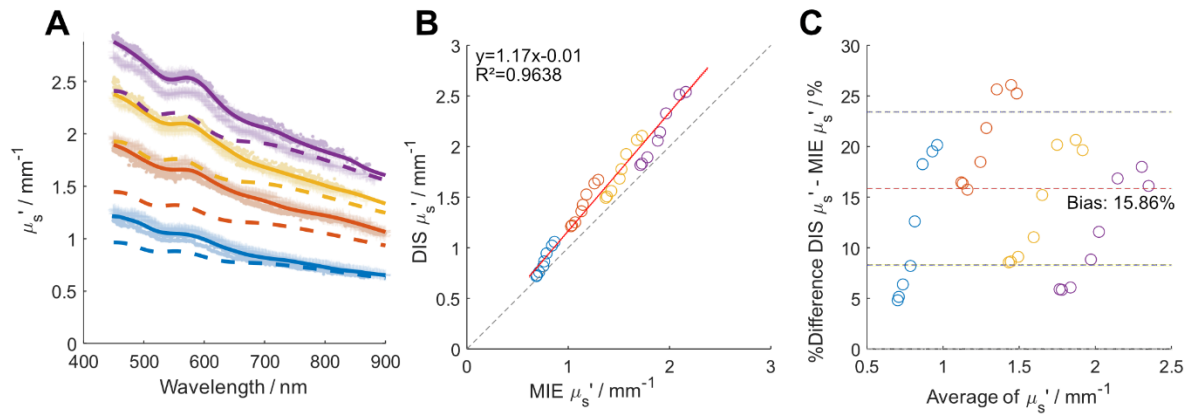


**Figure 3.5: Comparison of experimental  $\mu_s'$  values with simulated ones using Mie theory.**

(A)  $\mu_s'$  values of experimental (solid line) and simulated (dotted line) for phantoms containing microspheres (0.75  $\mu\text{m}$  diameter) in different volume fractions: 0.0055 (purple), 0.0044 (yellow), 0.0033 (orange), 0.0022 (blue). For the experimental values, the mean of 6 independent samples of both 2 mm ( $n=3$ , marker: dot) and 1 mm ( $n=3$ , marker: cross) was taken. (B) Correlation of reduced scattering values measured with double-integrating sphere method (DIS) and simulated values (MIE) (displayed for wavelengths: 532 nm, 586 nm, 620 nm, 660 nm, 700 nm, 770 nm, 800 nm, 808 nm). (C) Bland-Altman plot (percentage difference calculated as  $\mu_s'^{\text{DIS}} - \mu_s'^{\text{MIE}}$  divided by the average) for reduced scattering parameters is shown. Deviation from 0 (grey dotted line) is plotted as red dotted line (bias), limits of agreement are plotted as grey dotted lines.

#### *Comparison of DIS measurements with time-domain measurements*

To provide an experimental ground truth for both reduced scattering and absorption values, stable phantoms were prepared and a comparison was performed between the DIS system and a time-domain system available at the PTB (National Metrology Institute Germany). Overall, similar trends were observed in the two sets of measurements considering the variation in absorption and reduced scattering (Figure 3.6A,B). For optical absorption, a higher percentage difference was observed for samples with low optical absorption (mean percentage difference: -14.5%, Figure 3.6C,D). This is also reflected in the percentage difference analysed as a function of wavelength (Table 3.5) where high variations are observed in longer wavelengths (i.e. less absorbing). For the reduced scattering values, the systematic bias appeared to be constant (+17.9%, Figure 3.6E,F) across scattering concentrations and wavelengths (Table 3.5) and was of a magnitude and trend comparable to that observed in the theoretical investigation using Mie theory.

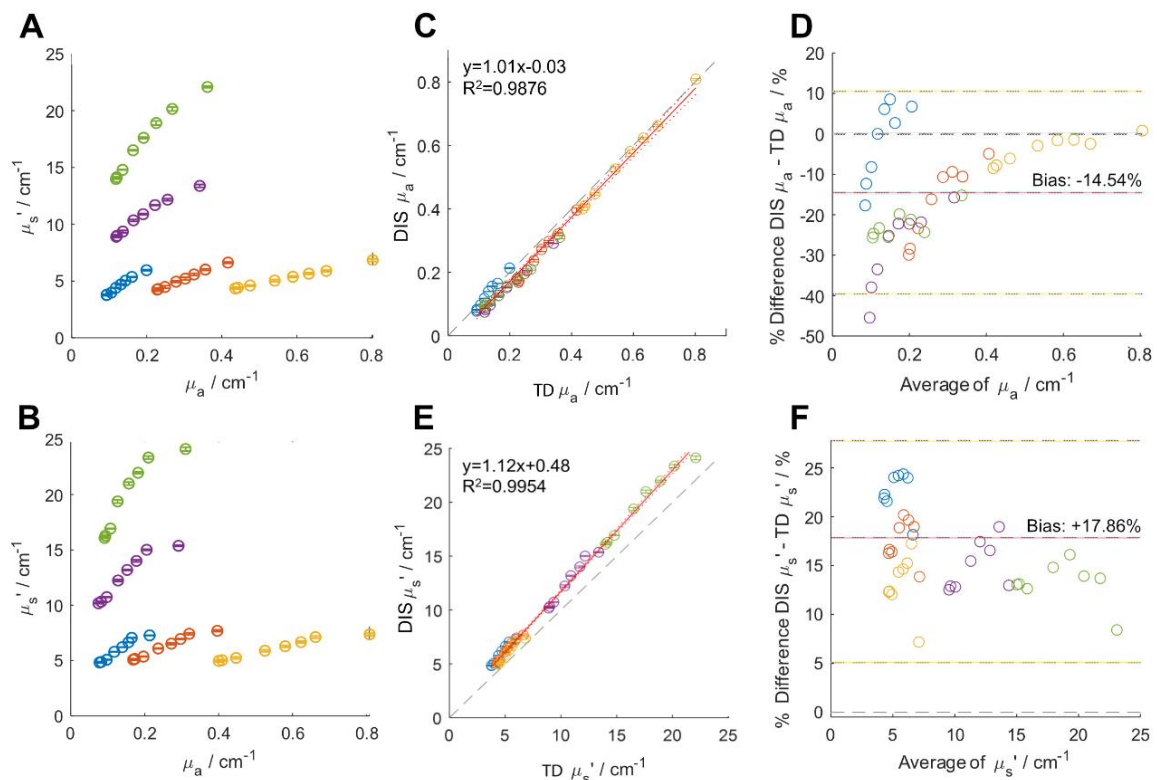


**Figure 3.6: Comparison of the DIS technique with time-domain optical characterisation method.**

Optical absorption and reduced scattering values of five copolymer-in-oil phantoms characterised by time-domain (TD) (A) and double-integrating sphere (DIS) method (B). Phantoms properties are given in Table 3.2: Phantom 1 (orange), Phantom 2 (yellow), Phantom 3 (blue), Phantom 4 (purple), Phantom 5 (green). Each dot depicts a measurement wavelength: 532 nm, 586 nm, 620 nm, 660 nm, 700 nm, 770 nm, 800 nm, 808 nm. (C) Correlation between values measured TD and DIS method for optical absorption parameters. (D) Bland-Altman plot (percentage difference) for optical absorption parameters. (E) Correlation between TD and DIS values for reduced scattering parameters. (F) Bland-Altman plot (percentage difference) for reduced scattering parameters. For the Bland-Altman plots, deviation from 0 (grey dotted line) is plotted as red dotted line (Bias) and limits of agreement are plotted as yellow dotted lines.

**Table 3.5: Overview of percentage difference between double-integrating sphere and time-domain optical characterisation methods.**

Error defined as mean error  $\mu_s'^{DIS} - \mu_s'^{TD}$  across all wavelengths.

Wavelength	Mean Error $\pm$ STD Mean Error $\pm$ STD	
	(%, n=5)	(%, n=5)
$\lambda$ (nm)	$\mu_a$	$\mu_s'$
532	-5.16 $\pm$ 9.39	14.02 $\pm$ 5.80
586	-10.23 $\pm$ 10.60	23.01 $\pm$ 5.68
620	-8.14 $\pm$ 12.24	22.13 $\pm$ 6.42
660	-8.70 $\pm$ 11.11	22.95 $\pm$ 5.86
700	-12.57 $\pm$ 10.66	21.46 $\pm$ 6.23
770	-16.86 $\pm$ 9.65	17.99 $\pm$ 5.82
800	-19.56 $\pm$ 9.94	18.53 $\pm$ 6.12
808	-22.04 $\pm$ 10.81	18.16 $\pm$ 5.94
Average	-12.90 $\pm$ 5.60	19.54 $\pm$ 2.60

### 3.1.4 Discussion

A detailed technical validation of the DIS system was conducted to evaluate the available precision and accuracy in optical characterisation of material samples. First, precision studies were performed. A high repeatability of both reference and sample measurements was determined, strengthening the position of the system as a reliable tool for precise characterisation of optical properties. A higher variability was found in samples of 1 mm thickness compared to 2 mm thickness. Reduced thickness of brittle materials such as agar slabs impedes handling of the sample and raises the probability of sample damage and breakage, thereby increasing inter-sample variability. Moreover, in thinner samples, small inhomogeneities in material composition may have a more pronounced effect on the measurement results<sup>399</sup> and – in particular for samples with low absorbing / scattering properties – it is more difficult for the IAD algorithm to distinguish measured spectra from background noise. Conversely, a smaller thickness minimises lateral light loss from the sides of the sample holder, which could erroneously lead to high absorption coefficients as all lost light is attributed to sample absorption<sup>383,387</sup>. Whilst the current version of the IAD algorithm attempts to correct for this offset<sup>387</sup>, reduction of light losses is still recommendable for more accurate optical property estimation<sup>400</sup>. Light loss depends on the size of the incident beam, the sample geometry and sample optical properties<sup>383</sup>. In our setup (sample port diameter: 9.92 mm, beam diameter: 8 mm), 1 mm and 2 mm sample thicknesses were shown to give similar reduced scattering and absorption values, suggesting that the light loss effect is negligible in this context. This leaves the 2 mm samples as the preferred thickness to use for future studies with specimen of similar properties.

Subsequently, the impact of measurement variations in anisotropy factor, refractive index and sample thickness on the measurement output were tested. As in the precision studies, sample thickness was found to have the largest impact on the estimated optical properties of the IAD program. These findings suggest that careful measurements are required to determine the experimental sample thickness with the highest accuracy possible. In our experimental setup, 3D printed spacers with specified thicknesses (1 or 2 mm) between glass slides ensure homogenous sample thickness and an isotropic smooth surface of the sample. As a further control, the thickness of each sample is confirmed with vernier callipers (three measurements per sample) before data acquisition. Finally, a motorized stage is used to accurately set the distance between the spheres, and to avoid squeezing of the samples which can impact the measurements.

Thirdly, accuracy studies were performed. Both simulation and experimental studies revealed a consistent percentage overestimation of the  $\mu_s$ ' values measured by our DIS system, whereas  $\mu_a$  values appeared to be underestimated. A common limitation of DIS systems is sphere "crosstalk"<sup>383,400,401</sup> referring to the fact the total reflectance/transmittance may contain part of the secondary reflected/transmitted light from the transmission/reflection sphere, thus resulting in errors in measurements of  $\mu_a$  (decrease) and  $\mu_s$ ' (increase) estimations, consistent with our observations. This

error is particularly pronounced in lower absorbing/reflecting samples<sup>383,401</sup>, which should be considered when interpreting data from respective material samples. Additionally, samples with weaker scattering/absorbing characteristics are characterised by spectra that are less distinct from background noise, resulting in a more variable result. Furthermore, at low optical depths the scattered reflected and transmitted light may not be totally diffuse (Lambertian) as is assumed in the IAD calculations for the DIS system<sup>401</sup>. While these effects can be accounted for by adjusting the sample thickness (e.g., higher sample thickness for lower absorbing samples), the more pronounced variability in samples with lower optical depths needs to be considered for future measurements.

Zhu et al stated that the IAD is most suitable for highly scattering ( $>16\text{mm}^{-1}$ ) and highly absorbing ( $>0.2\text{mm}^{-1}$ ) samples<sup>399</sup>. Compared to these benchmark values, the optical properties of our testing samples employed lower scattering ( $<2.2\text{mm}^{-1}$ ) and absorption ( $<0.08\text{mm}^{-1}$ ) characteristics, designed to cover the optical properties of soft tissues of relevance to future *in vivo* studies, which are of lower scattering and absorption<sup>183</sup>. Simulation<sup>399</sup> and experimental<sup>383</sup> data have demonstrated that the error of optical properties estimation by the IAD method is reduced for greater optical depths of samples, so accuracy should be improved for samples with higher scattering and absorbing properties.

In the Mie simulation studies, the  $\mu_s'$  values agreed better at higher wavelengths compared to lower wavelengths. This wavelength offset may be caused by smaller contributions of Rayleigh scattering at lower wavelengths (with a  $\lambda^{-4}$  dependence)<sup>183</sup>, potentially caused by agarose and Nigrosin particles, which must be added to provide sufficient mechanical stability and base absorption of the samples.

Compared to Mie simulations and time-domain measurements, the error of our system was found to be around 16% for scattering and 15% for absorbing (down to 3% for higher absorbing) samples. These values are in line with accuracy values that are found in the literature: Pickering et al found a  $\mu_a$  percentage difference of around 21% and 34% when validating their DIS system using intralipid-10% and Evans Blue<sup>383</sup>, respectively, and comparing the values with previously published data (no values stated for  $\mu_s'$ ). Using a single integrating sphere technique, Hu et al found relative errors of 17.4% and 14.4% for  $\mu_a$  values at the wavelengths of 810 nm and 850 nm, respectively<sup>400</sup>. The uncertainty in DIS measurements at the National Institute of Standards and Technology (NIST, Maryland, United States) is estimated to be between 4.0% and 5.0% for  $\mu_a$  and between 11% and 12% for  $\mu_s'$ <sup>188</sup>. This system employs considerably larger spheres with a larger sample port diameter (internal diameter: 196 mm vs. 50 mm; entrance port diameter: 25.1 mm vs. 4.86 mm; sample port diameter: 63.5 mm reduced to 38.1 mm by a removable port diameter reducer vs. 9.92 mm; for NIST system versus Cambridge system, respectively) and a HeNe Laser with smaller beam diameter (0.8mm vs. 8 mm for NIST system versus Cambridge system, respectively). A large ratio of sample port diameter to beam diameter has been shown to improve the accuracy of the optical characterisation<sup>399,400</sup>. However, the NIST system allows the acquisition of two wavelengths only ( $\lambda=543.5\text{nm}$ ,  $\lambda=632.8\text{nm}$ ), while our light source enables broadband characterisation over a large wavelength spectrum (400–1000 nm). Moreover, analysis at

NIST is performed with a slightly different inversion procedure to Prahl's IAD, also allowing for the computation of a complete uncertainty budget for each sample measurement<sup>188</sup>. When comparing our system performance with the time-domain system, it also needs to be considered that the time-domain method itself has some measurement uncertainty (although this is estimated to be <2%<sup>391</sup>), and that intra-sample heterogeneity of the phantom may affect the measurements.

Taking into account the limitations of our system design, sample composition and general difficulty in accurate optical characterisation, the performance of our DIS system compares favourably to other sphere setups and fulfils the need within the present thesis for investigating optical properties in phantoms mimicking soft tissue, where  $\mu_a$  and  $\mu_s'$  cover the ranges 0.005–0.16 mm<sup>-1</sup> and 0.1–4 mm<sup>-1</sup>, respectively (Table 4.1). The knowledge of the limitations of the system, e.g., higher accuracy with increased optical depth, will guide the phantom material measurements performed for this thesis, and will help for interpretation of the acquired data. Following a more extensive validation on a wider range of material types and properties, the results presented here may support the development of a correcting algorithm that accounts for the observed bias in future.

In summary, the following recommendations for data acquisition can be made: (1) Samples should be homogeneously composed with a smooth sample surface and constant thickness. (2) If no constraints are set to the IAD, a minimum absorption and scattering coefficient must be provided to allow for spectra distinct from background noise. These minimum values depend on the sample thickness. For 2 mm sample thickness, coefficients of 0.01 mm<sup>-1</sup> for  $\mu_a$  and 0.5 mm<sup>-1</sup> for  $\mu_s'$  are recommended. (3) Sample thickness should be adapted to sample properties: smaller thickness is preferred to minimise lateral light loss, but integrity of the sample and recording of spectra distinct from background must be ensured. (4) The sample thickness should be determined as accurately as possible to ensure accuracy of the IAD algorithm (usage of vernier callipers, motorized stage). (5) Multiple ( $\geq 3$ ) measurements per sample at different positions should be performed to reduce intra-sample variability. (6) A clean surface of the spheres and reference standard must be ensured, as reference values of the reflectivity can change after long-term use and/or due to the adherence of dust or other contaminants<sup>400</sup>.

## 3.2 Creation and validation of small-scale acoustic system

### 3.2.1 Introduction

PAI phantoms require both optical and acoustic characterisation to account for both the optical illumination and subsequent acoustic signal propagation. Techniques developed for measuring the speed of sound and acoustic attenuation in the frequency range of 1 to 10 MHz<sup>402-405</sup> can be broadly divided into continuous wave techniques<sup>406</sup> and broadband pulse techniques<sup>407</sup>. Continuous wave techniques are highly accurate and beneficial for detecting small changes in the attenuation or sound velocity, but are time consuming and subject to errors due to reflections or other interfering signals<sup>408</sup>. Pulsed techniques are often preferred for material characterisation due to their easy operation, lower cost and rapid, non-invasive measurement<sup>409</sup>. They can be categorized into the pulse-echo technique (one transducer as transmitter-receiver) and the through-transmission technique (two transducers as receiver/transducer respectively). Through-transmission techniques compare the time-of-flight of the ultrasonic signal with and without the sample in immersion fluid. From the phase and magnitude of the received spectra, the speed of sound and acoustic attenuation can be calculated as function of frequency over a wide bandwidth. Here, a small-scale acoustic characterisation setup based on the through-transmission technique was built, and its performance in evaluating the speed of sound and acoustic attenuation in solid materials was tested.

### 3.2.2 Methods

#### 3.2.2.1 System Setup

Individual system components were designed using the Autodesk Inventor software (version 2018, Autodesk Co., USA) and fabricated in collaboration with the physics workshop of the Cavendish Laboratory, University of Cambridge (Figure 3.7A, B). The system is immersed in a water bath (width: 25 cm × length: 45 cm × height: 50 cm, wall thickness: 8 mm, material: perspex) filled with distilled water to provide efficient and uniform coupling of the acoustic waves between the sample and transducers<sup>410</sup>. To resist rust and corrosion of the system's components, stainless steel was chosen as the base material. Sample and transducer holders are mounted on a base plate with handles attached to the side to facilitate lifting of the system in and out of the water (Figure 3.7A). The base plate can be clipped onto the frame of the water bath to minimise movement and vibrations during data acquisition. For the measurements, phantom samples are placed at the shared focus of a pair of coaxially aligned broadband immersion transducers (Olympus Industrial, Essex UK) with one transducer acting as transmitter and the other as receiver.

The system has been designed to allow interchange of several transducer pairs, allowing for acoustic characterisation over a wide frequency bandwidth [centre frequencies of available transducers: 1 MHz (diameter(d)=1.5 in); 2.25 MHz (d=1.5 in); 3.5 MHz (d=1 in); 5 MHz (d=1 in); 10 MHz (d=0.75 in)].

For the validation studies reported here, the 2.25 MHz transducer (U8421059; A395S-SU) was used. Transducers are mounted on stainless steel holders that are connected to motorized stages (Thorlabs, KMTS50E/M) to enable variation of the positioning with high precision (Figure 3.7C). Transducers are connected to a pulser-receiver (Model DPR300, JSR Ultrasonics, USA) using water-proof cables (BCU-62-6W, Olympus Industrial, Essex UK), and measured ultrasound signals were digitized (8 bit, 50 MHz) using an oscilloscope (InfiniiVision 3000A X-Series, Keysight Technologies, USA). Each of the digitized waveforms was averaged 5000 times to improve the signal to noise ratio (SNR). The following acquisition parameters were used for the measurements: gain: 5 dB, pulse repetition frequency: 1 kHz, time division: 1  $\mu$ s/div (10 div in total). Before each run, the temperature of the water was recorded using a digital thermometer (Fisher Scientific, 15-077-9D, USA).

### 3.2.2.2 Sample holder/mould and sample types

A rigid sample holder (field of view: 4  $\times$  4 cm) was constructed of stainless steel (Figure 3.7C). The sample holder allows the insertion of rectangular samples (5  $\times$  5 cm) of different thicknesses (1, 2, 5, and 10 mm) and can be converted into a sample mould (Figure 3.7D). By allowing the direct transition between sample mould and holder, precise sample thickness is ensured, and handling of the sample is minimised, limiting measurement inaccuracies arising from e.g., surface inhomogeneities or sample damage. Sample thickness was confirmed before each measurement using vernier callipers. For testing of the acoustic setup, polymethylmethacrylate (PMMA) plates (Engineering Design Plastics LTD, Cambridge, thickness 5 mm/10 mm) were chosen as PMMA is a common material choice for a validation of acoustic setups<sup>411</sup>. For evaluating the impact of input variables, a copolymer in-oil phantom sample was used (see Section 3.1.2.3) fabricated from 30% SEBS and 10% Polystyrene-block-polybutadiene-block-polystyrene (SBS, 182877-250G Sigma Aldrich).

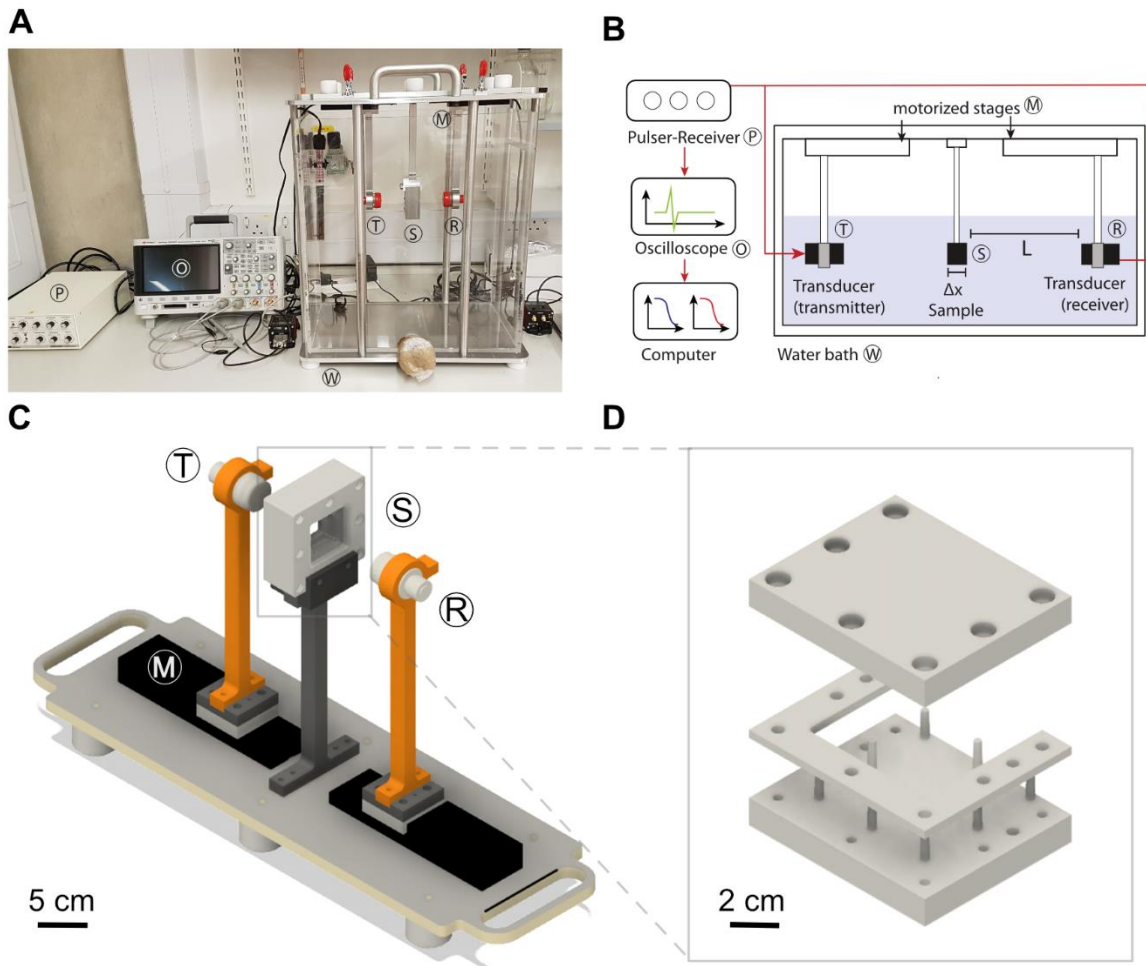


**Figure 3.7: Setup of the acoustic characterisation system.**

Photograph (A) and schematic (B) of the acoustic characterisation system. The pulser/receiver [P] sends a pulse via the transmitting transducer [T] through the sample [S] to the receiving transducer [R] which is coaxially aligned to the transmitter. The transducers are fixed with custom-made holders on motorized stages [M] which can be controlled via manual controllers. The whole setup is immersed in a water tank for acoustic coupling [W]. The pulser/receiver is connected to an oscilloscope [O]. All components can be controlled via a custom-made LABVIEW program. Computer-aided design (CAD) of the main transducer assembly (C) and sample mould (D). The sample mould can be directly mounted onto the system.

### 3.2.2.3 Data analysis

Data acquisition was performed using LabVIEW 2018 (National Instruments Inc., USA) and further analysis was conducted in MATLAB (v. 2016b, MathWorks, USA). All recorded waveforms (Figure 3.8) were pre-processed to remove direct current (DC) shifts, aligned to the centre of the acquisition window, padded with zeros if required and a time windowing (4-term Blackman-Harris window) was applied (according to the acoustic data processing procedure of NPL, London). The speed of sound in the sample can be identified by measuring the pulse delay  $\Delta t = t_s - t_0$ , where  $t_0$  depicts the arrival time of the acoustic pulse in absence of the test sample and  $t_s$  the arrival time with presence of the sample. Consequently, the speed of sound can be calculated as<sup>412–414</sup>:

$$c_s = \frac{c_w}{1 + \frac{\Delta t}{\Delta d} \cdot c_w} \quad 3$$

where  $c_w$  is the speed of sound in water and  $\Delta d$  is the sample thickness.

The acoustic attenuation can be calculated<sup>210</sup> as

$$\alpha_s = -\frac{20}{d} \log_{10} \left( \frac{U_s(f)}{U_w(f)} \right) + \alpha_w \quad 4$$

Where  $d$  is the sample thickness,  $U_s(f)$  and  $U_w(f)$  the voltage magnitude spectra for through-sample transmission, and reference/water-path transmission, respectively, and  $\alpha_w$  the acoustic attenuation in water. This approach is only valid for samples whose specific acoustic impedance,  $Z$  (density  $\times$  phase velocity), is similar to that of water. If the acoustic impedance is not known or different to that of water then the interfacial effects must be accounted for by using two test samples of two different thicknesses  $d_1$  and  $d_2$ :

$$\alpha_s = \left( \frac{TL_2 - TL_1}{d_2 - d_1} \right) + \alpha_w \quad 5$$

where  $TL_1$  and  $TL_2$  depict the transmission loss of the first and second sample, respectively.

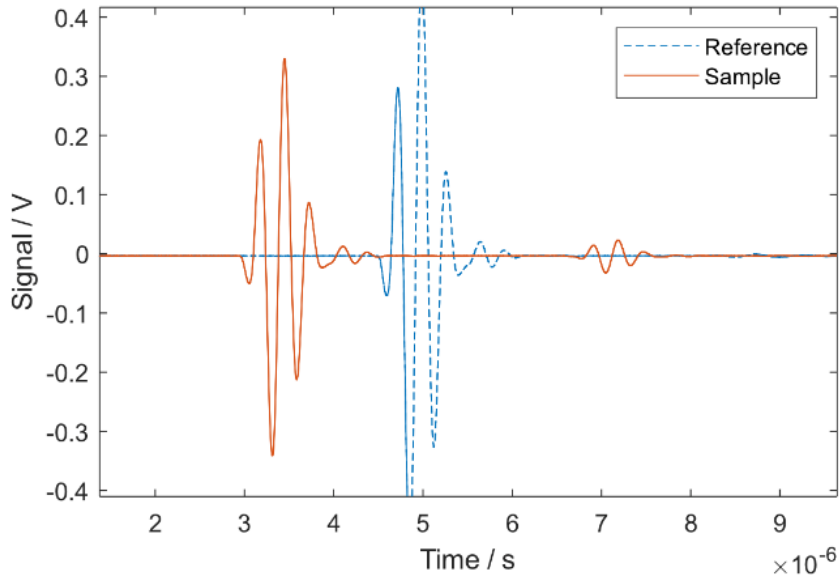


**Figure 3.8: Raw acoustic pulses.**

Unprocessed acoustic pulses for  $n=3$  repeated reference (dotted line, blue) and sample (full line, orange) measurements of a PMMA sample (5 mm thickness).

### 3.2.3 Results

#### 3.2.3.1 System accurately measures speed of sound in water

To validate the acoustic set up, the speed of sound in water was measured on different days and compared to literature values<sup>415-417</sup>. In the temperature range of 0–95 °C, the dependence of speed of sound in water can be approximated by a 5<sup>th</sup> order polynomial<sup>417</sup>:

$$c_w = \sum_{n=0}^5 a_n t_{90}^n \quad 6$$

with the polynomial coefficients described in Table 3.6. An excellent agreement between literature values<sup>417</sup> and experimental values was found (Figure 3.9A), confirming the functioning of the system (21.25°C:  $c_{\text{exp}} = 1486.1 \pm 0.23$  vs.  $c_{\text{lit}} = 1486.1 \text{ m}\cdot\text{s}^{-1}$ ; 21.6°C:  $c_{\text{exp}} = 1487.3 \pm 0.20$  vs.  $c_{\text{lit}} = 1487.2 \text{ m}\cdot\text{s}^{-1}$ ; 22.3°C:  $c_{\text{exp}} = 1489.2 \pm 0.06$  vs.  $c_{\text{lit}} = 1489.2 \text{ m}\cdot\text{s}^{-1}$ ). The mean measurement variability for the water (reference) measurement was found to be low (COV=0.01% for n=5 independent measurements at 3 different temperatures, Figure 3.9A).

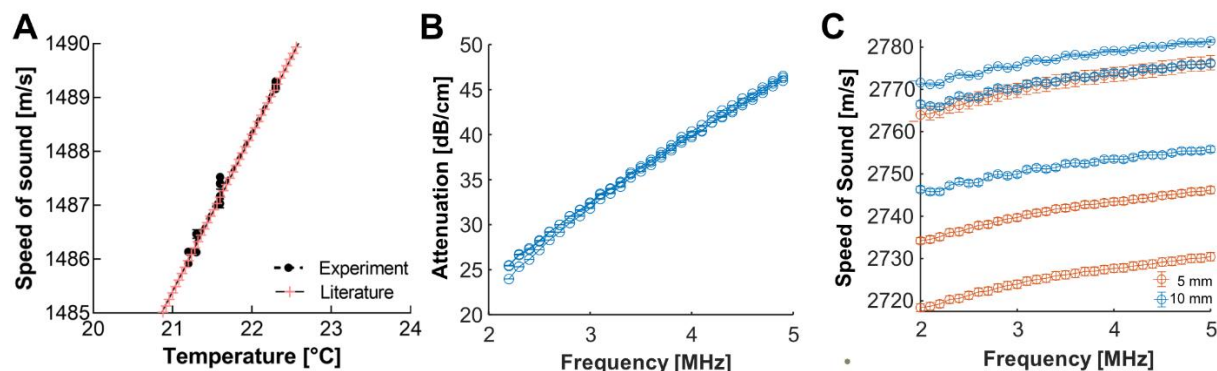


**Figure 3.9: Performance of the acoustic characterisation system in measuring liquid and solid samples.** (A) Comparison of experimentally acquired speed of sound values in water (n=5 measurements taken on 3 different days, black circular markers) with literature values<sup>417</sup> (red cross markers, fitted line according to equation 6). (B) Acoustic attenuation and (C) speed of sound for PMMA plates (5 mm (orange) and 10 mm (blue) thickness, temperature: 20.1°C, 3 replicates shown). Data displayed as mean ± SEM, error bars within symbols.

**Table 3.6: Polynomial coefficients  $a_i$  for formula describing the temperature dependence of speed of sound in water<sup>417</sup>.**

i	$a_i$
0	$1.40238754 \times 10^3$
1	$5.03711129 \times 10^0$
2	$-5.799136 \times 10^{-2}$
3	$3.287156 \times 10^{-4}$
4	$-1.398845 \times 10^{-6}$
5	$2.787860 \times 10^{-9}$

### 3.2.3.2 System shows acceptable measurement repeatability for solid samples

Subsequently, the measurement variability for solid samples was tested with and without repositioning. Using PMMA samples, the mean measurement variability across all frequencies was first determined without repositioning of the sample. For the speed of sound, it was found to be  $COV_{sos}=0.04\%$  and  $COV_{sos}=0.02\%$  for samples with 5 and 10 mm thicknesses, respectively, while the acoustic attenuation (calculated using both thicknesses according to Equation 5) varied with  $COV_{AA}=0.18\%$ . With repositioning of the sample, the measurement variability increased to  $COV_{sos}=0.85\%$  and  $COV_{sos}=0.49\%$  for 5 and 10 mm thicknesses respectively, and the acoustic attenuation to  $COV_{AA}=1.19\%$ . The mean speed of sound  $c(5\text{ MHz})=2751 \pm 23.3\text{ m}\cdot\text{s}^{-1}$  and  $2771 \pm 13.5\text{ m}\cdot\text{s}^{-1}$  for 5 and 10 mm thicknesses respectively, and acoustic attenuation  $\alpha(5\text{ MHz})=46.7\text{ dB}\cdot\text{cm}^{-1}$  corresponded to the acoustic properties of PMMA found in the literature ( $\sim 2750\text{ m}\cdot\text{s}^{-1}$ <sup>418,419</sup> and  $\sim 43\text{ dB}\cdot\text{cm}^{-1}$ <sup>420</sup> at 20°C and 5 MHz).

### 3.2.3.3 Evaluating the impact of input variables

The calculation of the acoustic properties requires information of two additional independent measurement variables: (1) sample thickness and (2) temperature. To assess the impact of these variables on the sample measurements, a simulation was performed with variation of the testing parameters in realistic error ranges ( $\pm 1\text{ }^\circ\text{C}$  for temperature and  $\pm 1\text{ mm}$  for sample thickness) based on a dataset acquired from a copolymer-in-oil phantom. Variation of the temperature by  $\pm 1\text{ }^\circ\text{C}$  did not impact the acoustic attenuation (Figure 3.10A) or transmission loss (Figure 3.10B), but led to a change of  $\pm 2.95\text{ m}\cdot\text{s}^{-1}$  (0.2%) at 5 MHz for the speed of sound (Figure 3.10C). Variation of the sample thickness to up to  $\pm 1\text{ mm}$  did not change transmission loss (Figure 3.10E), but led to a  $\pm 4.45\text{ dB}\cdot\text{cm}^{-1}$  (11.2%) change in acoustic attenuation (Figure 3.10D), and  $\pm 2.25\text{ m}\cdot\text{s}^{-1}$  (0.14%) change in speed of sound (Figure 3.10F) across the tested frequency range, respectively. The results suggest that variations in sample thickness measurement are a major source in variation, affecting both the acoustic attenuation and speed of sound, whilst variations in temperature only affect the speed of sound.

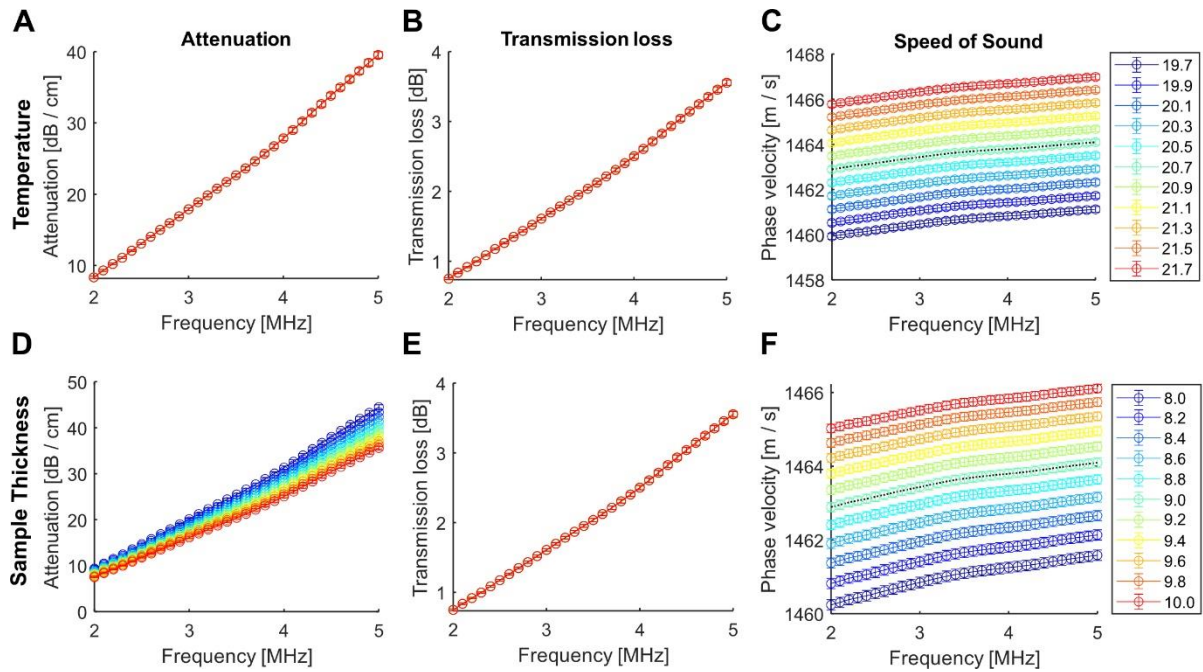


**Figure 3.10: Impact of variation in sample thickness and temperature on acoustic properties.**

The influence of changes in temperature ( $\pm 1^\circ\text{C}$ ) on acoustic attenuation (A), transmission loss (B) and speed of sound (C) and are displayed. Similarly, the influence of changes in sample thickness ( $\pm 1\text{ mm}$ ) on acoustic attenuation (D), transmission loss (E) and speed of sound (F) are displayed. Actual measurements (black dotted line):  $20.7^\circ\text{C}$  and  $9\text{ mm}$ . Data is displayed as mean  $\pm$  SD ( $n=3$  measurements). Error bars within data points.

### 3.2.4 Discussion

A through-transmission acoustic characterisation setup was constructed for the evaluation of the speed of sound and acoustic attenuation coefficient in solid material samples. The system showed excellent accuracy and precision for evaluation of the acoustic properties of water. For characterising solid samples, the system showed good agreement with literature values, but less precision compared to the water measurement. Whilst the standard deviation of three repeated measurements was found to be in an acceptable range when compared with other systems<sup>148,418,420,421</sup>, the precision (in particular for the speed of sound) may not be sufficient for optimization of tissue-mimicking phantom recipes, where the required ranges for speed of sound and acoustic attenuation are typically in the ranges  $1450\text{--}1575\text{ m}\cdot\text{s}^{-1}$  and  $0.5\text{--}30\text{ dB}\cdot\text{cm}^{-1}\cdot\text{MHz}^{-1}$ <sup>156</sup>, respectively. An acoustic characterisation system available at the National Physical Laboratory (NPL, London, UK) allows for acoustic measurements with an uncertainty of  $3.1\text{ m}\cdot\text{s}^{-1}$  and  $0.03\text{ dB}\cdot\text{cm}^{-1}\cdot\text{MHz}^{-1}$  for phase velocity and acoustic attenuation, respectively, across a frequency range  $1\text{--}60\text{ MHz}$ <sup>210</sup>. As access to the system was available during this PhD, all subsequent measurements in this thesis were performed using the NPL acoustic setup to improve accuracy for the phantom characterisation and enable NIST traceability.

For future studies, several measures could be introduced to increase the precision of the Cambridge acoustic system. The precision of sample through transmission measurements is highly affected by the

positioning of the sample between the transducers<sup>410</sup>. Small variations in sample angle will affect the time the pulse is travelling through the medium leading to significant discrepancies in the measurements. Future work should address this shortfall by developing a more advanced sample holder with several controllable degrees of freedom, i.e., linear translation in x, y and z direction, tilt, and rotation ability. The angle with normal incidence,  $\theta_i=0$ , can then be found by identifying the maximum signal amplitude, allowing for a more reliable and repeatable adjustment of the sample<sup>210</sup>. A more precise sample positioning will also enable the implementation of an improved version of data acquisition<sup>422</sup> which involves recording of two transmitted and two reflected pulses, one of each from the front surface and one of each from the back surface of the sample. The collection of all four pulses will allow for a more accurate determination of the acoustic attenuation (and sample thickness). For a more exact calculation of acoustic parameters, the impact of diffraction effects<sup>423</sup> should also be assessed in future work.

The impact of variations in temperature and sample thickness have also been evaluated. To minimise these sources of error, a high precision thermometer was used to measure temperatures and Vernier callipers with a high accuracy ( $\pm 0.03$  mm) and resolution ( $\pm 0.01$  mm) were used to measure sample thickness. The dual-purpose sample holder/mould further allows for precise adaption of the sample thickness.

For acoustic data acquisition, the following recommendations can be made: (1) homogenous composition and uniform thickness of the sample should be ensured (2); water bath temperature and sample thickness should be determined as accurately as possible before data acquisition (3); clean, deionized and degassed water should be used for filling the water tank as water impurities, content of dissolved air, and the isotopic composition of water have been shown to impact acoustic measurements<sup>417,424,425</sup>; (4) multiple ( $\geq 3$ ) measurements per sample at different positions should be performed.

### 3.3 Conclusion

In this chapter, the validation groundwork was undertaken to understand the available precision and accuracy for optical and acoustic characterisation of phantom material, thus supporting development of novel phantom materials in subsequent studies. A DIS system for characterisation of the reduced scattering and optical absorption coefficient was compared to reference measurements, displaying acceptable precision and accuracy values relative to the current state of the art. Equally, an acoustic characterisation system for the evaluation of the speed of sound and acoustic attenuation coefficient was set up and characterised. While an excellent congruency of water measurements with the literature values could be determined, the available frequency range and the precision for solid sample measurements with repositioning could be improved relative to the current state of the art devices used in metrology, hence, an external calibrated system available at NPL was used for acoustic characterisation studies in the remainder of this thesis.



# 4 DEVELOPMENT OF A COPOLYMER-IN-OIL TISSUE MIMICKING PHANTOM MATERIAL

*This chapter uses material from Hacker et al (2021) “A copolymer-in-oil tissue-mimicking material with tuneable acoustic and optical characteristics for photoacoustic imaging phantoms”, IEEE Transactions on Medical Imaging (see publications list). I wish to thank Dr. James Joseph, Dr. Srinath Rajagopal, Dr. Aoife M. Ivory and Prof. Dr. Bajram Zeqiri for their general guidance, and for reviewing and editing the manuscript. In particular, I would like to thank Dr. Srinath Rajagopal and Dr. Aoife Ivory for assisting me in acquiring and analysing data using the acoustic characterisation system available at NPL, London. Moreover, I would like to thank Dr. Mohand O. Saed for his assistance in performing the mechanical stability studies.*

## 4.1 Introduction

As outlined in Chapter 2, copolymer-in-oil materials hold high potential as a phantom material in PAI, being characterised by distinct benefits, such as tissue-mimicking acoustic and optical properties, long-term stability, cost-effectiveness, and biological inertness and safety<sup>221,376,426,427</sup>. However, recipes based on commercial polymer or gel wax<sup>164,339</sup> result in high batch-to-batch variation, impairing the reproducibility of the phantom fabrication. Moreover, copolymer-in-oil materials can be highly thermosensitive and the reported tunability of the acoustic properties is currently limited to  $1480 \text{ m}\cdot\text{s}^{-1}$ <sup>220</sup> for speed of sound, which is lower than the ultrasound soft tissue standard of  $1540 \text{ m}\cdot\text{s}^{-1}$ <sup>378</sup> (Table 4.1). While speed of sound can be increased by using oil with increased viscosity<sup>221</sup> or employing additives such as paraffin wax<sup>165</sup> or glycerol<sup>161</sup>, these can result in high acoustic attenuation<sup>165,221</sup> or backscattering<sup>161</sup>. LDPE has been employed as a tuning agent<sup>220,426</sup>, but a comprehensive comparison of different polyethylene types has not yet been performed.

To overcome these limitations, this chapter focusses on the optimization of a copolymer-in-oil formulation for use as a biologically relevant phantom material for PAI. The formulation has a facile manufacturing process, with all ingredients being low-cost, having defined Chemical Abstracts Service (CAS) numbers, and being readily available from standard scientific suppliers. This chapter focusses on the characterisation of the proposed material type. Firstly, it is shown that the material can provide independently tuneable, tissue-mimicking characteristics in the relevant optical excitation and acoustic detection ranges for biomedical PAI. Secondly, it is demonstrated that the material exhibits sufficient photo-, thermomechanical- and longitudinal- stability for short- and long-term precision studies. Finally, it is shown that the material is suitable to create phantoms of different architectures for mesoscopic and macroscopic PAI instruments. By fulfilling the aforementioned criteria for an ideal PAI phantom (Chapter 2, Figure 2.2) the developed material could facilitate PAI technical validation studies, and represents an excellent candidate for future routine quality control in preclinical and clinical PAI applications.

**Table 4.1: Overview of acoustic and optical properties found in soft tissues.**

Optical properties cover a spectrum from 600 to 900 nm.

Tissue type	Acoustic properties		Optical properties		Ref
	c (m·s <sup>-1</sup> )	$\alpha$ (dB·cm <sup>-1</sup> ) at f(MHz)	$\mu_a$ (cm <sup>-1</sup> )	$\mu_s'$ (cm <sup>-1</sup> )	
Soft tissue	1450–1575	0.5–30 at 1-10 MHz	0.1–0.5	10–20	156,211
Breast fat	1430–1480	1–18 at 1-10 MHz	0.05–0.4	3–8	156,211
Breast parenchyma	1460–1520	2–25 at 1-10 MHz	0.1–0.3	5–15	156
Blood	1560-1570	0.1-0.2 dB·cm <sup>-1</sup> ·MHz <sup>-1</sup>	2.0–10.0	10–15	183,352, 428
Liver	1510–1590	0.5-0.9 dB·cm <sup>-1</sup> ·MHz <sup>-1</sup>	1.15–1.56	22–30	183,378, 428
Prostate	1614	1.86 dB·cm <sup>-1</sup> ·MHz <sup>-1</sup>	0.05–0.72	1–40	183,352
Skin	~1600	2-4 dB·cm <sup>-1</sup> ·MHz <sup>-1</sup>	0.05–1.11	2–21	183,352, 378
Muscle	1540-1580	1.3 – 3.3 at 1 MHz	0.05-0.17	6-10	183,428
Tendon	1670	4.7 dB·cm <sup>-1</sup> ·MHz <sup>-1</sup>	*		352
Water	1480	0.0022 dB·cm <sup>-1</sup> ·MHz <sup>-1</sup>	0.006-0.07	0.003	235,352

\*No specific reference found.

## 4.2 Methods

### 4.2.1 Phantom fabrication

A summary of the phantom material compositions used for the acoustic study can be found in Table 4.2 and for the optical study in

Table 4.3. In order to reduce batch-to-batch variability, all specified components have defined CAS numbers and are readily available from large scientific suppliers. For the acoustic study the following thermoplastic elastomers were tested: high molecular weight (MW) SEBS (Sigma Aldrich 200557-250G), SEBS-graft maleic anhydride (Sigma Aldrich 432431-250G), low MW SEBS (Sigma Aldrich 200565-250G) and Polystyrene-block-polybutadiene-block-polystyrene (SBS, Sigma Aldrich 182877-250G). Moreover, the following polyolefins were tested in order to increase the mechanical stability of the base material: LDPE (Alfa Aesar 43949.30), Polystyrene (Sigma Aldrich 182427-500G), Polypropylene (Sigma Aldrich 427888-1KG), high MW Polyethylene (Sigma Aldrich 427772-250g), linear LDPE (Sigma Aldrich 428078-1KG), low MW Polyethylene (Sigma Aldrich 427795-250g) and high-density Polyethylene (HDPE, Sigma Aldrich 427985-1KG). Mineral oil (Sigma Aldrich-330779-1L) was used as a base with a viscosity of 14.20 – 17.00 mm<sup>2</sup>·s<sup>-1</sup> at 40°C, a speed of sound of 1440

$\text{m}\cdot\text{s}^{-1}$  and a density of  $0.838 \text{ g}\cdot\text{mL}^{-1}$  at  $25^\circ\text{C}$ . 5% butylated hydroxytoluene (HT, Sigma Aldrich W218405-1KG-K) was added as an antioxidant to all samples to increase the stability of material and prevent discolouration of SEBS at high temperatures<sup>429</sup>. After optimization, remaining studies combined a representative concentration of 30% high MW SEBS with 8% LDPE.  $\text{TiO}_2$  (Sigma Aldrich 232033-100g) was added to provide optical scattering and alcohol-soluble Nigrosin (Sigma Aldrich 211680-100G) to provide optical absorption. To increase the accuracy of the optical adjustment, a working stock solution of Nigrosin in mineral oil ( $2.5 \text{ mg/ml}$ ) was prepared. The fabrication can be summarized in six steps (Figure 4.1). All components are weighed and the optical scattering ( $\text{TiO}_2$ ) and absorbing agents (e.g., Nigrosin) are added to the mineral oil in a glass beaker. For homogenous distribution within the base phantom matrix, the mixture is sonicated at  $90^\circ\text{C}$  (sonication frequency: 44 kHz) until the scattering and absorbing agents are dissolved and no aggregates are visually detectable (60-90 mins). Polymers and stabilizer are added to the mineral oil solution in their respective ratios. The complete mixture is heated up to  $150^\circ\text{C}$  in an oil bath under low stirring conditions (150 rpm) until all components are dissolved and no aggregates are visually detectable. If the polymer appears to float over the oil, the mixture is manually stirred using a metallic spatula. The solution is vacuumed for removal of air bubbles in a vacuum chamber for 3-5 minutes and then carefully poured from low height into a suitable phantom mould. Alternatively, a vacuum oven (Gallenkamp D8B, Germany, 30 mins at  $120^\circ\text{C}$  (248F) and 30 inches/Hg pressure) can be used. Once set, samples may be stored at room temperature.

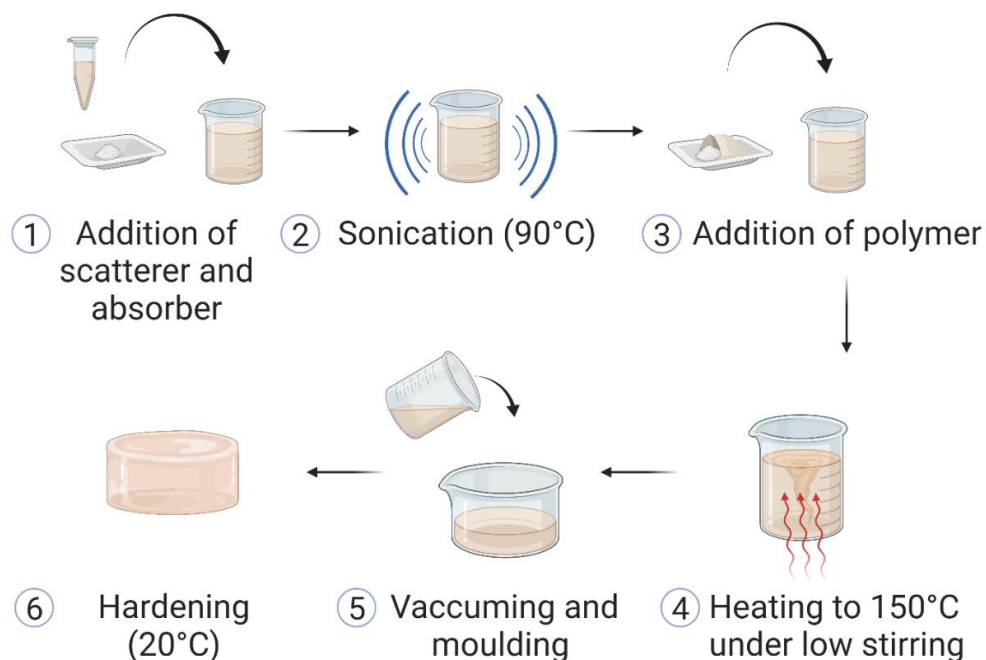


**Figure 4.1: Fabrication of the copolymer in oil-material.**

The six-step fabrication procedure of the copolymer-in-oil material is displayed. (1) Materials for optical scattering and absorption are added to mineral oil and (2) sonicated at  $90^\circ\text{C}$  until dissolved. (3) Polymer(s) and stabilizer are added, and (4) the mixture is heated up in an oil bath to  $150^\circ\text{C}$  under low stirring. (5) Upon dissolution of all components, the sample is poured in a suitable phantom mould and (6) left to harden at room temperature. Created with BioRender.

**Table 4.2: Summary of the phantom compositions for the acoustic analysis.**

Values are given in weight percentage of the base solution (mineral oil).

Polymer	CAS/Manufacturer	Set A					Set B			Set C				Set D			
High MW SEBS	66070-58-4 Sigma Aldrich 200557-250G	40					30	30	30	30	30	30	30	30	30	30	30
Butylated Hydroxytoluene	128-37-0 Sigma Aldrich W218405-1KG-K	10	10	10	10	10	5	5	5	5	5	5	5	5	5	5	5
Low-density Polyethylene	9002-88-4 Alfa Aesar 43949.30						8								4	8	12
Polystyrene	9003-53-6 Sigma Aldrich 182427-500G							8									
Polypropylene	9003-07-0 Sigma Aldrich 427888-1KG								8								
High MW Polyethylene	9002-88-4 Sigma Aldrich 427772-250g									8							
Low MW Polyethylene	9002-88-4 Sigma Aldrich 427795-250g										8						
Linear Low-density Polyethylene	9002-88-4 Sigma Aldrich 428078-1KG											8					
High-density Polyethylene	9002-88-4 Sigma Aldrich 427985-1Kg												8				
SEBS-graft maleic anhydride	124578-11-6 Sigma Aldrich 432431-250G			40													
Low MW SEBS	66070-58-4 Sigma Aldrich 200565-250G		40			30											
Polystyrene-block-polybutadiene-block-polystyrene	9003-55-8 Sigma Aldrich 182877-250G				40	10											

**Table 4.3: Summary of the phantom compositions for the optical analysis.**

Scattering and absorption characteristics were varied in a representative phantom sample composed of 30% high MW SEBS, 8% LDPE and 5 %HT. Values are given in w/v%.

Com-ponent	CAS/Manufacturer	Set E					Set F			
TiO <sub>2</sub>	1317-70-0 Sigma Aldrich 232033-100g	0	0.03	0.07	0.1	0.13	0.03	0.03	0.03	0.03
Nigrosin stock solution	11099-03-9 Sigma Aldrich 211680-100G	0.004	0.004	0.004	0.004	0.004	0.004	0.007	0.011	0.014

#### 4.2.2 Acoustic characterisation

The frequency-dependent speed of sound,  $c(f)$ , and acoustic attenuation,  $\alpha(f)$ , were evaluated using a broadband through-transmission substitution method employing the materials acoustic characterisation facility at the National Physical Laboratory (NPL), UK <sup>414</sup>. A 10 MHz centre frequency ultrasound transducer of active element diameter 10 mm (Force Technology, Brondby, Denmark) was placed within a water tank filled with de-ionised water and driven by an Olympus 5073PR pulser–receiver (Olympus NDT, Waltham, MA, USA). A broadband hydrophone (30 mm active element diameter

bilaminar membrane hydrophone, GEC Marconi) was used for detection. Waveforms were acquired using a DPO 7254 oscilloscope (Tektronix UK, Bracknell, UK).

Four acoustic pulses were acquired in each measurement set: a reference through-water pulse, with no sample present in the acoustic path; a through-sample transmission; together with acoustic reflections received at the transmitter from the front and rear surfaces of the sample.

To assess the inherent measurement system uncertainty, four measurements were taken per sample, in which pulse energy, damping and the transducer-sample distance (up to 5 mm) was varied, making the measurements independent of these variables. The sample average and standard error of the mean (SEM) of the four measurements per sample were then calculated. The system-specific Type B effects on the measurements are reviewed elsewhere<sup>210</sup>. Circular samples of a diameter of 7 cm and a thickness ranging between 6 and 9 mm were prepared for acoustic testing. The water tank temperature was recorded immediately before measurements on any test sample using a UKAS-calibrated IP 39C spirit-in-glass thermometer (G. H. Zeal, London, UK).

The transmission loss (TL) of a given sample (expressed in  $\text{dB}\cdot\text{cm}^{-1}$ ) at the frequency  $f$  was calculated using the expression<sup>210</sup>:

$$TL(f) = -\frac{20}{d} \log_{10} \left[ \frac{U_s(f)}{U_w(f)} \right] + \alpha_w(f) \quad 7$$

, where  $d$  is the sample thickness (in cm),  $U_w(f)$  and  $U_s(f)$  are the respective voltage magnitude spectra of the through-water and through-sample pulse, and  $\alpha_w(f)$  is the attenuation coefficient of ultrasound (in  $\text{dB}\cdot\text{cm}^{-1}$ ) of pure water at the specific water tank temperature<sup>430</sup>. To remove the influence of interfacial losses in calculating the frequency-dependent attenuation coefficient ( $\alpha_i(f)$ ) of the material, two thicknesses  $d_1$  and  $d_2$  ( $d_2 > d_1$ ) of a representative sample were taken and the acoustic attenuation was calculated using the two-sample substitution technique<sup>210</sup>:

$$\alpha_i(f) = -\frac{20}{d_2-d_1} \left( \log_{10} \left[ \frac{U_{s2}(f)}{U_{w2}(f)} \right] - \log_{10} \left[ \frac{U_{s1}(f)}{U_{w1}(f)} \right] \right) + \alpha_w(f) \quad 8$$

For the most promising material recipe, the attenuation accounting for the interfacial losses was assessed, finding that the impact of the interfacial losses is negligible. The speed of sound  $c(f)$  (in  $\text{m}\cdot\text{s}^{-1}$ ) was calculated using the expression<sup>210</sup>

$$c(f) = c_w \left[ 1 + 2 \cdot \frac{\theta_w(f) - \theta_s(f)}{\theta_2(f) - \theta_1(f)} \right] \quad 9$$

, where  $c_w$  depicts the temperature dependent speed of sound in water and,  $\theta_1(f)$ ,  $\theta_2(f)$ ,  $\theta_w(f)$  and  $\theta_s(f)$  the corresponding unwrapped phase spectra of the front-reflected, back-reflected, through-water and through-sample voltage pulses.

### 4.2.3 Optical characterisation

The previously validated DIS system was used to determine the optical absorption ( $\mu_a$ ) and reduced scattering coefficients ( $\mu'_s$ ) of the material samples. The system setup is detailed in Section 3.1.2.1. Rectangular samples with a width of 5.9 cm, a height of 1.8 cm and a thickness ranging between 2 and 3 mm were prepared for optical testing. Sample thicknesses were determined before each measurement using vernier callipers. Based on previous reports on a similar material type (gel wax), the scattering anisotropy factor ( $g$ ) was taken to be  $g=0.7$  and the refractive index  $n=1.4$ <sup>375</sup>. Three measurements at distinct positions on the sample were taken in a wavelength range of 450 to 900 nm.

### 4.2.4 Stability studies

Photo-, thermomechanical and longitudinal stability of the acoustic and optical properties were tested on representative phantoms composed of 30% high MW SEBS, 8% LDPE, 0.03 w/v% TiO<sub>2</sub> and 300  $\mu$ L Nigrosin stock solution. A consistent PAI readout from the phantom requires good photostability. Thermomechanical stability was assessed as materials based on thermoplastic elastomers exhibit temperature sensitive viscoelastic properties<sup>374</sup> and stability over the relevant working range (20-40 °C) is important. Finally, longitudinal stability of the phantom acoustic and optical properties was assessed regularly over a period of eleven months. It should be noted that while an assessment of the thermoelastic Grüneisen parameter was not conducted in this study, a detailed characterisation in a similar material was recently reported by Bakaric et al<sup>223</sup>.

#### 4.2.4.1 Photostability

To assess the photostability of the phantom material, a cylindrical phantom (length: 40 mm, diameter: 28 mm) was fabricated from the stated composition and placed within a commercial photoacoustic tomography instrument (MSOT inVision 256-TF; iThera Medical GmbH), described in detail elsewhere<sup>431</sup>. Excitation pulses were provided by a tuneable (660–1300 nm) optical parametric oscillator (OPO), pumped by a nanosecond (ns) pulsed Nd:YAG laser (10 Hz repetition rate up to 7 ns pulse duration). A custom optical fibre assembly creates a diffuse ring of uniform illumination over the imaging plane within the sample. The sample is coupled to the transducers using heavy water in a water bath. For ultrasound detection, 256 toroidally focused ultrasound transducers covering an angle of 270° are used (centre frequency of 5 MHz, 60% bandwidth) allowing tomographic reconstruction. To assess the photostability, a fixed position within the phantom was irradiated with 17,500 laser pulses over a time period of 30 minutes using wavelengths between 660 and 850 nm in 10 nm steps. Data analysis was performed using ViewMSOT software (v3.6.0.119; iThera Medical GmbH). Model-based image reconstruction was applied and the mean photoacoustic signal within a region of interest (ROI) drawn around the circular cross Section of the phantom was quantified.

#### 4.2.4.2 Thermal stability

The degradation characteristics of the material were determined by thermal gravimetric analysis (TGA). TGA was performed using a Thermal Analysis TG Q500 instrument (TA instruments, New Castle, DE, USA). Sample measurements (sample weight approximately 4 mg) were conducted in the temperature range from 25 to 300 °C at a heating rate of 5 °C min<sup>-1</sup>. The temperature at 5 % of mass loss was determined using universal analysis software (TA instruments, USA).

#### 4.2.4.3 Thermo-mechanical stability

The viscoelastic properties of the material were analysed by conducting a dynamic mechanical analysis (DMA) using DMAQ850 instrument (TA instruments, New Castle, DE, USA). Length, width, and thickness of the sample were measured using vernier callipers (approximate size: 30 (length) x 10 (width) x 5 (thickness) mm<sup>3</sup>). Samples were tested in tensile mode, with the active length measuring approximately 15 mm. A strain of 0.01 (1%) was applied to the sample at a frequency of 1 Hz while the temperature was increased from -100 to +100 °C at a rate of 3 °C·min<sup>-1</sup>. The glass transition temperature ( $T_g$ ) was measured at the peak of tan delta and the plastic flow temperature ( $T_f$ ) was marked by the drop of the storage modulus to zero. The loss modulus, storage modulus and tan( $\delta$ ) were recorded using the TA instruments TRIOS software (v 5.0.0). The loss modulus ( $E''$ ) refers to the energy loss due to the viscous response of the material, whereas the storage modulus ( $E'$ ) refers to the energy storage caused by the elastic response of the material. The vectoral addition of these two moduli is the complex modulus ( $E^*$ )<sup>432,433</sup>

$$E^* = \sqrt{E''^2 + E'^2} \quad \mathbf{10}$$

which can be regarded as the Young's modulus ( $E$ ) in Hookean materials such as biological soft tissues<sup>434,435</sup>.

#### 4.2.5 Photoacoustic imaging

Photoacoustic imaging was performed using the tomography system described above and a commercial photoacoustic mesoscopy system (RSOM Explorer P50; both iThera Medical GmbH, München, Germany), described in detail elsewhere<sup>145</sup>. Laser light is generated by a 532 nm laser (pulses: 1 ns;  $\leq 1$  mJ/pulse) and delivered through a customized 2-arm fibre bundle (spot size: 3.5x5 mm). Photoacoustic signals are detected by a spherically focused LiNbO<sub>3</sub> detector (centre frequency: 50 MHz; bandwidth: 10 – 90 MHz; focal diameter: 3 mm; focal distance: 3 mm; f-number: 1). The recorded data is amplified by a low noise amplifier of 63 dB gain. The scanning head is attached to two motorised stages and coupled to the sample surface by an interchangeable water-filled (2 mL) interface.

The base material of the phantoms was composed of 30% high MW SEBS, 8% LDPE, 0.03 w/v% TiO<sub>2</sub> and 0.0007 w/v% Nigrosin. For the mesoscopic system, stainless steel was used to create a heat-resistant rectangular phantom mould of the following dimensions: length: 50 mm, width: 50 mm, height: 7 mm.

For imaging targets, three red fibres (diameter: 126  $\mu\text{m}$ , smilco) were positioned at different depths (0.5, 1.5 and 2.5 mm). These demonstrate the use of our base material combined with user-selected targets of a different material. Although the fibres were not purchased from a large scientific supplier, after testing of different types of targets (e.g., wires, sutures, and threads), they presented the best compromise for an appropriate size target without introducing artefacts. For the tomographic system, a heat-resistant cylindrical glass phantom mould (diameter: 28 mm) was fabricated out of an open-top 50 ml glass syringe (Sigma-Aldrich, CADG5157). Two equally distanced stainless-steel rods (diameter: 4 mm; rod-rod distance: 10 mm) on a Polytetrafluoroethylene (PTFE) base were inserted into the glass mould. The moulds were filled with the copolymer-in oil material until the phantoms reached a length of 50 mm. After hardening, the phantoms were removed from the mould and the inclusions were filled, demonstrating a phantom where both the background matrix and target inclusions are formed of the same copolymer-in-oil base. For the inclusion material, a green oil-soluble dye was chosen (0.04 w/v%, GRC 43104, Caligo safe wash relief inks, Cranfield Colours, Cwmbran, UK) due to its absorbing properties in the first near infra-red window<sup>164</sup> and suspended in the base material.

For the RSOM image acquisition, the phantom was placed underneath the water-filled interface covering the scan head. For coupling of the phantom to the interface, degassed commercial ultrasound gel (Aquasonic Clear, Parker Labs) was used. Images were acquired over a field of view of  $12 \times 12$  mm (step size: 20  $\mu\text{m}$ ) at 85% laser energy. For the MSOT image acquisition, the same sample preparations were used as in our standard operating procedure for *in vivo* imaging<sup>145</sup> to make our *in vivo* and *in vitro* imaging approach as comparable as possible. This involved wrapping the phantom in a thin polyethylene membrane using degassed commercial ultrasound gel as a coupling medium and inserting it into the supplied holder (iThera Medical). The holder was then immersed in degassed heavy water maintained at 34°C within the MSOT system. After a stabilisation period of 15 minutes, images were acquired through the centre of the phantom using the following wavelengths: 660 nm, 700 nm, 730 nm, 760 nm, 800 nm, 850 nm, 900 nm, 950 nm, 1040 nm (with an average of 10 pulses per wavelength).

#### 4.2.6 Image and Statistical analysis

Tomographic imaging data were reconstructed using a model-based algorithm and analysis was performed using ViewMSOT software (v3.6.0.119; iThera Medical GmbH). Mesoscopic imaging data were reconstructed using a beam-forming algorithm provided by the vendor (iThera Medical GmbH), which models the sensitivity field of the focused detector and generates 3-dimensional images. The subsequent images were analysed using MATLAB.

All measurements in the acoustic and optical characterisations were performed at least three times per sample. Statistical analysis was performed using Prism (GraphPad) and MATLAB. All data are shown as mean  $\pm$  SEM unless otherwise stated. The COV was calculated as the ratio of SD to the mean, expressed as a percentage.



## 4.3 Results

### 4.3.1 Systematic optimisation of copolymer-in-oil materials results in high speed of sound.

First, the copolymer-in-oil material composition was refined to bring the speed of sound closer to the ultrasound soft tissue average, while keeping the acoustic attenuation close to tissue relevant values. To achieve this, the acoustic performance of different base polymers of the material were compared, which are thermoplastic styrenic elastomers. Phantoms were produced employing 40% low and high molecular weight (MW) SEBS, SEBS-graft-maleic anhydride and SBS, the dehydrogenated version of SEBS. A high percentage of polymer was chosen for these studies, since increasing the SEBS concentration has been shown to increase the speed of sound<sup>221</sup>. The sample containing high MW SEBS was characterised by the highest speed of sound ( $1471.9 \pm 0.3 \text{ m}\cdot\text{s}^{-1}$  at 5 MHz, Figure 4.1A) whilst having similar attenuation values (Figure 4.1B) compared to the remaining polymers tested. Higher molecular weight usually leads to enhanced thermal and mechanical properties (e.g., increase in strength, toughness and chemical stress crack resistance), but also to higher stiffness due to higher chain entanglement and decreased molecular mobility<sup>436</sup>. Notably, the sample containing SBS had the lowest attenuation value ( $4.11 \pm 0.11 \text{ dB}\cdot\text{cm}^{-1}$  at 5 MHz, Figure 4.1B), but as SBS is more susceptible to degradation at high temperatures and more prone to oxidation in the absence of antioxidants<sup>374</sup>, the focus was laid on high MW SEBS as the base polymer. It is known that SEBS samples with low polymer concentrations are susceptible to plastic deformation<sup>437</sup>. Therefore, it was aimed to strengthen the mechanical stability of the material by addition of a second polymer, which could also further improve the acoustic properties. The acoustic performance of samples containing (low density) polyethylene (LDPE), polystyrene and polypropylene as additive second polymers was compared.

Polypropylene gave the highest speed of sound within the tuning range ( $1486 \pm 0.10 \text{ m}\cdot\text{s}^{-1}$  at 5 MHz, Figure 4.1C), but also the highest acoustic attenuation ( $9.27 \pm 0.15 \text{ dB}\cdot\text{cm}^{-1}$  at 5 MHz, Figure 4.1D). By comparison, the sample containing LDPE was considerably less attenuating ( $6.27 \pm 0.12 \text{ dB}\cdot\text{cm}^{-1}$  at 5 MHz, Figure 4.1D) with a similar speed of sound ( $1482 \pm 0.2 \text{ m}\cdot\text{s}^{-1}$  at 5 MHz, Figure 4.1C), which makes it preferable as a second polymer additive for acoustic studies. In order to identify the most suitable type of polyethylene, the speed of sound (Figure 4.1E) and acoustic attenuation (Figure 4.1F) of different polyethylene subtypes were compared, including: high density polyethylene (HDPE), linear LDPE (LLDPE), low MW PE and high MW PE (all at 8%).

Here again, LDPE gave the most favourable characteristics. With LDPE identified as a suitable strengthening agent, the speed of sound in material samples with a set concentration of 30% SEBS was tuned by variation of LDPE content. In this way, the speed of sound could be increased up to a value of  $1516 \pm 0.65 \text{ m}\cdot\text{s}^{-1}$  (Figure 4.1G) at the expense of increasing acoustic attenuation to  $17.3 \pm 0.26 \text{ dB}\cdot\text{cm}^{-1}$  at 5 MHz (Figure 4.1H.)

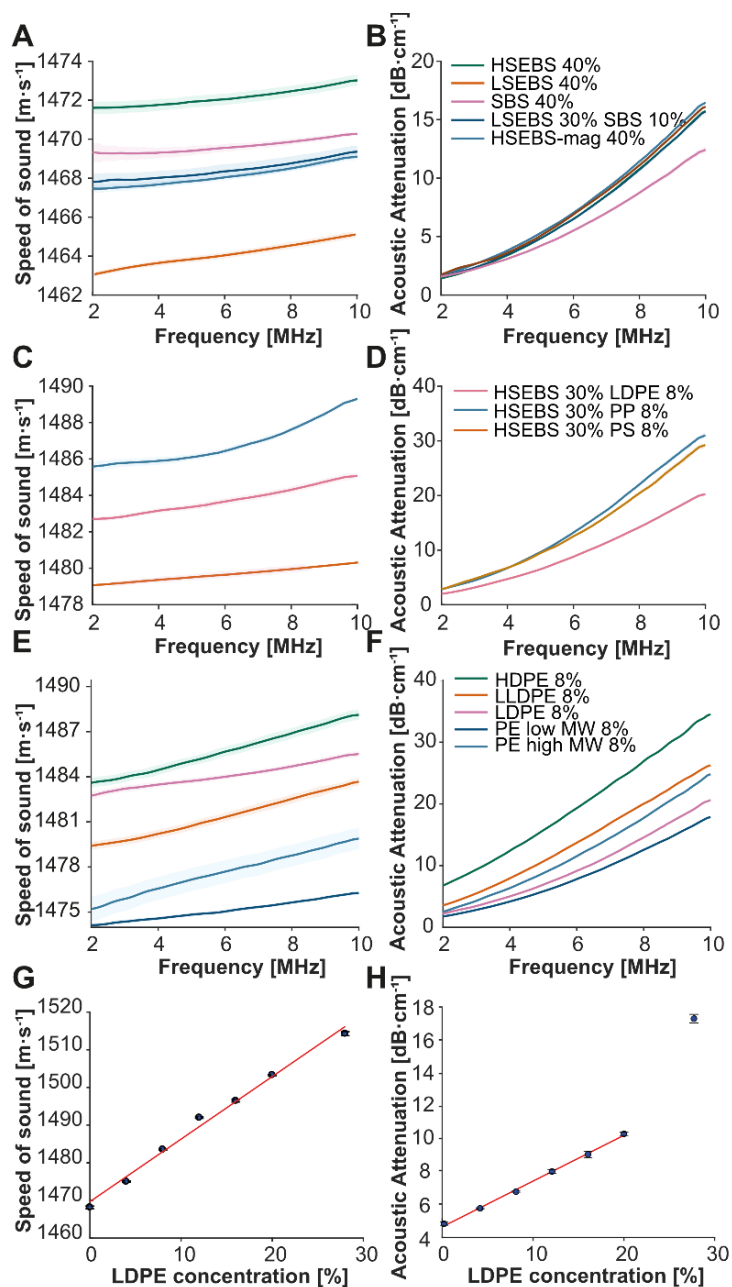


**Figure 4.1: Comparison of speed of sound and acoustic attenuation coefficient of samples composed of different polymer types.**

The speed of sound (A) and acoustic attenuation coefficient (B) for samples composed of mineral oil containing 40% high and low MW SEBS (HSEBS=green, LSEBS=yellow), SBS (pink), SEBS-graft-maleic anhydride (HSEBS-mag=light blue) and one sample composed of 30% low MW SEBS and 10% SBS (dark blue) in a frequency range of 2 to 10 MHz. After selecting high MW SEBS for further study, the speed of sound (C) and acoustic attenuation coefficient (D) were then evaluated for samples composed of mineral oil containing 30% high MW SEBS, and a second polymer at 8%, which was either (low density) polyethylene (LDPE=pink), polystyrene (PS=yellow), or polypropylene (PP=blue). After identifying LDPE (pink) as a suitable candidate, the speed of sound (E) and acoustic attenuation (F) of different types of polyethylene (PE) were compared, including: high density polyethylene (HDPE, green), linear LDPE (LLDPE, yellow), low MW PE (dark blue) and high MW PE (light blue; all at 8%). Finally, the speed of sound (G;  $R^2=0.9862$ ;  $f(x)=1.662 \cdot x + 1470$ ;  $SSE=21.6214$ ) and acoustic attenuation coefficient (H;  $R^2=0.9980$ ;  $f(x)=0.276 \cdot x + 4.65$ ;  $SSE=0.0450$ ) at 5 MHz were evaluated for samples composed of mineral oil containing 30% high MW SEBS and increasing LDPE concentration. For all panels, data is shown as mean  $\pm$  SEM for  $n=4$  measurements per sample (error bars given as shaded area in A-F or explicit error bars in G, H; if not visible, errors are contained within the line or point). Values are given in weight percentage of the base solution (mineral oil).

For LDPE concentrations under 20%, the acoustic attenuation appeared to increase linearly (Figure 4.1H), with a more substantial increase in attenuation noted at 30%. Overall, the results suggest that the material would be suitable for mimicking the speed of sound of tissues such as breast fat and parenchyma ( $1450\text{-}1490\text{ m}\cdot\text{s}^{-1}$ ), but still does not provide sufficient speed of sound such for tissues such as skin, muscle, kidney or prostate ( $>1520\text{ m}\cdot\text{s}^{-1}$ ; Table 4.1). For mimicking fatty tissues, LDPE concentrations under 8% are preferable, as the acoustic attenuation becomes too large otherwise.

#### 4.3.2 Negligible optical absorption and scattering of the copolymer-in-oil material facilitates tuning of optical properties through additives.

Next, the optical properties of the fabricated material were examined. The optical absorption and scattering properties of the material only appeared to increase slightly with LDPE concentration, however, even with one of the highest LDPE concentrations tested (20%) the samples showed negligible absorption at 800 nm and did not exceed a reduced scattering value of  $0.24\text{ mm}^{-1}$ , which is still below the threshold of most soft tissues<sup>438</sup>. As a result, it was possible to tune the optical properties of the material through further additives. Using material incorporating 30% SEBS and 8% LDPE, a tissue-mimicking range of optical properties<sup>183</sup> were obtained through addition of  $\text{TiO}_2$  (Figure 4.2A) or Nigrosin (Figure 4.2B) for reduced scattering and absorption, respectively. The selected concentrations of  $\text{TiO}_2$  and Nigrosin aimed to achieve  $\mu_a$  and  $\mu_s'$  values in the lower range of soft tissues, such as breast fat ( $\mu_s'=0.3\text{-}0.8\text{ mm}^{-1}$ ;  $\mu_a=0.005\text{-}0.03\text{ mm}^{-1}$ )<sup>183</sup>, but higher values can be easily achieved by increasing the concentration of  $\text{TiO}_2$  and/or absorbing dye. The addition of  $\text{TiO}_2$  resulted in a linear increase in scattering (Figure 4.2C), whilst addition of Nigrosin led to a linear increase in absorption (Figure 4.2D). The optical adjustment did not significantly affect the speed of sound ( $p=0.2204$ ) or the acoustic attenuation ( $p=0.3159$ ) of the sample. These results suggest that the optical characteristics of the proposed material can be independently tuned and adapted to any soft tissue type of interest.

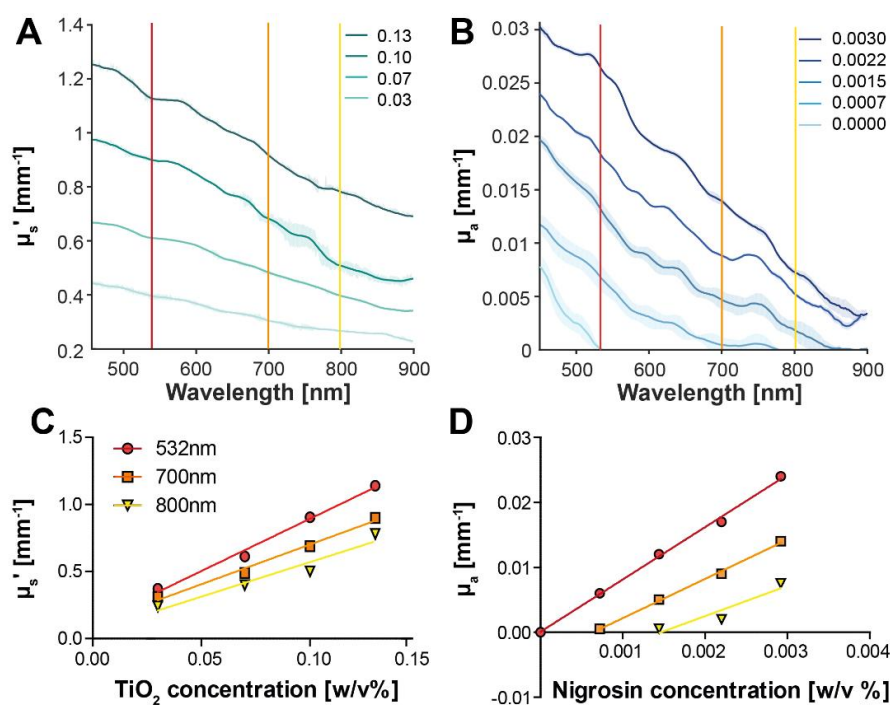


**Figure 4.2: Independent tuning of the reduced scattering and optical absorption coefficients by variation of titanium dioxide and Nigrosin concentrations.**

The (A) reduced scattering coefficient ( $\mu_s'$ ) and (B) optical absorption coefficient ( $\mu_a$ ) of a material sample composed of 30 % high MW SEBS and 8 % LDPE were measured at a wavelength range of 450 to 900 nm at varying concentrations of TiO<sub>2</sub> and Nigrosin using the DIS system. The variation of  $\mu_s'$  (C) and  $\mu_a$  (D) with TiO<sub>2</sub> and Nigrosin content is plotted for common PAI wavelengths (indicated with vertical lines in A and B) of 532 nm (red), 700 nm (orange) and 800 nm (yellow). For all panels, data is shown as mean  $\pm$  SEM for n=3 measurements per sample (error bars given as shaded area in A, B; within symbols in C, D).

### 4.3.3 The copolymer-in-oil material demonstrates good photo and thermomechanical stability.

With the use of pulsed lasers in PAI, it is important to test whether a material can withstand photobleaching during laser illumination. Firstly, the photostability of the phantom material was evaluated by exposing it to 17,500 laser pulses in the wavelength range of 700 to 850 nm in a time frame of 30 minutes (Figure 4.3A). No significant change (slope:  $0.000016 \pm 0.000017$ ,  $p=0.4147$ ) was observed in the normalized photoacoustic amplitude, indicating that our material is photostable for at least that exposure period.

Since many PAI systems can be expected to operate over a wide range of temperatures and copolymer-in-oil materials have previously shown a tendency to deform at elevated temperatures, the thermomechanical stability of the material assessed, which incorporates a second polymer for increased mechanical stability. For thermostability studies, a thermogravimetric analysis was conducted for one representative formulation containing 8% LDPE and found less than 5% weight loss up to 152°C, suggesting that no major irreversible degradation occurs up to this temperature (Figure 4.3B). For assessment of the viscoelastic properties, a dynamic mechanical analysis (Figure 4.3C) was conducted. The material was found to be stable from -63°C (= glass temperature  $T_g$ ) to 60°C, which covers well

the relevant working range of 20 to 40°C. The storage modulus for this representative formulation varied in this range between 0.44 (at 20°C) and 0.39 MPa (at 40°C), which resembles elastic values of stiffer soft tissue types (e.g., meniscus (0.3-0.8 MPa) <sup>439</sup>.

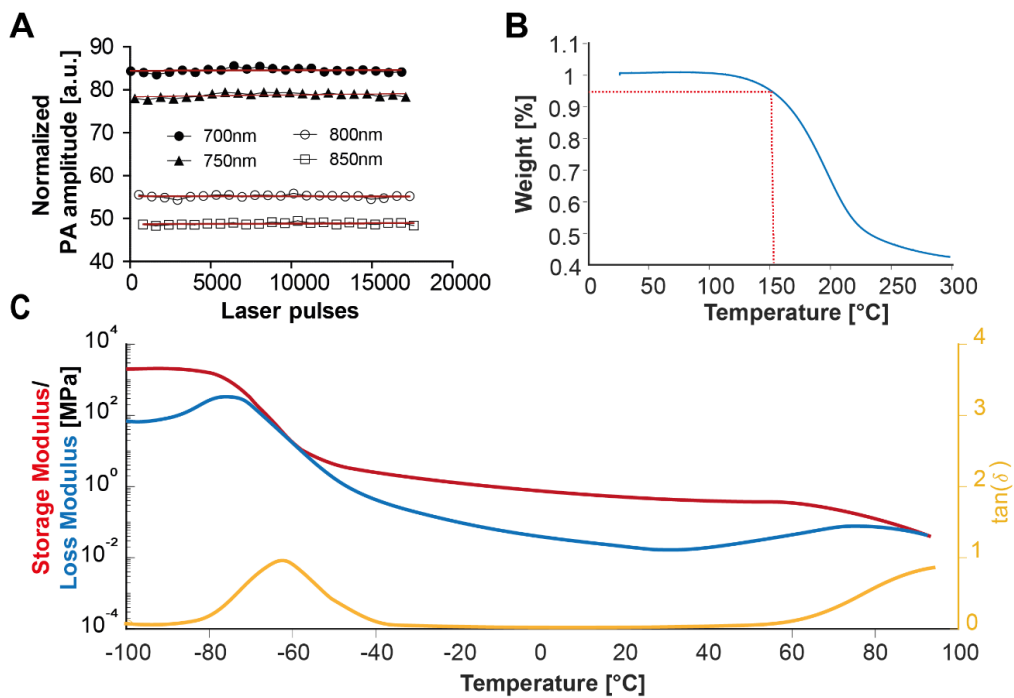


**Figure 4.3: Photo and thermomechanical stability of the phantom material.**

(A) When exposed to up to 17,500 laser pulses in the range of 700 nm to 850 nm (10 nm steps) within a PAI system, no significant change in the normalised photoacoustic signal amplitudes could be detected, representatively shown here for 700 nm (black circle), 750 nm (black triangle), 800 nm (white circle) and 850 nm (white square). Using a sample composed of mineral oil containing 30% high MW SEBS and 8% LDPE, a thermogravimetric (B) and dynamic mechanical analysis (C) were performed. The thermogravimetric test revealed 95 % weight preservation up to a temperature of 152 °C, denoted by the dashed line. The sample was found to be stable in a range of -60 to 60 °C by dynamic mechanical analysis. The storage modulus  $E'$  is depicted in red, the loss modulus  $E''$  in blue and the damping factor  $\tan(\delta)$  ( $E''/E'$ ) in yellow.

#### 4.3.4 Defined acoustic and optical properties in the material are repeatable and temporally stable.

Copolymer-in-oil materials based on thermoplastic elastomers are thermo-reversible, allowing the material to be recast. Recasting affords the opportunity to prepare large batches of material that can later be formed into specific phantom objects with different geometries. Thus, it was evaluated whether recasting affects the intrinsic properties of the material and these studies found the impact to be minimal: for the acoustic properties, mean COVs of  $0.010 \pm 0.005$  % (over  $n=3$ ) for the speed of sound and  $3.1 \pm 1.8$  % for the acoustic attenuation could be measured in a frequency range of 2 to 10 MHz. For the optical properties, mean COVs of  $7.5 \pm 0.2$  % for the measured transmission spectra and  $2.1 \pm 0.1$  % for the reflectance spectra could be determined in a wavelength range of 450 to 900 nm.

Having the main constituents of the phantom material established, the intra-centre repeatability of our recipe was tested by comparing the acoustic and optical properties of three independently fabricated samples made by the same operator at the same site (Department of Physics, University of Cambridge). The acoustic repeatability was found to be excellent with a mean COV of  $0.03 \pm 0.002$  % for the speed of sound and  $3.1 \pm 1.3$  % for the acoustic attenuation in a frequency range of 2 to 10 MHz. For the optical properties, repeatability was also found to be in an acceptable range, with COVs of  $2.6 \pm 0.005$  % for the measured transmission spectra and  $2.7 \pm 0.001$  % for the reflectance spectra in a wavelength range of 450 to 900 nm.

Finally, the long-term stability of the acoustic and optical properties of our phantom material was assessed. Acoustic and optical measurements were undertaken regularly over a time frame of eleven months. Linear fits gave slopes of  $0.0014 \pm 0.0043$   $\text{m}\cdot\text{s}^{-1}$  for the speed of sound (Figure 4.4A),  $0.00030 \pm 0.00019$   $\text{dB}\cdot\text{cm}^{-1}$  for the acoustic attenuation (Figure 4.4B),  $0.00044 \pm 0.00038$   $\text{mm}^{-1}$  for the reduced scattering coefficient (Figure 4.4C) and  $0.0010 \pm 0.0013$   $\text{mm}^{-1}$  for the optical absorption coefficient (Figure 4.4D). The slopes were not significantly non-zero ( $c(f)$ :  $p=0.77$ ;  $\alpha(f)$ :  $p=0.21$ ;  $\mu_s'$ :  $p=0.27$ ,  $\mu_a$ :  $p=0.45$ ), suggesting stability of the acoustic and optical properties over the investigated time frame. These findings taken together indicate a high repeatability of the material properties after recasting, with replicate fabrications and over time, supporting the potential of the material for use as a PAI phantom.

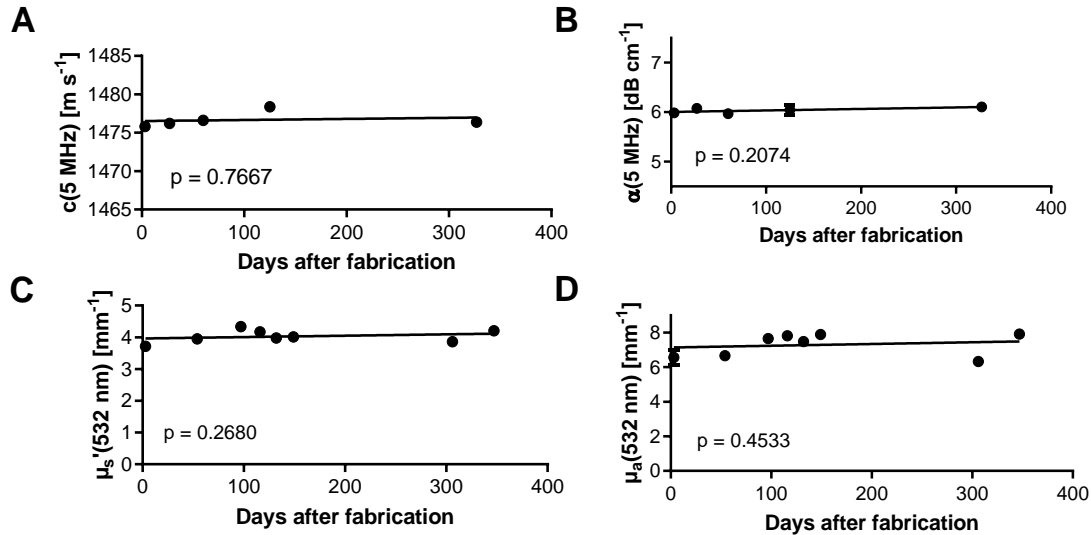


**Figure 4.4: Stability of acoustic and optical properties over time.**

The speed of sound (A), acoustic attenuation (B), optical scattering coefficient ( $\mu_s$ ) (C) and optical absorption coefficient ( $\mu_a$ ) (D) of a material sample composed of 30% high MW SEBS, 8% LDPE, 0.03 w/v%  $\text{TiO}_2$  and 0.0007 w/v% Nigrosin stock solution are shown over a time frame of eleven months. For all panels, data is shown as the mean  $\pm$  SEM of  $n=4$  measurements per sample (error bars within symbols in all cases).

#### 4.3.5 Phantom design and field testing

For field-testing of the material, system-specific phantom designs for two distinct PAI systems were created. For the mesoscopic PAI system, a rectangular phantom was designed with three linearly spaced fibres embedded at specific depths (0.5, 1.5 and 2.5 mm) (Figure 4.5A, B) to test the homogeneity of the material in a high resolution PAI system and to evaluate how well targets of other materials could be embedded within the phantom material. The measured size of the fibre using PAI was found to correspond to the actual diameter of the fibre (average width of the signal peak 128  $\mu\text{m}$  vs. 126  $\mu\text{m}$ ; Figure 4.5C, D). For the tomographic PAI system, a cylindrical phantom was created with two inclusions (diameter 4 mm) containing a green oil-soluble dye dissolved in the same base material (Figure 4.5E, F). The measured diameters extracted from the photoacoustic image were found to correspond with the designed dimensions of the phantom (outer part: 28 mm vs  $27.7 \pm 0.05$  mm; inclusions: 4 mm vs  $3.8 \pm 0.07$  mm and  $3.8 \pm 0.06$  mm respectively, Figure 4.5G,H). Furthermore, the phantom was cut cross-sectionally at 6 months after formation and no diffusion of the dye from the inclusion to the background was observed. In both photoacoustic systems, the material appeared homogeneous and no distortions of the target dimensions were observed, supporting the suitability of the material for use in PAI.

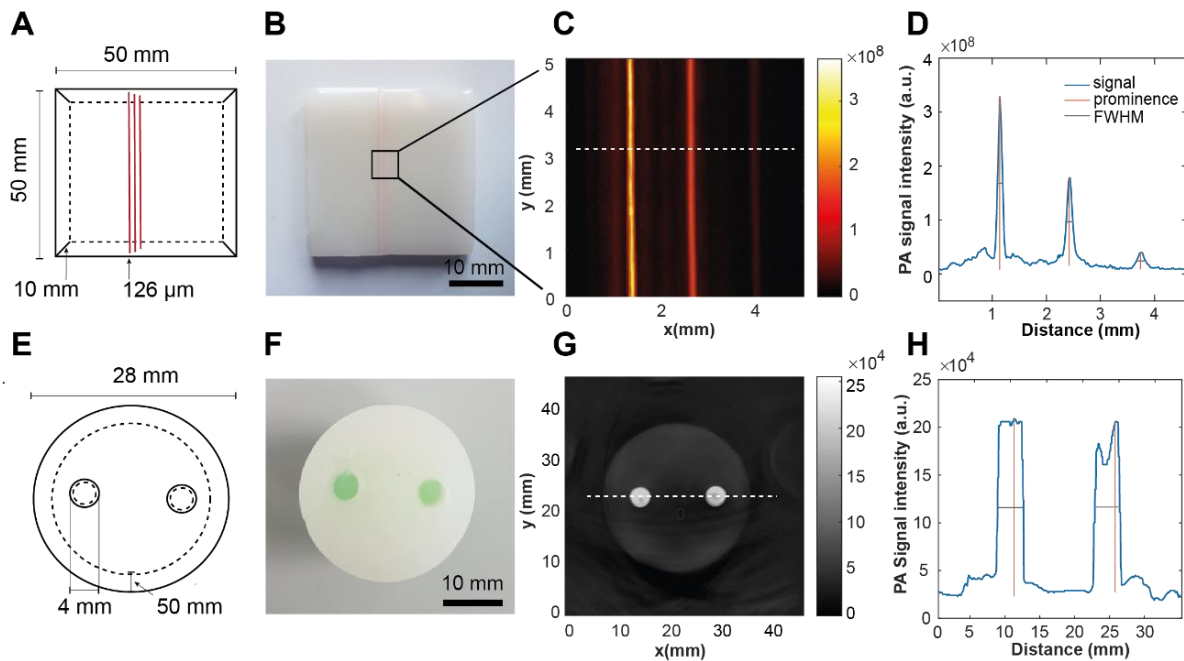


**Figure 4.5: Copolymer-in oil material allows the creation of versatile phantom designs for different system configurations.**

The design (A) and photograph (B) of a rectangular phantom for the mesoscopic system is shown. Three red fibres at different depths (0.5, 1.5 and 2.5 mm) act as imaging targets. (C) The photoacoustic x-y maximum intensity projection at 532 nm of the zoomed-in black square in (B) is displayed. (D) The intensity line profile of the white dotted line is shown (signal=blue, prominence=orange, width of signal peak at half maximum=grey). Correspondingly, the design (E), photograph (F) and photoacoustic image at 800 nm (G) of a cylindrical phantom for the tomographic system is shown. A green oil-soluble dye (GRC 43104; Caligo safe wash relief inks, Cranfield Colours, Cwmbran, UK) has been used as an absorber for the inclusions. (H) The intensity line profile of the white dotted line is shown (signal=blue, prominence=orange, width of signal peak at half maximum=grey).

## 4.4 Discussion

For accurate and precise performance evaluation of PAI systems, a stable copolymer-in-oil phantom material with biologically relevant properties was developed, optimised, and extensively characterised, thereby addressing Aim 1 of this thesis.

Initially, the tunability of acoustic properties was enhanced in the tissue-mimicking range. By optimising the polymer composition and ratio, the speed of sound of the material was tuned to over  $1500 \text{ m}\cdot\text{s}^{-1}$ , which is higher than described before in similarly composed materials<sup>159,164,165,221,339,440</sup>. This allows the adaptation of the acoustic phantom properties to match those of tissues relevant for photoacoustic clinical applications, including breast tissue<sup>441</sup> and fat<sup>378</sup> ( $c=1450 - 1480 \text{ m}\cdot\text{s}^{-1}$ ; for LDPE concentrations 8%). Notably, LDPE concentrations over 20% should be avoided to avoid substantial elevation of acoustic attenuation. In particular, lower LDPE concentrations may be preferred for high frequency PAI systems and these can be easily fabricated by decreasing the polymer concentration, as shown for similar SEBS-based material recipes<sup>221,442</sup>. Higher speed of sound values required for mimicking tissues, such as muscle or kidney ( $>1520 \text{ m}\cdot\text{s}^{-1}$ ; Table 4.1), could be achieved by choosing a plasticizer with higher viscosity<sup>221</sup> or by adding compounds such as glycerol<sup>160</sup>, but these would lead respectively to higher acoustic attenuation<sup>221</sup> or acoustic backscattering<sup>160</sup>, and reduced ease of the phantom fabrication. For independent tuning of acoustic backscattering properties, glass microspheres could be tested in future<sup>165</sup>.

After establishing an optimal acoustic composition for the material, optical absorption and reduced scattering coefficients were independently tuned by the addition of oil-based inks and  $\text{TiO}_2$ . Here, Nigrosin was used as a representative absorber, but other photostable oil-soluble inks mimicking the absorption spectra of endogenous chromophores can be incorporated instead, as shown by Maneas et al<sup>164</sup>. The high adaptability of both acoustic and optical properties supports the production of phantoms tailored to specific tissue types and applications of interest.

Further important criteria for a PAI phantom are photo- and thermomechanical- stability of the intrinsic properties to enable reliable short- and long-term performance assessment of PAI systems. The material was found to be photostable under the tested conditions and mechanically stable in the relevant working range of 20 to  $40^\circ\text{C}$ . It is known that the mechanical properties of copolymer-in-oil materials can be tuned in the tissue-mimicking range by adjusting the polymer concentration<sup>160,221</sup>. The choice of plasticizer (e.g., viscosity, paraffinic content or molecular weight) also has been shown to affect the mechanical properties<sup>443,444</sup>. While the adaptability to tissue-relevant mechanical properties has been shown for tissues with lower stiffness (2-150 kPa)<sup>221</sup>, the material formulation tested here (with 8% LDPE) was found to be similar to tissues with higher stiffness, such as meniscus or soft tendons (0.3-0.8 MPa)<sup>439</sup> due to the higher polymer concentration used.

The concomitant change of the acoustic and mechanical properties with adjustment of the polymer concentration needs to be considered by the user when choosing an appropriate formulation to use for their application. However, the adaptability of copolymer-in-oil materials to a wide range of tissue-relevant elasticities, as well as their large linear viscoelastic domain <sup>221</sup>, make this class of material a promising candidate also for mechanically-relevant fields, such as ultrasound elastography <sup>221,377,445</sup>.

Further, it was demonstrated that the material can be used to create versatile phantom designs for PAI systems of different configurations. The material showed high homogeneity during photoacoustic image acquisition and both endogenous inclusions made out of the same material type (as shown with the tomographic phantom) as well as exogenous targets (as shown with the mesoscopic phantom) can be embedded into the base matrix. Increasing polymer concentration also increases the viscosity of the melt and the stiffness of the solidified material. This should be considered when fabricating phantoms containing small and delicate structures or inclusions, as for this purpose, a lower viscosity substance is preferable. Concomitantly, it was observed that with increased viscosity the melt becomes less prone to air-bubble trapping, a problem observed in prior studies with lower viscosity copolymer-in-oil materials <sup>165</sup>.

High reproducibility of the phantom fabrication procedure and ready availability of ingredients and equipment are further key requirements to enable widespread and comparable phantom manufacture in different laboratories. To optimise these parameters, only non-toxic ingredients available from large scientific suppliers were used and the fabrication procedure was simplified as far as possible while maintaining high manufacturing precision. A high intra-centre repeatability of the phantom fabrication procedure by the same operator was confirmed. Additionally, it was shown that the material can be reused and remoulded without significantly affecting the acoustic and/or optical properties, which constitutes a further considerable advantage of the fabrication process. Importantly, no statistically significant drift was observed over a time frame of almost a year, thereby confirming expectations based on prior observations of longitudinal studies on the stability of oil-based materials <sup>221,375,426,427</sup>. Controllable mechanical robustness in the tissue-mimicking range and high intrinsic stability permit long-term usage of the material in a wide variety of phantom applications, which also has potential for application in biophotonic and ultrasound imaging.

While the reported material appears to be an excellent candidate for a PAI phantom to enable technical validation studies, there remain some limitations of the study. Firstly, the impact of including additives to tune acoustic backscattering could not be evaluated due to limitations in our testing equipment. Secondly, fabrication and imaging studies were performed in only a single centre; future studies should also establish the inter-centre reproducibility to exclude the impact of variables such as equipment or operator. Moreover, acoustic characterisation was focused in the clinically relevant range of 1-10 MHz. Future studies should also analyse the acoustic properties in a higher frequency range relevant for photoacoustic mesoscopy and microscopy. Finally, only relatively basic performance assessment

phantoms for PAI systems were generated. Increased anatomical realism may be achieved in future using 3D-printed moulds, potentially even with patient-derived vascular networks, as shown in similar studies<sup>165,446-448</sup>. Preliminary tests performed by other laboratories indicate that the material is also 3D-printable, offering an even wider range of flexibility in terms of processing and fabrication.

## 4.5 Conclusion

In this chapter, a copolymer-in-oil material was optimised and its potential for use as a PAI phantom was demonstrated. The formulation presented holds significant promise for future adoption as a widespread phantom in PAI, with potential applications in calibration, performance evaluation, and multi-centre standardisation of PAI systems, as well as for training of new users. Key beneficial properties of the material are:

- i. tuneable and stable acoustic and optical properties;
- ii. good mechanical, thermo- and photo-stability in the relevant working range;
- iii. non-proprietary and non-toxic ingredients and
- iv. high flexibility of phantom design and fabrication.



# 5 EVALUATION OF PRECISION AND ACCURACY IN PHOTOACOUSTIC MESOSCOPY

*I would like to thank Dr. Paul Sweeney and Thierry Lefebvre for assisting me with processing of the in vivo data. Moreover, I wish to thank Dr. Emma Brown for helping me with the in vivo photoacoustic data acquisition.*

## 5.1 Introduction

Extending the range of macroscopic and microscopic PAI approaches, raster-scanning mesoscopy has recently been introduced<sup>449</sup> for visualization of tissue structures up to 2-3 mm depth<sup>450,451</sup>. The innovative nature of mesoscopy lies in combining wide bandwidth, high-frequency detectors with fast nanosecond-pulsed laser excitation, enabling three-dimensional imaging of optically absorbing molecules such as haemoglobin and melanin<sup>452,453</sup> at the mesoscopic scale (in-plane spatial resolution:  $\sim 20 \mu\text{m}$ )<sup>450,451</sup>.

In the preclinical setting, photoacoustic mesoscopy has already been demonstrated for: longitudinal *in vivo* studies in several mouse models of cancer<sup>137,454</sup>; whole body imaging of zebrafish using a 360° multi-orientation approach<sup>455</sup>; and gastrointestinal imaging<sup>456</sup>. In clinical studies, it has shown particular potential in skin imaging, revealing individual skin layers, benign nevi<sup>457,458</sup>, hyperthermia effects<sup>459</sup>, and pathophysiological biomarkers of inflammatory skin diseases<sup>450,460</sup>.

Volumetric visualization of vasculature and skin layers is one of the key strengths and main applications of photoacoustic mesoscopy, however, the accuracy and precision for delineating targets of interest, such as vessel structures, has yet to be evaluated. A well-known limitation of non-tomographic PAI systems lies in the limited angular coverage of their illumination and detection arrays, enabling only visualization of targets that are quasi-perpendicular to the transducer array<sup>461</sup>. Moreover, the non-isotropic illumination from the sides of the ultrasound detector array results in inefficient light delivery to the region of interest<sup>462</sup>, thereby leading to limited penetration depth, particularly in specimens that exhibit high absorption. Finally, the limited view can cause in-plane or out-of-plane artefacts, impeding the clarity of the images<sup>463-466</sup>. In addition to these technical limitations impacting accuracy, precision-related variations in imaging data arise from temporal, positioning or operator-dependent factors. Detailed precision studies have been performed for other commercially available PAI systems, including a preclinical tomography system<sup>145</sup> and a handheld clinical system<sup>467,468</sup> which have established relevant bounds on the reliability and biological relevance of the extracted photoacoustic data. Such studies are crucial to ensure data reproducibility and accurate data interpretation, in particular as the application of mesoscopic PAI in preclinical and clinical research expands.

In this chapter, a thorough technical validation of a commercial photoacoustic mesoscopy instrument is conducted to assess its potential in extracting perfusion and vessel-related biomarkers from tissues to inform studies on perfusion-limited hypoxia. First, the imaging limitations of photoacoustic mesoscopy are evaluated by investigating common artefact types impacting image quality. Second, signal variations resulting from the restricted angular coverage of the illumination and detection arrays are systematically analysed. Finally, precision is considered, using tailored phantoms and mouse models to assess the impact of temporal variation, target repositioning and user experience. The chapter concludes by outlining recommendations for data acquisition. The presented validation framework for

photoacoustic mesoscopy systems will guide users with similar PAI setups, assisting them in system validation, data handling and data interpretation.

## 5.2 Methods

### 5.2.1 Phantom preparation

#### 5.2.1.1 Base material

For systematic evaluation of artefacts using geometric phantoms, agar was chosen as the bulk phantom material to provide structural support for imaging targets due to its facile and fast preparation method. A 1.5% agar mixture was prepared according to the protocol by Joseph et al<sup>145</sup>. Briefly, intralipid (2.08 v/v%; Merck, 68890-65-3) was used to mimic tissue-like scattering conditions and Nigrosin (0.62 v/v% of Nigrosin stock solution [0.5 mg/ml Nigrosin in deionised water, Merck, 8005-03-6]) was added to mimic tissue-like absorption. Acoustic properties available from the literature for similar concentrated agar phantoms (2%)<sup>469</sup> suggest a speed of sound of around  $1460 \pm 7 \text{ m}\cdot\text{s}^{-1}$  and an acoustic attenuation of  $0.32 \pm 0.06 \text{ dB}\cdot\text{cm}^{-1}$  at 5 MHz<sup>469</sup>. The optical properties were determined using the previously validated DIS system<sup>168</sup> (Section 3.1.2.1), yielding a reduced scattering coefficient of  $1.71 \pm 0.29 \text{ mm}^{-1}$  at 532 nm.

For evaluation of long-term system precision, copolymer-in-oil base material was chosen<sup>220</sup>. The material was prepared according to Section 4.2.1<sup>168</sup>. Briefly, the phantom was composed of 30% high molecular weight SEBS (Sigma Aldrich 200557-250G) and 8% LDPE (Alfa Aesar 43949.30) in mineral oil (Sigma Aldrich-330779-1L), with 0.03 w/v% TiO<sub>2</sub> (Sigma Aldrich 232033-100g) added to provide optical scattering and 0.0007 w/v% Nigrosin (Sigma Aldrich 211680-100G) added to provide optical absorption. The acoustic properties were characterised using a through transmission substitution system (available at NPL, London, UK)<sup>168</sup> (Section 4.2.2), yielding a speed of sound of  $1483.5 \pm 0.17 \text{ m}\cdot\text{s}^{-1}$  and an acoustic attenuation of  $6.73 \pm 0.04 \text{ dB}\cdot\text{cm}^{-1}$  at 5 MHz. A reduced scattering coefficient of  $0.4 \text{ mm}^{-1}$  and an optical absorption coefficient of  $0.01 \text{ mm}^{-1}$  were measured using the previously validated DIS system at 532 nm.

#### 5.2.1.2 Phantom mould and inclusions

For phantom studies, a versatile, modular phantom mould was created by 3D-printing (Figure 5.1). Phantom moulds were designed in Autodesk Fusion 360 (San Rafael, CA, USA) and printed using an Anet A6 Printer and polylactic acid (PLA PRO 1.75 mm PLA 3D Printer Filament 832-0232 (Yellow) / 832-0223 (White) RS Components, Corby, UK) as a base material. The phantom mould consists of two modules (Figure 5.1A). The inner module acts as the actual testing module and allows the measurement of specific testing parameters. The outer module functions as a frame for the inner module and prevents leaking of the bulk material and enables a firm positioning of the phantom. Indentations in the corners of the outer module allow insertion of structural support blocks to control the distance between detector and phantom surface. Customized handles can be inserted on diagonal sides of the inner module to facilitate the insertion and removal of the inner module from the outer module. Two

inner modules were developed. The first inner module, the string module (Figure 5.1B), allows for the examination of technical parameters such as the sensitivity of the system to angularity or penetration depth through insertion of strings at different depths and angles. The second module, the tubing module (Figure 1C), permits the analysis of liquid contrast agents by including tubing (Fine Bore Polythene Tubing 0.58 mm inner diameter, 0.96 mm outer diameter, Portex, USA) at different depths and in different directions.

For evaluation of imaging artefacts, a dilution series of red ink (Cranfield Colours, Wales, UK) was used in the tubing module. For geometric sensitivity studies, the string module was deployed with red-coloured synthetic fibres (Smilco, Houston, TX, USA). These were chosen as imaging targets for the string module due to their similar size<sup>470,471</sup> to murine vessels and high absorption at 532 nm.

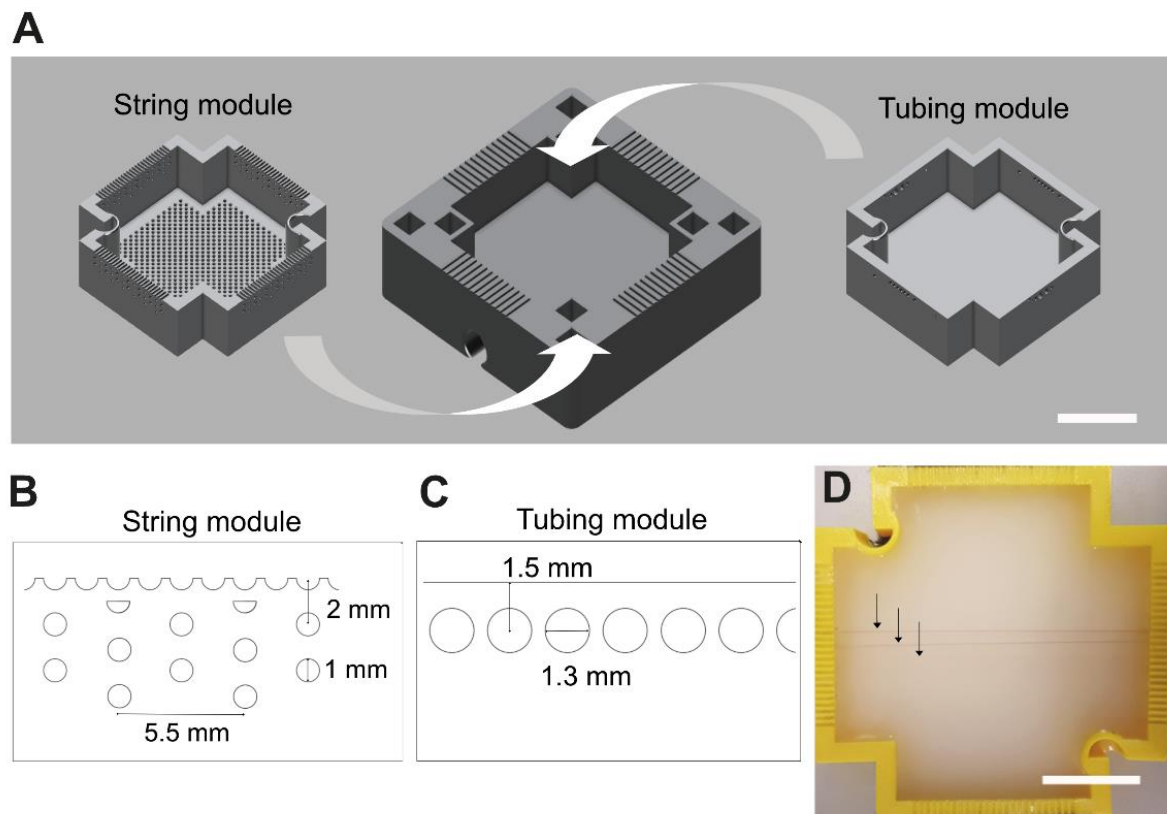


**Figure 5.1: Phantom design for the technical validation studies.**

(A) The computer-aided designs of the outer (middle) and inner (right, left) modules used for this study are shown. Close-up side view of the image quality phantom modules: (B) String array allowing penetration depth and angular studies; (C) Tubing array allowing sensitivity studies. (D) Photograph of the 3D-printed string phantom module filled with agar and featuring targets at different depths (black arrows) is shown. Scalebars = 20 mm.

### 5.2.2 Animal handling

Procedures on small animals were performed under the authority of project (PE12C2B96) and personal (IA70F0365, I544913B4) licenses issued by the Home Office, UK. Studies were approved by the CRUK Cambridge Institute local animal welfare and ethical review bodies under compliance form numbers: CFSB2112, CFSB1361, CFSB1567, CFSB1745 and CFSB1979. All mice were housed in Tecniplast Green Line individually ventilated cages with APB6 bedding on a 12-h on/off light/dark cycle (7 AM to 7 PM) with 5R58 diet (PicoLab).

To evaluate precision of photoacoustic mesoscopy in preclinical small-animal cancer imaging, a common application for photoacoustic mesoscopy, a cell line xenograft model and two patient-derived xenograft (PDX) models were used. For the cell line model, subcutaneous tumours were established in male BALB/c nude mice (Charles River, age 8-10 weeks).  $1.5 \times 10^6$  PC3 prostate adenocarcinoma cells suspended in a mixture of 50  $\mu$ L PBS and 50  $\mu$ L matrigel (354248; Corning) were inoculated subcutaneously in both lower flanks of  $n=5$  mice (resulting in  $n=10$  tumours). For the PDX models, two luminal B patient-derived xenograft (PDX) models (AB580, STG143) and two basal PDXs (STG139, STG321) were implanted subcutaneously into the flank of 6-9 week-old NOD SCID gamma (NSG) mice (Jax Stock #005557) using the standard protocols of the originating biobank<sup>472</sup> ( $n_{AB580} = 12$ ,  $n_{STG143} = 10$ ;  $n_{STG139} = 26$ ,  $n_{STG321} = 18$ ). Before surgical implantation, cryopreserved breast patient-derived xenograft tumour fragments ( $\sim 2 \text{ mm}^3$ ) in freezing media (Foetal Bovine Serum, heat-activated Thermo Fisher Scientific 10500064 +10% dimethyl sulfoxide Sigma D2650) were defrosted at 37°C, washed with Dulbecco's modified eagle's medium (Gibco 41966) and mixed with matrigel (Corning 354262). For *in vivo* imaging, mice were anaesthetised using 3% isoflurane delivered in 50% oxygen and 50% medical air. If needed, the hair was removed around the area to be imaged by shaving and application of commercial hair removal cream. Mice were placed on a heat-pad maintained at 37°C inside the system chamber. Respiratory rate was maintained at 70-80 bpm using isoflurane ( $\sim 1.5$ -2.0% concentration) throughout image acquisition.

### 5.2.3 Image acquisition

The photoacoustic mesoscopy system (RSOM Explorer P50, iThera Medical GmbH, Germany; Figure 5.2, A,B) has been described in detail elsewhere<sup>473</sup>. Briefly, laser light is generated by a 532-nm laser (pulses: 1 ns;  $\leq 1$  mJ/pulse) and delivered through a customized 2-arm fibre bundle (spot size: 3.5 $\times$ 5mm). Photoacoustic signals are detected by a spherically focused LiNbO<sub>3</sub> detector (centre frequency: 50 MHz; bandwidth: 10-90 MHz; focal diameter: 3 mm; focal distance: 3 mm; f number: 1). The recorded data is amplified by a low noise amplifier of 63 dB gain. The scanning head is attached to two motorized stages and coupled to the sample surface by an interchangeable water-filled (2 mL) interface. For coupling of the object to the lower side of the interface, commercial ultrasound-gel (Aquasonic Clear, Parker Laboratories, USA) was used. The ultrasound gel was centrifuged to remove

air bubbles and warmed before application. The interface was positioned on the object by moving the stage in x, y, and z directions. Images were acquired over a field of view of  $12 \times 12$  mm (step size: 4  $\mu\text{m}$  along the x axis, and 5  $\mu\text{m}$  along the y axis). The acquisition of one image took approximately 7 min.

For phantom imaging, the phantom was placed underneath the transducer and aligned to the transducer direction in the position of interest. About 10 ml of ultrasound gel was used to couple the transducer surface to the phantom medium. Care was taken for the transducer interface not to touch the phantom surface.

For *in vivo* imaging, temporal variability with and without replacement *in vivo* was assessed over a time frame of 35 mins (n=5 images) with an n=5 per sample group. ‘With replacement’ is defined as full removal of the mouse from the heat pad including cleaning off the coupling ultrasound gel. For evaluation of the impact of operator experience, an operator with > 1-year experience in preclinical photoacoustic mesoscopy imaging was regarded as experienced, and an operator with < 10 days experience in preclinical photoacoustic mesoscopy imaging was regarded as inexperienced.



**Figure 5.2: Overview of the photoacoustic mesoscopy system.**

(A) Photograph of the system. (i) denotes the scan head and (ii) the heated mouse bed. The scan head is enlarged in the second photograph. Top arrows are pointing to the two illumination fibres, whilst the bottom arrow points to the ultrasound (US) transducer. (B) Schematic illustrating the functioning of the system. Created with BioRender.

#### 5.2.4 Image and statistical analysis

Imaging data were reconstructed using a beam-forming algorithm, which models the sensitivity field of the focused detector and generates 3-dimensional images<sup>474–476</sup>. The reconstructed images were analysed using MATLAB (v2020, MathWorks, Natick, MA, USA) and Fiji (v2.1.0)<sup>477</sup>. Statistical analysis was performed using Prism (v9, Graphpad Software, San Diego, CA, USA). All data are shown as mean  $\pm$  SD unless otherwise stated. The COV was calculated as the ratio of the SD to the mean, expressed as percentage. For multiple comparisons, one-way ANOVA followed by Tukey’s test was conducted. Correlation analysis between dorsal and lateral imaging positions was conducted using Spearman’s correlation coefficient due to non-normal data distribution.

#### 5.2.4.1 Phantom data

For the phantom image analysis, a fixed-sized rectangular region of interest spanning the length of the string was placed around each string within the image. For each string, the line profiles perpendicular to the string were extracted. The background was subtracted and a gaussian curve was fitted to the signal. The full width at half maximum (FWHM) and mean intensity value were extracted from the fit for each line profile. Subsequently, the mean and SD of all FWHMs and signal intensities of all line profiles were calculated to achieve final values for each string.

#### 5.2.4.2 *In vivo* data

For the *in vivo* repeatability studies, the blood volume was chosen as a comparison metric, as it is a commonly used variable of interest in preclinical studies, and sometimes used as a precursor for further downstream analysis of morphological features<sup>478</sup>. For quantification, an existing pipeline previously reported elsewhere was used<sup>478</sup>. Briefly, imaging data were filtered in the Fourier domain in the x/y plane to remove reflection lines, before being reconstructed using a backprojection algorithm in viewRSOM software (v2.3.5.2 iThera Medical GmbH, Germany) with motion correction and a voxel size of  $20 \times 20 \times 4 \mu\text{m}^3$  (x,y,z). Reconstructed images were subjected to a high-pass filter<sup>145</sup> to remove echo noise, followed by a Wiener filter to remove stochastic noise. Afterwards, a slice-wise rolling ball background correction<sup>479</sup> was performed to achieve a homogenous background intensity. Segmentation was performed using a random forest classifier (ilastik v1.3.3<sup>480</sup>). For the classifier, n=20 *in vivo* images were used for training and n=14 *in vivo* images were used for testing. Then, all segmented images were passed through a 3D median filter to smooth and remove impulse noises.

## 5.3 Results

### 5.3.1 Overview of the dominant artefact types in photoacoustic mesoscopy

To initiate the characterisation of photoacoustic mesoscopy performance, dominant artefact types present in the images were systematically analysed. Artefacts emerging from absorbing vessel-like structures can lead to considerable misinterpretation of the signal structures and degrade image contrast. Speckle and clutter artefacts<sup>481-483</sup> can be observed in the image background, affecting the overall imaging signal-to-noise ratio. Artefacts that can directly affect vessel analysis can be summarized into three main categories (Figure 5.3).

First, illumination artefacts arise due to the limited illumination of the field of view, leading to optical excitation and acoustic wave generation only in the upper part of absorbing structures that face the illumination and transducer array (Figure 5.3A). The result is inaccurate diameter estimations in the  $x/z$  plane compared to the  $x/y$  plane<sup>478</sup>. For example, in the string phantom module, where the true diameter of each string is  $d_{act} = 126 \mu\text{m}$ , the measurements from the reconstructed images agree only in the  $x/y$  plane ( $d_{x/y} = 122 \pm 7.8 \mu\text{m}$ ) and substantially underestimate the value in the  $x/z$  plane ( $d_{x/z} = 27 \pm 3.2 \mu\text{m}$ ).

Second, shadow artefacts arise from obscuring objects, causing a signal loss in underlying objects due to strong optical or acoustic attenuation of the overlaying structure (Figure 5.3B). Third, reflection artefacts occur due to presence of acoustic reflectors/scatterers or strong acoustic reverberations of the absorbing object itself<sup>464,484,485</sup>, leading to a signal echo near the object of interest (Figure 5.3C). They can occur in-plane or out-of-plane depending on the position of the absorber/reflector<sup>486</sup>. Awareness of these artefacts is of particular importance as illumination artefacts can lead to inaccuracies in quantification of vessel size, but more importantly, shadow and reflection artefacts can be mistaken for real structures in the image plane.

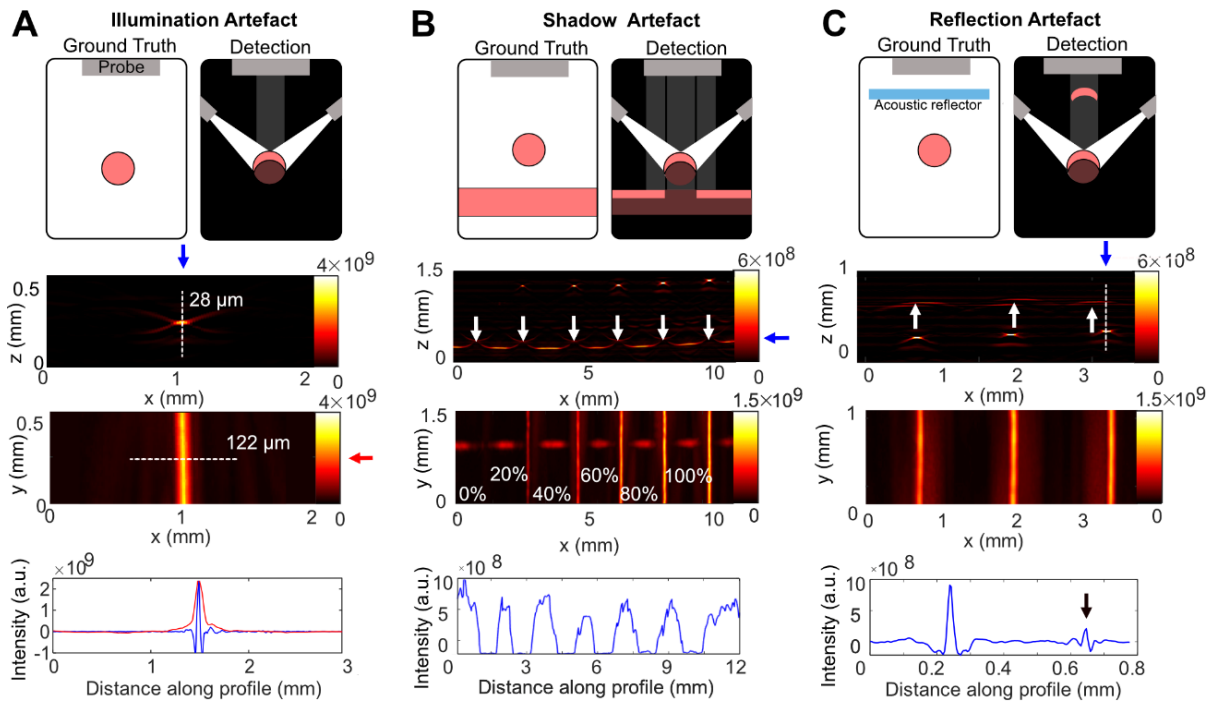


**Figure 5.3: Overview of artefacts arising in photoacoustic mesoscopy.**

Explanatory schematics (first row), x/y MIPs (second row), x/y MIPs (third row), and line profiles (fourth row) for the respective white dotted lines in the RSOM images for: (A) illumination artefact; (B) shadow artefact; and (C) reflection artefact. In A, a single string is shown, whilst in B, and C dilutions of red ink in tubing are displayed. In B, a tube of absorber is positioned perpendicular and beneath tubes of varying relative concentrations (up to 100%). The underlying tubing has the same concentration as the overlaying tubing with the highest concentration (100%). Shadow artefacts are created by attenuation of the acoustic waves by the overlaying tubing, rather than by optical attenuation, as the length of the signal gap is independent on the signal intensity in the overlaying tubes. In C, the agar phantom/ultrasound gel interface acts as an acoustic reflector. White arrows depict the respective artefact; blue and red arrows indicate the respective line profiles plotted in the last row; the black arrow depicts the reflection artefact in the line profile.

### 5.3.2 Geometric sensitivity of photoacoustic mesoscopy

We sought to systematically analyse how the geometric positioning of a vessel-like target in three-dimensional (3D) space affects the acquired signal. First, the impact of different target depths on signal intensity and measured spatial dimensions was evaluated (Figure 5.4A,B). As expected, a significant signal loss occurred with increasing string depth (Figure 5.4C). Depth also impacted the quantified FWHM in the x/y direction with a significant decrease in measured FWHM with increasing depth (Figure 5.4D). Second, the impact of horizontal target rotation on the acquired signal was tested. A phantom with strings in a star-shaped pattern (Figure 5.4E,F) was imaged and the signal from each angled string quantified. To minimise inaccuracies in the target depth arising from the experimental preparation of stacking of the strings, the phantom was rotated by  $90^\circ$  between image acquisitions. The angle between the string and the direction of illumination was found to significantly impact the quantified mean PAI signal (Figure 5.4G) with the string in line with the two illumination fibres having

the highest signal intensity. There was no significant difference in the calculated FWHM between 90° and 0° or in the strings between the rotation steps (Figure 5.4H). Third, the impact of vertical target rotation on the acquired signal was tested. A clear signal decay was found with increasing angle to the phantom surface (Figure 5.4I-K). At 24°, the string could not be detected anymore in tissue-mimicking phantoms (Figure 5.4K). The size of the FWHM quantified from the MIPs remained stable for angles up to 20°, but beyond that it increased and became more variable due to the lower signal (Figure 5.4L). These results highlight depth- and angle-related limitations of the system resulting from the limited angular coverage of the illumination and transducer array, affecting signal detection and quantification.

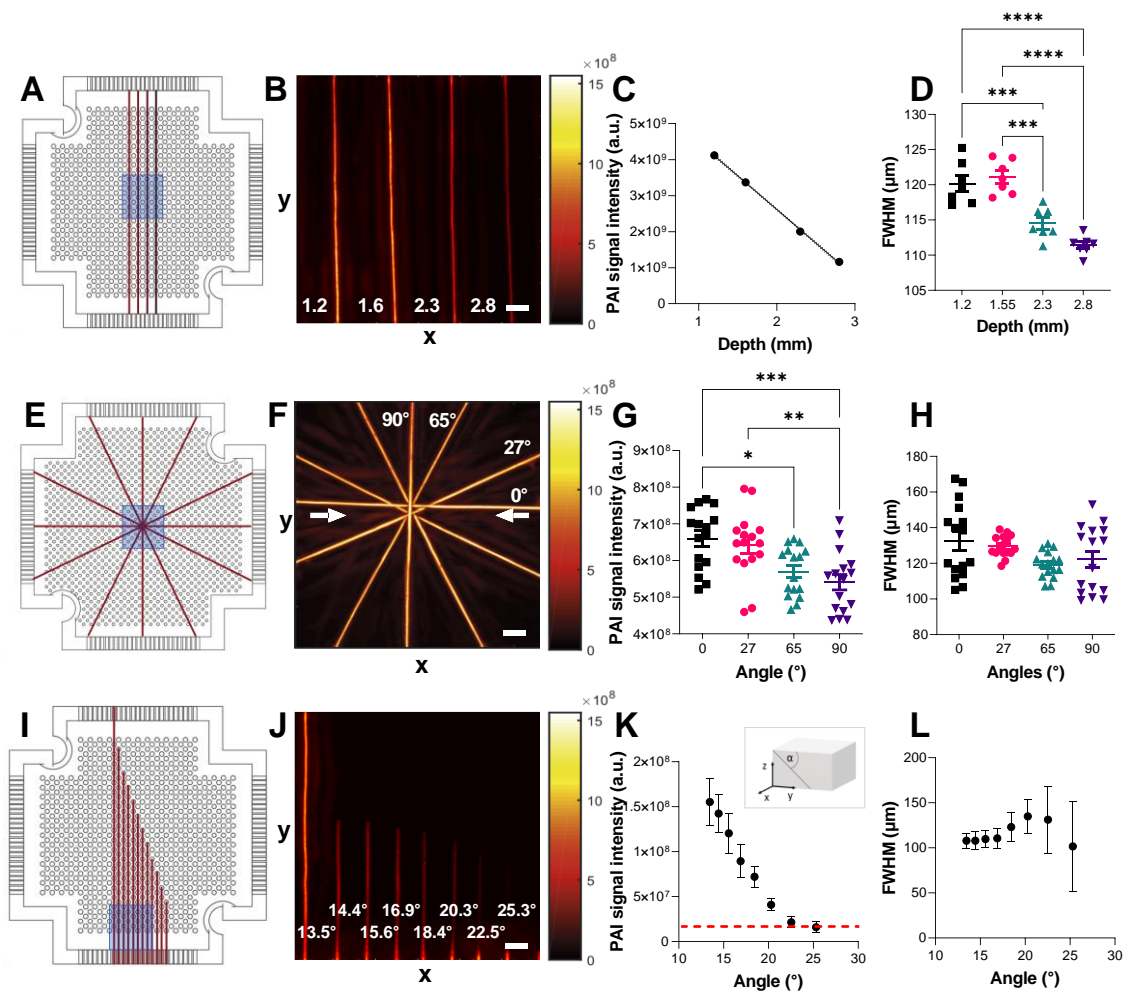


**Figure 5.4: Geometric sensitivity of the photoacoustic mesoscopy system.**

Phantom configuration (first column), x/y MIPs (second column), quantified signal intensity values (third column) and FWHM (fourth column) for: phantom with strings at different depths (A-D,  $n=3$ ,  $R^2=0.9991$ ), phantom with horizontally angled strings (E-H,  $n=8$ ), phantom with vertical angled strings (I-L,  $n=3$ ). The field of view in the phantom configurations (corresponding to the MIPs) is marked in blue. The numbers in B depict the depth of the neighbouring string in mm. The direction of the optical fibres in F is marked with white arrows. Data displayed as mean  $\pm$  SD. For figures D and G, significance was assigned using ANOVA (\* $p < 0.05$ , \*\* $p < 0.01$ , \*\*\* $p < 0.001$ ). Scale bar=1.2 mm.

### 5.3.3 Photoacoustic mesoscopy shows high precision for repeated measurement

Next, the temporal stability of photoacoustic mesoscopy phantom measurements was evaluated (Table 5.1, Figure 5.5). A mean COV of  $1.2 \pm 0.7\%$  (Figure 5.5A) was determined for a single imaging session without repositioning. With repositioning, a slightly higher COV of  $4.1 \pm 2.4\%$  was found (Figure 5.5B) for short-term studies (without switching off the system in between each runs), which increased to 9.6% for long-term studies (25 days, with switching off the system between each run and waiting for at least 12 hours). No slopes were significantly non-zero [without repositioning:  $p=0.1551$ ; with repositioning (short term):  $p=0.2858$ , with repositioning (long term):  $p= 0.3955$ ]. The COVs were similar across different depths (Figure 5.5A,B), suggesting a reasonable longitudinal repeatability for the system.

**Table 5.1: Coefficients of variation (COV) for temporal stability of the photoacoustic mesoscopy system.**

			COV (%) Mean $\pm$ STD	Slope (%) Mean $\pm$ STD	n
Phantom	Without Repositioning (9x)		1.16 $\pm$ 0.71	-0.05 $\pm$ 0.07	4
	With Repositioning (7x)	Short term (1 hour)	4.06 $\pm$ 2.36	0.14 $\pm$ 0.11	4
		Long term (25 days)	9.6%	0.004	1
In vivo	Without Repositioning (5x)				
		Healthy	5.70 $\pm$ 3.81	-0.004 $\pm$ 0.003	5
		Tumour	11.13 $\pm$ 5.78	0.003 $\pm$ 0.004	9
	With Repositioning (5x)				
		Experienced	15.89 $\pm$ 6.26	0.06 $\pm$ 0.03	5
		Inexperienced	20.17 $\pm$ 9.92	0.04 $\pm$ 0.05	5

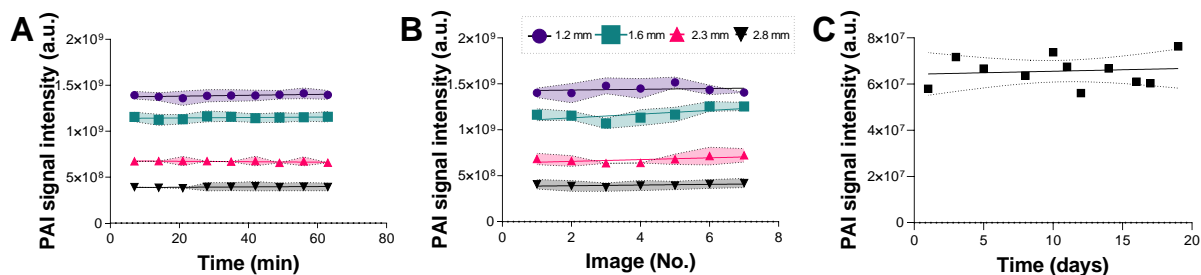


**Figure 5.5: Temporal stability of the photoacoustic mesoscopy system.**

Signal stability in an agar phantom over time is shown along four strings embedded at four different depths (A) without replacement of the phantoms and (B) with replacement of the phantom between each sequential image acquisition. Legend indicates string depth. Shaded areas represent SD of FWHMs along each string. (C) Signal stability of a string embedded in a copolymer-in-oil phantom over a time frame of 20 days.

### 5.3.4 Photoacoustic mesoscopy shows high precision during *in vivo* application

Next, the temporal stability of photoacoustic mesoscopy phantom measurements was evaluated *in vivo*, where additional sources of variation can arise as summarized in Figure 5.6. Contributions from motion are minimised by appropriate positioning of the animals within the mouse bed and by application of a motion correction algorithm during image reconstruction. The results of the *in vivo* repeatability studies are summarized and compared to repeatability measured in phantoms in Table 5.1.

Static imaging without repositioning *in vivo* led to a mean COV of  $5.7 \pm 3.8\%$  in the thresholded blood volume in healthy tissue (ear, Figure 5.8A). The mean COV increased to  $11.1 \pm 5.8\%$  in pathological tissue (tumour, Figure 5.8B). Whilst the blood volume did not significantly change over time for pathological vasculature ( $p=0.3622$ ), a significant decrease over time was found in our study for the healthy vasculature ( $p=0.0065$ , Table 5.1).

Next, the impact of mouse repositioning on signal stability was assessed. Here, the influence of operator experience was also evaluated. Optimal image acquisition in photoacoustic mesoscopy depends on a variety of factors, such as (1) adequate coupling of the of the tissue of interest to the transducer interface, (2) intactness of the coupling foil, (3) purity of the coupling medium, and (4) compression of the transducer interface on the target tissue (Figure 5.7). With repositioning of the mouse (full removal of the mouse from the heat pad including cleaning off the ultrasound gel), mean COVs of  $15.9 \pm 6.3\%$  were found for an experienced (preclinical RSOM imaging experience > 1 year) operator for tumour imaging, whilst mean COVs of  $20.2 \pm 9.9\%$  were found for an inexperienced operator (no significant preclinical RSOM imaging experience; Figure 5.8D, Table 5.1).

Finally, the impact of mouse positioning on the quantified blood volume was assessed for tumour imaging (Figure 5.8E). The tumour position on the flank allows for several different methods of animal positioning to be used, which will lead to different sub-volumes of the tumour being captured by the imaging system. A significant correlation in the quantified blood volume between dorsal and lateral

positioning of the mouse was found (Figure 5.8F). Taken together, our *in vivo* results suggest that photoacoustic mesoscopy provides a robust quantification of vascular data once users are experienced with the system.

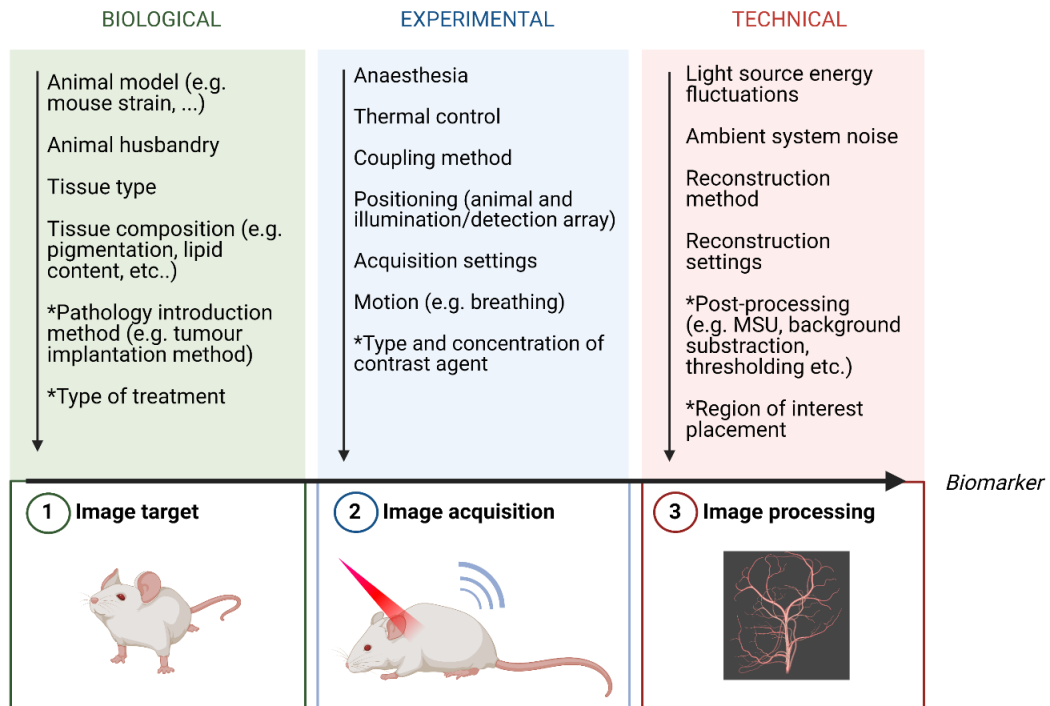


**Figure 5.6: Overview of biological and technical variation factors in photoacoustic imaging (MSU=Multispectral unmixing).**

Parameter marked with an asterisk describe variation factors that are only applicable in certain experiments/system types. Created with BioRender.

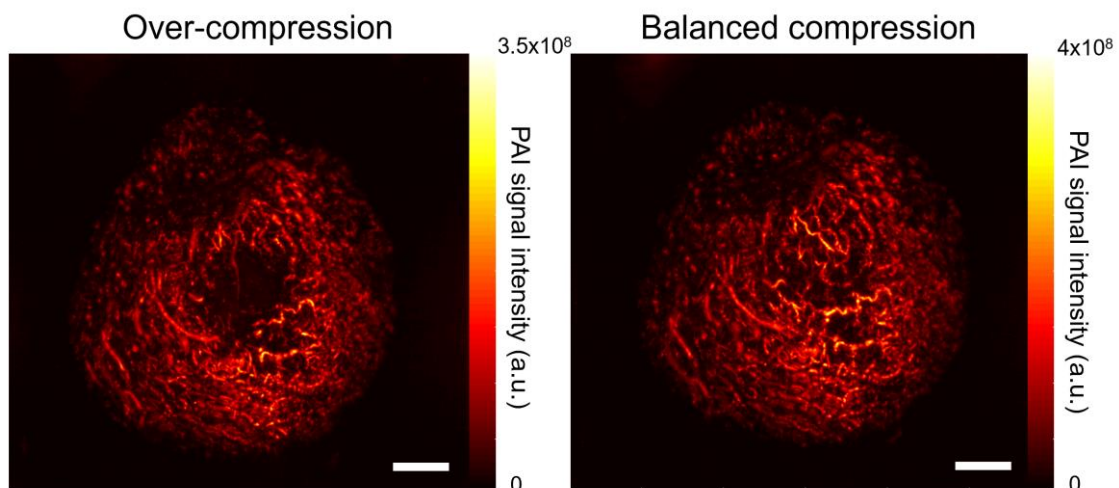


**Figure 5.7: Transducer compression impacts vessel visualisation.**

Image acquisition in photoacoustic mesoscopy requires a balanced compression of the transducer interface on the tissue of interest. Whilst compression minimizes movement artefacts, it can also impact blood flow if applied too strongly, leading to signal loss (first image). Balanced compression enables full visualization of all vessels (second image). x/y MIP of a PC3 tumour. Scale bar=1.5 mm.

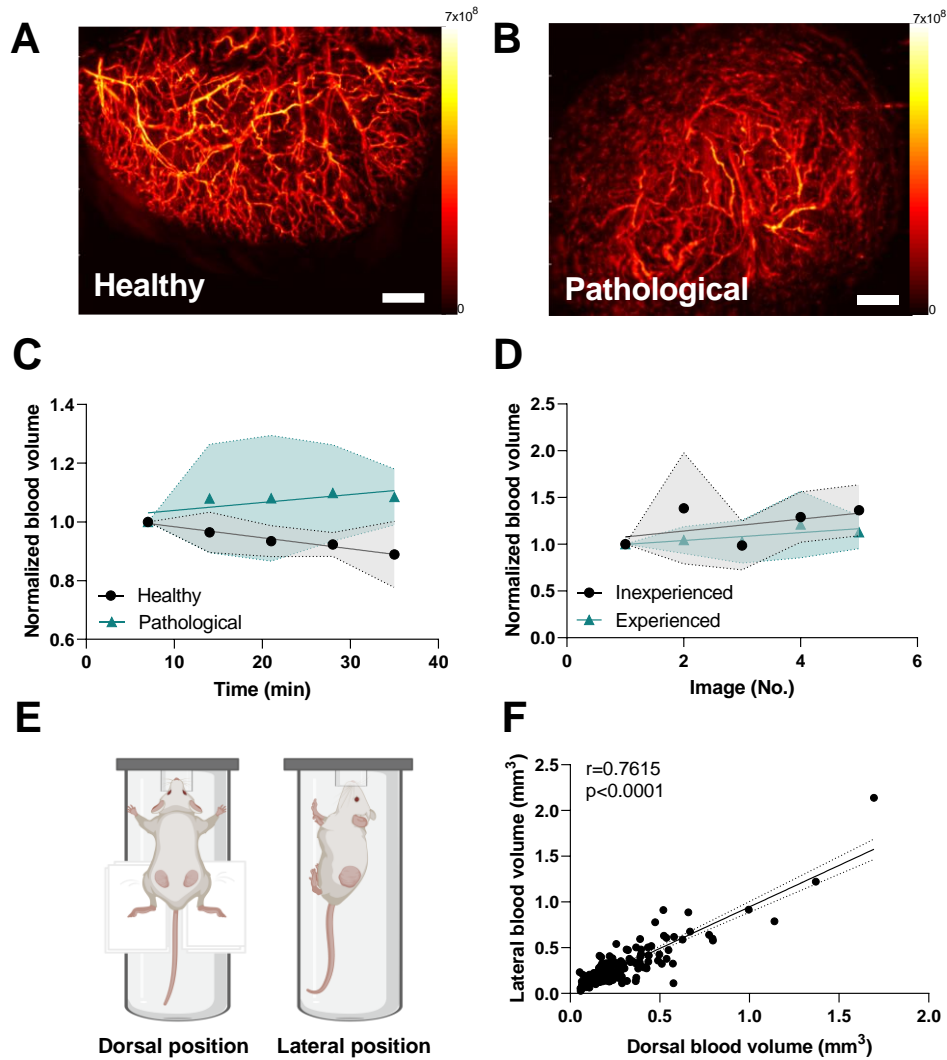


**Figure 5.8: Impact of time, positioning, tissue, and operator-dependent variation sources on the signal stability of the mesoscopic system *in vivo*.**

Representative mesoscopic x/y MIPs for healthy (ear, A) and pathological (tumour, B) tissue are shown. Scale bar=1.5 cm. (C) Normalised blood volume is shown over time in healthy (black, n=6 ears, cell line model) and tumour tissue (green, n=9 tumours, cell line tumour model) without replacement of the mouse. (D) Normalised blood volume is shown in tumour tissue with replacement of the mouse by two different operators (each n=5, inexperienced operator =black, experienced operator=green, PDX model). (E) Dorsal (left) and lateral (right) positioning of the mouse are indicated. Created with BioRender. (F) Correlation of calculated blood volume between dorsal and lateral positioning of the mouse is shown (n=161, PDX model, Spearman  $r=0.7615$ ,  $R^2=0.7687$ ). All data is shown as mean  $\pm$  SD.

## 5.4 Discussion

Photoacoustic mesoscopy has shown potential to derive perfusion and vessel-related biomarkers in studies of perfusion-limited hypoxia, but detailed technical validation is required to provide confidence in temporal repeatability and vascular quantification. Using custom phantoms, a structured testing framework was applied to systematically analyse the impact of different variation sources on precision and accuracy of photoacoustic mesoscopy, thus helping to define its strengths and limitations in assessing characteristics of biological tissues.

First, various artefact types that commonly appear in photoacoustic mesoscopy studies were exemplified and quantified. These lessons learned impact interpretation of vascular structures, which will be necessary in later studies for this thesis. Accurate representation of vascular lumens is fundamentally limited in the photoacoustic mesoscopy geometry: since vessels are only illuminated from the top, images do not depict the full vessel volume (illumination artefact); signal loss also occurs for high angles of vessels relative to the detector, at increasing depth, or due to the presence of overlaying structures (shadow artefact). The limited detection bandwidth of 10-90 MHz of the transducer translates to accurate representation of structures that are sized 12-120  $\mu\text{m}$ <sup>487</sup>. Furthermore, reflection artefacts can occur that may be mistaken for actual vessel structures. While some studies have attempted to identify and remove reflection artefacts, approaches are elaborate, using for example additional ultrasound measurements<sup>481,484</sup>, tissue deformations<sup>463</sup>, localized vibrations using acoustic radiation force impulses<sup>466,482</sup>, multi-wavelength illumination<sup>464</sup>, or training of convolutional neural networks<sup>485</sup>. Nonetheless, the full range of photoacoustic mesoscopy artefacts cannot yet be automatically detected or corrected and as such, understanding the resulting limitations on the acquired data is of utmost importance to prevent misinterpretation.

Second, limitations of the system were analysed that arise from three geometric factors that significantly affect the measured signal intensity: (1) the depth, (2) the horizontal orientation, and (3) the vertical orientation of the target. In the commercial system tested, light is delivered from two optical fibres spaced 180° apart around the ultrasound transducer, leading to different light fluence at the sides orthogonal to this plane. Whilst these horizontal orientation effects are minimal, and did not affect the quantification of target size, they significantly impact any associated measurements of signal amplitude. Illumination from four optical fibres placed at 90° around the ultrasound transducer, such as done in other setups<sup>488</sup>, could help to mitigate this problem, but would increase system cost. The limited numerical aperture of the ultrasound transducer<sup>455</sup> also enabled signal quantification only up to a vertical angle of 24° in our phantom, meaning structures angled more steeply could be missed. The relative impact of these factors also depends on the optical and acoustic properties of the surrounding medium, with higher signal loss in more attenuating media. As all these factors can significantly compromise accuracy of a measured structure, they should be considered when positioning a target within the system, or quantifying and evaluating acquired data.

After assessing accuracy-related factors, the precision of the system was evaluated. The system was found to be characterised by a high signal stability in both short-term and long-term phantom studies. This is in line with other studies showing less than 10% variation<sup>145,467</sup> in PAI systems. The values reported here are higher than those found previously for a commercial tomography system by the same vendor<sup>145</sup> ( $COV_{MSOT}=2.8\%$  vs  $COV_{RSOM}=9.6\%$ ), which is likely due to the fact that the distance between the target and detector is manually controlled by the user in the present system, affecting the measured signal intensity. Moreover, due to the higher resolution of the system, inhomogeneities in the coupling media will have a more pronounced effect on signal quantification. Ensuring constant transducer-target distance, as well as clear, bubble-free coupling agents, intact coupling foil and – if working with phantoms – homogeneous base media, will minimise the impact of these variation factors.

Finally, sources of variation *in vivo* were investigated considering time, tissue type, positioning and operator-dependent sources. As expected, a higher variability was found *in vivo* compared to in phantoms due to additional variations arising from motion and changes in vessel perfusion. When comparing healthy and tumour tissue, a higher variability was found in tumour tissue, which can be explained by the tortuous and leaky nature of tumour vasculature. Interestingly, a significant decrease in thresholded blood volume in healthy vasculature was observed over time. Similar observations have been made before in murine spleen and kidney at the macroscopic scale in a tomographic PAI system<sup>145</sup>, owing to perfusion changes under anaesthesia. Here, the ear was chosen as the healthy tissue of interest, as it is easily accessible by the system and often used as a site of interest in PAI studies<sup>489–491</sup>. However, as a peripheral organ the ear is not directly heated by the heat pad during image acquisition, which may have led to temperature-related vasoconstriction and thereby reduction of measured blood volume over time. Future work should explore the impact of temperature and isoflurane-related sources in more detail. A high correlation was found between the quantified blood volumes measured at two different data acquisition positions, demonstrating robustness in assessment of specimen-specific blood parameters. Variability between different operators was assessed, with only slightly higher values for an unexperienced user, confirming observations from other studies on photoacoustic precision<sup>467</sup>. Taken together, these observations demonstrate good precision of photoacoustic mesoscopy measurements in preclinical oncology models, across time and with different user experience.

Several limitations remain. Inter-scanner variability has not been assessed as part of this technical validation framework due to the extensive logistical challenges of such a study. Similarly, the impact of motion correction, image reconstruction algorithms and data post-processing has not been investigated. First steps towards analysis of these computational variation sources in mesoscopic imaging have been taken elsewhere<sup>478</sup>, but future work should explore these technical factors of variability in more depth for further user guidance.

In summary, the following actions can be taken to minimise the impact of the identified sources of variation and maximise information retrieval in perfusion-limited hypoxia studies:

#### General recommendations:

- Before image acquisition, it should be ensured that the interface unit and coupling foil are clean and intact.
- For acoustic coupling, air bubble free ultrasound gel should be used (or degassed water for phantom studies). Temperature should be maintained at a similar temperature to the sample.
- It should be considered that target intensities are impacted by vertical and horizontal rotation, and penetration depth. If possible, the same positioning of the imaging object with respect to the illumination and detection plane should be used. For optimal quantification, the target of interest should be as close to the scan head and as horizontal relative to the scan head as possible.
- Care should be taken to maintain a constant transducer-target distance across repeated imaging sessions.
- Accurate dimensions can be retrieved only for targets in x/y direction.

#### *In vivo* recommendations:

- Hair should be removed from the field of view.
- The transducer setup should be adjusted for the right amount of compression: Too much compression can lead to vessel blockage, leading to signal loss, whereas too little compression leads to a limited field of view in z direction and potentially increased movement artefacts.
- The movement of the imaging target should be minimised, this may require optimisation of mouse positioning.
- For preclinical studies, respiration rate should be monitored on the live camera and maintained at a consistent value.
- Ensure target temperature is maintained at 37°C throughout image acquisition.

# 6 APPLICATION OF PHOTOACOUSTIC MESOSCOPY AND MACROSCOPY TO STUDIES ON PERFUSION- LIMITED HYPOXIA

*I would like to thank Thomas Else, Thierry Lefebvre, and Dr. Paul Sweeney for their advice and help on the PAI data analysis. Moreover, I wish to acknowledge the research support of the CRUK CI core facilities: the biorepository unit for their assistance with the mouse studies, the histopathology core (in particular Cara Brodie) for assisting me with the histopathology analysis, and the genomics and bioinformatics cores (in particular Chandra Sekhar Reddy Chilamakuri) for their help with the RNA sequencing analysis.*

## 6.1 Introduction

As introduced in Chapter 1, blood vessels formed by angiogenesis in tumours are structurally and functionally abnormal, leading to heterogeneous perfusion<sup>492</sup> with both diffusion- and perfusion-limited hypoxia in the tumour tissue microenvironment<sup>5,6,493</sup>. Diffusion-limited hypoxia is found in cells distant from the blood supply, and is caused by limitations in oxygen diffusion from tumour microvessels into the surrounding tissue. Perfusion-limited hypoxia occurs closer to the blood vessels, and is thought to arise from variations in red blood cell flux<sup>5,6,493</sup> resulting from arteriolar vasomotion<sup>60,494</sup>, fast vascular remodeling<sup>495</sup>, disorganized vascular architecture<sup>51,496</sup>, temporary shutdown of vessels<sup>36</sup> or increased transcapillary permeability<sup>497</sup>. The resulting pO<sub>2</sub> fluctuations are considered to be of approximately 20 mmHg<sup>5</sup> magnitude and can occur with periodicities of minutes to hours<sup>52,498</sup>. To a greater extent than diffusion-limited (or chronic) hypoxia, perfusion-limited hypoxia has been shown to lead to intra-tumoural inflammation, tumour metastasis, and resistance to radio- and chemotherapy<sup>1</sup>. Thus, investigation of the magnitude and distribution of hypoxia dynamics may help in the selection of optimal therapeutic strategies<sup>7,9</sup>.

PAI can visualise haemoglobin-related biomarkers across a range of temporal and spatial resolutions<sup>499</sup>. Having established the robustness of PAI systems through technical validation in the previous chapters, this chapter addresses the task of developing and validating PAI biomarkers to investigate the spatial-temporal dynamics of tumour oxygenation. The technical validation studies give confidence in the ability of the PAI systems used to resolve both fluctuations in sequential imaging within a single session and longitudinal changes over longer time periods as tumours grow. Using two breast-cancer cell line xenograft models with distinct vascular phenotypes<sup>169</sup>, PAI is employed at two different scales to investigate hypoxic dynamics: mesoscopic PAI, with associated caveats highlighted in the prior chapter, was used to assess vascular morphology and perfusion dynamics on a vessel-specific basis, whilst multispectral tomographic PAI was used to investigate oxygenation and perfusion across the whole tumour. The extracted PAI biomarkers were compared against histopathological and gene expression markers, providing further insight into the underlying biological processes that give rise to the imaging signals.

## 6.2 Methods

### 6.2.1 Cell lines

The human adenocarcinoma cell lines MCF7 (Oestrogen Receptor+, OR+) and MDA-MB-231 (Oestrogen Receptor-, OR-) were obtained from the Cancer Research UK (CRUK) Cambridge Institute Biorepository, University of Cambridge. The experiments were performed when cells were in passage 21 (MCF7) and 28 (MDA-MB-231). Authentication using Genemapper 5.0 (Genetica) by STR Genotyping showed 100% match with the reference sequence in both cases. Cells were maintained in Dulbecco's Modified Eagle Medium (DMEM, Gibco) supplemented by 10% of Foetal Bovine Serum (FBS, Gibco) at 37 °C in 5% CO<sub>2</sub>. Oestrogen receptor status of the tumours was confirmed using RNA sequencing.

### 6.2.2 Mouse models

Procedures on small animals were performed under the authority of project (PE12C2B96) and personal (IA70F0365) licenses issued by the Home Office, UK issued under the United Kingdom Animals (Scientific Procedures) Act, 1986 and were reviewed by the Animal Welfare and Ethical Review Board at the CRUK Cambridge Institute (Compliance form number CFSB2178). Seven-week-old immunodeficient female nude (BALB/c nu/nu) mice (n=13; Charles River) were inoculated orthotopically in the mammary fat pad of both flanks with  $1 \cdot 10^6$  cells (either MCF-7, n = 7 or MDA-MB-231, n = 6, random group assignment) in a final volume of 100  $\mu$ L of 1:1 phosphate-buffered saline (PBS, Gibco) and matrigel (BD). For MCF7, oestrogen implants (E2-M - 17 $\beta$ -estradiol 90 days release, daily dose: 41.2 – 105.6 pg/ml, Belma Technologies) were implanted subcutaneously in the scruff of the neck 3 days before tumour cell injection. Animals were kept in hermetic cages with individual air supply through an efficiency particulate air (EPA) filter to guarantee sterile conditions, in 12/12 h ON/OFF light cycles, with enriched environment and food and water ad libitum. To assess growth, tumours were measured before each imaging session using vernier callipers. Tumour volumes were calculated using the formula  $V = a \cdot b \cdot b \cdot \pi/6$  with “a” being the longest axis of the tumour and “b” the shortest. Tumours were assessed up to an average volume of around 400 mm<sup>3</sup> after which mice bearing MCF7 tumours had to be sacrificed due to development of side effects from the oestrogen implants.

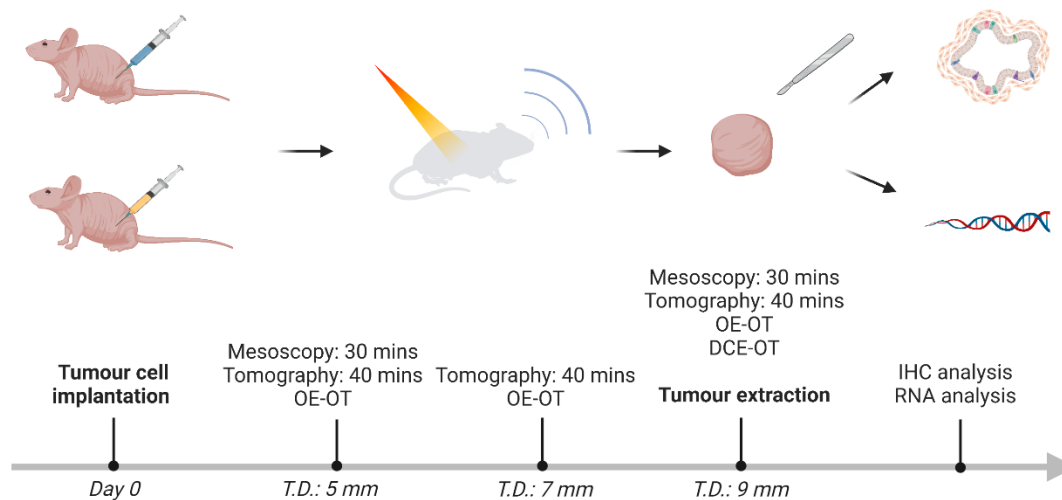


**Figure 6.1: Schematic overview on the experimental schedule.**

T.D.=mean tumour diameter. OE-OT refers to oxygen enhanced (OE) opto(photo)acoustic tomographic imaging and DCE-OT refers to dynamic contrast enhanced (DCE) opto(photo)acoustic tomographic imaging. Created with BioRender.

### 6.2.3 Tomographic photoacoustic imaging

Imaging was performed at three time points during tumour growth as illustrated in Figure 6.1. For tomographic PAI, the commercial multispectral photoacoustic tomography system described in Chapter 4 was used (MSOT inVision 256-TF; iThera Medical GmbH, Figure 6.2A, B). Mice were prepared according to a previously published standard operating procedure<sup>145</sup>. Briefly, mice were anaesthetised using <3% isoflurane in 100% oxygen and placed in a custom animal holder (iThera Medical), wrapped in a thin polyethylene membrane, with ultrasound gel (Aquasonic Clear, Parker Labs) used to couple the skin to the membrane. The holder was then placed within the MSOT system and immersed in degassed water maintained at 36 °C for RHb and HbO<sub>2</sub> imaging acquisition. The animal respiratory rate was maintained in the range 70–80 bpm with ~1.8% isoflurane concentration in 50% oxygen and 50% medical air unless otherwise stated.

Mice were allowed to stabilize their physiology for 15 minutes within the system prior to initialization of the scan. The respiration rate was monitored by observing the breathing motion of the animal using a video feed from an optical camera positioned within the imaging chamber and counting the breaths over a minute using a stopwatch. After acclimatisation, the full volume tumours were imaged using a step size of 0.3 mm and the wavelength from 660 nm to 900 nm in 10 nm steps with an average of 10 pulses per wavelength. Following volumetric imaging, a single slice was chosen in which one of the tumours presented its maximal cross section for temporal imaging. In some cases, this slice also aligned with the tumour on the contralateral flank, which means that both tumours were visualized for the temporally resolved imaging, but this was not always the case (Table 6.1). Imaging was then performed

continuously for 40 mins. To increase the temporal resolution, fewer wavelengths (700, 730, 750, 760, 770, 800, 820, 840, 850 and 880 nm) and averages (6) were set for the temporal study.

Following the temporal scan, oxygen enhanced optoacoustic tomography (OE-OT) was performed in the same slice using the same settings. OE-OT enables the visualization of the spatio-temporal heterogeneity of tumour vascular function<sup>500</sup>. It involves manual switching of the breathing gas from medical air (21% oxygen) to pure oxygen (100% oxygen) using separate flow meters<sup>500</sup>. At the final timepoint (mean tumour diameter = 9 mm), dynamic contrast enhanced (DCE)-OT was performed in a subset of mice ( $n_{MCF7}=4$ ,  $n_{MDA}=6$  tumours, Table 6.1). DCE-OT was initiated after OE-OT in the same imaging slice according to the protocol by Tomaszewski et al<sup>171</sup>. DCE-OT involves the injection of a contrast agent to enable the visualization of perfused areas within the tumour. Images were acquired using 6 wavelengths (700, 730, 760, 780, 800 and 850 nm) with an average of 6 pulses per wavelength. After 1 minute of continuous imaging to establish the baseline signal, a single bolus of 100  $\mu$ l of indocyanine green (ICG, Sigma, I2633-50MG; 40 nmol/20 g mouse in PBS) was injected intravenously through a catheter. PAI was continued for a further 15 minutes to record the enhancement curve.

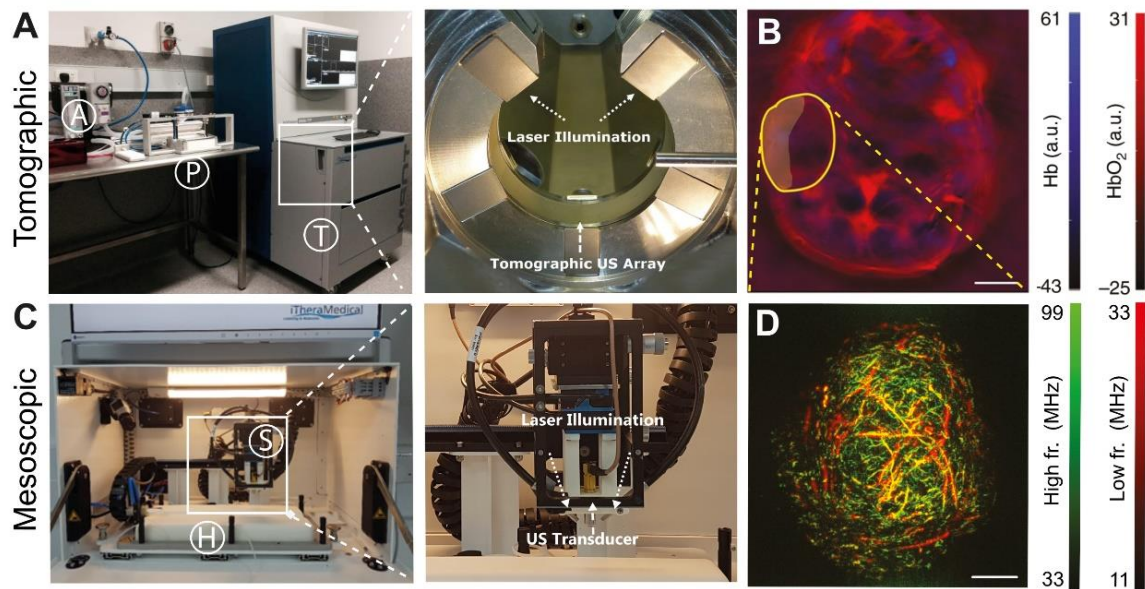


**Figure 6.2: System configurations of the tomographic and mesoscopic PAI system.**

(A) The tomographic PAI system features a 360° ring illumination and 270° acoustic detection setup placed inside a heated water tank [T]. Next to the system an animal preparation station [P] can be found with anaesthesia supply [A], a heating pad and animal and phantom holders that allow repeatable positioning. (B) Representative tomographic image of a tumour-bearing mouse (tumour marked in yellow, Scalebar=5 mm). (C) The scan-head [S] of the mesoscopic PAI system is placed inside a light-tight imaging chamber and a heated animal bed [H] with integrated anaesthesia supply. Two illumination fibres (532 nm) raster-scan in tandem with an ultrasound (US) transducer over the imaging plane. (D) Tumour vasculature with color-coded frequency bands depicting vessels of different sizes (Scalebar=2 mm).

**Table 6.1: Overview of sample distributions.**

Colours: Green = Tumour was included in the analysis. Grey = Tumour was not imaged, either because it was not in line with the contralateral tumour (n.i.l.) or because it did not enter the study (n.e.). Yellow = Tumour was not included in the temporal variation analysis due to motion artefacts, but was included in the analysis of the static parameters. Red = Sample had to be excluded due to artefacts (e.g., caused by skin lesions) or difficulties in sample processing. Blue = Data has not yet been analysed (MS=multi-slice imaging across the whole tumour volume).

Tumour Type	Mouse	Tumour	RNA	IHC	RSOM		MSOT				
					5 mm	9 mm	MS	Temporal Variation			DCE
								5 mm	7 mm	9 mm	
MCF7	A	1						M			n.e.
		2						n.i.l.	n.i.l.		n.e.
	B	3						M			
		4						n.i.l.			
	C	5						M			n.e.
		6						M			n.e.
	D	7						M		A	n.e.
		8						M		A	n.e.
	E	9						M		M	
		10						n.i.l.		M	
	F	11						M			n.e.
		12						M		n.i.l.	n.e.
	G	13						M			n.e.
		14						n.i.l.	n.i.l.	n.i.l.	n.e.
MDA-MB-231	H	1						M			
		2						n.i.l.			
	I	3						M			
		4						n.i.l.	n.i.l.	n.i.l.	n.i.l.
	J	5						M			
		6						n.i.l.	n.i.l.	n.i.l.	n.i.l.
	K	7						M			
		8						M			
	L	9		A				M		A	n.e.
		10						n.i.l.	n.i.l.	n.i.l.	n.e.
	M	11						M	M	A	n.e.
		12						n.i.l.	n.i.l.	n.i.l.	n.e.

#### 6.2.4 Mesoscopic photoacoustic imaging

The mesoscopic photoacoustic system introduced in Chapters 4 and 5 was used in this study (RSOM Explorer P50, iThera Medical GmbH, München, Germany, Figure 6.2C-D)<sup>473</sup>. For *in vivo* imaging, mice were anaesthetised using 3% isoflurane in 50% oxygen and 50% medical air. Mice were placed on a heat-pad maintained at 37°C inside the chamber. Respiratory rate was maintained at 70-80 bpm using isoflurane (~2% concentration) throughout image acquisition. Images were acquired at 81% laser energy and a laser pulse repetition rate of 1 kHz. Per imaging time point, at least one image of with a field of view of  $\leq 12 \times 12$  mm (step size: 20  $\mu$ m, acquisition time: ~7 mins) was acquired per tumour. For the first and last tumour imaging timepoint, 15 consecutive images were acquired over a field of view of  $\leq 6 \times 6$  mm of each tumour (step size: 20  $\mu$ m, acquisition time: ~2 mins per image, 30 mins in total) to evaluate perfusion over a time span of 30 mins.

#### 6.2.5 Tissue processing for histopathology and image analysis

Tumour tissue was fixed in neutral buffered 10% formalin for 24 hours, and then processed by the Cancer Research UK Cambridge Institute Histopathology core facility. The tissue samples were embedded in paraffin, sectioned, and rehydrated. Following deparaffinising and rehydration, IHC was performed using a BOND automated stainer with a bond polymer refine detection kit (Leica Biosystems) and 3,3'-diaminobenzadine as a substrate. The markers chosen, working dilutions, and antigen retrieval methods are detailed in Table 6.2. Adjacent serial sections were used for CD31 and ASMA staining. Haematoxylin and Eosin (H&E) staining was performed using an automated system (ST5020 Leica, Biosystems). Stained formalin-fixed paraffin-embedded (FFPE) sections were scanned at 20 $\times$  magnification using an Aperio AT2 with a resolution of 0.5 $\mu$ m/pixel (Leica Biosystems). N=1 tumour (MDA-MB-231) was excluded from the analysis due to processing difficulties (Table 6.1).

For analysis of histopathological images, regions of interest (ROIs) were drawn on the scanned images over the whole viable tumour area, excluding skin and necrotic regions. Using HALO (v3.2, Indica Labs), a random-forest tissue classifier was trained for analysing the samples. Typically, the classifier was trained using 50 plus annotations per tissue class per image on a training set of 20-40% of the images. Necrotic area, CD31 positive and CAIX positive area ( $\mu$ m<sup>2</sup>) were quantified as a percentage of the total classified tumour area ( $\mu$ m<sup>2</sup>). For HIF-1 $\alpha$  quantification, the percentage of positive nuclei from all nuclei within the tumour area was counted since nuclear location of HIF-1 $\alpha$  indicates its transcriptional activity<sup>501</sup>. To quantify ASMA coverage of blood vessels, a classifier was run on an adjacent CD31 section to identify CD31 positive areas, and then overlaid onto the ASMA section. An area quantification module was then used to identify areas that were both ASMA and CD31 positive. The fraction of the ASMA positive area within the CD31 positive area was taken as the ASMA vessel coverage (%).

**Table 6.2: Overview of histological and IHC markers used.**  
(HIER=heat-induced antigen (epitope) retrieval).

Marker	Full Name	Supplier	Antibody retrieval method	Visualisation	Ref.
Anti-mouse CD31	Cluster of differentiation 31	Cell signalling 77699	1:100, Tris-EDTA HIER 20min	Stable and highly expressed endothelial cell marker; indicates vessel density	502
Anti-mouse ASMA	Alpha smooth muscle actin	Abcam, ab5694	1:500, Tris-EDTA HIER 10min	Smooth muscle and pericyte marker; indicates vascular maturity	169
Anti-human CA-IX	Carbonic anhydrase IX	BioScience Slovakia, AB1001	1:1000, Sodium Citrate HIER 20min	Chronic hypoxia marker, downstream target of HIF-1 $\alpha$ (half-life 2-3 days)	503
Anti-human HIF-1 $\alpha$	Hypoxia inducible factor 1 $\alpha$	Abcam, ab51608.	1:50, Sodium Citrate HIER 20min	Acute hypoxia marker (half-life 5-8 mins)	504
H&E	Haematoxylin & Eosin	Leica Microsystems Eosin 1%, Haem. 3801560E		Marker of general tissue architecture	169

### 6.2.6 RNA analysis

Total RNA was extracted from flash frozen tumour tissue using the Maxwell® RSC miRNA from Tissue kit (AS1680; Promega) following the standard protocol. RNA concentration was quantified using the Qubit 4 RNA Broad Range Assay kit (Life Technologies, Thermo Fisher Scientific Inc.) with a Qubit™ 4.0 Fluorometer (Life Technologies, Thermo Fisher Scientific Inc.). RNA integrity number (RIN) scores were measured using the Agilent Bioanalyzer (Agilent Technologies, Santa Clara, Calif) to assess RNA quality. All samples had a RIN > 7, which was considered acceptable for further analysis. Libraries for RNA-seq were prepared with an Illumina TruSeq stranded mRNA workflow. One pool of 24 libraries was sequenced on Illumina NovaSeq 600 with paired-end and 50 bp long reads. Each sample had about 35 million reads on average. Each sample group had 3 or 4 replicates. All analysis was conducted in R. Reads were aligned against human genome assembly GRCh38 (hg38) using the STAR alignment tool<sup>505</sup>. Reads were counted against genes using featureCounts from the Subread package<sup>506</sup>. Principal Component analysis (PCA) was used to assess variation between the samples. The first two principal components were used to visualize the data and the percentage variance was calculated. For differential expression analysis, the DEseq2<sup>507</sup> package was used. Gene set enrichment analysis (GSEA)<sup>508</sup> was performed against the Molecular Signature Database (MSigDB)<sup>509</sup> for downstream functional annotation. The Bioconductor package<sup>510</sup> was used to perform gene set variation analysis (GSVA).

## 6.2.7 Photoacoustic data analysis

### 6.2.7.1 Tomographic image analysis

Tomographic image analysis was performed in Python (version 3.8.12). PAI reconstruction was performed using an acoustic backprojection algorithm. Images were reconstructed with a pixel size of  $100\ \mu\text{m} \times 100\ \mu\text{m}$ . Linear spectral unmixing was performed for HbO<sub>2</sub>, RHb, and ICG if present. ROIs were drawn manually around the tumour area (excluding the skin) and spinal tissue (as reference region) in the grayscale 800 nm (isosbestic) image taken from the first frame of each scan to reduce bias in the analysis. The spinal tissue was used as a reference region as it was present on all the scans and could be confidently identified. The reconstructed images were down sampled by a factor of 3 for further analysis, to improve response classification (see below).

As PAI cannot accurately measure the absolute sO<sub>2</sub> without the precise knowledge of optical energy distribution, the approximate oxygenation metric derived in this study was denoted as sO<sub>2</sub><sup>MSOT</sup> rather than absolute sO<sub>2</sub>. sO<sub>2</sub><sup>MSOT</sup> was computed as the ratio of HbO<sub>2</sub> weighted signals to total haemoglobin weighted signals (THb=HbO<sub>2</sub> + RHb) from linear spectral unmixing. The spatial variability of the signal was assessed by calculating the standard deviation of the sO<sub>2</sub><sup>MSOT</sup> values in each tumour ROI.

To analyse oxygenation dynamics, an analysis procedure described previously was followed<sup>99,113,511</sup>. Briefly, the following processing steps were applied to the time profiles of each pixel: (i) linear detrending; (ii) calculation of the autocovariance; (iii) calculation of the power spectral density via the Lomb-Scargle method<sup>512,513</sup> and (iv) thresholding according to a confidence interval, assuming that the signal is affected by Gaussian noise. The Lomb-Scargle method has been chosen over other methods of frequency analysis (e.g., fast Fourier transform (FFT)), as it allows more accurate identification of frequency peaks<sup>514</sup>. For each tumour, the Lomb-Scargle method was applied to individual pixel sO<sub>2</sub><sup>MSOT</sup> time courses and the resulting spectra were combined into a single average tumour frequency spectrum. Data sets were included in the analysis only if they were free of motion artefacts to avoid propagating artefacts into the frequency spectra (Table 6.1). The spectral mean and standard deviation for each tumour type was then computed independently for each of the 3 time points during tumour growth. Dominant frequencies of sO<sub>2</sub><sup>MSOT</sup> oscillation were assessed based on spectral power. Pixels having a peak within frequency band of 0 to 0.005 Hz (0–18 cycles per hour) were defined as cyclic pixels (3–18 cycles per hour is considered the relevant physiologic range<sup>99,115</sup>). The cyclic fraction per tumour was calculated as the ratio between the number of cyclic pixels and the total pixel count.

For analysis of the OE-OT and DCE-OT data, previous established analysis pipelines were followed<sup>171</sup>. For OE-OT data analysis, average sO<sub>2</sub><sup>MSOT</sup> was calculated in each pixel for air and oxygen breathing periods. Per pixel, the amplitude of response to the oxygen gas  $\Delta\text{sO}_2^{\text{MSOT}} = \text{sO}_2^{\text{MSOT}}(\text{O}_2) - \text{sO}_2^{\text{MSOT}}(\text{Air})$  was then calculated. Each pixel was classified as *responding* to the oxygen challenge if  $\Delta\text{sO}_2^{\text{MSOT}}$  exceeded  $2 \times \text{SD}_{\text{OE}}$  where  $\text{SD}_{\text{OE}}$  denotes the standard deviation of the sO<sub>2</sub><sup>MSOT</sup> values between the

individual scans acquired during air breathing. Artefactual negative Hb or HbO<sub>2</sub> pixels were classified as nonresponding. The OE responding fraction was calculated for each tumour as the number of responding pixels divided by the total number of pixels in the tumour ROI.

DCE-OT analysis was performed similarly to the OE-OT data analysis. The amplitude of ICG enhancement,  $\Delta\text{ICG}$ , was quantified as the difference between the average baseline ICG signal and the maximum signal recorded in the first 3 minutes after injection. Each pixel was then classified as enhancing when  $\Delta\text{ICG}$  exceeded  $2 \times \text{SD}_{\text{DCE}}$ , where  $\text{SD}_{\text{DCE}}$  denotes the SD of the individual images acquired before contrast agent injection. As for the OE-OT data, artefactual negative pixels were classified as nonresponding and responding fraction was calculated as the number of responding pixels divided by the total number of pixels in the tumour ROI.

#### 6.2.7.2 Mesoscopic photoacoustic imaging analysis

To extract morphological features of mesoscopic data, the existing analysis pipeline<sup>478</sup> used in Chapter 5 was followed. After skeletonization, structural and topological data analysis (STA) of the vascular networks was performed using previously reported software that applies a central method of STA, persistent homology, to calculate the topological invariants of the data at different scales by studying filtrations of simplicial complexes<sup>515</sup>. The vascular metrics extracted include statistical descriptors: vessel diameters and lengths, vessel tortuosity (sum-of-angles measure, SOAM=the average change in angle per unit length); and network topology descriptors: the number of connected components (Betti number  $\beta_0$ , the number of vascular subnetworks), edges and nodes. For the mesoscopic time series data, co-registration was performed to investigate perfusion fluctuations in the vessels. Images were down sampled to quasi-isotropic voxel resolution (FOV, 300×300×300; resolution, 20×20×10 microns cube) to accelerate the convergence of the evolutionary optimizer, enabling more uniform weighting of intensities in each 3D direction during co-registration. Using a built-in MATLAB function (*imregtform* - ‘multimodal’ setting) an affine co-registration method was applied to co-register the 3D-data time series (Figure 6.3). The first image within the time series served as the reference image in the co-registration procedure. The co-registration method intended to remove major movement shifts in the time series data. A perfect overlap of the images is not expected as perfusion changes will naturally lead to dis-/re-appearance of vessels, and minor physiological tissue deformations can occur over time.

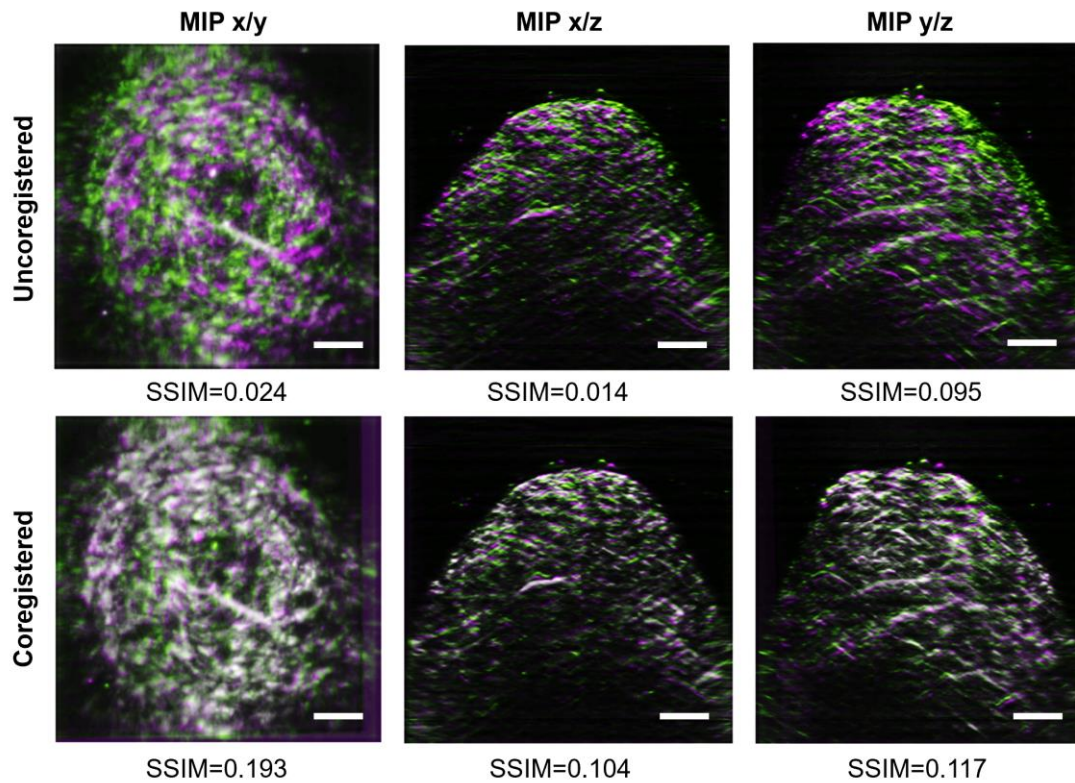


**Figure 6.3: 3D coregistration of mesoscopic PAI time series data.**

Representative uncoregistered (top) and coregistered (bottom) 3D RSOM image cubes displayed as maximum intensity projections (MIP) in x/y (left), x/z (middle), and y/z (right) direction. Coregistration of the first and last 3D image in the RSOM time series is displayed. Grey areas correspond to areas that have similar intensities, while magenta and green areas indicate locations where signal intensities differ. Similarity is summarized by the structural similarity index measure (SSIM), an image quality metric that assesses the visual impact of luminance, contrast, and structure. The range of SSIM values extends between 0 and 1, where a value of 1 indicates absolute equivalence of two images. Scale bar=1 mm.

### 6.2.8 Statistical analysis

Statistical analysis was performed using GraphPad Prism v.9. Each tumour was considered as an independent biological replicate. To compare means between the two cell lines, an unpaired two-tailed student's t-test was performed unless the data violated the assumption of a Gaussian distribution, in which case a Mann-Whitney test was conducted. To compare means between different time points a paired two-tailed t-test was conducted. For correlation analysis, the Pearson correlation coefficient was determined. Significance was assigned for p-values <0.05.

## 6.3 Results

### 6.3.1 MDA-MB-231 shows more aggressive tumour growth than MCF7

In line with the observations of other studies<sup>169</sup>, the MDA-MB-231 tumour model displayed a more aggressive, faster growth phenotype compared to the MCF7 model. On average the MDA-MB-231 model reached a tumour volume of 400 mm<sup>3</sup> after 37 days; the MCF7 model required 48 days to reach the same size (Figure 6.4).

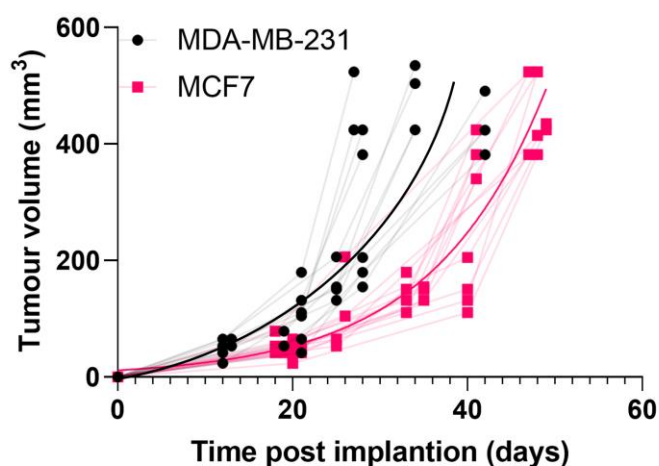


**Figure 6.4: Growth curves of MCF7 (n=14, pink) and MDA-MB-231 (n=12, black) tumours.** Each line represents one tumour (biological replicate) measured at multiple time points (data points).

### 6.3.2 Photoacoustic tomography reveals differences in oxygen availability and distribution between both models

First, macroscopic photoacoustic tomography was used to assess differences in static haemoglobin-related biomarkers between the MCF7 and MDA-MB-231 tumour model. Along tumour growth, a significant decrease in blood oxygenation, as measured by  $sO_2^{MSOT}$  was observed (Figure 6.5A,  $p_{MCF7}=0.0287$ ,  $p_{MDA}=0.0143$ ). Pooling data across all time points, the MDA-MB-231 model was found to be less well oxygenated than the MCF7 model (Figure 6.5B,  $p<0.0001$ ). The decrease in  $sO_2^{MSOT}$  as a function of tumour growth was accompanied by a significant increase in the spatial heterogeneity of the oxygen distribution in both models (Figure 6.5C,  $p_{MCF7}=0.0011$ ,  $p_{MDA}=0.0480$ ). Spatial heterogeneity of oxygen distribution was globally more pronounced in MDA-MB-231 compared with in MCF7 (Figure 6.5D  $p<0.0001$ ). For  $THb^{MSOT}$ , a surrogate marker of perfusion, a significant decrease with tumour growth could be determined in the MCF7 model ( $p_{MCF7}=0.0073$ ), and although a similar trend was observed in the MDA-MB-321 model it was not quite significant (Figure 6.5E,  $p_{MDA}=0.0698$ ). Overall, no significant difference in  $THb^{MSOT}$  could be observed between the models (Figure 6.5F,  $p=0.4823$ ). The spatial variation of  $THb^{MSOT}$  was not affected by tumour volume (Figure 6.5G,  $p_{MCF7}=0.6101$ ,  $p_{MDA}=0.2918$ ), but was generally higher in MDA-MB-231 (Figure 6.5H,  $p=0.0006$ ).

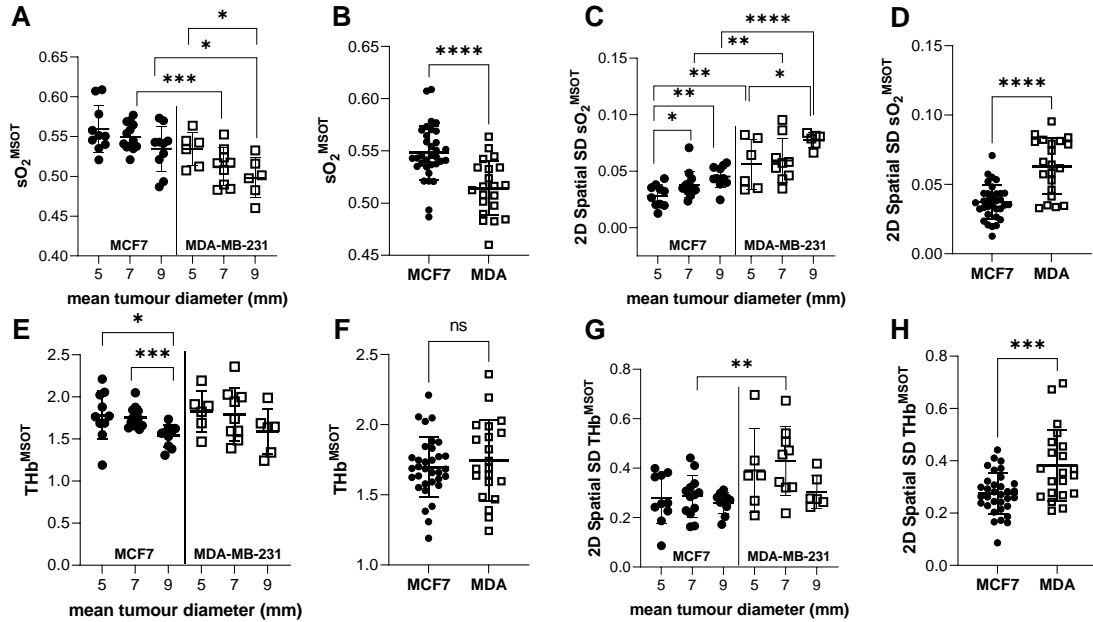


**Figure 6.5: Photoacoustic tomography reveals poorer oxygenation and greater heterogeneity in oxygenation in MDA-MB-231 tumours compared to MCF7.**

Static hypoxia and perfusion parameter of MCF7 (black circle) and MDA-MB-231 (white square) tumours at three different time points: mean tumour diameter 5 mm ( $n_{\text{MCF7}}=10$ ,  $n_{\text{MDA}}=6$ ), mean tumour diameter 7 mm ( $n_{\text{MCF7}}=13$ ,  $n_{\text{MDA}}=9$ ), mean tumour diameter 9 mm ( $n_{\text{MCF7}}=10$ ,  $n_{\text{MDA}}=6$ ). Individual values over time and summarizing comparison between the tumour types for photoacoustically measured oxygen saturation ( $s\text{O}_2^{\text{MSOT}}$ , A,B), 2D spatial standard deviation in oxygen distribution (2D spatial SD  $s\text{O}_2^{\text{MSOT}}$  C,D), total haemoglobin ( $\text{THb}^{\text{MSOT}}$  E,F), and 2D spatial standard deviation in total haemoglobin (2D spatial SD  $\text{THb}^{\text{MSOT}}$  G,H). Data expressed as mean  $\pm$  SD, \* $p < 0.05$ , \*\* $p < 0.01$ , \*\*\* $p < 0.001$ , \*\*\*\* $p < 0.001$  by unpaired two-tailed t-test.

### 6.3.3 MDA-MB-231 tumours show higher variability in oxygenation than MCF7 tumours

After assessing static PAI biomarkers, dynamic oxygenation variability was investigated. As data for the smallest tumour size was compromised by pronounced movement artefacts, oxygen variability analysis was only conducted on medium and large tumour volumes. Both models were characterised by significantly higher variability in  $s\text{O}_2^{\text{MSOT}}$  in the tumour region compared to the reference region (spinal tissue,  $p_{\text{MCF7}}=0.0004$ ,  $p_{\text{MDA}}=0.0004$ , Figure 6.6A,B). Pooled over both time points, a higher COV in  $s\text{O}_2^{\text{MSOT}}$  over time was found in MDA-MB-231 compared to MCF7 (Figure 6.6D,  $p=0.0034$ ), with no significant changes over tumour growth (Figure 6.6C,  $p_{\text{MCF7}}=0.8682$ ,  $p_{\text{MDA}}=0.8693$ ). Following previous analysis pipelines<sup>99,113,511</sup>, the tumour region was separated into high- and low fluctuating fraction, revealing a higher fluctuating fraction in MDA-MB-231 (Figure 6.6E,F,  $p=0.0001$ ) with no significant changes longitudinally (Figure 6.6E,  $p_{\text{MCF7}}=0.6636$ ,  $p_{\text{MDA}}=0.7486$ ). The general mean cycling fractions  $cf$  were found to be  $cf=19.7 \pm 17.6\%$  and  $cf=50.1 \pm 21.2\%$  for MCF7 and MDA-MB-231, respectively, resembling fractions of 17% to 59% as previously reported for PAI<sup>113</sup>, 13% to 52% reported for  $^{18}\text{F}$ -miso PET<sup>103</sup> and  $21 \pm 6\%$  to  $41 \pm 3\%$  measured by EPRI<sup>516</sup>. To further characterise the

variation in oxygen fluctuation, the frequency spectra of the longitudinal  $sO_2^{MSOT}$  data were explored (Figure 6.6G,H). For medium and large tumours (7 mm and 9 mm), MDA-MB-231 tumours showed higher peak power than MCF7 tumours (Figure 6.6G,H). Peak frequencies could be observed in the range of  $f_{low}=1.8$  cycles (0.0005 Hz) to around  $f_{high}=15.1$  cycles (0.0042 Hz) per hour. Spontaneous fluctuations appeared not to depend on tumour size in our models.

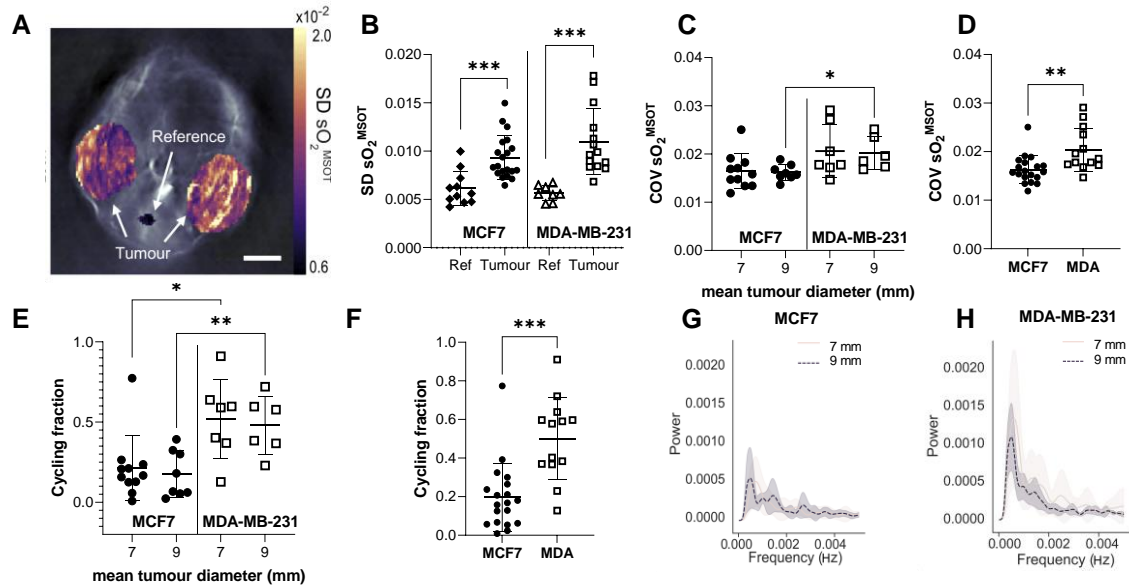


**Figure 6.6: Oxygen variability analysis of the  $sO_2^{MSOT}$  curves in MDA-MB-231 and MCF7 tumour-bearing mice.**

(A) Representative standard deviation map of mouse cross section (MDA-MB-231 tumour). Tumour and reference regions are indicated with white arrows. Scale bar=6 mm. (B)  $sO_2^{MSOT}$  standard deviation compared between reference region (spinal tissue) and tumour. (C-F) Data over time and pooled data for oxygen variability (coefficient of variation=COV  $sO_2^{MSOT}$ ) (C,D) and cycling fraction (E,F). Mean power spectra for MCF7 (G) and MDA-MB-231 (H) at tumours sizes with mean diameter of 7 mm (beige full line) and 9 mm (black dotted line). Shaded area depicts the standard deviation. Mean tumour diameter 7 mm:  $n_{MCF7}=11$ ,  $n_{MDA}=8$ ; mean tumour diameter 9 mm:  $n_{MCF7}=7$ ,  $n_{MDA}=6$ . Data expressed as mean  $\pm$  SD, \* $p < 0.05$ , \*\* $p < 0.01$ , \*\*\* $p < 0.001$  by unpaired two-tailed t-test.

### 6.3.4 OE- and DCE-OT underline differences in vascular functionality and perfusion

To connect underlying differences in vascular perfusion and functionality with measured oxygen variability over time, OE-OT and DCE-OT were performed<sup>171</sup> (Figure 6.7A).

No significant changes in  $\Delta sO_2$  could be detected for both tumour types during tumour growth (Figure 6.7B). Combined over all longitudinal timepoints, a higher  $\Delta sO_2$  was observed for MCF7 tumours (Figure 6.7C,  $p=0.0354$ ), suggesting overall better vascular function in this model. In a subset of mice, DCE-OT was conducted at the final timepoint to assess areas of vascular perfusion. A higher responding fraction could be found for the MCF7 model (Figure 6.7D),  $p=0.0454$  indicating better perfusion than in the MDA-MB-231 tumours (no significant differences between  $\Delta ICG$ ; Figure 6.7E;  $p=0.3899$ ).

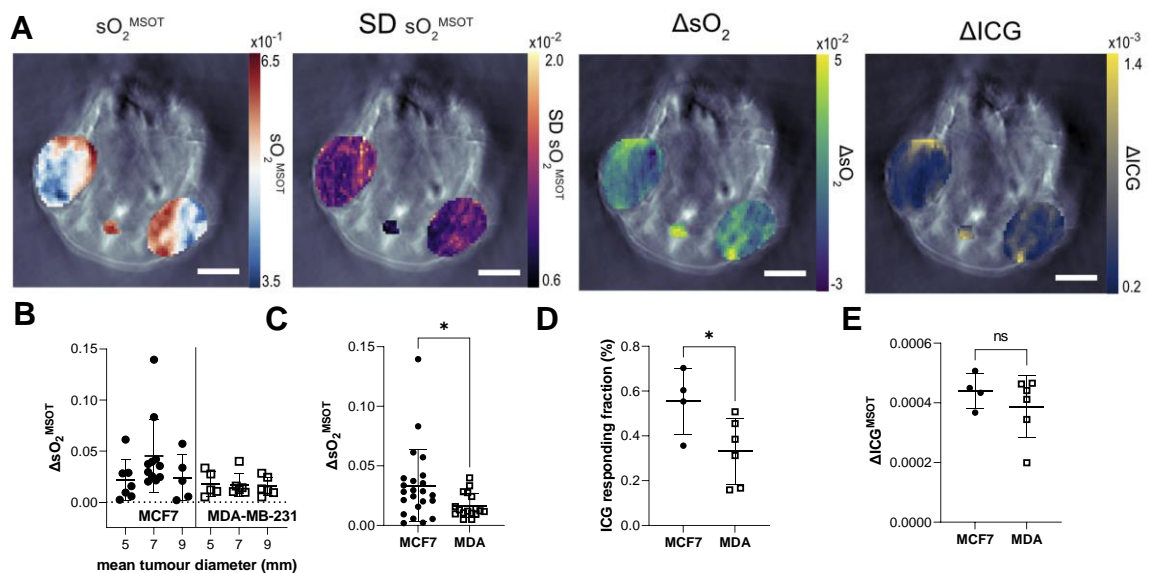


**Figure 6.7: Photoacoustic tomography reveals spatial distribution of oxygen and perfusion dynamics.**

(A) Representative photoacoustic tomography slices highlighting tissue hypoxia (first image,  $sO_2^{MSOT}$ ), fluctuations in oxygenation (second image,  $SD\ sO_2^{MSOT}$ ), vascular functionality (third image,  $\Delta sO_2$ ), and vascular perfusion (fourth image,  $\Delta ICG$ ). Scale bar=7mm. (B)  $\Delta sO_2$  data over different tumour volumes in MCF7 (black circle) and MDA-MB-231 (white square). (C)  $\Delta sO_2$  data pooled over all timepoints. ICG responding fraction (D) and  $\Delta ICG$  (E) for both tumour models are displayed ( $n_{MCF7}=4$ ,  $n_{MDA}=6$ , final longitudinal timepoint). Data displayed as mean  $\pm$  SD, \* $p < 0.05$ , \*\* $p < 0.01$  by unpaired two-tailed t-test.

### 6.3.5 Photoacoustic mesoscopy reveals morphological changes along tumour growth

Using photoacoustic mesoscopy, differences in vascular morphology between the two tumour models were investigated to provide further insight into the mechanisms that underly the hypoxia and perfusion dynamics seen in the tomographic biomarkers. Using our STA pipeline, vascular network descriptors were compared between the two cell lines along tumour growth (Figure 6.8). MDA-MB-231 tumours were characterised by vessels with significantly smaller diameter (Figure 6.9A,B,  $p=0.0004$ ). Notably, the vessels also appeared to be shorter in lengths, albeit not quite significant (Figure 6.9C,D,  $p=0.0571$ ). Interestingly, the vessel length significantly decreased for the MCF7 tumours with increasing tumour volume (Figure 6.9C,  $p=0.0074$ ), whilst the MDA-MB-231 was characterised by short vessels at small and large tumour volumes. MDA-MB-231 tumours also featured a higher number of vascular subnetworks (connected components) than MCF7 tumours (Figure 6.9E,F,  $p=0.0176$ ). Again, the number of subnetworks increased for the MCF7 tumours with increasing tumour volume, whilst a high number of subnetworks was already found for MDA-MB-231 tumours at the earlier timepoint (Figure 6.9F,  $p=0.0149$ ). 3D vascular tortuosity, as captured by the sum-of-angles measure, increased for both tumour models with increasing tumour volume (Figure 6.9G,H,  $p_{\text{MCF7}}=0.0010$ ,  $p_{\text{MDA}}=0.0310$ ). Notably, a significant correlation was found between the MSOT cycling fraction and the number of nodes (Pearson  $r=0.63$ ,  $p=0.0148$ ), edges (Pearson  $r=0.59$ ,  $p=0.0272$ ) and vessel lengths (Pearson  $r=-0.59$ ,  $p=0.0271$ ), and also between the temporal  $\text{COV}_{\text{MSOT}}$  and the number of nodes (Pearson  $r=0.66$ ,  $p=0.0271$ ) and edges (Pearson  $r=0.68$ ,  $p=0.0271$ ), indicating higher variation in denser vascular networks with smaller vessel sizes.

Taken together, these results point towards a more immature vascular phenotype in the MDA-MB-231 model with a denser vascular network structure, and potentially an earlier onset of tumour angiogenesis.

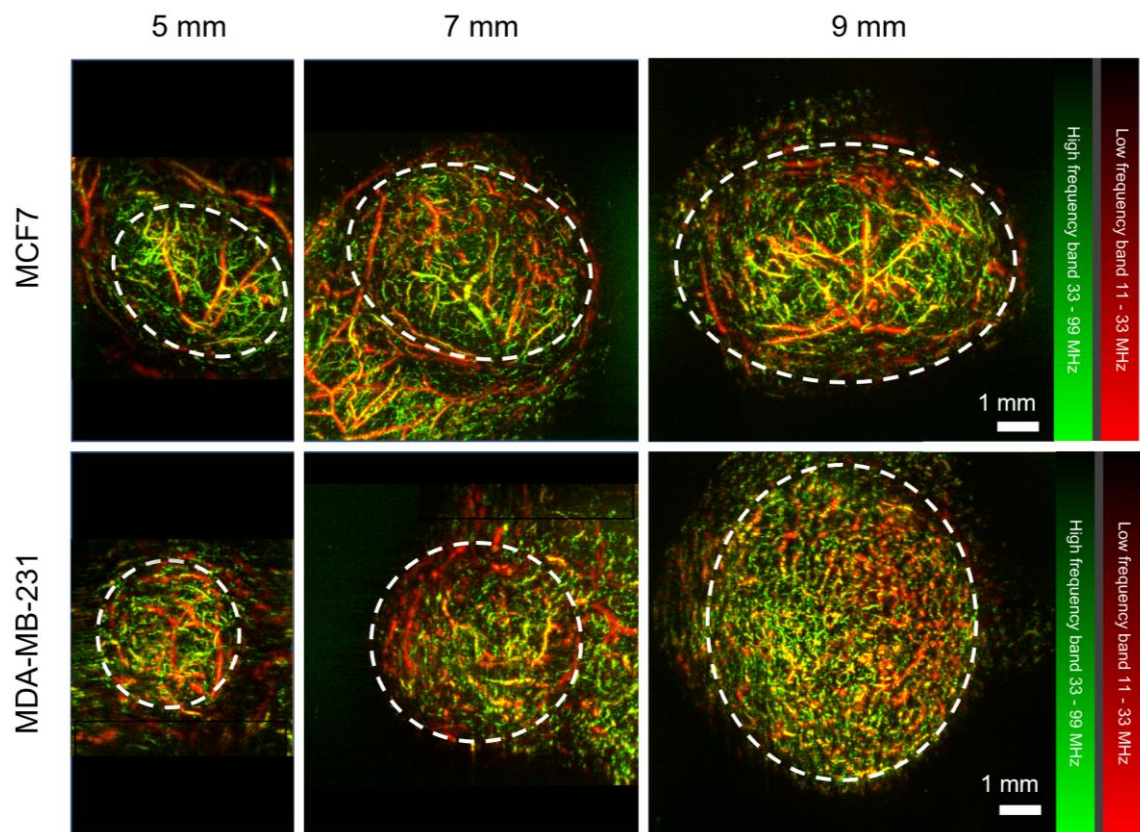


**Figure 6.8: Photoacoustic mesoscopy reveals development of distinct vascular phenotypes over time.** X/Y MIPs of MCF7 (top) and MDA-MB-231 (bottom) tumours at small (left, mean diameter (m.d.)=5 mm), medium (middle, m.d.=7 mm) and large (right, m.d.=9 mm) tumour volume. Larger vessels (11–33 MHz) are indicated in red and smaller vessels (33–99 MHz) are indicated in green; merge/overlap of high- and low-frequency signals is indicated in yellow.

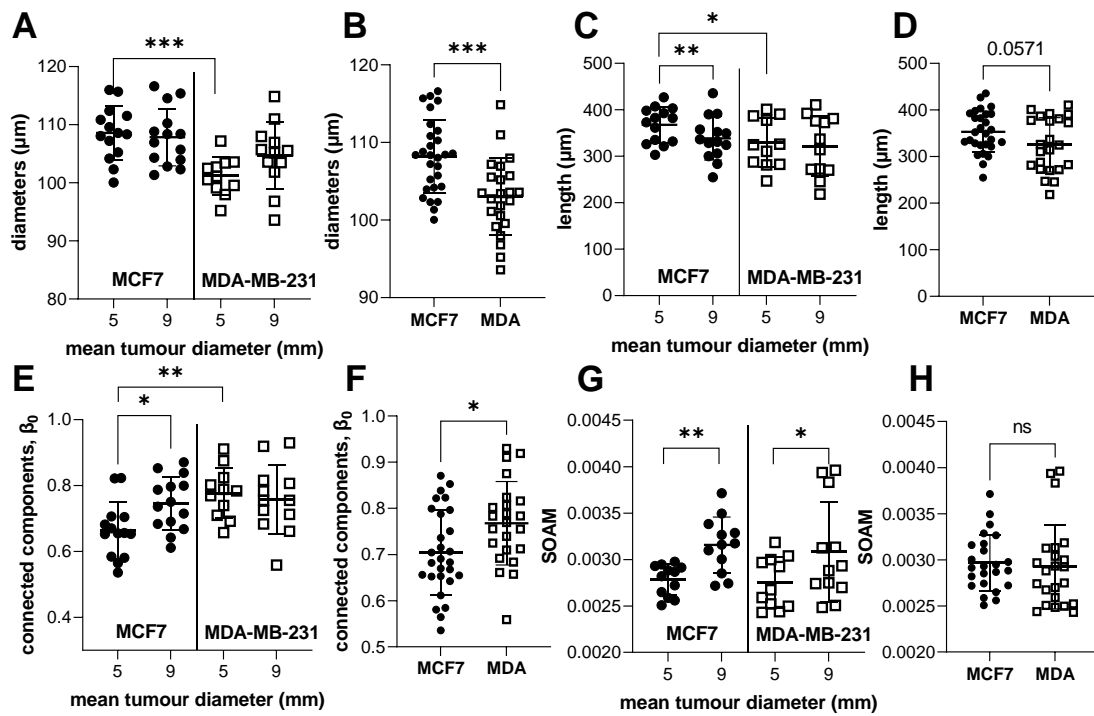


**Figure 6.9: Vascular morphology metrics of MCF7 and MDA-MB-231 tumours investigated longitudinally during tumour growth.**

Vascular network metrics are displayed for MCF7 (black dots) and MDA-MB-231 (white squares) tumours of a mean diameter of 5 mm ( $n_{\text{MCF7}}=14$ ,  $n_{\text{MDA}}=12$ ) and 9 mm ( $n_{\text{MCF7}}=14$ ,  $n_{\text{MDA}}=12$ ) individually, and pooled for both tumour volumes: vessel diameter (A,B), length (E,F), connected components (E,F), and sum-of angles measure (SOAM, G,H). Data displayed as mean  $\pm$  SD, Significance (\* $p < 0.05$ , \*\* $p < 0.01$ , \*\*\* $p < 0.001$ ) assigned between different time points by paired two-tailed t-test, and between different models by unpaired two-tailed t-test.

### 6.3.6 Photoacoustic mesoscopy reveals differences in perfusion

After assessing static differences between the models during tumour growth, dynamic differences in perfusion were investigated using the sequential photoacoustic mesoscopy data. Variations in perfusion can impact the measured signal intensities in vessels, and could potentially lead to their full disappearance in the photoacoustic images if perfusion is insufficient or lacking. Thus, increased heterogeneity in perfusion may be reflected by a higher variation in STA metrics over time. To test this hypothesis, COVs of STA metrics at small (mean diameter 5 mm) and large (mean diameter 9 mm) tumour volumes were compared. Indeed, a significantly higher variation in the number of nodes (Figure 6.10A,  $p=0.0281$ ) and edges (Figure 6.10B,  $p=0.0205$ ) of the vessel network, as well as in the average vessel length (Figure 6.10C,  $p=0.0109$ ) and sum-of-angles metric (Figure 6.10D,  $p=0.0039$ ) could be observed for the MDA-MB-231 model at the earlier longitudinal time point. No significant changes could be seen for the later longitudinal imaging time point. Interestingly, the two models displayed different dynamics during tumour growth: whilst the MCF7 model showed increased heterogeneity in perfusion with growing tumour size (as assessed by increased variability in number of nodes [Figure

6.10A,  $p=0.0384$ ] and sum-of-angles measure [Figure 6.10D,  $p=0.0384$ ]), the MDA-MB-231 model showed higher variability in vessel lengths at the earlier longitudinal time point (Figure 6.10C,  $p=0.0259$ ). Visual inspection of the images revealed constant perfusion in larger vessels, whilst perfusion appeared to be more variable in smaller vessels in both models (Figure 6.11).

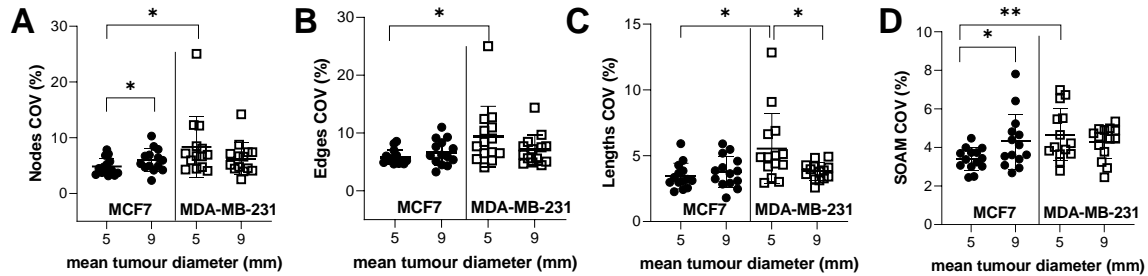


**Figure 6.10: Variation of vascular morphology metrics in MDA-MB-231 and MCF7 tumours.**

Coefficient of variations (COV) of vascular morphology metrics during sequential mesoscopic PAI over a time span of 30 minutes for MCF7 ( $n_{MCF7}=14$ ) and MDA-MB-231 ( $n_{MDA}=12$ ) tumours (mean diameter 5 and 9 mm): number of nodes (A), edges (B), lengths (C) and sum-of-angles measure (SOAM, D). Data displayed as mean  $\pm$  SD, significance assigned between different tumour models by unpaired two-tailed t-test, and between different time points by paired two-tailed t-test.

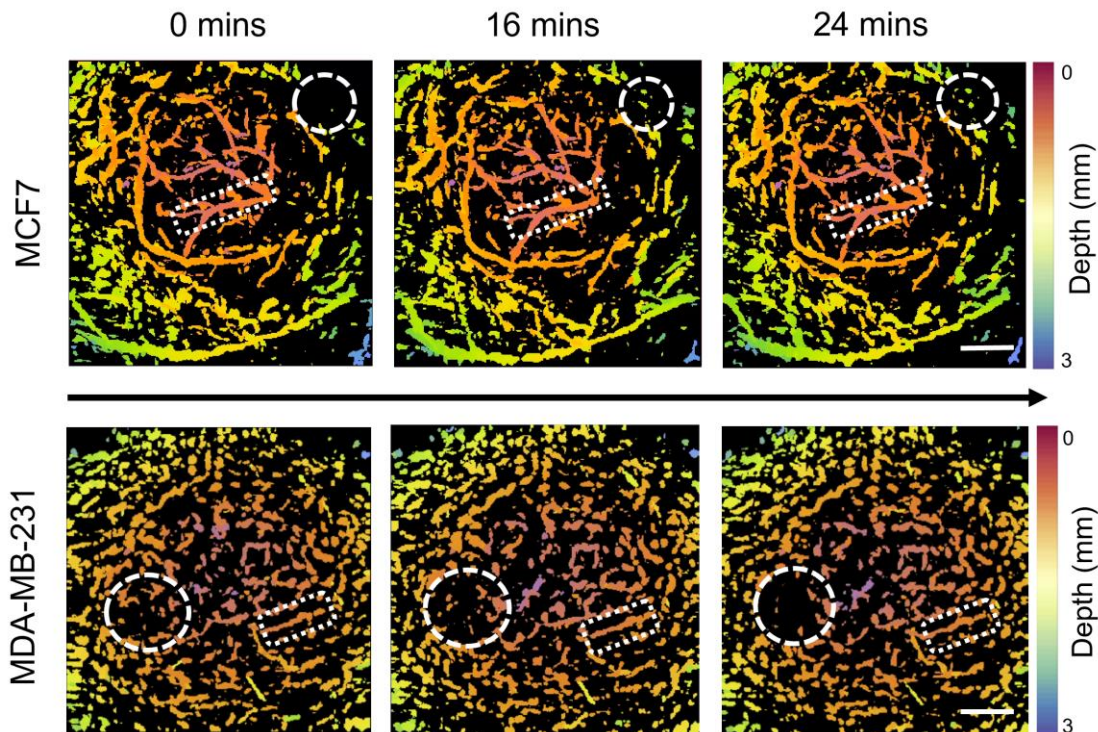


**Figure 6.11: MDA-MB-231 and MCF7 display variation in perfusion over time.**

(A) Representative mesoscopic segmentation masks (depth-encoded) at different timepoints of MCF7 (top row) and MDA-MB-231 (bottom row). Variations in perfusion accumulate in smaller vessels (dashed line) and are less pronounced in larger, mature vessels (dotted line). Scale bar=1 mm.

### 6.3.7 Immunohistochemistry analysis supports the finding of a less mature, more hypoxic vascular phenotype in MDA-MB-231

For validation of the PAI biomarkers, the underlying tumour tissue structure was investigated using IHC at the final longitudinal time point. In line with the PAI  $sO_2^{MSOT}$  results, MDA-MB-231 tumours showed a higher hypoxic fraction as assessed with both nuclear HIF-1 $\alpha$  (Figure 6.12A,C,  $p=0.0322$ ) and CAIX (Figure 6.12A,B,  $p=0.0055$ ), a downstream target of HIF-1). A higher necrotic fraction was found in MDA-MB-231 ( $p=0.0031$ , Figure 6.12D), reflecting its more aggressive tumour growth. In line with previous reports<sup>169,517</sup>, the MDA-MB-231 model was characterised by a higher vessel density ( $p < 0.0001$ , Figure 6.13B), but these vessels were found to be less mature than MCF7 vasculature when analysing the pericyte coverage as assessed with ASMA ( $p=0.0285$ , Figure 6.13C). Interestingly, the non-cycling fraction appeared to map to necrotic regions on qualitative observation (Figure 6.14). For PAI biomarkers of perfusion-limited hypoxia, significant correlations (Table 6.3) could be found between MSOT cycling fraction and spatial  $SD^{MSOT}$  with vessel density (CD31), hypoxia (CAIX) and necrotic fraction (H&E). Temporal  $SD^{MSOT}$  was also found to correlate with necrotic fraction and hypoxia (CAIX) (Table 6.3, approaching significance for vessel density (CD31):  $r=0.50$ ,  $p=0.0672$ ). These results indicate higher variability in oxygenation in more angiogenic areas with poor vascular functionality.

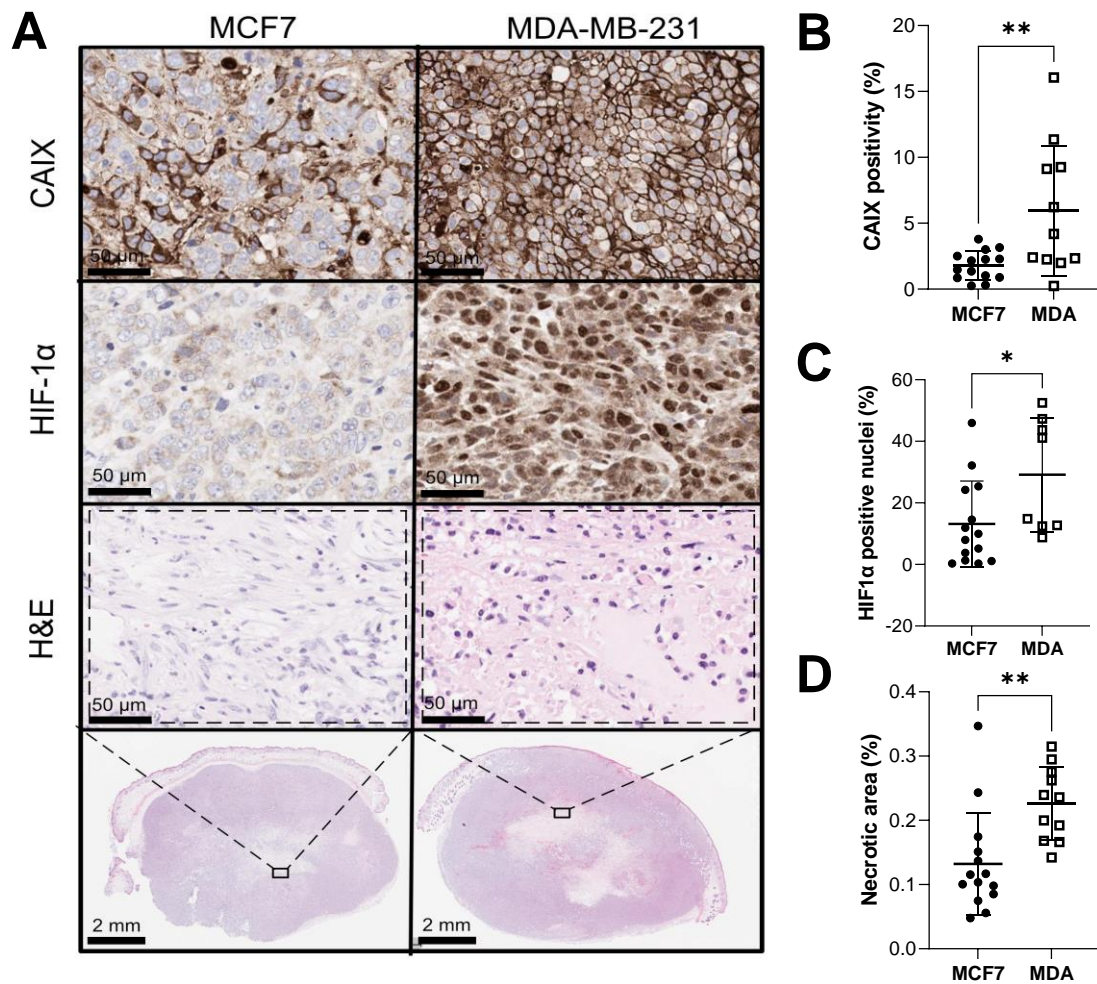


**Figure 6.12: MDA-MB-231 are characterised by higher hypoxia and necrosis at the final time point.**

(A) Representative CAIX (first row, brown staining at plasma membrane), HIF1- $\alpha$  (second row, brown staining at nucleus) and H&E (third and fourth row) of MCF7 (black dots) and MDA-MB-231 model (white squares). Quantified CAIX (B) and HIF-1  $\alpha$  positivity (C) of MCF7 and MDA-MB-231 model are displayed. (D) Percentage necrotic area quantified from H&E sections of MCF7 and MDA-MB-231 model are shown. Data expressed as mean  $\pm$  SD, \* $p < 0.05$ , \*\* $p < 0.01$  by unpaired two-tailed t-test.  $n_{\text{MCF7}}=14$ ,  $n_{\text{MDA}}=11$ .

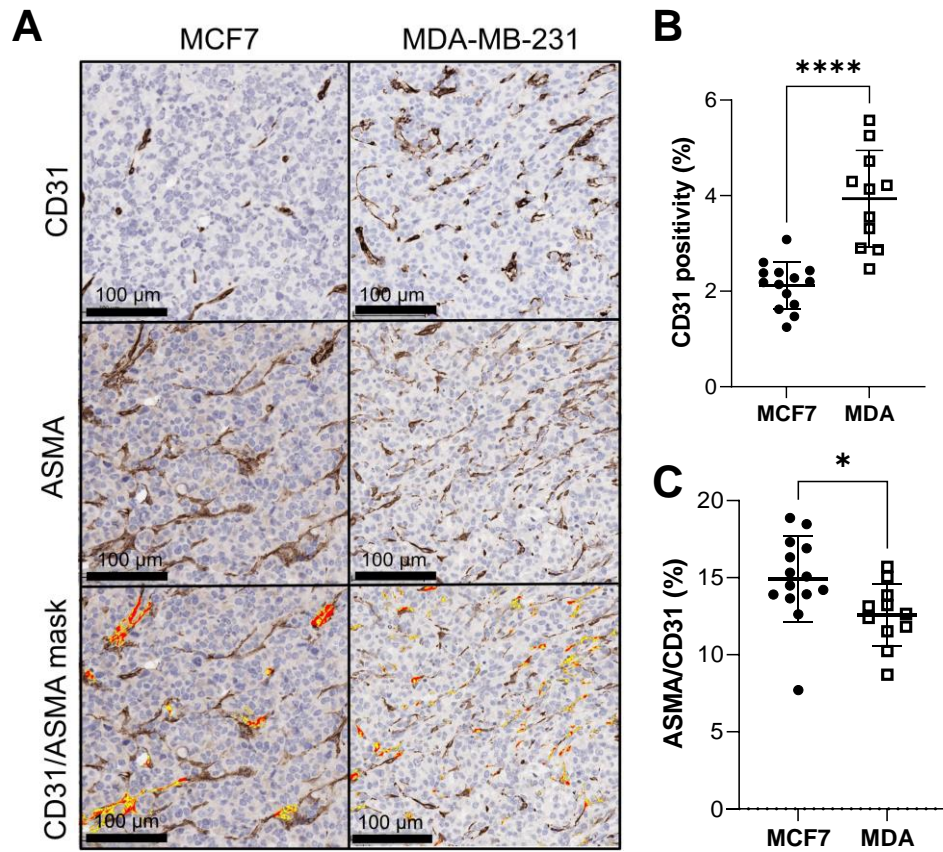


**Figure 6.13: MDA-MB-231 show higher vessel density with lower maturity at the final time point.**

(A) Representative IHC images of CD31 (top), ASMA (middle) and CD31/ASMA mask (bottom). Brown staining indicates positive expression of marker. In the CD31/ASMA overlay, red indicates areas where CD31 and ASMA are colocalised (ASMA vessel coverage) and yellow indicates areas where CD31 is alone. (B) CD31 staining area quantified from CD31 IHC sections and normalised to tumour area for MCF7 (black dots) and MDA-MB-231 model (white squares). (C) ASMA vessel coverage of CD31+ vessels on ASMA IHC sections shown for both models, respectively. Data expressed as mean  $\pm$  SD, \* $p < 0.05$ , \*\* $p < 0.01$  by unpaired two-tailed t-test.  $n_{MCF7}=14$ ,  $n_{MDA}=11$ .

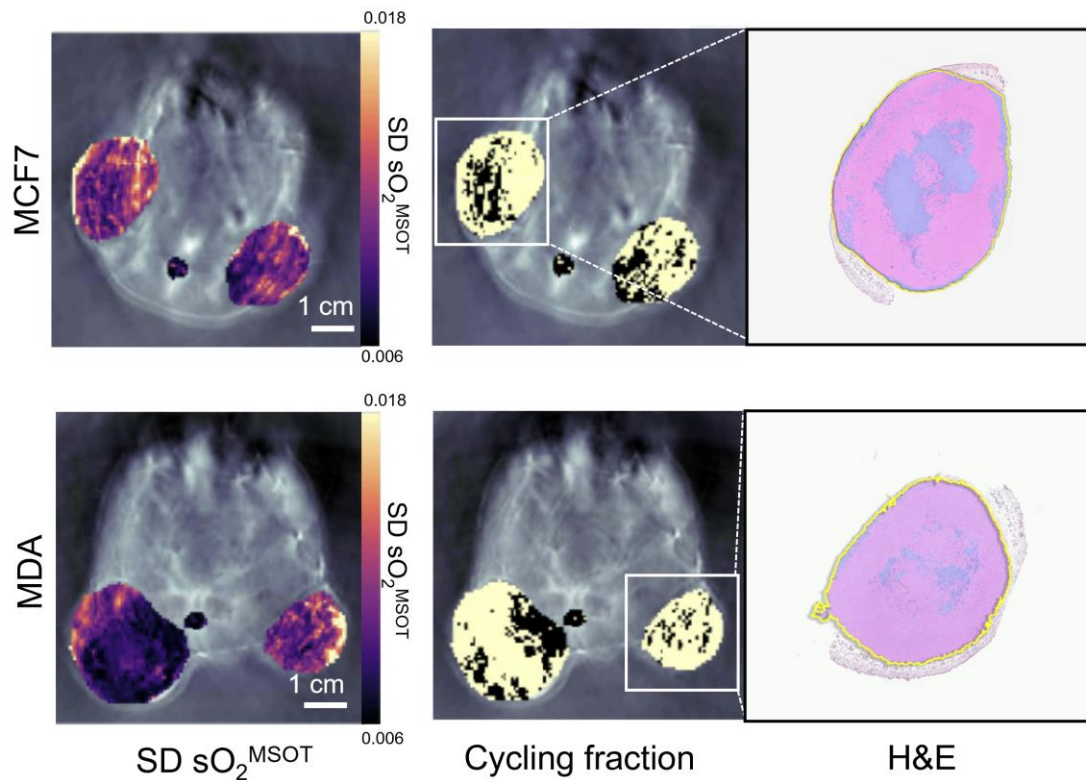


**Figure 6.14: Non-cycling fractions qualitatively appear to map to necrotic regions.**

Representative photoacoustic MCF7 (top) and MDA-MB-231 (bottom) tumour cross sections showing SD  $sO_2^{MSOT}$  map (left), cycling fractions (middle, black=non-varying, beige=varying) and thresholded H&E maps (right) highlighting necrotic (dark purple) and non-necrotic (pink) regions.

**Table 6.3: Correlation between perfusion-limited hypoxia PAI biomarkers and IHC markers.**

SD=standard deviation, n.s.=not significant.

	MSOT Cycling fraction		Temporal SD <sup>MSOT</sup>		Spatial SD <sup>MSOT</sup>	
	Pearson r	p-value	Pearson r	p-value	Pearson r	p-value
CD31	0.71	0.0042**	0.50	0.0672 (n.s.)	0.77	0.0005***
H&E	0.58	0.0305*	0.69	0.0063**	0.74	0.0011**
CAIX	0.82	0.0003***	0.57	0.0319*	0.72	0.0018**

### 6.3.8 Gene expression supports a more hypoxic, angiogenic phenotype of MDA-MB-231

To further explore the underlying mechanisms that cause the variations in hypoxia and perfusion, the gene expression of both models was analysed. Initial exploration of the RNA sequencing data using PCA showed distinct transcriptomes between MCF7 and MDA-MB-231 (PC1: 74.36% variance, PC2: 7.06% variance), with MCF7 clustering more closely together than MDA-MB-231 (Figure 6.15A). Differences in angiogenesis- and hypoxia-related gene expression were assessed to explore whether differences in transcriptomes supported PAI and IHC observations. Using GSEA and GSVA, highly significant differences could be found between the models in hypoxia (Figure 6.15B,C, Figure 6.16) and angiogenesis-related gene expression (Figure 6.15D,E, Figure 6.17) with higher enrichment in the

MDA-MB-231 model (p values indicated in Figure 6.15) . MDA-MB-231 also displayed significantly higher expression in apoptosis-related gene expression than MCF7 (GSVA:  $p < 0.0001$ , not plotted). Notably, the GSVA scores correlated with histopathological markers. A positive correlation could be found between the hypoxia gene signature and hypoxia markers CAIX ( $r=0.53$ ,  $p=0.0087$ ) and HIF-1 $\alpha$  ( $r=0.53$ ,  $p=0.0172$ ), between the angiogenesis gene signature and CD31 ( $r=0.64$ ,  $p=0.001$ ), and between the apoptosis gene signature and the necrotic fraction as evaluated via H&E ( $r=0.53$ ,  $p=0.0104$ ), thereby providing confidence in the transcriptomic data.

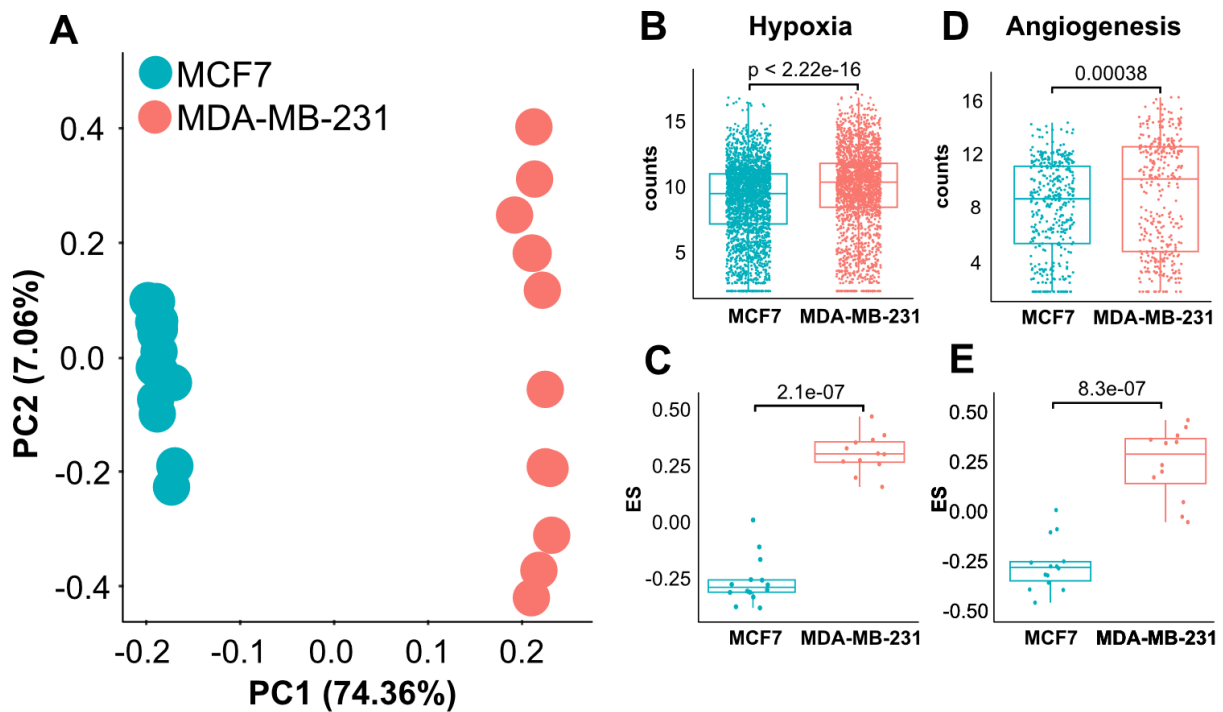


**Figure 6.15: MDA-MB-231 and MCF7 display significant differences in hypoxia and angiogenesis-related gene expression.**

(A) PCA displays distinct transcriptomes between MCF7 (blue) and MDA-MB-231 (red;  $n_{\text{MCF7}}=14$ ,  $n_{\text{MDA}}=12$ ). GSEA (B) and GSVA (C) analysis of hypoxia gene signature. GSEA (D) and GSVA (E) analysis of angiogenesis gene signature (ES=enrichment score). Boxes between 25th and 75th percentiles; line at median. Significance assigned unpaired two-tailed t-test (p-values shown in figure).

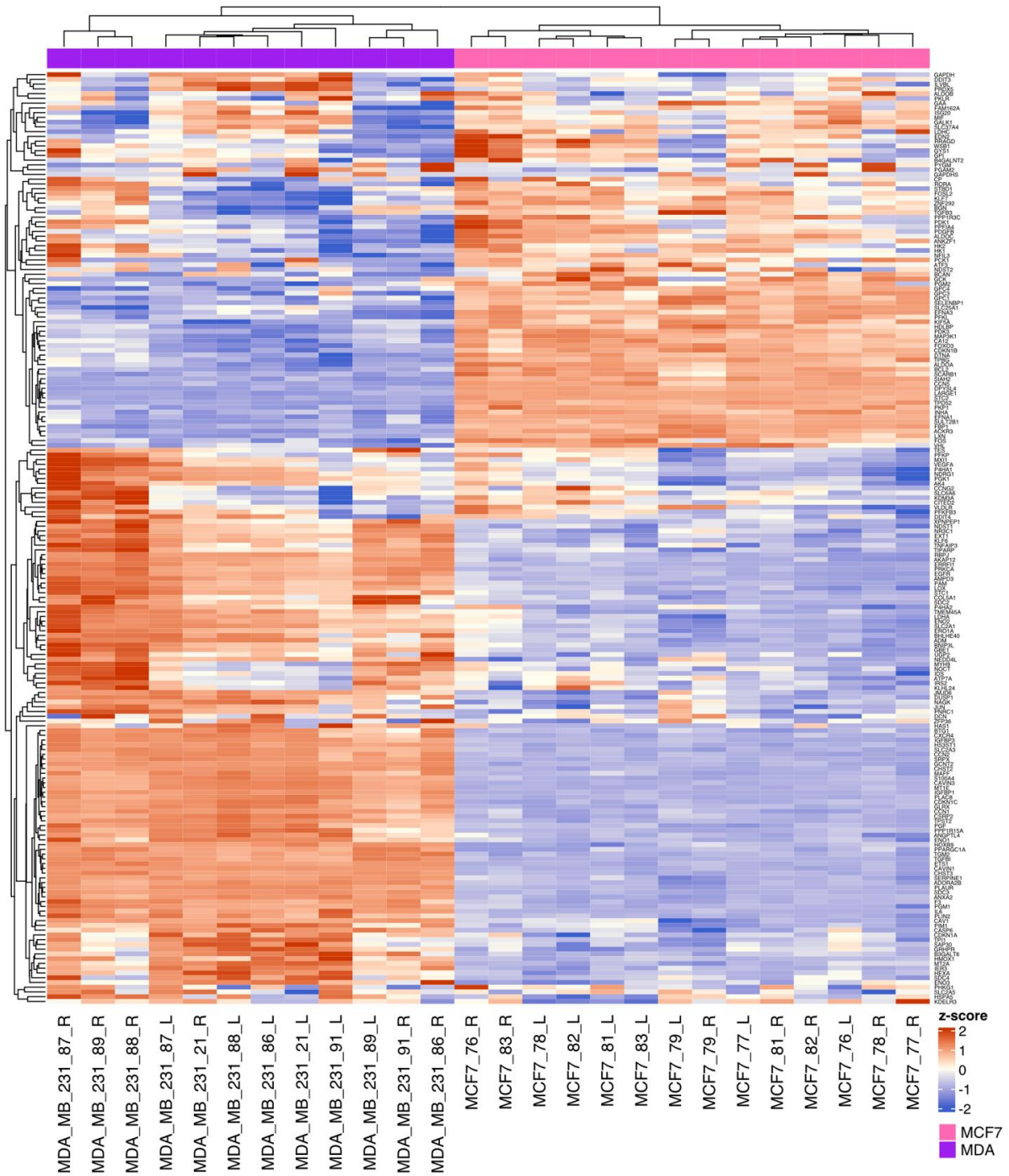


**Figure 6.16: Heatmap displaying relative expression of 196 genes in a hypoxia gene signature in MCF7 and MDA-MB-231 tumours.**

Each row denotes a gene in the signature, labelled on the right-hand side. Each column corresponds to one sample of either MCF7 (pink) or MDA-MB-231 (purple) tumours. The strength of expression (displayed as relative z-scores with red to blue colour coding) decreases from left to right in the heatmap.  $n_{\text{MCF7}}=14$ ,  $n_{\text{MDA}}=12$ .

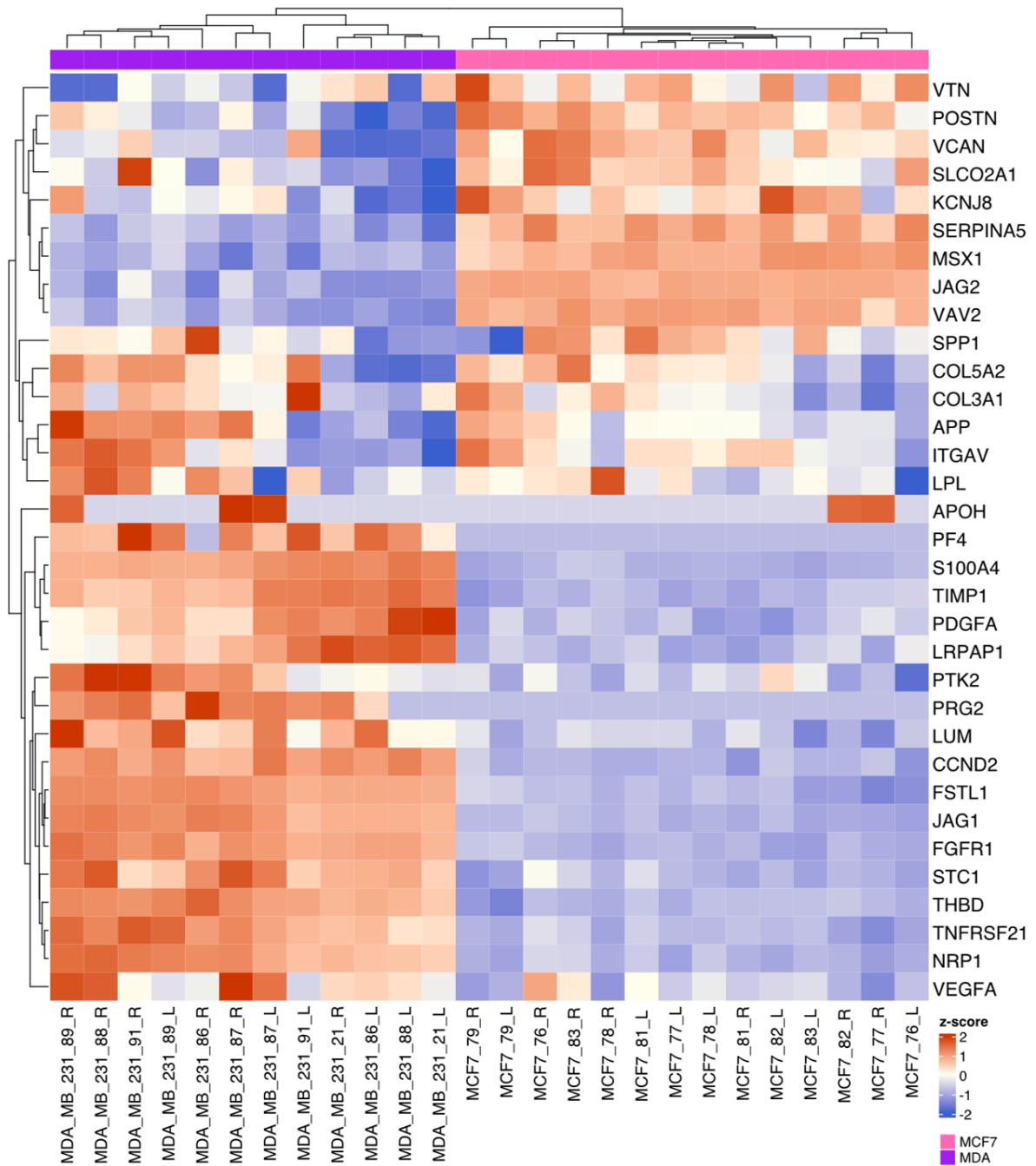


**Figure 6.17: Heatmap displaying relative expression of 33 genes in an angiogenesis gene signature in MCF7 and MDA-MB-231 tumours.**

Each row denotes a gene in the signature, labelled on the right-hand side. Each column corresponds to one sample of either MCF7 (pink) or MDA-MB-231 (purple) tumours. The strength of expression (displayed as relative z-scores with red to blue colour coding) decreases from left to right in the heatmap.  $n_{MCF7}=14$ ,  $n_{MDA}=12$ .

### 6.3.9 Histopathological and photoacoustic biomarkers correlate with underlying genetic phenotype

After assessing general differences in gene expression between the two models, and confirming correspondence to IHC markers, the correlation between the photoacoustic biomarkers and the underlying gene expression was analysed (Table 6.4). Tomographic perfusion-limited hypoxia biomarkers from the dynamic measurements (MSOT cycling fraction, temporal SD, and 2D spatial SD) were found to be positively correlated to the three gene signatures, suggesting higher oxygenation variability in hypoxic, angiogenic and apoptotic tumour environments. Notably, a particularly strong relationship was found between apoptosis GSVA scores and spatial SD<sup>MSOT</sup> ( $p < 0.0001$ ).  $sO_2^{MSOT}$  values were negatively correlated to the three gene signatures, confirming a more viable, normalized environment in better oxygenated tumours. For the mesoscopic PAI data, the mean average vessel diameter was found to be negatively correlated with all three GSVA scores, indicating a relationship between thinner, less mature vessels and more hypoxic, angiogenic and apoptotic tumours. The number of nodes and edges were found to be positively correlated with all three GSVA scores, pointing towards a correspondence between higher vessel density and higher hypoxia, angiogenesis, and cell death.

**Table 6.4: Correlation between perfusion-limited hypoxia PAI biomarkers and GSVA scores.**

Pearson r and respective p-value are displayed for each parameter. SD=standard deviation, n.s.=not significant. Colours correspond to p-values: red: p=n.s., light green: \*p < 0.05, green: \*\*p < 0.01, dark green: \*\*\*p < 0.001.

Modality		GSVA Hypoxia	GSVA Angiogenesis	GSVA Apoptosis
Tomography	$sO_2^{MSOT}$	r=-0.58 p=0.0187*	r=-0.50 p=0.0497*	r=-0.61 p=0.0217*
	MSOT Cycling fraction	r=0.47 p=0.0913 (n.s.)	r=0.46 p=0.0973 (n.s.)	r=0.68 p=0.0143*
	Temporal SD <sup>MSOT</sup>	r=0.50 p=0.0698 (n.s.)	r=0.55 p=0.0396*	r=0.61 p=0.0362*
	2D Spatial SD <sup>MSOT</sup>	r=0.56 p=0.0253*	r=0.56 p=0.0245*	r=0.87 p<0.0001****
Mesoscopy	Diameters	r=-0.44 p=0.0285*	r=-0.44 p=0.0288*	r=-0.43 p=0.040*
	Nodes	r=0.42 p=0.0357*	r=0.437248 p=0.0288*	r=0.40 p=0.0558 (n.s.)
	Edges	r=0.48 p=0.0160*	r=0.56 p=0.0038**	r=0.48 p=0.0209*

## 6.4 Discussion

By employing PAI at multiple scales, an initial analysis framework was developed and applied to assess perfusion and hypoxia dynamics in two murine breast cancer xenograft models, and validated by thorough histopathological and transcriptomic analysis. Based on the detailed technical validation performed in the previous chapters, this chapter provides first indications that PAI is sufficiently sensitive to resolve differences related to dynamics in tumour blood supply and oxygenation between different tumour types.

First, macroscopic differences in functional static and dynamic haemoglobin-related biomarkers were compared between the two models using photoacoustic tomography. In line with previous observations<sup>104,133,169,518</sup>,  $sO_2^{MSOT}$  and THb level decreased with increasing tumour size in both models, reflecting development of tumour hypoxia and poorer blood supply during tumour growth<sup>519</sup>. Confirming observations from previous studies on the same tumour models<sup>169</sup>, higher hypoxia was observed in the MDA-MB-231 model, whilst both models displayed similar THb levels. Macroscopic PAI also revealed the development of significantly higher spatial heterogeneity in oxygenation over the imaged tumour cross section, with a more pronounced effect in the MDA-MB-231 than in MCF7. This observation was supported by overall higher spatial variation in THb level in MDA-MB-231, signifying higher heterogeneity in blood content, and resulting oxygen availability in this model. The finding of a more hypoxic, heterogenous tumour phenotype in the MDA-MB-231 model was also supported by an overall lower  $\Delta sO_2$ , and ICG responding fraction, suggesting impaired vessel functionality and perfusion in this model. Notably, our assessment of spatial heterogeneity has been so far limited to a 2D-slice to enable direct comparison to IHC. Since multi-slice tomographic PAI data has also been collected for each tumour, THb and  $sO_2$  heterogeneity analysis could be extended to cover the whole 3D tumour volume in future.

Next, dynamic tumour oxygenation variability was investigated during sequential imaging of the two tumour types. Globally, a higher variability in oxygenation could be found for MDA-MB-231, accompanied with an increased cycling fraction. This underpins the findings of previous studies observing higher oxygenation fluctuations in more aggressive cancer types<sup>1,5,516</sup>. Reassuringly, our cycling fractions were found to be in the range reported in previous work<sup>103,113,516</sup>. The presence of oscillatory behaviour in oxygenation was confirmed by the identification of frequency peaks in the power spectra, with oscillatory periods ( $f_{low}=1.8$  cycles to around  $f_{high}=15.1$  cycles) being in a similar interval to the ones observed in other mouse<sup>99,118,520</sup>, rat<sup>60,62,521</sup>, canine<sup>522</sup>, human xenograft<sup>98,523</sup>, and human<sup>524</sup> tumours. Interestingly, oxygen variability, cycling fractions, and peak power did not increase with growing tumour volumes in our models. Other work has found a dependence of cycling oxygenation fluctuations on tumour size<sup>36,516</sup>; however, these studies were conducted in different tumour models (SCCVII and HT29) at larger tumour volumes ( $>500 \text{ mm}^3$ )<sup>36,516</sup>. Gonçalves et al established an elaborate pipeline based on independent component analysis to distinguish between

systemic and tumour-specific fluctuations in MRI images<sup>115</sup>, finding that tumour-specific fluctuation patterns did not increase with tumour size, whilst systemic fluctuations increased with tumour size. In future work, a similar pipeline could be established for tomographic PAI data to give further insights into the origin of the fluctuation dynamics and their dependence on tumour growth. Future studies would also benefit from the application of a co-registration algorithm to align individual image frames for minimising the impact of motion-related noise. In the current analysis, scans were included only if they were visibly free from motion artefacts, so implementation of this additional processing step would broaden the applicability of the approach since more data sets could be included.

To confirm the relationship of oxygenation heterogeneity with abnormal vascular morphology, mesoscopic PAI was performed to investigate underlying differences in vascular architecture and perfusion between the models. Overall, MDA-MB-231 displayed a more immature vascular phenotype with thinner, shorter vessels, and a denser vessel network structure with a higher number of vascular subnetworks. These observations are in line with IHC and previous studies<sup>169,525</sup>, highlighting higher vessel immaturity and density in the MDA-MB-231 model. To verify the vascular dimensions measured with PAI, vascular diameters could be compared to dimensions of vessel lumens outlined by CD31 in future work. Mesoscopic vessel density descriptors (e.g., number of nodes/edges) and decreasing vessel length were found to correlate with MSOT cycling fraction and temporal COV<sup>MSOT</sup>. This aligns with previous work<sup>91</sup> finding that tumours exposed to cycling hypoxia show enhanced vessel density with an increased number of smaller vessels and decreased interstitial distances. In our dynamic mesoscopic data, significantly smaller variation of the STA metrics over time could be observed in the MCF7 model at the smaller tumour volume, which may indicate less perfusion dynamics and a more normalized vasculature at this earlier longitudinal time point. Further work is required to understand the tumour size- and type-specific perfusion dynamics during tumour evolution. Under visual inspection, perfusion variations in photoacoustic mesoscopy appeared to accumulate in smaller, less mature vessels. For quantification of this observation, perfusion variation in separate vessel sizes should be analysed in future work. Mesoscopic PAI data can be split into different frequency bands (10–33 MHz and 33–90 MHz) allowing for data quantification in discrete vessel sizes (~40–230  $\mu\text{m}$  and 10–40  $\mu\text{m}$  diameter, respectively)<sup>137,526</sup>. Using this feature would help to pinpoint whether variations arise from larger, more mature vessels, or smaller, less mature ones.

Our histopathological analysis confirmed the findings from the PAI biomarkers, revealing higher vessel density and immaturity, and increased necrosis and hypoxia in the more aggressive MDA-MB-231 model. Finding higher oxygenation variability in the model with more immature vasculature is consistent with previous studies, highlighting a connection between pO<sub>2</sub> fluctuations and maturity of the microvascular network<sup>61,104,117</sup>. MDA-MB-231 are known to express higher VEGF levels<sup>527</sup> and are more prone to vascular mimicry formation than MCF7<sup>169,528</sup>, further supporting the results seen in our studies. An initial comparison also revealed that cycling fractions do not seem to occur in necrotic cores

of the tumour, but rather in the periphery. This confirms studies employing MRI<sup>49,100,115</sup>, finding higher cycling fluctuations in the tumour periphery, but not in the centre of tumours where avascular necrotic nodes are located. To better understand the spatial emergence of the fluctuations, a rim-core analysis<sup>113,169</sup> could be performed in future. Both tomographic and mesoscopic images could also be exposed to radiomics pipelines to further uncover specific spatial patterns and characteristics that could help in elucidating perfusion-limited hypoxia in more depth. These pipelines could be used to quantify textural information, and to mathematically extract the spatial distribution of signal intensities and pixel interrelationships, thereby potentially giving clearer insight into the mechanics that underly variability in oxygenation.

Finally, the underlying gene expression of the individual tumours was investigated, uncovering the more angiogenic and hypoxic phenotype of the MDA-MB-231 model, and thereby supporting our previous findings. Reassuringly, correlations between transcriptomic, IHC and PAI markers were clearly established. Interestingly, tomographic perfusion-limited hypoxia markers showed a particularly strong correlation with apoptosis-related gene expression markers, strengthening the observations of previous studies that a direct correspondence of oxygenation variability and regulation of apoptotic pathways exists<sup>529</sup>. Studies in spheroids have shown that apoptosis occurs mainly in peri-necrotic cells<sup>530,531</sup>. For further validation, a cleaved caspase 3 (CC3) and TUNEL (Terminal deoxynucleotidyl transferase dUTP nick end labelling) staining could be used in future to assess apoptotic cell fractions and their spatial distributions using IHC.

The present study has several limitations. First, multispectral photoacoustic tomography does not allow for absolute tissue pO<sub>2</sub> measurements, but only the assessment of relative values of haemoglobin concentration and oxygenation. Derivation of absolute values would require advanced light fluence correction, which is subject of current research<sup>532,533</sup> and is not yet validated for routine use *in vivo*. Second, mesoscopic PAI only captures vasculature in periphery and not vessels in the tumour core due to limitations in light penetration and system field of view (see Chapter 5). However, the peripheral data should give sufficient insight on the tumour-specific vascular phenotype, since tumour cores are often necrotic and poorly vascularized. Third, the temporal resolution of photoacoustic mesoscopy is limited. Developments to increase the temporal resolution of photoacoustic mesoscopy systems are currently underway<sup>534</sup>, and may could help for a more detailed assessment of perfusion dynamics in future. Finally, the presented studies were performed in orthotopic xenograft models with two cell lines in nude mice. Whilst the two models used in this study capture oestrogen-dependent and independent subtypes, other disease sub-groups should be assessed as well, ideally in patient-derived tumour models before moving to a clinical setting. Nude mice also lack an adaptive immune system, which may affect tumour development and the resulting perfusion and hypoxia dynamics.

Taken together, our results emphasize the potential of PAI to unravel oxygenation and perfusion variability in tumour tissues. Perfusion-limited hypoxia related PAI biomarkers were found to directly

correlate with IHC and underlying gene expression, and may could be used in future to better evaluate cancer aggressiveness and assist in patient stratification.



# 7 CONCLUSION AND OUTLOOK

Perfusion-limited hypoxia is a poorly understood phenomenon, but is known to promote tumour aggressiveness, metastatic potential, and therapy resistance. Deciphering the complex interplay of perfusion and oxygenation dynamics may foster the adaption of the new therapy regimes and could lead to the emergence of promising new cancer treatments that improve patient outcomes. This task demands the development of novel biomarkers that are thoroughly validated and characterised.

This thesis presents a thorough validation and subsequent initial application of PAI biomarkers to characterise hypoxia and perfusion dynamics in cancer. Building on an extensive literature review on phantom materials in biophotonics (Chapter 2), it moves on to establishing and validating material characterisation systems that are required for accurate determination of relevant material properties (Chapter 3). On this basis, a phantom material is developed with tuneable tissue-mimicking acoustic, optical and mechanical properties that are stable over time (Chapter 4). Using this material, as well as further targeted phantom setups, a mesoscopic PAI system is validated to assess its accuracy and precision in determining perfusion- and vessel-related biomarkers (Chapter 5). Finally, studies on perfusion-limited hypoxia are performed at different spatio-temporal scales: using both mesoscopic and macroscopic systems are extracted and correlated to transcriptomic and histopathological analysis (Chapter 6). The phantom development and validation work conducted in this thesis does not only provide confidence in the PAI measurements performed herein, but will hopefully guide photoacoustic studies in a broader context, strengthening efforts towards a future in which photoacoustic measures can be robust over time, between subjects, imaging sites, operators, and manufacturers.

To advance the work presented here, further efforts could be applied in several areas. The phantom material review, validation of material characterisation systems, and phantom material development (Chapter 2–4) reveal the need for precise evaluation and understanding of the reproducibility of fabrication of a material type — independent of equipment, operator, or manufacturing centre. Only if this is provided, can confidence in phantom measurements across centres be established, making the material suitable for broader adoption in the community. For the phantom material developed in Chapter 4, a study to assess multi-centre manufacturing reproducibility is now planned, involving >10 international partner labs through IPASC. In the near future, this will be central in establishing a PAI phantom that can be easily and reproducibly fabricated across laboratories, supporting the characterisation, comparison, and calibration of the wide range of PAI systems in use around the world.

Ultimately, going beyond preclinical imaging systems towards potential clinical application, phantom production should be scaled for manufacturing, for example by a commercial vendor, creating identical test objects with well controlled properties and geometries to comply with the recommendations. Similar commercially available phantoms exist for more mature technologies such as computed tomography, X-ray mammography, ultrasound and magnetic resonance imaging, which have been independently validated and conform to, for example, the Mammography Quality Standards Act (MQSA), and/or the ACR Quality Control Programs<sup>535</sup>. As PAI has not yet reached the maturity of other imaging modalities, and systems are still constantly developed and optimized, dissemination of a flexible reproducible phantom recipe might be the more future-proof option to manifest standardisation, strengthening the path towards clinical translation.

In Chapter 5, a structured framework was applied to validate photoacoustic mesoscopy, with the overall goal to enhance our understanding of the limitations of its visualization capabilities. Here, the phantom designs were simple, tailored towards systematically characterising specific (geometric) restrictions of the imaging system. Tissue composition *in vivo* is more complex, with diverse vessel morphologies, additional chromophores (e.g., melanin, lipid, collagen etc), and acoustic and optical background inhomogeneities compromising visualization of the target of interest. A direct comparison to another imaging modality would provide a more accurate view on the visualization capabilities of our system in an *in vivo* setting. Suitable imaging modalities that provide sufficient resolution and penetration depth include Micro-CT<sup>536,537</sup> or Light-Sheet-Fluorescence Microscopy<sup>538</sup>. *Ex vivo* validation studies using these modalities (with respective vascular contrast agents) could confirm vascular dimensions and network architecture, providing a direct comparator for the PAI *in vivo* measurements. Preliminary efforts towards this goal have already been explored in parallel to this thesis, and will be extended in future studies.

In Chapter 6, the now well-characterised PAI framework was applied to an initial study of perfusion-limited hypoxia in mouse models of breast cancer. Validated by transcriptomic and histopathology, distinct differences in vascular architecture, tumour oxygenation and perfusion were highlighted between an oestrogen-dependent and oestrogen-independent mouse model using PAI. In future, the observed frequencies and morphological parameters will be used to inform studies on the effects of varying hypoxia levels on a molecular level, exploiting novel *in silico* approaches and advanced *in vitro* analysis using specialist hypoxia chambers. This multidisciplinary framework will hopefully assist in deciphering the complex interplay of perfusion and oxygenation dynamics in breast cancer, thereby guiding us on the adaption of treatment responses.

In the long term, it would be of interest to extend this analysis pipeline to other tumour models where hypoxia is strongly implicated in therapeutic response, such as head and neck and colorectal cancers. Given the methodology available with PAI, it may be possible to define biomarkers specific to diffusion- and perfusion-limited hypoxia, which would enable us to define the balance between these

hypoxia types in tumour models. Additionally, it would be valuable to assess how the relative balance between diffusion- and perfusion-limited hypoxia impacts the response to different treatment types, as well as how the balance changes in response to treatment. Using a Small Animal Radiation Research Platform (SARRP) system, the connection between perfusion-limited hypoxia and the efficacy / dose dependence of radiotherapy<sup>2</sup> response could be explored, thereby extending current *in vivo* studies on this matter<sup>23</sup>. Vascular normalization agents, such as VEGF receptor inhibitors or multi-tyrosine kinase inhibitors<sup>101,539</sup>, could also be investigated in this context. In particular, the anti-angiogenic drug Sunitinib may be of interest in such study, as it was shown to suppress pO<sub>2</sub> fluctuations and increase tumour oxygenation during the vascular normalization window<sup>539</sup>. Other pharmacological agents to perturb perfusion-limited hypoxia include nicotinamide<sup>540,541</sup>, pyrazinamide<sup>542</sup> or pentoxifylline<sup>543</sup>, all of which have been proven effective at reducing variations in tumour perfusion and oxygenation and enhancing the radiation response<sup>544</sup>, making them promising targets to further interrogate the PAI biomarkers developed here.

Photoacoustic means to describe perfusion and hypoxia dynamics could also be extended to non-oncological applications, for example, in dermatology (e.g., inflammatory diseases such as rheumatoid arthritis) or neurology (e.g., whole-brain haemodynamics and brain disorders). First steps towards this direction have been already explored by other research groups<sup>545-548</sup> and may progress further with the methods developed in this thesis. In the long term, if further studies prove their value, the methodologies explored in this thesis may progress along the pathway towards clinical adoption. However, as highlighted in this thesis, it is through detailed biomarker validation and standardisation that clinical translation succeeds, and new frontiers are reached.



# 8 REFERENCES

1. Michiels, C., Tellier, C. & Feron, O. Cycling hypoxia: A key feature of the tumor microenvironment. *Biochim. Biophys. Acta - Rev. Cancer* **1866**, 76–86 (2016).
2. Dewhirst, M. W., Cao, Y. & Moeller, B. Cycling hypoxia and free radicals regulate angiogenesis and radiotherapy response. *Nat. Rev. Cancer* **8**, 425–437 (2008).
3. Hanahan, D. & Weinberg, R. A. Hallmarks of cancer: The next generation. *Cell* vol. 144 646–674 (2011).
4. Vaupel, P. & Mayer, A. Hypoxia in cancer: significance and impact on clinical outcome. *Cancer Metastasis Rev.* **26**, 225–239 (2007).
5. Dewhirst, M. W. Relationships between Cycling Hypoxia, HIF-1, Angiogenesis and Oxidative Stress. *Radiat. Res.* **172**, 653–665 (2009).
6. Bayer, C., Shi, K., Astner, S. T., Maftai, C.-A. & Vaupel, P. Acute Versus Chronic Hypoxia: Why a Simplified Classification is Simply Not Enough. *Int. J. Radiat. Oncol.* **80**, 965–968 (2011).
7. Bader, S. B., Dewhirst, M. W. & Hammond, E. M. Cyclic Hypoxia: An Update on Its Characteristics, Methods to Measure It and Biological Implications in Cancer. *Cancers (Basel)*. **13**, 23 (2020).
8. Kukwa, W., Migacz, E., Druc, K., Grzesiuk, E. & Czarnecka, A. M. Obstructive sleep apnea and cancer: effects of intermittent hypoxia? *Futur. Oncol.* **11**, 3285–3298 (2015).
9. Horsman, M. R. *et al.* Imaging hypoxia to improve radiotherapy outcome. **9**, 674–687 (2012).
10. Ferlay, J. *et al.* Global Cancer Observatory: Cancer Today. *Lyon Int. Agency Res. Cancer* (2020).
11. Lundgren, K., Holm, C. & Landberg, G. Hypoxia and breast cancer: prognostic and therapeutic implications. *Cell. Mol. Life Sci.* **64**, 3233–3247 (2007).
12. Hanahan, D. & Folkman, J. Patterns and emerging mechanisms of the angiogenic switch during tumorigenesis. *Cell* **86**, 353–364 (1996).
13. Carmeliet, P. & Jain, R. K. Angiogenesis in cancer and other diseases. *Nature* **407**, 249–257 (2000).
14. Carmeliet, P. VEGF as a key mediator of angiogenesis in cancer. *Oncology* **69 Suppl 3**, 4–10

- (2005).
15. Lugano, R., Ramachandran, M. & Dimberg, A. Tumor angiogenesis: causes, consequences, challenges and opportunities. *Cell. Mol. Life Sci.* **77**, 1745–1770 (2020).
  16. Hanahan, D. & Folkman, J. Patterns and emerging mechanisms of the angiogenic switch during tumorigenesis. *Cell* **86**, 353–364 (1996).
  17. Morikawa, S. *et al.* Abnormalities in pericytes on blood vessels and endothelial sprouts in tumors. *Am. J. Pathol.* **160**, 985–1000 (2002).
  18. Baluk, P., Morikawa, S., Haskell, A., Mancuso, M. & McDonald, D. M. Abnormalities of basement membrane on blood vessels and endothelial sprouts in tumors. *Am. J. Pathol.* **163**, 1801–1815 (2003).
  19. Rofstad, E., Galappathi, K., Mathiesen, B. & Ruud, E. Fluctuating and diffusion-limited hypoxia in hypoxia-induced metastasis. *Clin. cancer Res.* **13**, 1971–1978 (2007).
  20. Cairns, R. A., Kalliomaki, T. & Hill, R. P. Acute (Cyclic) Hypoxia Enhances Spontaneous Metastasis of KHT Murine Tumors. *Cancer Res.* **61**, (2001).
  21. Cairns, R. A. & Hill, R. P. Acute Hypoxia Enhances Spontaneous Lymph Node Metastasis in an Orthotopic Murine Model of Human Cervical Carcinoma. *Cancer Res.* **64**, 2054–2061 (2004).
  22. Tellier, C. *et al.* Cycling Hypoxia Induces a Specific Amplified Inflammatory Phenotype in Endothelial Cells and Enhances Tumor-Promoting Inflammation In Vivo. **17**, (2015).
  23. Hsieh *et al.* Cycling hypoxia increases U87 glioma cell radioresistance via ROS induced higher and long-term HIF-1 signal transduction activity. *Oncol. Rep.* **24**, 1629–1636 (2010).
  24. Martinive, P. *et al.* Preconditioning of the Tumor Vasculature and Tumor Cells by Intermittent Hypoxia: Implications for Anticancer Therapies. *Cancer Res.* **66**, 11736–11744 (2006).
  25. Chaplin, D. J., Durand, R. E. & Olive, P. L. Acute hypoxia in tumors: Implications for modifiers of radiation effects. *Int. J. Radiat. Oncol. Biol. Phys.* **12**, 1279–1282 (1986).
  26. Brown, J. Evidence for acutely hypoxic cells in mouse tumours, and a possible mechanism of reoxygenation. *Br. J. Radiol.* **52**, 650–656 (1979).
  27. Hsieh, C. H. *et al.* NADPH oxidase subunit 4 mediates cycling hypoxia-promoted radiation resistance in glioblastoma multiforme. *Free Radic. Biol. Med.* **53**, 649–658 (2012).
  28. Chou, C. *et al.* Tumor cycling hypoxia induces chemoresistance in glioblastoma multiforme by upregulating the expression and function of ABCB1. *Neuro. Oncol.* **14**, 1227–1238 (2012).
  29. Hashizume, H. *et al.* Openings between defective endothelial cells explain tumor vessel

- leakiness. *Am. J. Pathol.* **156**, 1363–1380 (2000).
30. Heldin, C. H., Rubin, K., Pietras, K. & Östman, A. High interstitial fluid pressure - an obstacle in cancer therapy. *Nat. Rev. Cancer* **4**, 806–813 (2004).
  31. Padera, T. P. *et al.* Pathology: cancer cells compress intratumour vessels. *Nature* **427**, 695 (2004).
  32. Gatenby, R. A. & Gillies, R. J. Why do cancers have high aerobic glycolysis? *Nat. Rev. Cancer* **2004 411 4**, 891–899 (2004).
  33. Parks, S. K., Chiche, J. & Pouyssegur, J. pH control mechanisms of tumor survival and growth. *J. Cell. Physiol.* **226**, 299–308 (2011).
  34. Rofstad, E. K., Mathiesen, B., Kindem, K. & Galappathi, K. Acidic extracellular pH promotes experimental metastasis of human melanoma cells in athymic nude mice. *Cancer Res.* **66**, 6699–6707 (2006).
  35. Estrella, V. *et al.* Acidity generated by the tumor microenvironment drives local invasion. *Cancer Res.* **73**, 1524–1535 (2013).
  36. Chaplin, D. J., Olive, P. L. L. & Durand, R. E. E. Intermittent blood flow in a murine tumor: radiobiological effects. *Cancer Res* **47**, 597–601 (1987).
  37. Gray, L. H., Conger, A. D., Ebert, M., Hornsey, S. & Scott, O. C. A. The Concentration of Oxygen Dissolved in Tissues at the Time of Irradiation as a Factor in Radiotherapy. <http://dx.doi.org/10.1259/0007-1285-26-312-638> **26**, 638–648 (2014).
  38. McKeown, S. R. Defining normoxia, physoxia and hypoxia in tumours—implications for treatment response. <http://dx.doi.org/10.1259/bjr.20130676> **87**, (2014).
  39. Overgaard, J. Sensitization of hypoxic tumour cells—clinical experience. *Int. J. Radiat. Biol.* **56**, 801–811 (1989).
  40. Vaupel, P., Thews, O. & Hoekel, M. Treatment resistance of solid tumors: role of hypoxia and anemia. *Med. Oncol.* **18**, 243–259 (2001).
  41. Rebucci, M. & Michiels, C. Molecular aspects of cancer cell resistance to chemotherapy. *Biochem. Pharmacol.* **85**, 1219–1226 (2013).
  42. Cosse, J.-P. & Michiels, C. Tumour Hypoxia Affects the Responsiveness of Cancer Cells to Chemotherapy and Promotes Cancer Progression. *Anticancer. Agents Med. Chem.* **8**, 790–797 (2012).
  43. Bristow, R. G. & Hill, R. P. Hypoxia, DNA repair and genetic instability. **8**, 180–192 (2008).
  44. Baudelet, C. & Gallez, B. Current Issues in the Utility of Blood Oxygen Level Dependent MRI

- for the Assessment of Modulations in Tumor Oxygenation. *Curr. Med. Imaging Rev.* **1**, 229–243 (2005).
45. Zhang, X., Ashcraft, K. A., Warner, A. B., Nair, S. K. & Dewhirst, M. W. Can Exercise-Induced Modulation of the Tumor Physiologic Microenvironment Improve Antitumor Immunity? *Cancer Res.* **79**, 2447–2456 (2019).
  46. Cuvier, C., Jang, A. & Hill, R. Exposure to hypoxia, glucose starvation and acidosis: effect on invasive capacity of murine tumor cells and correlation with cathepsin (L + B) secretion. *Clin. Exp. Metastasis* **15**, 19–25 (1997).
  47. Jaeger, K. De, Kavanagh, M.-C. & Hill, R. P. Relationship of hypoxia to metastatic ability in rodent tumours. *Br. J. Cancer* **84**, 1280 (2001).
  48. Moon, E., Brizel, D., Chi, J. & Dewhirst, M. The potential role of intrinsic hypoxia markers as prognostic variables in cancer. *Antioxid. Redox Signal.* **9**, 1237–1294 (2007).
  49. Panek, R. *et al.* Noninvasive Imaging of Cycling Hypoxia in Head and Neck Cancer Using Intrinsic Susceptibility MRI. *Clin. Cancer Res.* **23**, 4233–4241 (2017).
  50. Hoppe-Seyler, K., Mändl, J., Adrian, S., Kuhn, B. J. & Hoppe-Seyler, F. Virus/Host Cell Crosstalk in Hypoxic HPV-Positive Cancer Cells. *Viruses 2017, Vol. 9, Page 174* **9**, 174 (2017).
  51. Dewhirst, M. W. Concepts of oxygen transport at the microcirculatory level. *Semin. Radiat. Oncol.* **8**, 143–50 (1998).
  52. Matsumoto, S., Yasui, H., Mitchell, J. B. & Krishna, M. C. Imaging cycling tumor hypoxia. *Cancer Res.* **70**, 10019–23 (2010).
  53. Vaupel, P. & Harrison, L. Tumor hypoxia: causative factors, compensatory mechanisms, and cellular response. *Oncologist* **9 Suppl 5**, 4–9 (2004).
  54. Dewhirst, M. *et al.* Quantification of longitudinal tissue pO<sub>2</sub> gradients in window chamber tumours: impact on tumour hypoxia. *Br. J. Cancer* **79**, 1717–1722 (1999).
  55. Kavanagh, B., Coffey, B., Needham, D., Hochmuth, R. & Dewhirst, M. The effect of flunarizine on erythrocyte suspension viscosity under conditions of extreme hypoxia, low pH, and lactate treatment. *Br. J. Cancer* **67**, 734–741 (1993).
  56. Dewhirst, M. W., Secomb, T. W., Ong, E. T., Hsu, R. & Gross, J. F. Determination of local oxygen consumption rates in tumors. *Cancer Res.* **54**, 3333–6 (1994).
  57. Vaupel, P., Kallinowski, F. & Okunieff, P. Blood flow, oxygen and nutrient supply, and metabolic microenvironment of human tumors: a review. *Cancer Res.* **49**, 6449–65 (1989).
  58. Bennewith, K. L. & Durand, R. E. Quantifying Transient Hypoxia in Human Tumor Xenografts

- by Flow Cytometry. *Cancer Res.* **64**, 6183–6189 (2004).
59. Bennewith, K. L., Raleigh, J. A. & Durand, R. E. Orally administered pimonidazole to label hypoxic tumor cells. *Cancer Res.* **62**, 6827–30 (2002).
  60. Dewhirst, M. W. *et al.* Microvascular studies on the origins of perfusion-limited hypoxia. *Br. J. Cancer. Suppl.* **27**, S247-51 (1996).
  61. Ellingsen, C., Øvrebø, K. M., Galappathi, K., Mathiesen, B. & Rofstad, E. K. pO<sub>2</sub> Fluctuation Pattern and Cycling Hypoxia in Human Cervical Carcinoma and Melanoma Xenografts. *Int. J. Radiat. Oncol. Biol. Phys.* **83**, 1317–1323 (2012).
  62. Cárdenas-Navia, L. I. *et al.* Tumor-dependent Kinetics of Partial Pressure of Oxygen Fluctuations during Air and Oxygen Breathing. *Cancer Res.* **64**, 6010–6017 (2004).
  63. Durand, R. & LePard, N. Contribution of transient blood flow to tumour hypoxia in mice. *Acta Oncol.* **34**, 317–323 (1995).
  64. Gulliksrud, K., Vestvik, I. K., Galappathi, K., Mathiesen, B. & Rofstad, E. K. Detection of Different Hypoxic Cell Subpopulations in Human Melanoma Xenografts by Pimonidazole Immunohistochemistry. *Radiat. Res.* **170**, 638–650 (2008).
  65. Rofstad, E. & Måseide, K. Radiobiological and immunohistochemical assessment of hypoxia in human melanoma xenografts: acute and chronic hypoxia in individual tumours. *Int. J. Radiat. Biol.* **75**, 1377–1393 (1999).
  66. Rofstad, E. E. K. *et al.* Fluctuating and diffusion-limited hypoxia in hypoxia-induced metastasis. *Clin. cancer Res.* **13**, 1971–1978 (2007).
  67. Yamaura, H. & Matsuzawa, T. Tumour Regrowth after Irradiation. *Int. J. Radiat. Biol. Relat. Stud. Physics, Chem. Med.* **35**, 201–219 (1979).
  68. Brown, J. M. & Oxon, D. P. (. Evidence for acutely hypoxic cells in mouse tumours, and a possible mechanism of reoxygenation. <http://dx.doi.org/10.1259/0007-1285-52-620-650> **52**, 650–656 (2014).
  69. Trotter, M. J., Chaplin, D. J., Durand, R. E. & Olive, P. L. The use of fluorescent probes to identify regions of transient perfusion in murine tumors. *Int. J. Radiat. Oncol. Biol. Phys.* **16**, 931–934 (1989).
  70. Trotter, M. J., Chaplin, D. J. & Olive, P. L. Use of a carbocyanine dye as a marker of functional vasculature in murine tumours. *Br. J. Cancer* 1989 595 **59**, 706–709 (1989).
  71. Ljungkvist, A. S. E., Bussink, J., Kaanders, J. H. A. M. & Van Der Kogel, A. J. Dynamics of Tumor Hypoxia Measured with Bioreductive Hypoxic Cell Markers. *Radiat. Res.* **167**, 127–145 (2007).

72. Li, L. *et al.* Intermittent hypoxia promotes melanoma lung metastasis via oxidative stress and inflammation responses in a mouse model of obstructive sleep apnea. *Respir. Res.* 2018 191 **19**, 1–9 (2018).
73. Snyder, B., Shell, B., Cunningham, J. T. & Cunningham, R. L. Chronic intermittent hypoxia induces oxidative stress and inflammation in brain regions associated with early-stage neurodegeneration. *Physiol. Rep.* **5**, e13258 (2017).
74. Chen, W.-L., Wang, C.-C., Lin, Y.-J., Wu, C.-P. & Hsieh, C.-H. Cycling hypoxia induces chemoresistance through the activation of reactive oxygen species-mediated B-cell lymphoma extra-long pathway in glioblastoma multiforme. *J. Transl. Med.* 2015 131 **13**, 1–13 (2015).
75. Finkel, T. & Holbrook, N. J. Oxidants, oxidative stress and the biology of ageing. *Nat.* 2000 4086809 **408**, 239–247 (2000).
76. Sena, L. A. & Chandel, N. S. Physiological Roles of Mitochondrial Reactive Oxygen Species. *Mol. Cell* **48**, 158–167 (2012).
77. Koritzinsky, M. & Wouters, B. G. The Roles of Reactive Oxygen Species and Autophagy in Mediating the Tolerance of Tumor Cells to Cycling Hypoxia. *Semin. Radiat. Oncol.* **23**, 252–261 (2013).
78. Reczek, C. R. & Chandel, N. S. ROS-dependent signal transduction. *Curr. Opin. Cell Biol.* **33**, 8–13 (2015).
79. Liu, S. *et al.* Intermittent Hypoxia Reduces Microglia Proliferation and Induces DNA Damage In Vitro. *Chest* **149**, A577 (2016).
80. Hammond, E. M., Dorie, M. J. & Giaccia, A. J. ATR/ATM Targets Are Phosphorylated by ATR in Response to Hypoxia and ATM in Response to Reoxygenation \*. *J. Biol. Chem.* **278**, 12207–12213 (2003).
81. Kalliomäki, T. M., McCallum, G., Lunt, S. J., Wells, P. G. & Hill, R. P. Analysis of the effects of exposure to acute hypoxia on oxidative lesions and tumour progression in a transgenic mouse breast cancer model. *BMC Cancer* 2008 81 **8**, 1–13 (2008).
82. Malec, V. *et al.* HIF-1 $\alpha$  signaling is augmented during intermittent hypoxia by induction of the Nrf2 pathway in NOX1-expressing adenocarcinoma A549 cells. *Free Radic. Biol. Med.* **48**, 1626–1635 (2010).
83. Martinive, P. *et al.* Impact of cyclic hypoxia on HIF-1 $\alpha$  regulation in endothelial cells - New insights for anti-tumor treatments. *FEBS J.* **276**, 509–518 (2009).
84. Morgan, M. J. & Liu, Z. Crosstalk of reactive oxygen species and NF- $\kappa$ B signaling. *Cell Res.* 2011 211 **21**, 103–115 (2010).

85. Denko, N. C. Hypoxia, HIF1 and glucose metabolism in the solid tumour. *Nat. Rev. Cancer* 2008 89 **8**, 705–713 (2008).
86. Zeng, W., Liu, P., Pan, W., Singh, S. R. & Wei, Y. Hypoxia and hypoxia inducible factors in tumor metabolism. *Cancer Lett.* **356**, 263–267 (2015).
87. Pires, I. M. *et al.* Effects of acute versus chronic hypoxia on DNA damage responses and genomic instability. *Cancer Res.* **70**, 925 (2010).
88. Hammond, E. M., Kaufmann, M. R. & Giaccia, A. J. Oxygen sensing and the DNA-damage response. *Curr. Opin. Cell Biol.* **19**, 680–684 (2007).
89. Bristow, R. G. & Hill, R. P. Hypoxia and metabolism. Hypoxia, DNA repair and genetic instability. *Nat. Rev. Cancer* **8**, 180–192 (2008).
90. Toffoli, S. *et al.* Intermittent hypoxia is an angiogenic inducer for endothelial cells: role of HIF-1. *Angiogenesis* **12**, 47–67 (2009).
91. Gaustad, J. V., Simonsen, T. G., Roa, A. M. A. & Rofstad, E. K. Tumors exposed to acute cyclic hypoxia show increased vessel density and delayed blood supply. *Microvasc. Res.* **85**, 10–15 (2013).
92. Bhaskara, V. K., Mohanam, I., Rao, J. S. & Mohanam, S. Intermittent Hypoxia Regulates Stem-like Characteristics and Differentiation of Neuroblastoma Cells. *PLoS One* **7**, e30905 (2012).
93. Zhu, H. *et al.* Upregulation of autophagy by hypoxia-inducible factor-1 $\alpha$  promotes EMT and metastatic ability of CD133+ pancreatic cancer stem-like cells during intermittent hypoxia. *Oncol. Rep.* **32**, 935–942 (2014).
94. Yang, M. H. *et al.* Direct regulation of TWIST by HIF-1 $\alpha$  promotes metastasis. *Nat. Cell Biol.* 2008 103 **10**, 295–305 (2008).
95. Bayer, C. & Vaupel, P. Acute versus chronic hypoxia in tumors: Controversial data concerning time frames and biological consequences. *Strahlenther. Onkol.* **188**, 616–627 (2012).
96. Braun, R. D., Lanzen, J. L., Snyder, S. A. & Dewhirst, M. W. Comparison of tumor and normal tissue oxygen tension measurements using OxyLite or microelectrodes in rodents. <https://doi.org/10.1152/ajpheart.2001.280.6.H2533> **280**, (2001).
97. Brurberg, K. G., Graff, B. A., Olsen, D. R. & Rofstad, E. K. Tumor-line specific pO<sub>2</sub> fluctuations in human melanoma xenografts. in *International Journal of Radiation Oncology Biology Physics* vol. 58 403–409 (Elsevier Inc., 2004).
98. Brurberg, K. G., Graff, B. A. & Rofstad, E. K. Temporal heterogeneity in oxygen tension in human melanoma xenografts. *Br. J. Cancer* **89**, 350–356 (2003).

99. Baudelet, C. *et al.* Physiological noise in murine solid tumours using T2\*-weighted gradient-echo imaging: a marker of tumour acute hypoxia? *Phys. Med. Biol.* **49**, 3389–411 (2004).
100. Brurberg, K. G., Benjaminsen, I. C., Dørum, L. M. R. & Rofstad, E. K. Fluctuations in tumor blood perfusion assessed by dynamic contrast-enhanced MRI. *Magn. Reson. Med.* **58**, 473–481 (2007).
101. Gonçalves, M. R. *et al.* The effect of imatinib therapy on tumour cycling hypoxia, tissue oxygenation and vascular reactivity. *Wellcome Open Res.* **2**, 38 (2017).
102. Lee, N. *et al.* Prospective Trial Incorporating Pre-/Mid-Treatment [18F]-Misonidazole Positron Emission Tomography for Head-and-Neck Cancer Patients Undergoing Concurrent Chemoradiotherapy. *Int. J. Radiat. Oncol.* **75**, 101–108 (2009).
103. Wang, K., Yorke, E., Nehmeh, S. A., Humm, J. L. & Ling, C. C. Modeling acute and chronic hypoxia using serial images of F18-FMISO PET. *Med. Phys.* **36**, 4400–4408 (2009).
104. Yasui, H. *et al.* Low-Field Magnetic Resonance Imaging to Visualize Chronic and Cycling Hypoxia in Tumor-Bearing Mice. *Cancer Res.* **70**, 6427–6436 (2010).
105. Khan, N., Mupparaju, S., Hou, H., Williams, B. B. & Swartz, H. Repeated assessment of orthotopic glioma pO<sub>2</sub> by multi-site EPR oximetry: A technique with the potential to guide therapeutic optimization by repeated measurements of oxygen. *J. Neurosci. Methods* **204**, 111–117 (2012).
106. Nehmeh, S. A. *et al.* Reproducibility of Intratumor Distribution of 18F-Fluoromisonidazole in Head and Neck Cancer. *Int. J. Radiat. Oncol.* **70**, 235–242 (2008).
107. Carmona-Bozo, J. C. *et al.* Hypoxia and perfusion in breast cancer: simultaneous assessment using PET/MR imaging. *Eur. Radiol.* **31**, 333–344 (2021).
108. Hoskin, P. J. *et al.* Hypoxia in Prostate Cancer: Correlation of BOLD-MRI With Pimonidazole Immunohistochemistry—Initial Observations. *Int. J. Radiat. Oncol.* **68**, 1065–1071 (2007).
109. O’Connor, J. P. B. *et al.* Oxygen-Enhanced MRI Accurately Identifies, Quantifies, and Maps Tumor Hypoxia in Preclinical Cancer Models. *Cancer Res.* **76**, 787–795 (2016).
110. Skala, M. C., Fontanella, A. N., Lan, L., Izatt, J. A. & D.V.M., M. W. D. Longitudinal optical imaging of tumor metabolism and hemodynamics. *J. Biomed. Opt.* **15**, 011112 (2010).
111. Skala, M. C., Fontanella, A., Hendargo, H., Dewhirst, M. W. & Izatt, J. A. Combined hyperspectral and spectral domain optical coherence tomography microscope for noninvasive hemodynamic imaging. *Opt. Lett.* **34**, 289 (2009).
112. Yu, B. *et al.* Measuring tumor cycling hypoxia and angiogenesis using a side-firing fiber optic probe. *J. Biophotonics* **7**, 552 (2014).

113. Ron, A., Deán-Ben, X. L., Gottschalk, S. & Razansky, D. Volumetric optoacoustic imaging unveils high-resolution patterns of acute and cyclic hypoxia in a murine model of breast cancer. *Cancer Res.* **79**, 4767–4775 (2019).
114. Cárdenas-Navia, L. I. *et al.* The Pervasive Presence of Fluctuating Oxygenation in Tumors. *Cancer Res.* **68**, 5812–5819 (2008).
115. Gonçalves, M. R. *et al.* Decomposition of spontaneous fluctuations in tumour oxygenation using BOLD MRI and independent component analysis. *Br. J. Cancer* **113**, 1168–1177 (2015).
116. Connor, O., Robinson, J. P. & Waterton, S. P. *Imaging tumour hypoxia with oxygen-enhanced MRI and BOLD MRI.* *Br J Radiol* vol. 92 (2019).
117. Baudalet, C. *et al.* The role of vessel maturation and vessel functionality in spontaneous fluctuations of T2\*-weighted GRE signal within tumors. *NMR Biomed.* **19**, 69–76 (2006).
118. Magat, J., Jordan, B. F., Cron, G. O. & Gallez, B. Noninvasive mapping of spontaneous fluctuations in tumor oxygenation using 19F MRI. *Med. Phys.* **37**, 5434–5441 (2010).
119. Bell, A. G. On the production and reproduction of sound by light. *Am. J. Sci.* **s3-20**, 305–324 (1880).
120. Smith, A. M., Mancini, M. C. & Nie, S. Second window for in vivo imaging. *Nat. Nanotechnol.* **4**, 710–711 (2009).
121. Beard, P. Biomedical photoacoustic imaging. *Interface Focus* **1**, 602–631 (2011).
122. Ntziachristos, V. & Razansky, D. Molecular Imaging by Means of Multispectral Optoacoustic Tomography (MSOT). *Chem. Rev.* **110**, 2783–2794 (2010).
123. Zhang, H. F., Maslov, K., Stoica, G. & Wang, L. V. Functional photoacoustic microscopy for high-resolution and noninvasive in vivo imaging. *Nat. Biotechnol.* **24**, 848–851 (2006).
124. Hu, S. & Wang, L. V. Photoacoustic imaging and characterization of the microvasculature. *J. Biomed. Opt.* **15**, 011101 (2010).
125. Wang, L. V. & Yao, J. A Practical Guide to Photoacoustic Tomography in the Life Sciences. *Nat. Methods* **13**, 627 (2016).
126. Attia, A. B. E. *et al.* A review of clinical photoacoustic imaging: Current and future trends. *Photoacoustics* vol. 16 100144 (2019).
127. Weber, J., Beard, P. C. & Bohndiek, S. E. Contrast agents for molecular photoacoustic imaging. *Nat. Methods* **13**, 639–650 (2016).
128. Key, J. & Leary, J. F. Nanoparticles for multimodal in vivo imaging in nanomedicine. *Int. J. Nanomedicine* **9**, 711–726 (2014).

129. Hanahan, D. & Weinberg, R. A. Hallmarks of Cancer: The Next Generation. *Cell* **144**, 646–674 (2011).
130. Ku, G., Wang, X., Xie, X., Stoica, G. & Wang, L. V. Imaging of tumor angiogenesis in rat brains in vivo by photoacoustic tomography. *Appl. Opt.* **44**, 770–5 (2005).
131. Maslov, K., Zhang, H. F., Hu, S. & Wang, L. V. Optical-resolution photoacoustic microscopy for in vivo imaging of single capillaries. *Opt. Lett.* **33**, 929–31 (2008).
132. Laufer, J. *et al.* In vivo preclinical photoacoustic imaging of tumor vasculature development and therapy. *J. Biomed. Opt.* **17**, 056016 (2012).
133. Wilson, K. E., Bachawal, S. V., Tian, L. & Willmann, J. K. Multiparametric Spectroscopic Photoacoustic Imaging of Breast Cancer Development in a Transgenic Mouse Model. *Theranostics* **4**, 1062–1071 (2014).
134. Gerling, M. *et al.* Real-time assessment of tissue hypoxia in vivo with combined photoacoustics and high-frequency ultrasound. *Theranostics* **4**, 604–13 (2014).
135. Yang, Z. *et al.* Multi-parametric quantitative microvascular imaging with optical-resolution photoacoustic microscopy in vivo. *Opt. Express* **22**, 1500 (2014).
136. Meiburger, K. M. *et al.* Skeletonization algorithm-based blood vessel quantification using *in vivo* 3D photoacoustic imaging. *Phys. Med. Biol.* **61**, 7994–8009 (2016).
137. Haedicke, K. *et al.* High-resolution photoacoustic imaging of tissue responses to vascular-targeted therapies. *Nat. Biomed. Eng.* **4**, 286–297 (2020).
138. Bohndiek, S. E., Van de Sompel, D., Bodapati, S., Kothapalli, S. R. & Gambhir, S. S. Stable phantoms for characterization of photoacoustic tomography (PAT) systems. 858308 (2013) doi:10.1117/12.2005195.
139. Rich, L. J. & Seshadri, M. Photoacoustic Imaging of Vascular Hemodynamics: Validation with Blood Oxygenation Level–Dependent MR Imaging. *Radiology* **275**, 110–118 (2015).
140. Rich, L., reports, M. S.-S. & 2016, undefined. Photoacoustic monitoring of tumor and normal tissue response to radiation. *nature.com*.
141. Martinho Costa, M. *et al.* Quantitative photoacoustic imaging study of tumours in vivo: Baseline variations in quantitative measurements. *Photoacoustics* **13**, 53–65 (2019).
142. Cox, B., Laufer, J. G., Arridge, S. R. & Beard, P. C. Quantitative spectroscopic photoacoustic imaging: A review. *J. Biomed. Opt.* **17**, 61202 (2012).
143. Gröhl, J., Kirchner, T., Adler, T. & Maier-Hein, L. *Estimation of blood oxygenation with learned spectral decoloring for quantitative photoacoustic imaging (LSD-qPAI)*.

144. O'Connor, J. P. B. *et al.* Imaging biomarker roadmap for cancer studies. *Nat. Rev. Clin. Oncol.* **14**, 169–186 (2017).
145. Joseph, J. *et al.* Evaluation of Precision in Optoacoustic Tomography for Preclinical Imaging in Living Subjects. *J. Nucl. Med.* **58**, 807–814 (2017).
146. Laufer, J., Zhang, E. & Beard, P. Evaluation of Absorbing Chromophores Used in Tissue Phantoms for Quantitative Photoacoustic Spectroscopy and Imaging. *IEEE J. Sel. Top. Quantum Electron.* **16**, 600–607 (2010).
147. Cook, J. R., Bouchard, R. R. & Emelianov, S. Y. Tissue-mimicking phantoms for photoacoustic and ultrasonic imaging. *Biomed. Opt. Express* **2**, 3193 (2011).
148. Xia, W. *et al.* Poly(vinyl alcohol) gels as photoacoustic breast phantoms revisited. *J. Biomed. Opt.* **16**, 075002 (2011).
149. Kharine, A. *et al.* Poly(vinyl alcohol) gels for use as tissue phantoms in photoacoustic mammography. **48**, 357–370 (2003).
150. Avigo, C. *et al.* Organosilicon phantom for photoacoustic imaging. *J. Biomed. Opt.* **20**, 046008 (2015).
151. Ratto, F. *et al.* Hybrid organosilicon/polyol phantom for photoacoustic imaging. *Biomed. Opt. Express* **10**, 3719–3730 (2019).
152. Vogt, W. C., Jia, C., Garra, B. S. & Pfefer, T. J. Characterization of tissue-simulating polymers for photoacoustic vascular imaging. in (eds. Cullum, B. M. & McLamore, E. S.) vol. 9107 910719 (International Society for Optics and Photonics, 2014).
153. Bohndiek, S. E., Bodapati, S., Van De Sompel, D., Kothapalli, S.-R. R. & Gambhir, S. S. Development and Application of Stable Phantoms for the Evaluation of Photoacoustic Imaging Instruments. *PLoS One* **8**, 1–14 (2013).
154. Fonseca, M., Zeqiri, B., Beard, P. & Cox, B. Characterisation of a PVCP-based tissue-mimicking phantom for quantitative photoacoustic imaging. **9539**, 953911 (2015).
155. Jeong, E. *et al.* Fabrication and characterization of PVCP human breast tissue-mimicking phantom for photoacoustic imaging. *BioChip J.* **11**, 67–75 (2017).
156. Vogt, W. C., Jia, C., Wear, K. A., Garra, B. S. & Joshua Pfefer, T. Biologically relevant photoacoustic imaging phantoms with tunable optical and acoustic properties. *J. Biomed. Opt.* **21**, 101405 (2016).
157. Dantuma, M., van Dommelen, R. & Manohar, S. Semi-anthropomorphic photoacoustic breast phantom. *Biomed. Opt. Express* **10**, 5921–5939 (2019).

158. Fonseca, M., Zeqiri, B., Beard, P. C. & Cox, B. T. Characterisation of a phantom for multiwavelength quantitative photoacoustic imaging. *Phys. Med. Biol.* **61**, 4950–4973 (2016).
159. Grillo, F. *et al.* White-silicone rubber and copolymer-in-oil blend for ultrasound soft tissue mimicking material. in *IEEE International Ultrasonics Symposium, IUS* (IEEE Computer Society, 2017). doi:10.1109/ULTSYM.2017.8092238.
160. Cabrelli, L. C., Grillo, F. W., Sampaio, D. R. T., Carneiro, A. A. O. & Pavan, T. Z. Acoustic and Elastic Properties of Glycerol in Oil-Based Gel Phantoms. *Ultrasound Med. Biol.* **43**, 2086–2094 (2017).
161. Grillo, F. W., Cabrelli, L. C., Sampaio, D. R. T., Carneiro, A. A. O. & Pavan, T. Z. Glycerol in oil-based phantom with improved performance for photoacoustic imaging. *IEEE Int. Ultrason. Symp. IUS 1–4* (2017) doi:10.1109/ULTSYM.2017.8091705.
162. Gehrung, M., Bohndiek, S. E. & Brunker, J. Development of a blood oxygenation phantom for photoacoustic tomography combined with online pO<sub>2</sub> detection and flow spectrometry. *J. Biomed. Opt.* **24**, 1 (2019).
163. Vogt, W. C. *et al.* Phantom-based image quality test methods for photoacoustic imaging systems. *J. Biomed. Opt.* **22**, 1 (2017).
164. Maneas, E. *et al.* Gel wax-based tissue-mimicking phantoms for multispectral photoacoustic imaging. *Biomed. Opt. Express* **9**, 1151 (2018).
165. Maneas, E. *et al.* Anatomically realistic ultrasound phantoms using gel wax with 3D printed moulds. *Phys. Med. Biol.* **63**, 015033 (2018).
166. Bohndiek, S. Addressing photoacoustics standards. *Nature Photonics* vol. 13 298 (2019).
167. Jia, C., Vogt, W. C., Wear, K. A., Pfefer, T. J. & Garra, B. S. Two-layer heterogeneous breast phantom for photoacoustic imaging. *J. Biomed. Opt.* **22**, 1–14 (2017).
168. Hacker, L. *et al.* A copolymer-in-oil tissue-mimicking material with tuneable acoustic and optical characteristics for photoacoustic imaging phantoms. *IEEE Trans. Med. Imaging* 1–1 (2021) doi:10.1109/TMI.2021.3090857.
169. Quiros-Gonzalez, I. *et al.* Optoacoustics delineates murine breast cancer models displaying angiogenesis and vascular mimicry. *Br. J. Cancer* **118**, 1098–1106 (2018).
170. Mallidi, S., Watanabe, K., Timerman, D., Theranostics, D. S.- & 2015, undefined. Prediction of tumor recurrence and therapy monitoring using ultrasound-guided photoacoustic imaging. *ncbi.nlm.nih.gov*.
171. Tomaszewski, M. R. *et al.* Oxygen-Enhanced and Dynamic Contrast-Enhanced Optoacoustic Tomography Provide Surrogate Biomarkers of Tumor Vascular Function, Hypoxia, and

- Necrosis. *Cancer Res.* **78**, 5980–5991 (2018).
172. Shah, A., Bush, N., Box, G., Eccles, S. & Bamber, J. Value of combining dynamic contrast enhanced ultrasound and optoacoustic tomography for hypoxia imaging. *Photoacoustics* **8**, 15–27 (2017).
  173. Raes, F. *et al.* High Resolution Ultrasound and Photoacoustic Imaging of Orthotopic Lung Cancer in Mice: New Perspectives for Onco-Pharmacology. *PLoS One* **11**, e0153532 (2016).
  174. Eisenbrey, J. R. *et al.* Comparison of Photoacoustically Derived Hemoglobin and Oxygenation Measurements with Contrast-Enhanced Ultrasound Estimated Vascularity and Immunohistochemical Staining in a Breast Cancer Model. *Ultrason. Imaging* **37**, 42–52 (2015).
  175. Yuan Gao, Y. G. *et al.* Co-registration method for photoacoustic imaging and laser speckle imaging. *Chinese Opt. Lett.* **10**, 061101–061104 (2012).
  176. Nordstrom, R. J. Phantoms as standards in optical measurements. in (eds. Nordstrom, R. J. & Coté, G. L.) vol. 7906 79060H (International Society for Optics and Photonics, 2011).
  177. Hwang, J., Ramella-Roman, J. C. & Nordstrom, R. Introduction: Feature Issue on Phantoms for the Performance Evaluation and Validation of Optical Medical Imaging Devices. *Biomed. Opt. Express* **3**, 1399 (2012).
  178. Pogue, B. W. & Patterson, M. S. Review of tissue simulating phantoms for optical spectroscopy, imaging and dosimetry. *J. Biomed. Opt.* **11**, 041102 (2006).
  179. Lamouche, G. *et al.* Review of tissue simulating phantoms with controllable optical, mechanical and structural properties for use in optical coherence tomography. *Biomed. Opt. Express* **3**, 1381 (2012).
  180. Alexanderson-Rosas, E. *et al.* Current and future trends in multimodality imaging of coronary artery disease. *Expert Rev. Cardiovasc. Ther.* **13**, 715–731 (2015).
  181. Yankeelov, T. E., Abramson, R. G. & Quarles, C. C. Quantitative multimodality imaging in cancer research and therapy. *Nature Reviews Clinical Oncology* vol. 11 670–680 (2014).
  182. Kainz, W. *et al.* Advances in Computational Human Phantoms and Their Applications in Biomedical Engineering—A Topical Review. *IEEE Trans. Radiat. Plasma Med. Sci.* **3**, 1–23 (2018).
  183. Jacques, S. L. Optical properties of biological tissues: a review. *Phys. Med. Biol.* **58**, R37–R61 (2013).
  184. Cheong, W. F., Prah, S. A. & Welch, A. J. A Review of the Optical Properties of Biological Tissues. *IEEE J. Quantum Electron.* **26**, 2166–2185 (1990).

185. Duck, F. A. & Institute of Physics and Engineering in Medicine (Great Britain). *Physical properties of tissue : a comprehensive reference book*.
186. Azhari, H. Appendix A: Typical Acoustic Properties of Tissues. in *Basics of Biomedical Ultrasound for Engineers* 313–314 (John Wiley & Sons, Inc., 2010). doi:10.1002/9780470561478.app1.
187. Yao, D.-K., Zhang, C., Maslov, K. & Wang, L. V. Photoacoustic measurement of the Grüneisen parameter of tissue. *J. Biomed. Opt.* **19**, 017007 (2014).
188. Lemaillet, P., Bouchard, J.-P., Hwang, J. & Allen, D. W. Double-integrating-sphere system at the National Institute of Standards and Technology in support of measurement standards for the determination of optical properties of tissue-mimicking phantoms. *J. Biomed. Opt.* **20**, 121310 (2015).
189. Wilson, B. C. Measurement of Tissue Optical Properties: Methods and Theories. in *Optical-Thermal Response of Laser-Irradiated Tissue* 233–303 (Springer US, 1995). doi:10.1007/978-1-4757-6092-7\_8.
190. Cubeddu, R., Pifferi, A., Taroni, P., Torricelli, A. & Valentini, G. Experimental test of theoretical models for time-resolved reflectance. *Med. Phys.* **23**, 1625–1633 (1996).
191. Spinelli, L. *et al.* Determination of reference values for optical properties of liquid phantoms based on Intralipid and India ink. *Biomed. Opt. Express* **5**, 2037 (2014).
192. Pifferi, A. *et al.* Performance assessment of photon migration instruments: The MEDPHOT protocol. *Appl. Opt.* **44**, 2104–2114 (2005).
193. Collins, D. E. ICRU REPORT 61: Tissue substitutes, phantoms and computational modelling in medical ultrasound. *Radiol. Technol.* **71**, 215–215 (1999).
194. Bigio, I. J. & Fantini, S. *Quantitative Biomedical Optics. Quantitative Biomedical Optics* (Cambridge University Press, 2016). doi:10.1017/cbo9781139029797.
195. Nicholas, D. Evaluation of backscattering coefficients for excised human tissues: results, interpretation and associated measurements. *Ultrasound Med. Biol.* **8**, 17–28 (1982).
196. Grüneisen, E. Theorie des festen Zustandes einatomiger Elemente. *Ann. Phys.* **344**, 257–306 (1912).
197. Breitenberg, M. A. *NISTIR 7614 - The ABC's of Standards Activities*. (2009) doi:https://doi.org/10.6028/NIST.IR.7614.
198. J. Nordstrom, R. Translational Research and Standardization in Optical Imaging. *Curr. Mol. Imaging* **3**, 129–143 (2015).

199. Waterhouse, D. Translation of Optical Imaging Biomarkers: Opportunities and Challenges. *Nat. Biomed. Eng.* **3**, 339–353 (2019).
200. Cerussi, A. E. *et al.* Tissue phantoms in multicenter clinical trials for diffuse optical technologies. *Biomed. Opt. Express* **3**, 966 (2012).
201. Pikkula, B. M. *et al.* Instrumentation as a source of variability in the application of fluorescence spectroscopic devices for detecting cervical neoplasia. *J. Biomed. Opt.* **12**, 034014 (2007).
202. Anastasopoulou, M. *et al.* Comprehensive phantom for interventional fluorescence molecular imaging. *J. Biomed. Opt.* **21**, 091309 (2016).
203. Linford, J., Shalev, S., Bews, J., Brown, R. & Schipper, H. Development of a tissue-equivalent phantom for diaphanography. *Med. Phys.* **13**, 869–875 (1986).
204. Durkin, A. J., Jaikumar, S. & Richards-Kortum, R. Optically Dilute, Absorbing, and Turbid Phantoms for Fluorescence Spectroscopy of Homogeneous and Inhomogeneous Samples. *Appl. Spectrosc.* **47**, 2114–2121 (1993).
205. Bush, N. L. & Hill, C. R. Gelatine-alginate complex gel: A new acoustically tissue-equivalent material. *Ultrasound Med. Biol.* **9**, 479–484 (1983).
206. Madsen, E. L., Zagzebski, J. A., Banjavie, R. A. & Jutila, R. E. Tissue mimicking materials for ultrasound phantoms. *Med. Phys.* **5**, 391–394 (1978).
207. Zell, K., Sperl, J. I., Vogel, M. W., Niessner, R. & Haisch, C. Acoustical properties of selected tissue phantom materials for ultrasound imaging. *Phys. Med. Biol.* **52**, (2007).
208. Madsen, E. L., Frank, G. R. & Dong, F. Liquid or solid ultrasonically tissue-mimicking materials with very low scatter. *Ultrasound Med. Biol.* **24**, 535–542 (1998).
209. Burlew, M. M., Madsen, E. L., Zagzebski, J. A., Banjavic, R. A. & Sum, S. W. A new ultrasound tissue-equivalent material. *Radiology* **134**, 517–520 (1980).
210. Rajagopal, S., Sathoo, N. & Zeqiri, B. Reference Characterisation of Sound Speed and Attenuation of the IEC Agar-Based Tissue-Mimicking Material Up to a Frequency of 60MHz. *Ultrasound Med. Biol.* **41**, 317–333 (2015).
211. IEC. *IEC 60601-2-37:2007 Particular requirements for the basic safety and essential performance of ultrasonic medical diagnostic and monitoring equipment.* <https://webstore.iec.ch/publication/2652> (2007).
212. Cournane, S., Fagan, A. J. & Browne, J. E. Review of ultrasound elastography quality control and training test phantoms. *Ultrasound* **20**, 16–23 (2012).
213. McDonald, M., Lochhead, S., Chopra, R. & Bronskill, M. J. Multi-modality tissue-mimicking

- phantom for thermal therapy. *Phys. Med. Biol.* **49**, 2767–2778 (2004).
214. Prokop, A. F. *et al.* Polyacrylamide gel as an acoustic coupling medium for focused ultrasound therapy. *Ultrasound Med. Biol.* **29**, 1351–1358 (2003).
  215. Yokoyama, F., Masada, I., Shimamura, K., Ikawa, T. & Monobe, K. Morphology and structure of highly elastic poly(vinyl alcohol) hydrogel prepared by repeated freezing-and-melting. *Colloid Polym. Sci.* **264**, 595–601 (1986).
  216. Yamaura, K., Itoh, M., Tanigami, T. & Matsuzawa, S. Properties of gels obtained by freezing/thawing of poly(vinyl alcohol)/water/dimethyl sulfoxide solutions. *J. Appl. Polym. Sci.* **37**, 2709–2718 (1989).
  217. Malone, A. J., Cournane, S., Naydenova, I. G., Fagan, A. J. & Browne, J. E. Polyvinyl alcohol cryogel based vessel mimicking material for modelling the progression of atherosclerosis. *Phys. Medica* **69**, 1–8 (2020).
  218. Surry, K. J. M., Austin, H. J. B., Fenster, A. & Peters, T. M. Poly(vinyl alcohol) cryogel phantoms for use in ultrasound and MR imaging. *Phys. Med. Biol.* **49**, 5529–5546 (2004).
  219. Dong, E. *et al.* Three-dimensional fuse deposition modeling of tissue-simulating phantom for biomedical optical imaging. *J. Biomed. Opt.* **20**, 121311 (2015).
  220. Cabrelli, L. C. *et al.* Stable phantom materials for ultrasound and optical imaging. *Phys. Med. Biol.* **62**, 432–447 (2017).
  221. Oudry, J., Bastard, C., Miette, V., Willinger, R. & Sandrin, L. Copolymer-in-oil phantom materials for elastography. *Ultrasound Med. Biol.* **35**, 1185–97 (2009).
  222. Spirou, G., Oraevsky, A., Vitkin, I. & Whelan, W. Optical and acoustic properties at 1064 nm of polyvinyl chloride-plastisol for use as a tissue phantom in biomedical optoacoustics. *Phys Med Biol* **50**, (2005).
  223. Bakaric, M., Miloro, P., Zeqiri, B., Cox, B. T. & Treeby, B. E. The Effect of Curing Temperature and Time on the Acoustic and Optical Properties of PVCP. *IEEE Trans. Ultrason. Ferroelectr. Freq. Control* **67**, 505–512 (2020).
  224. Madsen, E. L. *et al.* Tissue-mimicking oil-in-gelatin dispersions for use in heterogeneous elastography phantoms. *Ultrason. Imaging* **25**, 17–38 (2003).
  225. Hungr, N., Long, J. J.-A. A., Beix, V. & Troccaz, J. A realistic deformable prostate phantom for multimodal imaging and needle-insertion procedures. **39**, 2031–2041 (2012).
  226. Lualdi, M., Colombo, A., Farina, B., Tomatis, S. & Marchesini, R. A phantom with tissue-like optical properties in the visible and near infrared for use in photomedicine. *Lasers Surg. Med.* **28**, 237–243 (2001).

227. Wilson, D. J., Ridgway, J. P. & Evans, A. *Clinical Physics and Physiological Measurement To cite this article: J Robertson et al. Clin. Phys. Physiol. Meas* vol. 13 (1992).
228. - Document - ICRU REPORT 61: TISSUE SUBSTITUTES, PHANTOMS AND COMPUTATIONAL MODELLING IN MEDICAL ULTRASOUND. <https://go.gale.com/ps/anonymous?id=GALE%7CA57827691&sid=googleScholar&v=2.1&it=r&linkaccess=abs&issn=00338397&p=AONE&sw=w>.
229. Cafarelli, A., Miloro, P., Verbeni, A., Carbone, M. & Menciassi, A. Speed of sound in rubber-based materials for ultrasonic phantoms. *J. Ultrasound* **19**, 251–256 (2016).
230. Vernon, M. L., Fréchet, J., Painchaud, Y., Caron, S. & Beaudry, P. Fabrication and characterization of a solid polyurethane phantom for optical imaging through scattering media. *Appl. Opt.* **38**, 4247 (1999).
231. Firbank, M. *et al.* An improved design for a stable and reproducible phantom material for use in near-infrared spectroscopy and imaging. *Phys. Med. Biol.* **40**, 955–961 (1995).
232. Firbank, M. & Delpy, D. T. A phantom for the testing and calibration of near infra-red spectrometers. *Phys. Med. Biol.* **39**, 1509–1513 (1994).
233. Sukowski, U., Schubert, F., Grosenick, D. & Rinneberg, H. Preparation of solid phantoms with defined scattering and absorption properties for optical tomography. *Phys. Med. Biol.* **41**, 1823–1844 (1996).
234. Clarke, A. J., Evans, J. A., Truscott, J. G., Milner, R. & Smith, M. A. *A phantom for quantitative ultrasound of trabecular bone. Phys. Med. Biol* vol. 39 (1994).
235. Hale, G. M. & Querry, M. R. Optical Constants of Water in the 200-nm to 200- $\mu$ m Wavelength Region. *Appl. Opt.* **12**, 555 (1973).
236. Hassan, C. M. & Peppas, N. A. Structure and applications of poly(vinyl alcohol) hydrogels produced by conventional crosslinking or by freezing/thawing methods. *Advances in Polymer Science* vol. 153 37–65 (2000).
237. Mori, Y., Tokura, H. & Yoshikawa, M. Properties of hydrogels synthesized by freezing and thawing aqueous polyvinyl alcohol solutions and their applications. *J. Mater. Sci.* **32**, 491–496 (1997).
238. Wan, W. K., Campbell, G., Zhang, Z. F., Hui, A. J. & Boughner, D. R. Optimizing the tensile properties of polyvinyl alcohol hydrogel for the construction of a bioprosthetic heart valve stent. *J. Biomed. Mater. Res.* **63**, 854–861 (2002).
239. Pazos, V., Mongrain, R. & Tardif, J. C. Polyvinyl alcohol cryogel: Optimizing the parameters of cryogenic treatment using hyperelastic models. *J. Mech. Behav. Biomed. Mater.* **2**, 542–549

- (2009).
240. Devi, C. U., Vasu, R. M. & Sood, A. K. Design, fabrication, and characterization of a tissue-equivalent phantom for optical elastography. *J. Biomed. Opt.* **10**, 044020 (2005).
  241. Flock, S. T., Jacques, S. L., Wilson, B. C., Star, W. M. & van Gemert, M. J. C. Optical properties of intralipid: A phantom medium for light propagation studies. *Lasers Surg. Med.* **12**, 510–519 (1992).
  242. van Staveren, H. J., Moes, C. J. M., van Marie, J., Prahl, S. A. & van Gemert, M. J. C. Light scattering in Intralipid-10% in the wavelength range of 400–1100 nm. *Appl. Opt.* **30**, 4507 (1991).
  243. Di Ninni, P., Bérubé-Lauzière, Y., Mercatelli, L., Sani, E. & Martelli, F. Fat emulsions as diffusive reference standards for tissue simulating phantoms? *Appl. Opt.* **51**, 7176 (2012).
  244. Di Ninni, P., Martelli, F. & Zaccanti, G. Intralipid: towards a diffusive reference standard for optical tissue phantoms. *Phys. Med. Biol.* **56**, N21–N28 (2011).
  245. Michels, R., Foschum, F. & Kienle, A. Optical properties of fat emulsions. *Opt. Express* **16**, 5907 (2008).
  246. Lepore, M. & Delfino, I. Intralipid-Based Phantoms for the Development of New Optical Diagnostic Techniques. *Open Biotechnol. J.* **13**, 163–172 (2019).
  247. Vishwanath, K., Pogue, B. & Mycek, M.-A. Quantitative fluorescence lifetime spectroscopy in turbid media: comparison of theoretical, experimental and computational methods. *Phys. Med. Biol.* **47**, 3387–3405 (2002).
  248. Saager, R. B., Quach, A., Rowland, R. A., Baldado, M. L. & Durkin, A. J. Low-cost tissue simulating phantoms with adjustable wavelength-dependent scattering properties in the visible and infrared ranges. *J. Biomed. Opt.* **21**, 067001 (2016).
  249. Ntombela, L., Adeleye, B. & Chetty, N. Low-cost fabrication of optical tissue phantoms for use in biomedical imaging. *Heliyon* **6**, (2020).
  250. Wróbel, M. S. *et al.* Multi-layered tissue head phantoms for noninvasive optical diagnostics. in *Journal of Innovative Optical Health Sciences* vol. 8 8 (World Scientific Publishing Co. Pte Ltd, 2015).
  251. Wróbel, M. S. *et al.* Use of optical skin phantoms for preclinical evaluation of laser efficiency for skin lesion therapy. *J. Biomed. Opt.* **20**, 085003 (2015).
  252. de Bruin, D. M. *et al.* Optical phantoms of varying geometry based on thin building blocks with controlled optical properties. *J. Biomed. Opt.* **15**, 025001 (2010).

253. Huang, X. & El-Sayed, M. A. Gold nanoparticles: Optical properties and implementations in cancer diagnosis and photothermal therapy. *Journal of Advanced Research* vol. 1 13–28 (2010).
254. Di Ninni, P., Martelli, F. & Zaccanti, G. The use of India ink in tissue-simulating phantoms. *Opt. Express* **18**, 26854 (2010).
255. Madsen, S. J., Patterson, M. S. & Wilson, B. C. The use of India ink as an optical absorber in tissue-simulating phantoms. *Phys. Med. Biol.* **37**, 985–993 (1992).
256. Iizuka, M., Sherar, M. & Vitkin, I. Optical Phantom Materials for Near Infrared Laser Photocoagulation Studies. *Lasers Surg. Med.* **25**, (1999).
257. Vitkin, I. A., Wilson, B. C. & Anderson, R. R. Analysis of layered scattering materials by pulsed photothermal radiometry: application to photon propagation in tissue. *Appl. Opt.* **34**, 2973 (1995).
258. Moffitt, T., Chen, Y.-C. & Prah, S. A. Preparation and characterization of polyurethane optical phantoms. *J. Biomed. Opt.* **11**, 041103 (2006).
259. Ramnarine, K. V., Anderson, T. & Hoskins, P. R. Construction and geometric stability of physiological flow rate wall-less stenosis phantoms. *Ultrasound Med. Biol.* **27**, 245–250 (2001).
260. Madsen, E. L., Zagzebski, J. A. & Frank, G. R. Oil-in-gelatin dispersions for use as ultrasonically tissue-mimicking materials. *Ultrasound Med. Biol.* **8**, 277–287 (1982).
261. D’Souza, W. D. *et al.* Tissue mimicking materials for a multi-imaging modality prostate phantom. *Med. Phys.* **28**, 688–700 (2001).
262. Quarto, G. *et al.* Recipes to make organic phantoms for diffusive optical spectroscopy. *Appl. Opt.* **52**, 2494–2502 (2013).
263. Merritt, S. *et al.* Comparison of Water and Lipid Content Measurements Using Diffuse Optical Spectroscopy and MRI in Emulsion Phantoms. *Technol. Cancer Res. Treat.* **2**, 563–569 (2003).
264. Linford, J., Shalev, S., Bews, J., Brown, R. & Schipper, H. Development of a tissue equivalent phantom for diaphanography. *Med. Phys.* **13**, 869–875 (1986).
265. Ebert, B. *et al.* Near-infrared fluorescent dyes for enhanced contrast in optical mammography: phantom experiments. *J. Biomed. Opt.* **6**, 134 (2001).
266. Cortese, L. *et al.* Liquid phantoms for near-infrared and diffuse correlation spectroscopies with tunable optical and dynamic properties. *Biomed. Opt. Express* **9**, 2068 (2018).
267. Hull, E. L., Nichols, M. G. & Foster, T. H. Quantitative broadband near-infrared spectroscopy of tissue-simulating phantoms containing erythrocytes. *Phys. Med. Biol.* **43**, 3381–3404 (1998).
268. Wang, D., Chen, Y. & Liu, J. T. C. A liquid optical phantom with tissue-like heterogeneities for

- confocal microscopy. *Biomed. Opt. Express* **3**, 3153 (2012).
269. Kleiser, S., Nasserri, N., Andresen, B., Greisen, G. & Wolf, M. Comparison of tissue oximeters on a liquid phantom with adjustable optical properties. *Biomed. Opt. Express* **7**, 2973 (2016).
270. Hyttel-Sorensen, S., Kleiser, S., Wolf, M. & Greisen, G. Calibration of a prototype NIRS oximeter against two commercial devices on a blood-lipid phantom. *Biomed. Opt. Express* **4**, 1662 (2013).
271. Kleiser, S., Hyttel-Sorensen, S., Greisen, G. & Wolf, M. Comparison of near-infrared oximeters in a liquid optical phantom with varying intralipid and blood content. in *Advances in Experimental Medicine and Biology* vol. 876 413–418 (Springer New York LLC, 2016).
272. Isler, H. *et al.* Liquid blood phantoms to validate NIRS oximeters: Yeast versus nitrogen for deoxygenation. in *Advances in Experimental Medicine and Biology* vol. 1072 381–385 (Springer New York LLC, 2018).
273. Hunter, R. J., Patterson, M. S., Farrell, T. J. & Hayward, J. E. Haemoglobin oxygenation of a two-layer tissue-simulating phantom from time-resolved reflectance: effect of top layer thickness. *Phys. Med. Biol.* **47**, 193–208 (2002).
274. Blumenröther, E., Melchert, O., Wollweber, M. & Roth, B. Detection, numerical simulation and approximate inversion of optoacoustic signals generated in multi-layered PVA hydrogel based tissue phantoms. *Photoacoustics* **4**, 125–132 (2016).
275. Kimbrough, C. W., Hudson, S., Khanal, A., Egger, M. E. & McNally, L. R. Orthotopic pancreatic tumors detected by optoacoustic tomography using Syndecan-1. *J. Surg. Res.* **193**, 246–254 (2015).
276. Loginova, D. A., Sergeeva, E. A., Krainov, A. D., Agrba, P. D. & Kirillin, M. Y. Liquid optical phantoms mimicking spectral characteristics of laboratory mouse biotissues. *Quantum Electron.* **46**, 528–533 (2016).
277. Bisailon, C.-É., Dufour, M. L. & Lamouche, G. Artery phantoms for intravascular optical coherence tomography: healthy arteries. *Biomed. Opt. Express* **2**, 2599 (2011).
278. Del Bianco, S. *et al.* Liquid phantom for investigating light propagation through layered diffusive media. *Opt. Express* **12**, 2102 (2004).
279. Moes, C. J. M., van Gemert, M. J. C., Star, W. M., Marijnissen, J. P. A. & Prahl, S. A. Measurements and calculations of the energy fluence rate in a scattering and absorbing phantom at 633 nm. *Appl. Opt.* **28**, 2292 (1989).
280. Samarov, D. V. *et al.* Algorithm validation using multicolor phantoms. *Biomed. Opt. Express* **3**, 1300 (2012).

281. Manohar, S., Kharine, A., Hespen, J. van, Steenbergen, W. & Leeuwen, T. van. Photoacoustic mammography laboratory prototype: imaging of breast tissue phantoms. *J Biomed Opt* **9**, (2004).
282. Richards-Kortum, R. & Sevick-Muraca, E. Quantitative optical spectroscopy for tissue diagnosis. *Annu. Rev. Phys. Chem.* **47**, 555–606 (1996).
283. Gorpas, D. *et al.* Multi-Parametric Standardization of Fluorescence Imaging Systems Based on a Composite Phantom. *IEEE Trans. Biomed. Eng.* **67**, 185–192 (2020).
284. Lee, J. Y. K. *et al.* Review of clinical trials in intraoperative molecular imaging during cancer surgery. *J. Biomed. Opt.* **24**, 1 (2019).
285. Ruiz, A. J. *et al.* Indocyanine green matching phantom for fluorescence-guided surgery imaging system characterization and performance assessment. *J. Biomed. Opt.* **25**, 1 (2020).
286. Glacomini, A. Ultrasonic Velocity in Ethanol-Water Mixtures. *J. Acoust. Soc. Am.* **19**, 701–702 (1947).
287. Doyley, M. M. *et al.* Shear modulus estimation using parallelized partial volumetric reconstruction. *IEEE Trans. Med. Imaging* **23**, 1404–1416 (2004).
288. Teirlinck, C. J. P. M. *et al.* Development of an example flow test object and comparison of five of these test objects, constructed in various laboratories. *Ultrasonics* **36**, 653–660 (1998).
289. Hall, T. J., Bilgen, M., Insana, M. F. & Krouskop, T. A. Phantom materials for elastography. *IEEE Trans. Ultrason. Ferroelectr. Freq. Control* **44**, 1355–1365 (1997).
290. Jiang, S. Near-infrared breast tomography calibration with optoelastic tissue simulating phantoms. *J. Electron. Imaging* **12**, 613 (2003).
291. Kleiser, S., Nasser, N., Andresen, B., Greisen, G. & Wolf, M. Comparison of tissue oximeters on a liquid phantom with adjustable optical properties. *Biomed. Opt. Express* **7**, 2973 (2016).
292. Afshari, A. *et al.* Cerebral oximetry performance testing with a 3D-printed vascular array phantom. *Biomed. Opt. Express* **10**, 3731 (2019).
293. Hussain, A., Petersen, W., Staley, J., Hondebrink, E. & Steenbergen, W. Quantitative blood oxygen saturation imaging using combined photoacoustics and acousto-optics. *Opt. Lett.* **41**, 1720 (2016).
294. Pfefer, T. J., Chan, K. F., Hammer, D. X. & Welch, A. J. Dynamics of pulsed holmium:YAG laser photocoagulation of albumen. *Phys. Med. Biol.* **45**, 1099–1114 (2000).
295. Takegami, K. *et al.* Polyacrylamide gel containing egg white as new model for irradiation experiments using focused ultrasound. *Ultrasound Med. Biol.* **30**, 1419–1422 (2004).
296. Khokhlova, V. A. *et al.* Effects of nonlinear propagation, cavitation, and boiling in lesion

- formation by high intensity focused ultrasound in a gel phantom. *J. Acoust. Soc. Am.* **119**, 1834–1848 (2006).
297. Lafon, C. *et al.* Gel phantom for use in high-intensity focused ultrasound dosimetry. *Ultrasound Med. Biol.* **31**, 1383–1389 (2005).
  298. Choi, M. J., Guntur, S. R., Lee, K. I. L., Paeng, D. G. & Coleman, A. A Tissue Mimicking Polyacrylamide Hydrogel Phantom for Visualizing Thermal Lesions Generated by High Intensity Focused Ultrasound. *Ultrasound Med. Biol.* **39**, 439–448 (2013).
  299. Krauter, P. *et al.* Optical phantoms with adjustable subdiffusive scattering parameters. *J. Biomed. Opt.* **20**, 105008 (2015).
  300. Avanaki, M. R. N., Podoleanu, A. G., Price, M. C., Corr, S. A. & Hojjatoleslami, S. A. Two applications of solid phantoms in performance assessment of optical coherence tomography systems. *Appl. Opt.* **52**, 7054–7061 (2013).
  301. Greening, G. J. *et al.* Characterization of thin poly(dimethylsiloxane)-based tissue-simulating phantoms with tunable reduced scattering and absorption coefficients at visible and near-infrared wavelengths. *J. Biomed. Opt.* **19**, 115002 (2014).
  302. Saager, R. B., Quach, A., Kennedy, G. T., Tromberg, B. J. & Durkin, A. J. From theory to practice: the broadening role of polydimethylsiloxane phantoms as an intermediary between model validation and instrument performance testing (Conference Presentation). in *Design and Quality for Biomedical Technologies IX* (eds. Raghavachari, R., Liang, R. & Pfefer, T. J.) vol. 9700 15 (SPIE, 2016).
  303. Kennedy, G. T. G. T. *et al.* Solid tissue simulating phantoms having absorption at 970 nm for diffuse optics. *J. Biomed. Opt.* **22**, 076013 (2017).
  304. Lurie, K. L., Smith, G. T., Khan, S. A., Liao, J. C. & Ellerbee, A. K. Three-dimensional, distendable bladder phantom for optical coherence tomography and white light cystoscopy. *J. Biomed. Opt.* **19**, 036009 (2014).
  305. Monte, A. F. G., Reis, A. F., Cruz Junior, L. B. & Antunes, A. Preparation and quantitative characterization of polydimethylsiloxane optical phantoms with zinc-phthalocyanine dye absorbers. *Appl. Opt.* **57**, 5865 (2018).
  306. Curatolo, A., Kennedy, B. F. & Sampson, D. D. Structured three-dimensional optical phantom for optical coherence tomography. *Opt. Express* **19**, 19480 (2011).
  307. Park, J., Ha, M., Yu, S. & Jung, B. Fabrication of various optical tissue phantoms by the spin-coating method. *J. Biomed. Opt.* **21**, 065008 (2016).
  308. Little, C. D. *et al.* Micron resolution, high-fidelity three-dimensional vascular optical imaging

- phantoms. *J. Biomed. Opt.* **24**, 1 (2019).
309. Beck, G. C., Akgün, N., Rück, A. & Steiner, R. Design and characterisation of a tissue phantom system for optical diagnostics. *Lasers Med. Sci.* **13**, 160–171 (1998).
310. Bays, R. *et al.* Three-dimensional optical phantom and its application in photodynamic therapy. *Lasers Surg. Med.* **21**, 227–234 (1997).
311. Baxi, J. *et al.* Retina-simulating phantom for optical coherence tomography. *J. Biomed. Opt.* **19**, 021106 (2013).
312. Diao, D. Y. *et al.* Durable rough skin phantoms for optical modeling. *Phys. Med. Biol.* **59**, 485–492 (2014).
313. Bykov, A. V., Popov, A. P., Priezzhev, A. V. & Myllyla, R. Multilayer tissue phantoms with embedded capillary system for OCT and DOCT imaging. in (eds. Leitgeb, R. A. & Bouma, B. E.) 80911R (2011). doi:10.1117/12.889923.
314. Bae, Y., Son, T., Park, J. & Jung, B. Fabrication of a thin-layer solid optical tissue phantom by a spin-coating method: pilot study. *J. Biomed. Opt.* **18**, 025006 (2013).
315. Hebden, J. C., Hall, D. J., Firbank, M. & Delpy, D. T. Time-resolved optical imaging of a solid tissue-equivalent phantom. *Appl. Opt.* **34**, 8038 (1995).
316. Koh, P. H., Elwell, C. E. & Delpy, D. T. Development of a dynamic test phantom for optical topography. in *Advances in Experimental Medicine and Biology* vol. 645 141–146 (Springer, Boston, MA, 2009).
317. Zhu, B., Tan, I. C., Rasmussen, J. C. & Sevick-Mraca, E. M. Validating the sensitivity and performance of near-infrared fluorescence imaging and tomography devices using a novel solid phantom and measurement approach. *Technol. Cancer Res. Treat.* **11**, 95–104 (2012).
318. Pifferi, A. *et al.* Mechanically switchable solid inhomogeneous phantom for performance tests in diffuse imaging and spectroscopy. *J. Biomed. Opt.* **20**, 121304 (2015).
319. Swartling, J., Dam, J. S. & Andersson-Engels, S. Comparison of spatially and temporally resolved diffuse-reflectance measurement systems for determination of biomedical optical properties. *Appl. Opt.* **42**, 4612 (2003).
320. Gorpas, D., Koch, M., Anastasopoulou, M., Klemm, U. & Ntziachristos, V. Benchmarking of fluorescence cameras through the use of a composite phantom. *J. Biomed. Opt.* **22**, 016009 (2017).
321. Zhu, B., Rasmussen, J. C., Litorja, M. & Sevick-Muraca, E. M. Determining the Performance of Fluorescence Molecular Imaging Devices Using Traceable Working Standards with SI Units of Radiance. *IEEE Trans. Med. Imaging* **35**, 802–811 (2016).

322. Pleijhuis, R. *et al.* Tissue-simulating phantoms for assessing potential near-infrared fluorescence imaging applications in breast cancer surgery. *J. Vis. Exp.* e51776 (2014) doi:10.3791/51776.
323. van Willigen, D. M. *et al.* Multispectral fluorescence guided surgery; a feasibility study in a phantom using a clinical-grade laparoscopic camera system. *Am. J. Nucl. Med. Mol. Imaging* **7**, 138–147 (2017).
324. Xie, Y. *et al.* Soft optically-tuneable fluorescence phantoms based on gel wax and quantum dots: a tissue surrogate for fluorescence imaging validation. in *Molecular-Guided Surgery: Molecules, Devices, and Applications V* (eds. Pogue, B. W. & Gioux, S.) 10 (SPIE, 2019). doi:10.1117/12.2508348.
325. Maggi, L. *et al.* Ultrasonic Attenuation and Speed in Phantoms Made of PVCP and Evaluation of Acoustic and Thermal Properties of Ultrasonic Phantoms Made of polyvinyl chloride-plastisol (PVCP).
326. Cortela, G., Benech, N., Pereira, W. C. A. & Negreira, C. Characterization of acoustical properties of a phantom for soft tissues (PVCP and Graphite Powder) in the range 20–45°C. in *Physics Procedia* vol. 70 179–182 (Elsevier, 2015).
327. De Carvalho, I. M. *et al.* Polyvinyl chloride plastisol breast phantoms for ultrasound imaging. *Ultrasonics* **70**, 98–106 (2016).
328. Li, W. *et al.* Polyvinyl chloride as a multimodal tissue-mimicking material with tuned mechanical and medical imaging properties. *Med. Phys.* **43**, 5577–5592 (2016).
329. Spinelli, L. *et al.* Calibration of scattering and absorption properties of a liquid diffusive medium at NIR wavelengths. Time-resolved method. *Opt. Express* **15**, 6589 (2007).
330. Spinelli, L. *et al.* Blood-lipid liquid phantom for assessing time and frequency domain tissue oximeter performances. in *Optics InfoBase Conference Papers* (eds. Dehghani, H. & Wabnitz, H.) vol. Part F142- 48 (SPIE, 2019).
331. Madsen, E. L., Hobson, M. A., Shi, H., Varghese, T. & Frank, G. R. Stability of heterogeneous elastography phantoms made from oil dispersions in aqueous gels. *Ultrasound Med. Biol.* **32**, 261–270 (2006).
332. Cubeddu, R., Pifferi, A., Taroni, P., Torricelli, A. & Valentini, G. A solid tissue phantom for photon migration studies. *Phys. Med. Biol.* **42**, 1971–1979 (1997).
333. Bini, M. G. *et al.* The Polyacrylamide as a Phantom Material for Electromagnetic Hyperthermia Studies. *IEEE Trans. Biomed. Eng.* **BME-31**, 317–322 (1984).
334. Chu, K. C. & Rutt, B. K. Polyvinyl alcohol cryogel: An ideal phantom material for MR studies of arterial flow and elasticity. *Magn. Reson. Med.* **37**, 314–319 (1997).

335. Jiang, S., Liu, S. & Feng, W. PVA hydrogel properties for biomedical application. *J. Mech. Behav. Biomed. Mater.* **4**, 1228–1233 (2011).
336. Fromageau, J., Brusseau, E., Vray, D., Gimenez, G. & Delachartre, P. Characterization of PVA cryogel for intravascular ultrasound elasticity imaging. *IEEE Trans. Ultrason. Ferroelectr. Freq. Control* **50**, 1318–24 (2003).
337. Hyon, S. H., Cha, W. I. & Ikada, Y. Preparation of transparent poly(vinyl alcohol) hydrogel. *Polym. Bull.* **22**, 119–122 (1989).
338. Yon, S. H. H. *et al.* Poly (Vinyl Alcohol) Hydrogels as Soft Contact Lens Material. *J. Biomater. Sci. Polym. Ed.* **5**, 397–406 (1994).
339. Cabrelli, L. C. *et al.* Copolymer-in-oil phantoms for photoacoustic imaging. in *2015 IEEE International Ultrasonics Symposium (IUS)* 1–4 (IEEE, 2015). doi:10.1109/ULTSYM.2015.0395.
340. Wabnitz, H. *et al.* Performance assessment of time-domain optical brain imagers, part 2: nEUROPt protocol. *J. Biomed. Opt.* **19**, 086012 (2014).
341. Ohmae, E. *et al.* Stable tissue-simulating phantoms with various water and lipid contents for diffuse optical spectroscopy. *Biomed. Opt. Express* **9**, 5792 (2018).
342. Andersson-Engels, S., Berg, R. & Svanberg, S. Effects of optical constants on time-gated transillumination of tissue and tissue-like media. *J. Photochem. Photobiol. B Biol.* **16**, 155–167 (1992).
343. Pogue, B. W., Patterson, M. S., Jiang, H. & Paulsen, K. D. Initial assessment of a simple system for frequency domain diffuse optical tomography. *Phys. Med. Biol.* **40**, 1709–1729 (1995).
344. Cubeddu, R., Pifferi, A., Taroni, P., Torricelli, A. & Valentini, G. Time-resolved imaging on a realistic tissue phantom:  $\mu_s'$  and  $\mu_a$  images versus time-integrated images. *Appl. Opt.* **35**, 4533 (1996).
345. Li, X. & Su, X. Multifunctional smart hydrogels: Potential in tissue engineering and cancer therapy. *Journal of Materials Chemistry B* vol. 6 4714–4730 (2018).
346. Khan, S., Ullah, A., Ullah, K. & Rehman, N. U. Insight into hydrogels. *Designed Monomers and Polymers* vol. 19 456–478 (2016).
347. Mustari, A. *et al.* Agarose-based tissue mimicking optical phantoms for diffuse reflectance spectroscopy. *J. Vis. Exp.* **2018**, e57578 (2018).
348. Wagnières, G. *et al.* An optical phantom with tissue-like properties in the visible for use in PDT and fluorescence spectroscopy. *Phys. Med. Biol.* **42**, 1415–1426 (1997).

349. Saiko, G., Zheng, X., Betlen, A. & Douplik, A. Fabrication and optical characterization of gelatin-based phantoms for tissue oximetry. in *Advances in Experimental Medicine and Biology* vol. 1232 369–374 (Springer, 2020).
350. Hielscher, A. H., Liu, H., Chance, B., Tittel, F. K. & Jacques, S. L. Time-resolved photon emission from layered turbid media. *Appl. Opt.* **35**, 719 (1996).
351. Geoghegan, R. *et al.* A tissue-mimicking prostate phantom for 980 nm laser interstitial thermal therapy. *Int. J. Hyperth.* **36**, 992–1001 (2019).
352. Culjat, M. O., Goldenberg, D., Tewari, P. & Singh, R. S. A Review of Tissue Substitutes for Ultrasound Imaging. *Ultrasound Med. Biol.* **36**, 861–873 (2010).
353. General Purpose Ultrasound Phantom - CIRS. <https://www.cirsinc.com/products/ultrasound/zerdine-hydrogel/general-purpose-ultrasound-phantom/>.
354. Yang, X., Tong, Y. Y., Li, Z. C. & Liang, D. Aggregation-induced microgelation: A new approach to prepare gels in solution. *Soft Matter* **7**, 978–985 (2011).
355. Goharian, M. *et al.* Modifying the MRI, elastic stiffness and electrical properties of polyvinyl alcohol cryogel using irradiation. *Nucl. Instruments Methods Phys. Res. Sect. B Beam Interact. with Mater. Atoms* **263**, 239–244 (2007).
356. Nagura, M., Nagura, M. & Ishikawa, H. State of water in highly elastic poly(vinyl alcohol) hydrogels prepared by repeated freezing and melting. *Polym. Commun. Guildf.* **25**, 313–314 (1984).
357. Mano, I., Goshima, H., Nambu, M. & Iio, M. New polyvinyl alcohol gel material for MRI phantoms. *Magn. Reson. Med.* **3**, 921–926 (1986).
358. Firbank, M. J. An improved design for a stable a reproducible phantom material for use in near infra red spectroscopy and imaging. *Artic. Phys. Med. Biol.* (1995) doi:10.1088/0031-9155/40/5/016.
359. Firbank, M., Oda, M. & Delpy, D. T. An improved design for a stable and reproducible phantom material for use in near-infrared spectroscopy and imaging. *Phys. Med. Biol.* **40**, 955–961 (1995).
360. Hebden, J. C. *et al.* An electrically-activated dynamic tissue-equivalent phantom for assessment of diffuse optical imaging systems. *Phys. Med. Biol.* **53**, 329–337 (2008).
361. Netz, U. J., Toelsner, J. & Bindig, U. Calibration standards and phantoms for fluorescence optical measurements. *Med. Laser Appl.* **26**, 101–108 (2011).
362. Zhu, B., Rasmussen, J. C. & Sevick-Muraca, E. M. A matter of collection and detection for

- intraoperative and noninvasive near-infrared fluorescence molecular imaging: To see or not to see? *Med. Phys.* **41**, (2014).
363. Tatarinov, A., Pontaga, I. & Vilks, U. *Modeling the influence of mineral content and porosity on ultrasound parameters in bone by using synthetic phantoms. Mechanics of Composite Materials* vol. 35 (1999).
364. Falardeau, T. & Belanger, P. Ultrasound tomography in bone mimicking phantoms: Simulations and experiments. *J. Acoust. Soc. Am.* **144**, 2937–2946 (2018).
365. Wydra, A. & Maev, R. G. A novel composite material specifically developed for ultrasound bone phantoms: cortical, trabecular and skull. *Phys. Med. Biol.* **58**, N303–N319 (2013).
366. Goldstein, A. The effect of acoustic velocity on phantom measurements. *Ultrasound Med. Biol.* **26**, 1133–1143 (2000).
367. Dernehl, C. Health Hazards Associated With Polyurethane Foams - PubMed. *J Occup Med.* 59–62 (1966).
368. Saager, R. B. *et al.* Multilayer silicone phantoms for the evaluation of quantitative optical techniques in skin imaging. in *Design and Performance Validation of Phantoms Used in Conjunction with Optical Measurement of Tissue II* (ed. Nordstrom, R. J.) vol. 7567 756706 (SPIE, 2010).
369. Bisailon, C. E., Lamouche, G., Maciejko, R., Dufour, M. & Monchalain, J. P. Deformable and durable phantoms with controlled density of scatterers. *Phys. Med. Biol.* **53**, (2008).
370. Homma, H., Mirley, C. L., Ronzello, J. A. & Boggs, S. A. Field and laboratory aging of RTV silicone insulator coatings. *IEEE Trans. Power Deliv.* **15**, 1298–1303 (2000).
371. Davis, D., McConnell, R., MF Meyer Jr - US Patent 4, 401,720 & 1983, undefined. *Poly (vinyl chloride) plastisol compositions.* Google Patents <https://patents.google.com/patent/US4401720A/en> (1982).
372. Rybachuk, G. V., Kozlova, I. I., Mozhukhin, V. B. & Guzeev, V. V. PVC plastisols: Preparation, properties, and application. *Polym. Sci. - Ser. C* **49**, 6–12 (2007).
373. Heudorf, U., Mersch-Sundermann, V. & Angerer, J. Phthalates: Toxicology and exposure. *Int. J. Hyg. Environ. Health* **210**, 623–634 (2007).
374. Legge, N. R.; Holden, G.; Schroeder, H. E. Thermoplastic Elastomers. *Hanser: Munich* (1996).
375. Jones, C. J. M. & Munro, P. R. T. Stability of gel wax based optical scattering phantoms. *Biomed. Opt. Express* **9**, 3495–3502 (2018).
376. Suzuki, A. *et al.* Oil Gel-Based Phantom for Evaluating Quantitative Accuracy of Speed of

- Sound Measured in Ultrasound Computed Tomography. *Ultrasound Med. Biol.* **45**, 2554–2567 (2019).
377. Oudry, J. *et al.* Cross-validation of magnetic resonance elastography and ultrasound-based transient elastography: A preliminary phantom study. *J. Magn. Reson. Imaging* **30**, 1145–1150 (2009).
378. Szabo, T. L. Diagnostic Ultrasound Imaging - Inside out. in *Diagnostic Ultrasound Imaging* 243–295 (Elsevier, 2004). doi:10.1016/B978-012680145-3/50010-4.
379. Azarov, I. *et al.* Rate of nitric oxide scavenging by hemoglobin bound to haptoglobin. *Nitric oxide Biol. Chem.* **18**, 296–302 (2008).
380. IEC TS 63081:2019 | IEC Webstore. <https://webstore.iec.ch/publication/32282>.
381. Sun, J. Y. *et al.* Highly stretchable and tough hydrogels. *Nature* **489**, 133–136 (2012).
382. Sjoding, M. W., Dickson, R. P., Iwashyna, T. J., Gay, S. E. & Valley, T. S. Racial Bias in Pulse Oximetry Measurement. *N. Engl. J. Med.* **383**, 2477–2478 (2020).
383. Pickering, J. W. *et al.* Double-integrating-sphere system for measuring the optical properties of tissue. *Appl. Opt.* **32**, 399 (1993).
384. Troy, T. L. & Thennadil, S. N. Optical properties of human skin in the near infrared wavelength range of 1000 to 2200 nm. *J. Biomed. Opt.* **6**, 167 (2001).
385. Zamora-Rojas, E. *et al.* Double integrating sphere measurements for estimating optical properties of pig subcutaneous adipose tissue. *Innov. Food Sci. Emerg. Technol.* **19**, 218–226 (2013).
386. Aernouts, B. *et al.* Supercontinuum laser based optical characterization of Intralipid® phantoms in the 500-2250 nm range. *osapublishing.org* (2013) doi:10.1364/OE.21.032450.
387. \* Oregon Tech, E. & Sw Parkway, A. *Everything I think you should know about Inverse Adding-Doubling*. <http://omlc.org> (2011).
388. Yang, L. *et al.* Space-enhanced time-domain diffuse optics for determination of tissue optical properties in two-layered structures. *Biomed. Opt. Express* **11**, 6570 (2020).
389. Alerstam, E., Svensson, T., Andersson-Engels, S. & Letters, J. Parallel computing with graphics processing units for high-speed Monte Carlo simulation of photon migration. <https://doi.org/10.1117/1.3041496> **13**, 060504 (2008).
390. Wang, L., Jacques, S. L. & Zheng, L. MCML—Monte Carlo modeling of light transport in multi-layered tissues. *Comput. Methods Programs Biomed.* **47**, 131–146 (1995).
391. Wabnitz, H. *et al.* Accurate characterization of phantoms for performance assessment and

- calibration in diffuse optics. <https://doi.org/10.1117/12.2588994> **11633**, 1163306 (2021).
392. Sedlacek, A. J. *et al.* SP2-induced charring of organic aerosol. *Aerosol Sci. Technol.* **52**, 1345–1350 (2018).
393. Jacques, S. L. Origins of Tissue Optical Properties in the UVA, Visible, and NIR Regions. *OSA Trends Opt. Photonics, Vol.2 Adv. Opt. Imaging Phot. Migr.* 364–371 (1996).
394. Mätzler, C. *MATLAB Functions for Mie Scattering and Absorption*. <https://omlc.org/software/mie/maetzlermie/Maetzler2002.pdf> (2002).
395. Pierscionek, B. Refractive Index of the Human Lens Surface Measured with an Optic Fibre Sensor. *Ophthalmic Res.* **26**, 32–35 (1994).
396. Polysciences, I. *TECHNICAL DATA SHEET 238, Polybead polystyrene microspheres*. <http://www.polysciences.com/skin/frontend/default/polysciences/pdf/238-Polystyrene-FAQ.pdf> (2016).
397. Giavarina, D. Understanding Bland Altman analysis. *Biochem. Medica* **25**, 141 (2015).
398. Hussain, B., Nawaz, M., Ahmed, M. & Yasin Akhtar Raja, M. Measurement of thickness and refractive index using femtosecond and terahertz pulses. *Laser Phys. Lett.* **10**, 055301 (2013).
399. Zhu, D., Lu, W., Zeng, S. & Luo, Q. Effect of light losses of sample between two integrating spheres on optical properties estimation. <https://doi.org/10.1117/1.2815691> **12**, 064004 (2007).
400. Hu, D., Lu, R., Huang, Y., Ying, Y. & Fu, X. Effects of optical variables in a single integrating sphere system on estimation of scattering properties of turbid media. *Biosyst. Eng.* **194**, 82–98 (2020).
401. Moes, C. J. M., Sterenborg, H. J. C. M., Pickering, J. W., Gemert, M. J. C. van & Prahl, S. A. Two integrating spheres with an intervening scattering sample. *JOSA A, Vol. 9, Issue 4, pp. 621-631* **9**, 621–631 (1992).
402. Zeqiri, B. An intercomparison of discrete-frequency and broadband techniques for the determination of ultrasonic attenuation. *Phys. Med. Ultrasound* 27–35 (1988).
403. Bamber, J. C. Attenuation and absorption. *Phys. Princ. Med. Ultrason.* **2**, 93–166 (1986).
404. Sachse, W. & Pao, Y. H. On the determination of phase and group velocities of dispersive waves in solids. *J. Appl. Phys.* **49**, 4320 (2008).
405. Kline, R. A. Measurement of attenuation and dispersion using an ultrasonic spectroscopy technique. *J. Acoust. Soc. Am.* **76**, 498 (1998).
406. Bolef, D. I. & De Klerk, J. Some Continuous-Wave Techniques for the Measurement of Velocity and Attenuation of Ultrasonic Waves Between 1 and 1000 Mc. *IEEE Trans. Ultrason. Eng.* **10**,

- 19–26 (1963).
407. McSkimin, H. J. Ultrasonic Methods for Measuring the Mechanical Properties of Liquids and Solids. *Phys. Acoust.* 271–334 (1964) doi:10.1016/B978-1-4832-2857-0.50010-1.
  408. Stephens, R. W. B. Ultrasonic spectral analysis for non-destructive evaluation. *Ultrasonics* **21**, 284 (1983).
  409. Povey, M. J. W. (Malcolm J. W. . *Ultrasonic techniques for fluids characterization*. (Academic Press, 1997).
  410. Bond, L. J. Basic Inspection Methods (Pulse-Echo and Transmission Methods). *Nondestruct. Eval. Mater.* 169–183 (2018) doi:10.31399/ASM.HB.V17.A0006469.
  411. Tran, H. T. K. & Hoff, L. *Characterization of Acoustic Material Properties Using Broadband Through-Transmission Technique. 117* (Høgskolen i Sørøst-Norge, 2016).
  412. Wu, J. Determination of velocity and attenuation of shear waves using ultrasonic spectroscopy. *J. Acoust. Soc. Am.* **99**, 2871–2875 (1996).
  413. Smith, J; Zimmermann, K. Ultrasound velocity in fixed human liver: empirical anova and regression modelling on histologically assessed abnormalities. in *Ultrason. Imaging* 280–94 (1983).
  414. Zeqiri, B., Scholl, W. & Robinson, S. P. Measurement and testing of the acoustic properties of materials: a review. *Metrologia* **47**, S156–S171 (2010).
  415. Greenspan, M. & Tschiegg, C. E. *Speed of Sound in Water by a Direct Method 1. Journal of Rese arch of the National Bureau of Standards* vol. 59 (1957).
  416. Del Grosso, V. A. & Mader, C. W. Speed of Sound in Pure Water. *J. Acoust. Soc. Am.* **52**, 1442–1446 (1972).
  417. Marczak, W. Water as a standard in the measurements of speed of sound in liquids. *J. Acoust. Soc. Am.* **102**, 2776 (1998).
  418. Xia, W., Piras, D., van Hespén, J. C. G., Steenbergen, W. & Manohar, S. A new acoustic lens material for large area detectors in photoacoustic breast tomography. *Photoacoustics* **1**, 9–18 (2013).
  419. Carlson, J. E., Van Deventer, J., Scolan, A. & Carlander, C. Frequency and temperature dependence of acoustic properties of polymers used in pulse-echo systems. *undefined* **1**, 885–888 (2003).
  420. Ono, K. A comprehensive report on ultrasonic attenuation of engineering materials, including metals, ceramics, polymers, fiber-reinforced composites, wood, and rocks. *Appl. Sci.* **10**, (2020).

421. Sutherland, H. J. & Lingle, R. An acoustic characterization of polymethyl methacrylate and three epoxy formulations. *J. Appl. Phys.* **43**, 4022 (1972).
422. He, P. & Zheng, J. Acoustic dispersion and attenuation measurement using both transmitted and reflected pulses.
423. Xu, W. & Kaufman, J. J. Diffraction correction methods for insertion ultrasound attenuation estimation. *IEEE Trans. Biomed. Eng.* **40**, 563–570 (1993).
424. Christiansen, W. N., Crabtree, R. W. & Laby, T. H. Density of light water: Ratio of deuterium to hydrogen in rain-water [1]. *Nature* **135**, 870 (1935).
425. Kell, G. S. Effects of isotopic composition, temperature, pressure, and dissolved gases on the density of liquid water. *J. Phys. Chem. Ref. Data* **6**, 1109–1131 (1977).
426. Ivory, A. M., Shah, A., Rajagopal, S. & Zeqiri, B. Development and investigation of the acoustic properties of tissue-mimicking materials for photoacoustic imaging techniques. in *IEEE International Ultrasonics Symposium, IUS* vols 2019-October 1489–1492 (IEEE Computer Society, 2019).
427. Cabrelli, L. C., Grillo, F. W., Carneiro, A. A. O. & Pavan, T. Z. Copolymer-in-oil tissue-mimicking material with tunable acoustic properties. in *2016 IEEE International Ultrasonics Symposium (IUS)* 1–4 (IEEE, 2016). doi:10.1109/ULTSYM.2016.7728859.
428. Mast, T. D. Empirical relationships between acoustic parameters in human soft tissues. *Acoust. Res. Lett. Online* **1**, 37–42 (2000).
429. Allen, N. S. *et al.* Degradation and stabilization of styrene-ethylene-butadiene-styrene (SEBS) block copolymer. *Polym. Degrad. Stab.* **71**, 113–122 (2000).
430. Pinkerton, J. M. M. The Absorption of Ultrasonic Waves in Liquids and its Relation to Molecular Constitution. *Proc. Phys. Soc. Sect. B* **62**, 129–141 (1949).
431. Dima, A., Burton, N. C. & Ntziachristos, V. Multispectral optoacoustic tomography at 64, 128, and 256 channels. *J. Biomed. Opt.* **19**, 036021 (2014).
432. Montalvão, D., Cláudio, R., Ribeiro, A. M. & Duarte-Silva, J. Experimental measurement of the complex Young's modulus on a CFRP laminate considering the constant hysteretic damping model. *Compos. Struct* **97**, 91–98 (2013).
433. Kishimoto, R. *et al.* Measuring shear-wave speed with point shear-wave elastography and MR elastography: A phantom study. *BMJ Open* **7**, (2017).
434. Nielsen, L. F., Wismer, N. J. & Gade, S. Improved method for complex modulus estimation. *Sound Vib* **34**, (2000).

435. Özkaya, N., Leger, D., Goldsheyder, D. & Nordin, M. Fundamentals of biomechanics: Equilibrium, motion, and deformation. (2016).
436. Nunes, R. W., Martin, J. R. & Johnson, J. F. Influence of molecular weight and molecular weight distribution on mechanical properties of polymers. *Polym. Eng. Sci.* **22**, 205–228 (1982).
437. Carvalho, A. J. F. Caracterização de géis termorreversíveis de SEBS. *Polímeros* **10**, 01–07 (2000).
438. Sandell, J. L. & Zhu, T. C. A review of in-vivo optical properties of human tissues and its impact on PDT. *J. Biophotonics* **4**, 773–787 (2011).
439. Chaudhuri, O., Cooper-White, J., Janmey, P. A., Mooney, D. J. & Shenoy, V. B. Effects of extracellular matrix viscoelasticity on cellular behaviour. *Nature* vol. 584 535–546 (2020).
440. Vieira, S. L., Pavan, T. Z., Junior, J. E. & Carneiro, A. A. O. Paraffin-gel tissue-mimicking material for ultrasound-guided needle biopsy phantom. *Ultrasound Med. Biol.* **39**, 2477–84 (2013).
441. Rajagopalan, B. & Greenleaf, J. *Variation of acoustic speed with temperature in various excised human tissues studied by ultrasound computerized tomography. Ultrasonic Tissue Characterization II.* vol. 525 (1977).
442. Cabrelli, L. C. *et al.* Oil-based gel phantom for ultrasound and optical imaging. in (eds. Kurachi, C., Svanberg, K., Tromberg, B. J. & Bagnato, V. S.) 95310L (2015). doi:10.1117/12.2180642.
443. Nguyen, M. M., Zhou, S., Robert, J. luc, Shamdasani, V. & Xie, H. Development of oil-in-gelatin phantoms for viscoelasticity measurement in ultrasound shear wave elastography. *Ultrasound Med. Biol.* **40**, 168–176 (2014).
444. Kim, J. K., Paglicawan, M. A. & Balasubramanian, M. Viscoelastic and gelation studies of SEBS thermoplastic elastomer in different hydrocarbon oils. *Macromol. Res.* **14**, 365–372 (2006).
445. Nicolas, E., Callé, S. & Remenieras, J.-P. Generating shear waves in the human brain for ultrasound elastography: a new approach. *Phys. Procedia* **70**, 1255–1259 (2015).
446. Grillo, F. W. *et al.* Patient-specific neurosurgical phantom: assessment of visual quality, accuracy, and scaling effects. *3D Print. Med.* **4**, (2018).
447. Nikitichev, D. I. *et al.* Construction of 3-Dimensional Printed Ultrasound Phantoms With Wall-less Vessels. *J. Ultrasound Med.* **35**, 1333–1339 (2016).
448. West, S. J. *et al.* Development of an ultrasound phantom for spinal injections with 3-dimensional printing. in *Regional Anesthesia and Pain Medicine* vol. 39 429–433 (Lippincott Williams and Wilkins, 2014).

449. Omar, M., Aguirre, J. & Ntziachristos, V. Optoacoustic mesoscopy for biomedicine. *Nat. Biomed. Eng.* **3**, 354–370 (2019).
450. Aguirre, J. *et al.* Precision assessment of label-free psoriasis biomarkers with ultra-broadband optoacoustic mesoscopy. *Nat. Biomed. Eng.* **1**, 0068 (2017).
451. Taruttis, A. & Ntziachristos, V. Advances in real-time multispectral optoacoustic imaging and its applications. *Nat. Photonics* **9**, 219–227 (2015).
452. Tanghetti MD, E. & Jennings, J. A comparative study with a 755 nm picosecond Alexandrite laser with a diffractive lens array and a 532 nm/1064 nm Nd:YAG with a holographic optic. *Lasers Surg. Med.* **50**, 37–44 (2018).
453. Schwarz, M., Buehler, A., Aguirre, J. & Ntziachristos, V. Three-dimensional multispectral optoacoustic mesoscopy reveals melanin and blood oxygenation in human skin *in vivo*. *J. Biophotonics* **9**, 55–60 (2016).
454. Omar, M., Schwarz, M., Soliman, D., Symvoulidis, P. & Ntziachristos, V. Pushing the Optical Imaging Limits of Cancer with Multi-Frequency-Band Raster-Scan Optoacoustic Mesoscopy (RSOM). *Neoplasia* **17**, 208–214 (2015).
455. Omar, M. *et al.* Optical imaging of post-embryonic zebrafish using multi orientation raster scan optoacoustic mesoscopy. *Light Sci. Appl.* **6**, e16186–e16186 (2017).
456. Knieling, F. *et al.* Raster-Scanning Optoacoustic Mesoscopy for Gastrointestinal Imaging at High Resolution. *Gastroenterology* **154**, 807-809.e3 (2018).
457. Aguirre, J. *et al.* Broadband mesoscopic optoacoustic tomography reveals skin layers. *Opt. Lett.* **39**, 6297 (2014).
458. Schwarz, M., Omar, M., Buehler, A., Aguirre, J. & Ntziachristos, V. Implications of Ultrasound Frequency in Optoacoustic Mesoscopy of the Skin. *IEEE Trans. Med. Imaging* **34**, 672–677 (2015).
459. Berezhnoi, A. *et al.* Assessing hyperthermia-induced vasodilation in human skin *in vivo* using optoacoustic mesoscopy. *J. Biophotonics* **11**, e201700359 (2018).
460. Yew, Y. W. *et al.* Investigation of morphological, vascular and biochemical changes in the skin of an atopic dermatitis (AD) patient in response to dupilumab using raster scanning optoacoustic mesoscopy (RSOM) and handheld confocal Raman spectroscopy (CRS). *Journal of Dermatological Science* vol. 95 123–125 (2019).
461. Li, G. *et al.* Tripling the detection view of high-frequency linear-array-based photoacoustic computed tomography by using two planar acoustic reflectors. *Quant. Imaging Med. Surg.* **5**, 57–62 (2015).

462. Li, M. *et al.* Linear array-based real-time photoacoustic imaging system with a compact coaxial excitation handheld probe for noninvasive sentinel lymph node mapping. *Biomed. Opt. Express* **9**, 1408 (2018).
463. Jaeger, M., Siegenthaler, L., Kitz, M. & Frenz, M. Reduction of background in optoacoustic image sequences obtained under tissue deformation. *J. Biomed. Opt.* **14**, 054011 (2009).
464. Nguyen, H. N. Y., Hussain, A. & Steenbergen, W. Reflection artifact identification in photoacoustic imaging using multi-wavelength excitation. *Biomed. Opt. Express* **9**, 4613–4630 (2018).
465. Nguyen, H. N. Y. & Steenbergen, W. Three-dimensional view of out-of-plane artifacts in photoacoustic imaging using a laser-integrated linear-transducer-array probe. *Photoacoustics* **19**, 100176 (2020).
466. Petrosyan, T., Theodorou, M., Bamber, J., Frenz, M. & Jaeger, M. Rapid scanning wide-field clutter elimination in epi-optoacoustic imaging using comb LOVIT. *Photoacoustics* **10**, 20–30 (2018).
467. Wagner, A. L. *et al.* Precision of handheld multispectral optoacoustic tomography for muscle imaging. *Photoacoustics* **21**, 100220 (2021).
468. Joseph, J., Ajith Singh, M. K., Sato, N. & Bohndiek, S. E. Technical validation studies of a dual-wavelength LED-based photoacoustic and ultrasound imaging system. *Photoacoustics* **22**, 100267 (2021).
469. Chen, P. *et al.* Acoustic characterization of tissue-mimicking materials for ultrasound perfusion imaging research. *Ultrasound Med. Biol.* **48**, 124–142 (2022).
470. Müller, B. *et al.* High-resolution tomographic imaging of microvessels. *Dev. X-Ray Tomogr. VI* **7078**, 70780B (2008).
471. Qian, B., Rudy, R. F., Cai, T. & Du, R. Cerebral artery diameter in inbred mice varies as a function of strain. *Front. Neuroanat.* **12**, (2018).
472. Bruna, A. *et al.* A Biobank of Breast Cancer Explants with Preserved Intra-tumor Heterogeneity to Screen Anticancer Compounds. *Cell* **167**, 260-274.e22 (2016).
473. Omar, M., Gateau, J. & Ntziachristos, V. Raster-scan optoacoustic mesoscopy in the 25–125 MHz range. *Opt. Lett.* **38**, 2472 (2013).
474. Omar, M., Soliman, D., Gateau, J. & Ntziachristos, V. Ultrawideband reflection-mode optoacoustic mesoscopy. *Opt. Lett.* **39**, 3911 (2014).
475. Schwarz, M. *et al.* Optoacoustic Dermoscopy of the Human Skin: Tuning Excitation Energy for Optimal Detection Bandwidth with Fast and Deep Imaging in vivo. *IEEE Trans. Med. Imaging*

- 36**, 1287–1296 (2017).
476. Schwarz, M., Buehler, A. & Ntziachristos, V. Isotropic high resolution optoacoustic imaging with linear detector arrays in bi-directional scanning. *J. Biophotonics* **8**, 60–70 (2015).
477. Schindelin, J. *et al.* Fiji: an open-source platform for biological-image analysis. *Nat. Methods* **9**, 676–682 (2012).
478. Brown, E. L. *et al.* Quantification of Vascular Networks in Photoacoustic Mesoscopy. *Photoacoustics* 100357 (2022) doi:10.1016/j.pacs.2022.100357.
479. Sternberg, S. R. Biomedical Image Processing. *Computer (Long. Beach. Calif.)*. **16**, 22–34 (1983).
480. Berg, S. *et al.* ilastik: interactive machine learning for (bio)image analysis. *Nat. Methods* **16**, 1226–1232 (2019).
481. Schwab, H.-M., Beckmann, M. F. & Schmitz, G. Photoacoustic clutter reduction by inversion of a linear scatter model using plane wave ultrasound measurements. *Biomed. Opt. Express* **7**, 1468 (2016).
482. Jaeger, M., Bamber, J. C. & Frenz, M. Clutter elimination for deep clinical optoacoustic imaging using localised vibration tagging (LOVIT). *Photoacoustics* **1**, 19–29 (2013).
483. Wu, D., Tao, C. & Liu, X. Photoacoustic tomography extracted from speckle noise in acoustically inhomogeneous tissue. *Opt. Express* **21**, 18061 (2013).
484. Kuniyil Ajith Singh, M. & Steenbergen, W. Photoacoustic-guided focused ultrasound (PAFUSion) for identifying reflection artifacts in photoacoustic imaging. *Photoacoustics* **3**, 123–131 (2015).
485. Allman, D., Reiter, A. & Bell, M. A. L. Photoacoustic Source Detection and Reflection Artifact Removal Enabled by Deep Learning. *IEEE Trans. Med. Imaging* **37**, 1464–1477 (2018).
486. Nguyen, H. N. Y. & Steenbergen, W. Reducing artifacts in photoacoustic imaging by using multi-wavelength excitation and transducer displacement. *Biomed. Opt. Express* **10**, 3124 (2019).
487. IThera Medical. Instruction Manual RSOM Explorer Part III. **1.1**, 8 (2018).
488. Wang, Y. *et al.* An Adjustable Dark-Field Acoustic-Resolution Photoacoustic Imaging System with Fiber Bundle-Based Illumination. *Biosensors* **11**, 262 (2021).
489. Liu, C., Liang, Y. & Wang, L. Optical-resolution photoacoustic microscopy of oxygen saturation with nonlinear compensation. *Biomed. Opt. Express* **10**, 3061 (2019).
490. Moothanchery, M. & Pramanik, M. Performance Characterization of a Switchable Acoustic

- Resolution and Optical Resolution Photoacoustic Microscopy System. *Sensors* **17**, 357 (2017).
491. Lu, J. *et al.* In vivo photoacoustic imaging of blood vessels using a homodyne interferometer with zero-crossing triggering. *J. Biomed. Opt.* **22**, 036002 (2017).
492. Otrrock, Z. K., Mahfouz, R. A. R., Makarem, J. A. & Shamseddine, A. I. Understanding the biology of angiogenesis: Review of the most important molecular mechanisms. *Blood Cells, Mol. Dis.* **39**, 212–220 (2007).
493. Lanzen, J. *et al.* Direct Demonstration of Instabilities in Oxygen Concentrations within the Extravascular Compartment of an Experimental Tumor. *Cancer Res.* **66**, 2219–2223 (2006).
494. Intaglietta, M., Myers, R. R., Gross, J. F. & Reinhold, H. S. Dynamics of microvascular flow in implanted mouse mammary tumours. *Bibl. Anat.* 273–6 (1977).
495. Patan, S., Munn, L. L. & Jain, R. K. Intussusceptive Microvascular Growth in a Human Colon Adenocarcinoma Xenograft: A Novel Mechanism of Tumor Angiogenesis. *Microvasc. Res.* **51**, 260–272 (1996).
496. Kiani, M. F., Pries, A. R., Hsu, L. L., Sarelius, I. H. & Cokelet, G. R. Fluctuations in microvascular blood flow parameters caused by hemodynamic mechanisms. *Am. J. Physiol. Circ. Physiol.* **266**, H1822–H1828 (1994).
497. Mollica, F., Jain, R. K. & Netti, P. A. A model for temporal heterogeneities of tumor blood flow. *Microvasc. Res.* **65**, 56–60 (2003).
498. Breathnach, A. *et al.* Assessment of cutaneous melanoma and pigmented skin lesions with photoacoustic imaging. in (eds. Choi, B. *et al.*) vol. 9303 930303 (International Society for Optics and Photonics, 2015).
499. Wang, L. V & Yao, J. A practical guide to photoacoustic tomography in the life sciences. *Nat. Methods* **13**, 627–638 (2016).
500. Tomaszewski, M. R. *et al.* Oxygen Enhanced Optoacoustic Tomography (OE-OT) Reveals Vascular Dynamics in Murine Models of Prostate Cancer. *Theranostics* **7**, 2900–2913 (2017).
501. Di Cristofano, C. *et al.* Nuclear expression of hypoxia-inducible factor-1alpha in clear cell renal cell carcinoma is involved in tumor progression. *Am. J. Surg. Pathol.* **31**, 1875–1881 (2007).
502. Ordóñez, N. G. Immunohistochemical endothelial markers: A review. *Adv. Anat. Pathol.* **19**, 281–295 (2012).
503. Potter, C. & Harris, A. L. Hypoxia inducible carbonic anhydrase IX, marker of tumour hypoxia, survival pathway and therapy target. *Cell Cycle* **3**, 164–7 (2004).
504. Jiang, B. H., Semenza, G. L., Bauer, C. & Marti, H. H. Hypoxia-inducible factor 1 levels vary

- exponentially over a physiologically relevant range of O<sub>2</sub> tension. *Am. J. Physiol. Physiol.* **271**, C1172–C1180 (1996).
505. Dobin, A. *et al.* STAR: ultrafast universal RNA-seq aligner. *Bioinformatics* **29**, 15–21 (2013).
506. Liao, Y., Smyth, G. K. & Shi, W. The Subread aligner: fast, accurate and scalable read mapping by seed-and-vote. *Nucleic Acids Res.* **41**, (2013).
507. Love, M. I., Huber, W. & Anders, S. Moderated estimation of fold change and dispersion for RNA-seq data with DESeq2. *Genome Biol.* **15**, (2014).
508. Subramanian, A. *et al.* Gene set enrichment analysis: a knowledge-based approach for interpreting genome-wide expression profiles. *Proc. Natl. Acad. Sci. U. S. A.* **102**, 15545–15550 (2005).
509. Liberzon, A. *et al.* The Molecular Signatures Database (MSigDB) hallmark gene set collection. *Cell Syst.* **1**, (2015).
510. Hänzelmann, S., Castelo, R. & Guinney, J. GSEA: Gene set variation analysis for microarray and RNA-Seq data. *BMC Bioinformatics* **14**, 1–15 (2013).
511. Baudelet, C. & Gallez, B. Cluster analysis of BOLD fMRI time series in tumors to study the heterogeneity of hemodynamic response to treatment. *Magn. Reson. Med.* **49**, 985–990 (2003).
512. Scargle, J. D. Studies in astronomical time series analysis. II - Statistical aspects of spectral analysis of unevenly spaced data. *Astrophys. J.* **263**, 835–853 (1982).
513. Press, W. H., Teukolsky, S. A., Vetterling, W. T. & Flannery, B. P. Numerical Recipes 3rd Edition: The Art of Scientific Computing. *Cambridge Univ. Press* **3**, 685-689. (2007).
514. Gonçalves, M. R. Characterisation of cycling tumour hypoxia with magnetic resonance imaging.
515. Stolz, B. J. *et al.* Multiscale topology characterises dynamic tumour vascular networks. *arXiv* (2020) doi:2008.08667.
516. Yasui, H. *et al.* Low-field magnetic resonance imaging to visualize chronic and cycling hypoxia in tumor-bearing mice. *Cancer Res.* **70**, 6427–6436 (2010).
517. Brown, E., Brunker, J. & Bohndiek, S. E. Photoacoustic imaging as a tool to probe the tumour microenvironment. *Dis. Model. Mech.* **12**, dmm039636 (2019).
518. Imai, T. *et al.* Direct measurement of hypoxia in a xenograft multiple myeloma model by optical-resolution photoacoustic microscopy. **18**, 101–105 (2017).
519. Hanahan, D. Hallmarks of Cancer: New Dimensions. *Cancer Discov.* **12**, 31–46 (2022).
520. Chaplin, D. J. & Hill, S. A. Temporal heterogeneity in microregional erythrocyte flux in experimental solid tumours. *Br. J. Cancer* **71**, 1210–1213 (1995).

521. Kimura, H. *et al.* Fluctuations in red cell flux in tumor microvessels can lead to transient hypoxia and reoxygenation in tumor parenchyma. *Cancer Res.* **56**, 5522–8 (1996).
522. Brurberg, K. G., Skogmo, H. K., Graff, B. A., Olsen, D. R. & Rofstad, E. K. Fluctuations in pO<sub>2</sub> in poorly and well-oxygenated spontaneous canine tumors before and during fractionated radiation therapy. *Radiother. Oncol.* **77**, 220–226 (2005).
523. Brurberg, K. G., Gaustad, J. V., Mollatt, C. S. & Rofstad, E. K. Temporal heterogeneity in blood supply in human tumor xenografts. *Neoplasia* **10**, 727–735 (2008).
524. Pigott, K. H., Hill, S. A., Chaplin, D. J. & Saunders, M. I. Microregional fluctuations in perfusion within human tumours detected using laser Doppler flowmetry. *Radiother. Oncol.* **40**, 45–50 (1996).
525. Alam, I. S. *et al.* Radiolabeled RGD tracer kinetics annotates differential  $\alpha v\beta 3$  integrin expression linked to cell intrinsic and vessel expression. *Mol. Imaging Biol.* **16**, 558–566 (2014).
526. Omar, M., Gateau, J. & Ntziachristos, V. Raster-scan optoacoustic mesoscopy in the 25-125 MHz range. *Opt. Lett.* **38**, 2472–4 (2013).
527. Comşa, Ş., Cîmpean, A. M. & Raica, M. The Story of MCF-7 Breast Cancer Cell Line: 40 years of Experience in Research. *Anticancer Res.* **35**, 3147–54 (2015).
528. Nisar, M. A. *et al.* IL-1 $\beta$  Promotes Vasculogenic Mimicry of Breast Cancer Cells Through p38/MAPK and PI3K/Akt Signaling Pathways. *Front. Oncol.* **11**, (2021).
529. Shi, Z. *et al.* Attenuation of intermittent hypoxia-induced apoptosis and fibrosis in pulmonary tissues via suppression of ER stress activation. *BMC Pulm. Med.* **20**, 1–11 (2020).
530. Bell, H. S., Whittle, I. R., Walker, M., Leaver, H. A. & Wharton, S. B. The development of necrosis and apoptosis in glioma: experimental findings using spheroid culture systems\*. *Neuropathol. Appl. Neurobiol.* **27**, 291–304 (2001).
531. Mehrabi, M., Amini, F. & Mehrabi, S. Active role of the necrotic zone in desensitization of hypoxic macrophages and regulation of CSC-fate: A hypothesis. *Front. Oncol.* **8**, 235 (2018).
532. Brochu, F. M., Joseph, J., Tomaszewski, M. & Bohndiek, S. E. Light fluence correction for quantitative determination of tissue absorption coefficient using multi-spectral optoacoustic tomography. in (eds. Ntziachristos, V. & Zemp, R.) 95390Z (SPIE, 2015). doi:10.1117/12.2182416.
533. Fadhel, M. N., Hysi, E., Assi, H. & Kolios, M. C. Fluence-matching technique using photoacoustic radiofrequency spectra for improving estimates of oxygen saturation. *Photoacoustics* **19**, 100182 (2020).
534. He, H. *et al.* Fast raster-scan optoacoustic mesoscopy enables assessment of human melanoma

- microvasculature in vivo. *medRxiv* 2021.05.25.21257525 (2021)  
doi:10.1101/2021.05.25.21257525.
535. Clarke, G. D. *Overview of the ACR MRI Accreditation Phantom*.
536. Hlushchuk, R. *et al.* Cutting-edge microangio-CT: New dimensions in vascular imaging and kidney morphometry. *Am. J. Physiol. - Ren. Physiol.* **314**, F493–F499 (2018).
537. Schaad, L. *et al.* Correlative Imaging of the Murine Hind Limb Vasculature and Muscle Tissue by MicroCT and Light Microscopy. *Sci. Reports 2017 71* **7**, 1–12 (2017).
538. Glaser, A. K. *et al.* Multi-immersion open-top light-sheet microscope for high-throughput imaging of cleared tissues. *Nat. Commun.* **10**, 2781 (2019).
539. Matsumoto, S. *et al.* Antiangiogenic agent sunitinib transiently increases tumor oxygenation and suppresses cycling hypoxia. *Cancer Res.* **71**, 6350–6359 (2011).
540. Chaplin, D. J., Horsman, M. R. & Trotter, M. J. Effect of Nicotinamide on the Microregional Heterogeneity of Oxygen Delivery Within a Murine Tumor. *JNCI J. Natl. Cancer Inst.* **82**, 672–676 (1990).
541. Horsman, M. R., Chaplin, D. J. & Overgaard, J. Combination of nicotinamide and hyperthermia to eliminate radioresistant chronically and acutely hypoxic tumor cells. *Cancer Res.* **50**, 7430–6 (1990).
542. Chaplin, D., Trotter, M., Skov, K. & Horsman, M. Modification of tumour radiation response in vivo by the benzamide analogue pyrazinamide. *Br. J. Cancer* **62**, 561–566 (1990).
543. Honess, D. J., Dennis, I. F. & Bleehen, N. M. Pentoxifylline: its pharmacokinetics and ability to improve tumour perfusion and radiosensitivity in mice. *Radiother. Oncol.* **28**, 208–218 (1993).
544. Horsman, M. R., Sørensen, B. S., Busk, M. & Siemann, D. W. Therapeutic Modification of Hypoxia. *Clin. Oncol.* **33**, e492–e509 (2021).
545. van den Berg, P. J., Daoudi, K. & Steenbergen, W. Review of photoacoustic flow imaging: its current state and its promises. *Photoacoustics* **3**, 89–99 (2015).
546. Razansky, D., Klohs, J. & Ni, R. Multi-scale optoacoustic molecular imaging of brain diseases. doi:10.1007/s00259-021-05207-4.
547. Zhu, X. *et al.* Real-time whole-brain imaging of hemodynamics and oxygenation at micro-vessel resolution with ultrafast wide-field photoacoustic microscopy. *Light Sci. Appl.* **11**, 138 (2022).
548. Stein, E. W., Maslov, K. & Wang, L. V. Noninvasive, in vivo imaging of blood-oxygenation dynamics within the mouse brain using photoacoustic microscopy. *J. Biomed. Opt.* **14**, 020502 (2009).

